THE UNIVERSITY *of* EDINBURGH

Microwave Imaging for Ultra-Wideband Antenna Based Cancer Detection

Haoyu Zhang

A thesis submitted for the

Degree of Doctor of Philosophy

The University of Edinburgh

2014

Declaration

I hereby declare that this thesis has been composed and originated by myself and that except where stated, the work contained is my own.

_____

Haoyu Zhang

July 2014

Acknowledgements

I wish to express my gratitude to my supervisors, Prof. Tughrul Arslan and Dr. Brian Flynn for their invaluable support, encouragement and guidance throughout my research.

I would also like to thank all my colleagues in the Embedded Wireless Systems Group for their friendship and support.

My special thanks are due to my family for their encouragement.

Abstract

Breast cancer is one of the most widespread types of cancer in the world. The key factor in treatment is to reliably diagnose the cancer in the early stages. Moreover, currently used clinical diagnostic methods, such as X-ray, ultra-sound and MRI, are limited by cost and reliability issues. These limitations have motivated researchers to develop a more effective, low-cost diagnostic method and involving lower ionization for cancer detection. In this thesis, radar based microwave imaging is proposed as a method for early breast cancer detection. This imaging system has advantages such as low cost, being non-invasive and easy to use, with high image resolution and its thus good potential for early cancer detection.

In the first stage, an ultra-wideband Vivaldi antenna and a slot Vivaldi antenna are proposed, simulated and fabricated for breast cancer detection. The designed antennas exhibit an ultra-wideband working frequency. The radiation patterns also achieve the desired directional radiation patterns.

The second stage of this study presents a planar breast phantom and a hemi-sphere breast phantom. These two breast phantoms are simulated and fabricated using CST microwave studio and tissue-mimicking materials respectively. Mono-static radar systems based on a single antenna configuration and an antenna pair configuration are then proposed. These two systems are used to measure the planar breast phantom and hemi-sphere breast phantom, with the scattering signals measured in the frequency and time domains. Based on the measurement results, it is concluded that the reflected energy increases when the antenna moves close to the tumour; otherwise, the reflected energy is reduced when the antenna moves away from the tumour.

The received time domain scattering signals are processed first and then used to create microwave images to indicate tumour position. A clutter removal method is proposed to extract the tumour response from the received signals. The microwave images are then created using the tumour response based on the simulation and

experimental results. The imaging results indicate that a 5 mm radius tumour can be detected.

The tumour burial depth is also studied. A multi bio-layer phantom which contains deep and shallow buried tumours is simulated and measured using the Vivaldi antenna. A spectrum analysis method is proposed to distinguish between different tumour depths. The results indicate that a difference in depth of 15 mm results in a mean change of 0.3 dB in the magnitude of the spectrum.

Discrimination between benign and malignant tumours is also considered in this study. The singularity expansion method (SEM) for breast cancer is proposed to discriminate between benign and malignant tumours based on their morphology. Two cancerous breast phantoms are developed in CST. The benign tumour is a 5mm radius sphere and the malignant tumour is a spiny sphere with an average radius of 5mm. The use of the SEM leads to the successful discrimination of these two tumours. This method provides a solution to discriminate between benign and malignant tumours similar size when the resulting images cannot provide sufficient resolution.

A preliminary study of brain cancer detection is also concluded. Research in this area has never been implemented. A cancerous brain model is designed and simulated in CST. The antenna pair configuration is then used to measure the cancerous brain, with the scattering signals measured. Microwave images for brain cancer detection are then created based on the measurement results. The tumour is correctly indicated in the resulting images.

TABLE OF CONTENT

List of Figures

List of Tables

Acronyms and Abbreviations

1D	**1 Dimensional**
2D	**2 Dimensional**
3D	**3 Dimensional**
FDTD	**Finite-difference time-domain**
MRI	**Magnetic Resonance Imaging**
GPR	**Ground Penetrating Radar**
UWB	**Ultra-Wideband**
TM	**Tissue Mimic**
SEM	**Singularity Expansion Method**
CNRs	**Complex Natural Resonances**
VNA	**Vector Network Analyzer**
HEBW	**Half Energy Beam Width**
HPBW	**Half Power Beam Width**
FCC	**Federal Communications Commission**
PCB	**Printed Circuit Board**
TSAs	**Tapered Slot Antennas**
LTSA	**Linearly Tapered Slot Antenna**
CWSA	**Constant Width Slot Antenna**

SAR	**Specific Absorption Rate**
LHS	**Left Hand Side**
RHS	**Right Hand Side**
PCS	**Perfect Conducting Sphere**
ETR	**Early Time Response**
LTR	**Late Time Response**
CT	**Computed Tomography**
CWT	**Continuous Wavelet Transform**
DWT	**Discrete Wavelet Transform**
MRA	**Multi-Resolution Algorithm**
IWT	**Inverse Wavelet Transform**
SNRs	**Signal to Noise Ratios**
TDI	**Tumour Depth Information**

Chapter 1 Introduction

1.1 Research Motivation

Breast cancer is one of the most widespread cancer types in the world. For example, in the USA, breast cancer is exceeded in frequency only by lung cancer [1]. Nearly 182,000 breast cancer cases are diagnosed in the USA every year. In Ireland [2], for example, 1 in 11 females are likely to suffer from this cancer. But it is encouraging that over 25,000 female patients have survived, which means that breast cancer is not an incurable disease. The key factor is to reliably diagnose it in the early stages. Given early breast cancer detection and treatment, the survival rate can even reach 97% in Ireland [2], which emphasises the urgent requirement for a reliable and highly efficient method of early breast cancer detection.

The most commonly used clinical diagnostic methods for breast cancer are X-ray Mammography, Ultra-sound and Magnetic Resonance Imaging (MRI) [3-4]. These three methods are used in regular medical examinations or for breast cancer diagnosis in patients with no symptoms. These three methods are painless compared with medical biopsy and are widely used in clinical diagnosis. However, X-ray Mammography [4] is quite painful due to breast compression. Beside this, the high level ionizing radiation involved are harmful to patients, and may even cause canceration of healthy tissues. With the use of the Ultra-sound system [4], it is difficult to detect deep-lying or solid cancerous tissue. The MRI system [4] provides extremely high resolution images of soft tissues, especially for small tumours. However, the

highly costly and time-consuming diagnostic processes are major shortcomings. These limitations have motivated researchers to develop a more effective with lower level ionization and low cost diagnosis method for cancer detection.

In this thesis, radar based microwave imaging is proposed as an early cancer detection method. This imaging system has advantages such as low cost, being non-invasive and easy-use, giving high image resolution and thus with potential for early cancer detection.

Microwave imaging for cancer detection is based on the high differences in electrical properties difference between cancerous and surrounding tissues. The electromagnetic properties of electromagnetic wave interacting with a medium mainly depend on the relative permittivity and conductivity of that medium. A wide range scale of studies [5-9] revealed that the content of water in tissues determines their relative permittivity. Tissues with high water content, such as tumour have higher relative permittivity compared to low water tissues such as fat. The relative permittivity of the tissue is related to its electromagnetic energy storability, while the conductivity of the tissue indicates the attenuation of microwave energy when the microwave interacts it. Cancer detection based on microwave imaging relies on high differences in relative permittivity between healthy and malignant tissues. The relative permittivity of breast tissue in different frequency ranges has been studied [5-9], and the results prove that differences in relative permittivity between tumours and healthy tissue are sufficient for microwave images to show.

Radar based imaging methods originating from ground-penetrating radar (GPR) were proposed for breast cancer detection by Hagness [10-13]. This radar based microwave imaging aims at focusing on the determination of objects such as tumours by creating images of back-scattering signals which arise the high dielectric constant difference between a tumour and surrounding healthy tissue. Compared with microwave tomography [14], the radar based microwave imaging only focuses on

detecting the tumour rather than the entire range of electrical properties. Therefore, the signal processing involved in radar based microwave imaging is much easier than that in microwave tomography. Beside this, radar based microwave imaging uses an Ultra-Wideband (UWB) pulse which includes low to high frequencies. The low frequency band ensures depth of penetration while the high frequency band ensures the resolution of the resulting images. Hence, both deeply buried and small size tumours can be detected based on the examination of the low frequency and high frequency bands.

1.2 Research Investigations and Novelty

The main components of the radar based microwave imaging in this study are the imaging system design based on ultra-wideband antennas, the design of breast phantom, signal processing and image processing methods. In this thesis, the following challenges have been addressed.

1.2.1 Challenges

1.2.1.1 Ultra-wideband Antenna Design

Currently, multi-static and mono-static radar systems are used for breast cancer detection [15-18]. The multi-static radar system [15, 17 and 18] uses an antenna array and a complex switch network controller. The antenna array normally consists of more than ten antennas in order to collect a large number of transmission coefficients and this will obtain images of high resolution. The problem here [18] is that the geometrical dimensions of the antennas used must be as small as possible in order to

maximise the number of antennas used in the array. This, in turn, will result in a higher working frequency band which lacks the required penetration of electromagnetic energy into the breast [18]. On the other hand, the mono-static radar system [16] uses a single antenna or an antenna pair to scan the breast with mechanical movement. Hence, the design of the antenna is only concerned with the gain, bandwidth, radiation pattern and beam width.

1.2.1.2 **Breast Phantom Design and Experimental Setup**

The phantom design for the UWB transmission can be simplified in an approximation as a multi-layer model, with each layer corresponding to a particular layer [19]. The breast can also be modelled as layers of skin and fat. Representations of tumours and glands can then be fabricated and inserted into these special layers. Based on this theory, the breast phantom is simulated in the CST Microwave Studio software using the FDTD method [20-21]. In CST, a library which consists of a range of materials is available for use in designing the microwave devices as well as bio-organs.

Electromagnetic based technology such as mobile phones and medical imaging applications works at microwave frequency. Therefore, the growing interest of the interaction of microwaves with bio-tissues has led the researchers to design bio-phantoms which mimic the electrical properties in the microwave frequency range. The most attractive tissue mimicking method is based on gelatine-oil [22-23]. This method has advantages such as giving stable mechanical properties at low cost and with easy fabrication.

A mono-static radar system is adopted in this thesis. The challenges involved concern the different antenna configurations such as a single antenna configuration

and configurations of antenna pair. The spatial relationship between the antenna and the breast phantom, and the reduction of the mutual coupling between the transmitting and receiving antennas also need to be considered.

1.2.1.3 **Signal Processing**

The scattering signals collected contain skin reflections, multiple reflections from different layers, the tumour response and environmental noise. The tumour response is quite weak, and could easily be drowned out in the noise. Hence, signal processing is required in order to remove all unwanted parts of the signal in order to obtain high resolution images with low noise level for diagnosis. Skin and clutter removal methods have been proposed in many publications [17, 24-25]. A commonly used method for the removal of the presence of an unwanted signal is to measure reference transient scattering signals using a breast without tumour being presence. The reference signals only contain the skin reflection and clutter, and can then be used to calibrate the originally received signals. The tumour response can be extracted by subtracting the reference signal. This method is easily applied and able to remove the unwanted parts of the signal effectively. However, the problem is that this method cannot be applied in practice since the tumour cannot be removed and an identical healthy breast is also unavailable. Signal de-noising is thus a serious challenge in signal processing.

1.2.1.4 **Discrimination between Benign and Malignant Tumours**

The discrimination of benign and malignant tumours is mainly based on the content of water within the tumour [26-28]. The increase of water content in a tumour

signifies the deterioration of cells, and this increases the values of dielectric constants and the conductivity of the tumour. Furthermore, the morphology of the tumour is another useful characteristic [29-31] which can be used to discriminate between benign and malignant tumours in terms of their size and surfaces. A malignant tumour usually has an irregular surface and spiculated periphery, while benign tumours have smoother surfaces and a roughly spherical shape. These two major discrimination criteria are often used in MRI and ultra-sonic imaging.

Previous radar based cancer detection research has assumed that tumours have uniform shapes such as a sphere or ellipsoid [32-38]. Actually, tumours can also be classified as benign or malignant. Hence, the discrimination between benign and malignant tumours is also very important and needs to be addressed.

1.2.1.5 **The Preliminary Study of Brain Cancer Detection**

Radar based breast cancer detection has been investigated by many research groups. However, the study of radar based cancer detection for other organs has not yet been considered. In the presented study, brain cancer detection is considered since the brain has a similar shape to that of the breast. Both the breast and the human head have a spherical shape, and moreover are all composed of different layers. The breast can be considered as layers of skin and fat and the human head can be considered as a combination of skin, fat, bone and white matter layers [19].

From electromagnetic theory, the discontinuities of the boundaries cause strong reflections of incident electromagnetic wave [32-38]. The reflection level is highly dependent on the dielectric difference. For example, in breast cancer detection, the dielectric difference between the tumour and the fat can reach 10:1 [17]. For the brain cancer detection, the dielectric difference between the tumour and the white matter

can reach 1.44:1. This dielectric constant difference in the brain can still be observed even though it is much smaller than that of the breast.

The ability of microwave to penetrate tissue is another important issue. In breast cancer detection, most of the incident wave is reflected by the skin and only very little energy reaches the tumour. Compared to this, the human head has more complex structure (skin, fat, skull and white matter) [19] and might reflect even more energy than the skin layer of the breast. This could be a major challenge for brain cancer detection.

1.2.2 Research Objectives

The main objectives in this thesis are as follows:

1. to design an ultra-wideband antenna for breast cancer detection,
2. to design a breast phantom for the microwave imaging system,
3. to develop a signal processing method to remove the skin response and clutter,
4. to develop a signal de-noising method to suppress noise,
5. to study electromagnetic theory in the near-field,
6. to develop a signal processing method to discriminate between benign and malignant tumours, and
7. to study radar based brain cancer detection.

1.2.3 Novelty

The novel aspects of the present work are as follows:

1. A novel ultra-wideband directional Vivaldi antenna and a modified slot-Vivaldi antenna are proposed, simulated and fabricated. This Vivaldi antenna operates as a breast cancer detector with the advantages of ultra-wideband performance (5-10 GHz), high near-field power flow density, and compact dimensions.
3. Two proposed antenna configurations are used to measure the simulated and fabricated planar and hemi-sphere phantoms, with the simulated and measured signals recorded and analyzed.
4. A novel signal processing method is proposed and applied to the received scattering signals. This method is able to remove the unwanted parts of signals such as skin reflections and clutters.
5. Microwave images based on the single antenna and antenna pair configurations are created to indicate tumour position. A tumour with radius of 5 mm is clearly detected.
6. The Singularity Expansion Method (SEM) is proposed for breast cancer detection and applied to discriminate between benign and malignant tumours both with a 5 mm radius benign tumour and malignant tumour can be distinguished using the SEM.
7. A spectrum analysis based method for the detection of tumour depth is proposed. The Vivaldi antenna and the slot Vivaldi antenna are used to measure tumour of different depth. The results indicate that the use of the slot Vivaldi antenna provides better detection capability.
8. A wavelet based de-noising method is proposed and applied to the scattering signals. The use of this method can significantly suppress the noise.
9. A preliminary study of brain cancer detection based on the microwave imaging is carried out. To the best knowledge, research such as this has never been conducted before.

1.3 Publications

Haoyu Zhang; Arslan, Tughrul; Flynn, Brian, "*Wavelet de-noising based microwave imaging for brain cancer detection,*" Antennas and Propagation Conference (LAPC), 2013 Loughborough , pp.482,485, 11-12 Nov. 2013

Haoyu Zhang; Arslan, Tughrul; Flynn, Brian, "*A single antenna based microwave system for breast cancer detection: Experimental results*," Antennas and Propagation Conference (LAPC), 2013 Loughborough , pp.477,481, 11-12 Nov. 2013

Haoyu Zhang; Arslan, Tughrul; Flynn, Brian, "*Microwave imaging of a realistic cancerous phantom using an ultra-wideband antenna transceiver system*," Antennas and Propagation Conference (LAPC), 2013 Loughborough ,pp.112,116, 11-12 Nov. 2013

Haoyu Zhang; Brian Flynn; Ahmet, T. Erdogan; Tughrul, Arslan, *"Microwave Imaging for Brain Tumour Detection Using an UWB Vivaldi Antenna Array"*, Loughborough Antennas & Propagation Conference 2012 (LAPC 2012), Loughborough, UK, November 12-13, 2012.

Haoyu Zhang; El-Rayis, A.O.; Haridas, N.; Noordin, N.H.; Erdogan, A.T.; Arslan, T., *"A smart antenna array for brain cancer detection,"* Antennas and Propagation Conference (LAPC), 2011 Loughborough , vol., no., pp.1,4, 14-15 Nov. 2011

Haoyu Zhang; Arslan, Tughrul; Flynn, Brian, "*Microwave imaging for Breast Cancer Detection: The Discrimination of Breast Lesion Morphology*," submitted to IEEE Journal of Biomedical and Health Informatics.

1.4 Thesis Structure

In chapter 2, a brief overview of issues related to breast cancer is presented. These include the physiology of the cancerous breast, currently used clinical diagnostic methods and microwave imaging for breast cancer detection.

In chapter 3, the principles and important parameters of the Vivaldi antenna are discussed and analyzed first. The final optimized Vivaldi antenna and the measurement results are then presented. A slot Vivaldi antenna which is modified from the original Vivaldi antenna design using the equivalent circuit model method is also proposed.

In chapter 4, a planar breast phantom and a hemi-sphere breast phantom are proposed. These two phantoms are simulated using CST software and fabricated using the Tissue Mimicking method. Two antenna configurations, with a single antenna or a pair of antenna are also proposed and used to measure the phantoms, with the simulated and measured scattering parameters recorded.

In chapter 5, the near-field electromagnetic theory for breast cancer detection is discussed, and then a skin effect and clutter removal method is proposed. The wavelet de-noising method is also proposed and applied to the scattering signals.

In chapter 6, the received scattering signals which are obtained from the Vivaldi antenna, slot Vivaldi antenna and single and antenna pair configurations are used to create the microwave images to indicate the position of tumour. The Singularity Expansion Method (SEM) for breast cancer detection is proposed and applied to discriminate between benign and malignant tumours. Furthermore, a method for the measurement of tumour depth based on spectrum analysis is proposed. Finally, the preliminary study of brain cancer detection is presented.

In chapter 7, the conclusions of the study and suggestions for future work are discussed.

1.5 Summary

Microwave imaging based breast cancer detection has the potential to be used for cancer diagnosis and to replace currently used clinical methods, based on its low cost, non-ionizing radiation, efficiency and small dimensions. The study of microwave imaging based cancer detection should focus on antenna and system design, signal and image processing.

Chapter 2 Background

2.1 Introduction

This chapter discusses the background of breast cancer in regard to the physiology of cancerous breast, and current breast cancer detection methods. This chapter provides necessary and important background information for the following chapters, especially for the cancerous breast phantom design. The structure of this chapter is organized as following. First, the physiology of the breast is introduced; followed by a discussion of current breast cancer detection methods. In the end, the final section focuses on the introduction of radar based microwave imaging for breast cancer detection.

2.2 Physiology of Breast

2.2.1 Anatomy of Breast

The anatomy of the breast [40] and its surrounding tissues are illustrated in Fig 2.1 [66]. In general, the breast is composed of skin, fat, connective tissue and glandular tissue. The breast lies on the chest wall with a shape which varies between individuals [41]. The proportions of fat, connective and glandular tissue also vary between different people and according to physiological periods such as pregnancy

and lactation [42]. The main function of the connective tissue (Copper's ligament) is to maintain the structure of the breast. The mammary gland which produces breast milk spreads inside the breast, connected by the lactiferous ducts and terminating at the nipple.

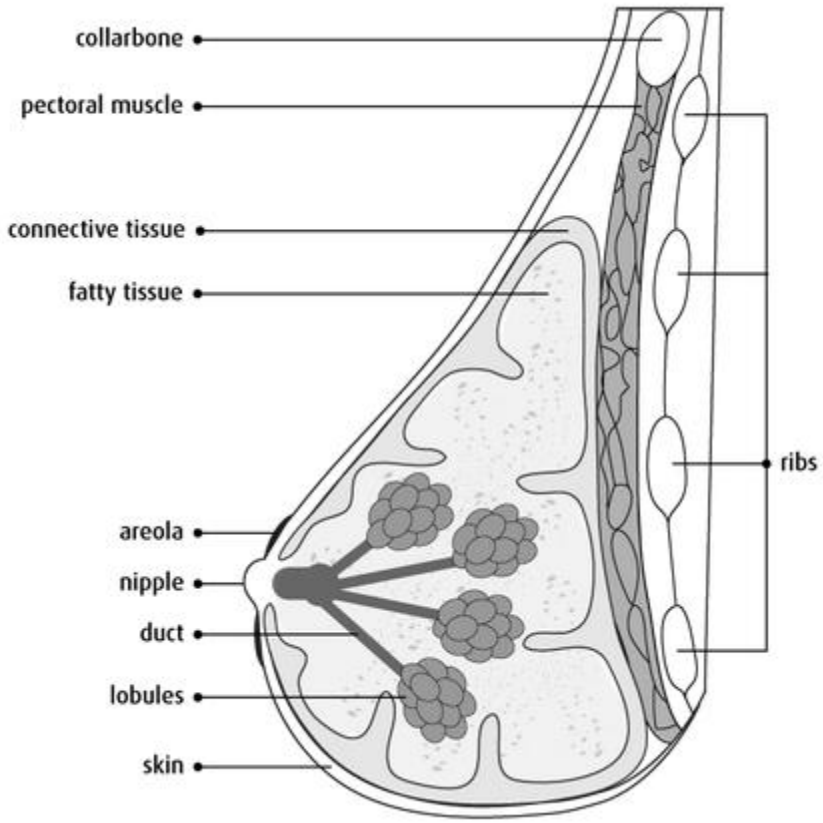

Fig 2.1 Anatomy of Breast. [66]

2.2.2 Breast Tumour

A tumour [43-44] is formed by a lump of tissue which is composed of abnormally growing cells called cancerous cells. Normally, a small number of cancerous cells can be destroyed by the immune system. However, if the growth rate of the tumour

reaches the limits of the immune system's response capability, the cancerous cells may be out of control and form a mass of tissue. Cancerous cell can originate from the excitation of oncogenes or gene mutations.

Tumours [44] can be mainly classified as benign, potentially malignant and malignant. A benign tumour grows with a controllable speed and does not become transformed into a malignant tumour. Besides, the benign tumour does not invade or destroy surrounding cells or tissues. A potentially malignant tumour is a transitional form of the malignant tumour, and may be transformed into a malignant tumour given enough time. During this period, the potentially malignant tumour acts as a benign tumour and does not destroy surrounding healthy cells. A malignant tumour invades and destroys healthy cells and may grow at a high rate or spread to other adjacent organs.

The discrimination between benign and malignant tumours is mainly based on the content of water within the tumour [45-47]. An increase in water content in tumour signifies the deterioration of cells, and this increases the values of the dielectric constant and conductivity of the tumour. Furthermore, morphology [45-48] is another useful characteristic in discriminating between benign and malignant tumours in terms of their size, surface and packing density. A malignant tumour usually has an irregular surface and spiculated periphery and a benign tumour has a smoother surface and roughly spherical shape. These two major criteria are often used in medical diagnosis, such as when using MRI and ultra-sonic imaging.

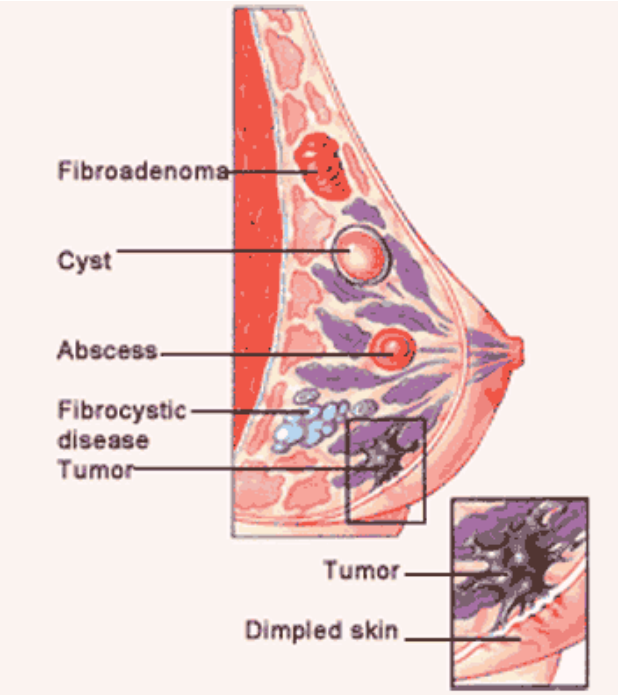

Fig 2.2 The Anatomy of the Cancerous Breast. [67]

Breast cancer [43] is a common cancer in women which usually originates from the lactiferous ducts. Genetic mutation, family history or environmental effects could cause breast cancer. **Fig 2.2** shows the anatomy of a cancerous breast. The types of cancer can be classified as non-invasive and invasive. The most common breast cancer is invasive breast cancer (90% of cases). Specifically, Invasive Ductal Carcinoma, which occurs in the ducts, is the most common form of invasive breast cancer, according for more than 75% of cases.

2.2.3 Electrical properties

Electromagnetic based microwave imaging for cancer detection is based on the electrical properties of cancerous and surrounding tissues. The electrical properties of the tissues include two main parameters called relative permittivity and conductivity. The electromagnetic properties of the electromagnetic wave interacting with a medium mainly depend on its relative permittivity and conductivity. Many studies [48-55] have revealed that the content of water in a tissue determines its relative permittivity. Tissues with high water content tissues such as tumour have higher relative permittivity than those with low water content tissues such as fat. The relative permittivity of a tissue is related to the storability of electromagnetic energy in the tissue while the conductivity of the tissue indicates the attenuation of microwave energy when the microwave interacts with it.

Cancer detection based on microwave imaging relies on large differences in electromagnetic properties between healthy and malignant tissues. The electromagnetic properties of breast tissue in different frequency ranges have been studied [48-52], proving that differences in the relative permittivity are sufficient for the microwave image. The contrast for relative permittivity and conductivity of normal and malignant breast tissues across 3MHz -3GHz range have been found to be 4.7:1 and 5:1 respectively [54]. The relative permittivity and conductivity of normal, benign and malignant tissues have also been measured in the range between 500MHz to 20 GHz [55]. A Cole-Cole model has been developed based on relative permittivity and conductivity, as given in Equation (2.2.1) [54-55]:

$$\varepsilon_\omega = \varepsilon_\infty + \frac{\varepsilon_s - \varepsilon_\infty}{1+(i\omega\tau)^{1-\alpha}} \qquad (2.2.1)$$

where, ω and α are the angular frequency and exponent parameter, ε_∞ and τ are the static frequency permittivity constants and time constant and ε_ω and ε_s are static and infinite frequency permittivity constants. Fig 2.3 shows the Cole-Cole model and several studies of the relative permittivity and conductivity of benign and malignant tissues.

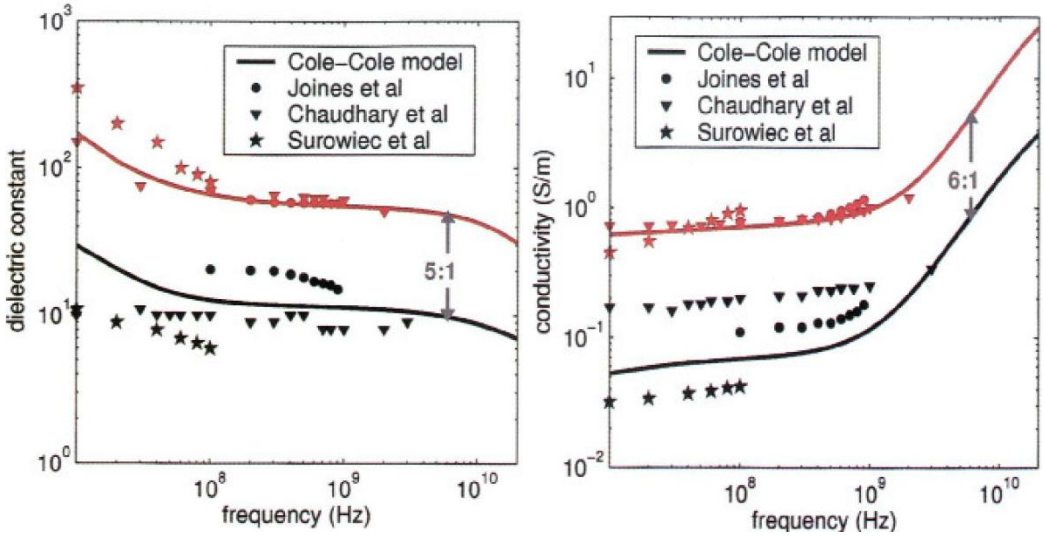

(a) **(b)**

Fig 2.3 Measured Relative Permittivity and Conductivity. Black: Benign tumour, Red: Malignant tumour. [54]

2.3 Currently Used Clinical Diagnostic Methods

The most commonly used clinical diagnostic methods for breast cancer are X-ray Mammography, Ultra-sound and Magnetic Resonance Imaging (MRI) [56]. These three methods are used in regular medical examinations or for breast cancer diagnosis for patients with no symptoms. These three methods are painless compared with the medical biopsy and are widely used in clinical diagnosis. The principles of these three methods are summarized as follows.

2.3.1 X-ray Mammography

X-ray Mammography [56-57] uses X-rays as the examination wave to pass through the breast which is compressed by two plates, as shown in **Fig 2.4**. Images of the breast are then recorded on film for diagnosis. This process is efficient in terms of time but is quite painful due to the breast compression. Besides, the high levels of ionizing radiation involved are harmful to patients, and may even cause canceration of healthy tissues. The resolution of the resulting images is sufficient for most diagnostic requirement, but not enough for a high dense breast.

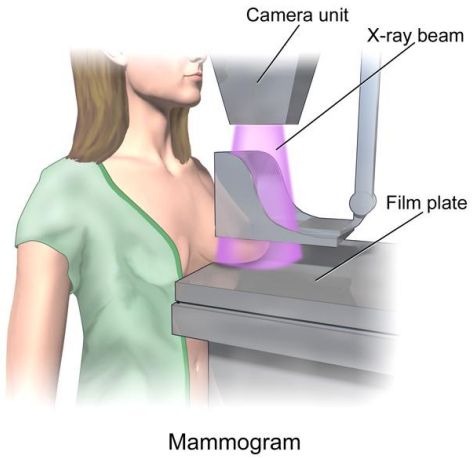

Fig 2.4 X-ray Mammography. [67]

2.3.2 Ultrasound imaging

Ultrasound Imaging System (**Fig 2.5**) [56] is based on the use of ultrasonic wave ranging from 1MHz to 15MHz. The radiation in this frequency range is not harmful to patients, however, it may be difficult to detect and distinguish deep lying and solid cancerous tissue. The resulting images can be in any orientation due to real time screening. Hence, the diagnosis of cancer is dependent on the doctor's experience.

Fig 2.5 Ultrasound Imaging. [69]

2.3.3 Magnetic Resonance Imaging (MRI)

Magnetic Resonance Imaging (MRI) [56, 58] is based on the use of magnets to generate a very strong magnetic field for the creation of a pathological image. The patient lies on an examination table with several small scanner devices placed around breast to examine, as shown in **Fig 2.6**. The high sensitivity of MRI provides extremely high resolution images for soft tissues, and especially for small tumours. However, its high cost and the time consuming diagnosis process are major shortcomings.

As discussed above, the advantages and disadvantages of diagnostic method can be classified as cost, safety, accuracy and scope of application. The limitations of these three methods have motivated researchers to develop a more effective, lower ionizing and low cost diagnosis method for cancer detection. For this purpose, microwave imaging has become a potentially significant method and is introduced in the next section.

Fig 2.6 Magnetic Resonance Imaging (MRI). [70]

2.4 Microwave Imaging for Breast Cancer Detection

Microwave imaging for cancer detection has advantages such as low-cost and the lack of dangerous radiation, and has attracted the attention of many research groups. Various types of microwave imaging methods, which can be classified as passive or active microwave imaging, have been proposed over the years. Passive microwave imaging [60] is based on the high temperature difference between the cancerous and healthy tissues when the breast is illuminated by microwave radiation. A radiometer is often used to transmit and receive the microwave signals and uses the received signals to map the temperature distribution for diagnosis. However, the challenge for passive microwave imaging is that the power radiated by tumour is not easy to detect. The

sensitivity of the radiometer must be high enough to detect small changes in radiated power. Besides, environmental heat source may easily interfere with the radiometer.

Active microwave imaging relies on large differences in electromagnetic properties between healthy and malignant tissues. Two active microwave imaging methods have been proposed, namely microwave tomography [61] and radar based imaging [62-65]. Active microwave imaging is of most interest in this thesis and is discussed in the next section.

2.4.1 Active microwave imaging

Microwave tomography and radar-based microwave imaging are two major active microwave imaging approaches. The microwave tomography seeks to reconstruct the electrical profile inside the breast by solving inverse scattering problems [62, 65]. This procedure involves the solving of non-linear functions which causes difficulties in signal processing and image reconstruction. The radar based imaging method originates from ground-penetrating radar (GPR) and was proposed for breast cancer detection. This method focuses on the detection of objects such as tumours by creating images based on the high dielectric difference between a tumour and surrounding healthy tissues.

2.4.1.1 Microwave Tomography

For typical microwave tomography [61], the patient lies on an examination table with the breast through a hole and surrounded by a tank, as shown in **Fig 2.7**. An antenna array configured in the tank is immersed in coupling liquid in order to reduce noise and the discontinued electrical boundaries which cause multi-reflections. This antenna array is composed of several antennas to transmit and receive microwave

signals. The signals are used to measure the electrical properties such as relative permittivity and conductivity. The amplitude of the electrical properties of the whole breast is then mapped to indicate the tumour position, based on the principle that the tumour attenuates the strength of the signal to increase the electrical properties. The increases in electrical properties can be used to determine the tumour's position. Normally, a small antenna such as a monopole antenna is used in a microwave tomography prototype in order to maximize the number of configured antennas. The antenna array rotates vertically in small step to scan the breast. At each stop position, one antenna is used as transmitting antenna to transmit incident wave and the rest antennas are as receiving antenna to receive scatter wave. These received signals are normally processed by the solving of non-linear functions, and this is the most difficult part of microwave tomography. It is worth noting that microwave tomography attempts to reconstruct a map of all of electrical properties of the breast, whereas radar based microwave imaging only focuses on imaging the tumour rather than the whole breast.

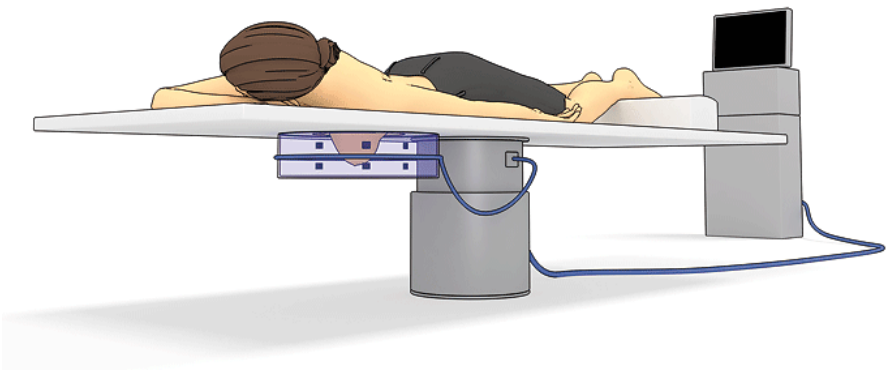

Fig 2.7 Microwave Tomography. [71]

2.4.1.2 Radar based Microwave Imaging

The radar based imaging method aims at focusing on the determination of the position of an object (tumour) by creating images using back-scattering signals. Compared with microwave tomography, radar based microwave imaging only focuses on imaging the tumour rather than the whole breast. Therefore, the signal processing involved in radar based microwave imaging is much easier than that in microwave tomography. Besides, radar based microwave imaging uses an Ultra-wideband (UWB) Pulse which includes low to high frequencies. The low frequency band ensures a sufficient depth of penetration while the high frequency band ensures the sufficient resolution of the resulting images. Hence, both the deeply buried and small size tumour can be detected based on the low frequency and high frequency bands. Radar based imaging prototype systems can be classified into multi-static radar [62, 64-65] and mono-static radar systems [63].

- *Multi-static radar system*

In the multi-static radar system, a synthesized pulse generated from a frequency sweep is beamed into the breast using a transmitter antenna, and scattering signals received by one or more receiver antennas placed around the breast. In [64], a hemi-spherical antenna array based on a prototype of the multi-static radar system was developed by the University of Bristol. This antenna array is formed with 16 cavity backed aperture stacked patch antennas connected with coaxial cables to an electromechanical switches network. This switch network chooses every possible pair of antennas in the antenna array and connects them to a Vector Network Analyzer (VNA), with one hundred and twenty measured transmission coefficients (S21) recorded for post-processing. During this experiment, the female patient lies prone with the breast falling through a hole in the examination plate, and the antenna array scans the breast, as shown in **Fig 2.8**[72]. The measured transmission coefficients are transformed into the time domain in cases where the VNA cannot process time

domain measurements and are then time-shifted to add coherently in order to enhance the tumour response and reduce clutter. These post-processed data are then used to create microwave images with the tumour highlighted.

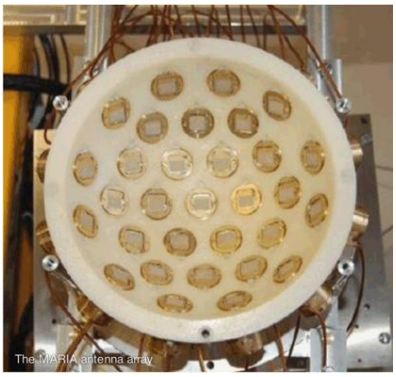

(a)

(b)

Fig 2.8 (a) The multi-static imaging system developed at the University of Bristol and (b) the clinical setup for breast cancer detection. [72]

- *Mono-static radar system*

Tissue Sensing Adaptive Radar has been developed based on the prototype of the mono-static radar system [63], as show in **Fig 2.9**. This system uses two antennas placed on opposite sides of the breast, with mechanical movement used to scan around the breast. The distance between these two antennas is aligned so as to achieve maximum sensitivity. A Vector Network Analyzer is connected to these two antennas,

and transmission coefficients are measured when they move to every observation position. These measured transmission coefficients are then post-processed to create microwave images highlighting the tumour.

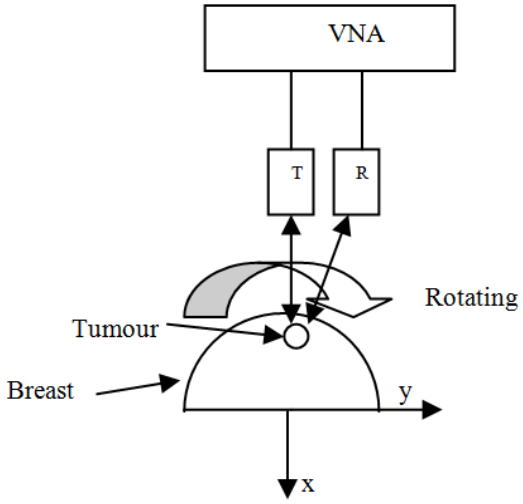

(a)

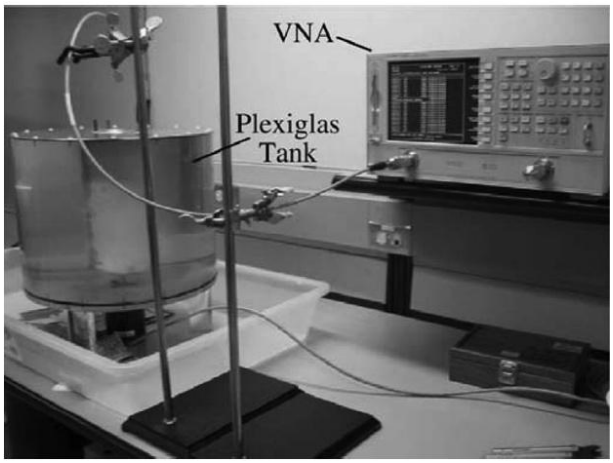

(b)

Fig 2.9 (a) The prototype and (b) experimental setup of the mono-static imaging system for breast cancer detection. [63]

- *Antenna design for radar based breast cancer detection*

Comparison of the prototypes of the multi-static and mono-static radar systems can

be based on the complexity of their structure, signal processing and the resolution of the resulting images. The multi-static radar system uses an antenna array and a complex switch network controller. The antenna array normally consists of more than ten antennas (16 antennas were used in [64], respectively) in order to collect a large number of transmission coefficients to obtain high resolution in the resulting images. Another problem is that the geometrical dimensions of the antenna used must be as small as possible in order to maximise the number of antennas used in the array. This, in turn, will increase the working frequency, and the required penetration depth of electromagnetic energy into the breast will not be achieved [65]. In [65], the University of Bristol develop a wide-slot antenna with the dimensions of 14 × 13 ×1.25 mm. A cavity is added at the back of the wide-slot antenna in order to absorb the back radiation and reduce mutual coupling, as shown in **Fig 2.10** (a). On the other hand, the mono-static radar system uses a single antenna (**Fig 2.10** (b) [73]) or an antenna pair to scan the breast with mechanical movement. Hence, the design of the antennas only targets their gain, bandwidth and fidelity. Furthermore, the reduced number of antenna decreases mutual coupling and the complexity of the signal post-processing required. Another issue is the resulting image resolutions. The multi-static radar system can detect smaller tumours compared to the mono-static radar system due to the greater number of collected transmission coefficients [64].

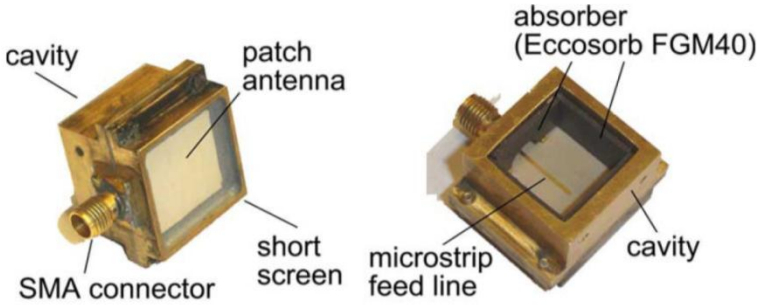

(a)

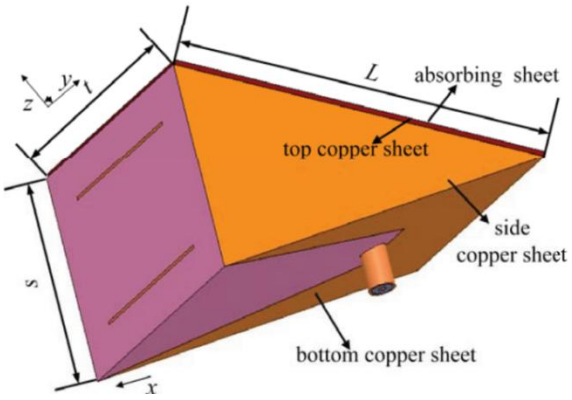

(b)

Fig 2.10 (a) Antenna designed at the University of Bristol used for multi-static imaging systems [26] and (b) antenna used for the mono-static imaging system. [73]

2.5 Conclusion

This chapter discusses the background of breast cancer and currently used breast cancer diagnosis methods. The anatomy of the breast and classification of tumours are discussed first. Tumours can be mainly classified as benign, potentially malignant and malignant tumour. The benign tumour grows with a controllable speed and does not invade or destroy the surrounding cell or tissues. The malignant tumour invades and destroys healthy cells and grows at a high rate or even spreads to other adjacent organs. The discrimination of benign and malignant tumours is mainly based on their electrical properties and morphology.

The most commonly used clinical diagnostic methods for breast cancer are X-ray Mammography, Ultra-sound and Magnetic Resonance Imaging (MRI). These three methods are painless compared with the medical biopsy. Their advantages and disadvantages are classified in terms of cost, ionizing radiation, accuracy and scope of application.

Microwave imaging for cancer detection has the advantages such as low-cost and non-ionizing radiation, which has attracted the attention of many research groups. Microwave imaging methods can be classified as passive and active microwave imaging. Passive microwave imaging is based on the high temperature difference between cancerous and healthy tissues when the breast is illuminated by a microwave radiator. However, the challenge for passive microwave imaging is that the power reflected by the tumour is not easy to detect. Breast cancer detection based on active microwave imaging relies on high differences in electromagnetic properties between healthy and malignant tissues. Two types of active microwave imaging methods have been proposed namely microwave tomography and radar based imaging. Microwave tomography seeks the reconstruction of the whole electrical profile inside the breast while radar based microwave imaging only focuses on detecting the tumour. Therefore, the signal processing in radar based microwave imaging is much easier than that in the microwave tomography. Types of radar based imaging prototype system include multi-static and mono-static radar systems. Their principles, prototypes and antenna design have been discussed and analyzed. Mono-static radar based microwave imaging is used in this thesis.

Chapter 3 Ultra-Wideband Antenna Design

3.1 Introduction

Radar based microwave imaging focuses on the determination of tumour location by creating images using back-scattering signals from the tumour. Radar based imaging prototype systems can be classified as multi-static and mono-static radar system. The multi-static radar system [74-87] uses an antenna array and a switch network controller. The antenna array normally consists of more than two antennas in order to collect a large number of transmission coefficients to obtain images of high resolution. On the other hand, the mono-static radar system [79] uses a single antenna or an antenna pair to scan the breast with mechanical movement.

Antenna design is an important issue in the radar based microwave imaging. Traditional methods of antenna design assume that antenna is in the free space. However, for antenna design in radar based imaging, it is assumed that the antenna will lie close to the breast in the near-field. The pulse generated from the antenna is radiated into a bio-like tissue. This bio-like tissue has similar electrical properties to those of the body tissue which surrounds the breast in order to reduce the electrical property discontinuity caused strong reflection from the skin layer. Another issue regarding antenna design is its dimensions. The multi-static radar system uses an antenna array; hence, the geometrical dimension of the antenna

must be as small as possible in order to maximise the number of antennas used in the array and this, in turn, will increase the working frequency and the penetration of electromagnetic energy into the breast will be insufficient [89]. Another issue of concern is mutual coupling. Mutual coupling means that one antenna can generate an induced current due to the current flowing in adjacent antennas. This induced current could change the impedance of the antenna, the radiation pattern and the scattering parameters which makes the antenna's properties unpredictable. Hence, the dimensions of the antenna and mutual coupling are the major challenges in antenna design for multi-static radar based imaging system [88-89]. However, the mono-static radar system uses a single antenna or an antenna pair to scan the breast with mechanical movement. Hence, the design of antennas focuses only on its gain, bandwidth, and fidelity. Furthermore, the reduced number of antenna decreases mutual coupling as well as the complexity of signal post-processing.

Ultra-wideband technology has been widely used in the radar and wireless communication fields for a long time. UWB systems use very short pulses (normally a few nanoseconds) and this, results in an ultra wideband spectrum [90-91]. The use of UWB provides several advantages, such as high capacity, low power transmission and high reliability [90-91]. Besides, another important application for UWB is radar based microwaving. The use of UWB provides high resolution in the resulting images due to the high bandwidth spectrum. Normally, the UWB working frequency contains both low and high frequency contents. The low frequency component provides a high penetration ability to detect relative deeply buried tumours while the high working frequency component lacks the penetration ability but offers high resolution to detect relatively small tumours. Hence, this unique feature is especially suitable for radar based breast cancer detection. Furthermore, the tumours in breast are often buried at shallow levels. Hence, the required depth penetration is only in the order of a few centimetres and

the corresponding working frequency is normally set to be a maximum of 10 GHz. Hence, the dimensions of the antenna can be very small, and this can provide a high working frequency, which helps to maximise the number of antenna in the multi-static radar system.

3.2 Antenna theory

This section describes the antenna theory relevant to the design of antenna for breast cancer detection.

3.2.1 Impendence Matching and Scatter Parameter

Fig 3.1 illustrates the transmission line model of the antenna [92]. The reflected energy can be reduced by matching the antenna's impedance to the characteristic impedance of the transmission line. The antenna impedance Z_A can be calculated as:

$$Z_A = (R_L + R_r) + j\ X_A \qquad (3.2.1)$$

where R_L, R_r and $j\ X_A$ are the loss resistance, radiation resistance and antenna reactance, respectively.

Normally, scatter parameters are used to describe the reflected energy [92]. Consider a black box with port 1 and port 2, where port 1 is the energy input port and port 2 is the output port. S_{11} represents reflected energy from port 1 while S_{21} shows

the transferred energy from port 1 to port 2. S_{11} and S_{21} are known as the reflection coefficient and forward transmission coefficient, respectively.

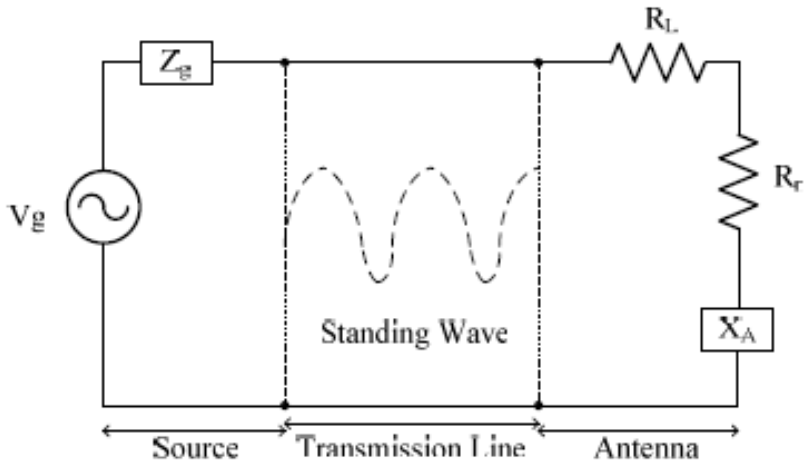

Fig 3.1 The transmission line model of the antenna. [92]

3.2.2 Power flow density

Power flow density is defined using the Poynting Vector, represented as (3.2.2):

$$\mathbf{S_{inst}} = \mathbf{E}\times\mathbf{H}\ (\mathrm{W/m^2}) \qquad (3.2.2)$$

where, $\mathbf{S_{inst}}$ is the Poynting Vector. **E** and **H** are the electric field and magnetic field, respectively. The radiated energy is calculated by summing $\mathbf{S_{inst}}$ over the whole radiation time. [92]

3.2.3 Near-field and Far-field

The radiation field can be represented by three regions: the reactive near field, radiating near field and far field, as shown in Fig 3.2. In the reactive near-field, the relationship between the E field and H field is unpredictable. Hence, the calculation of the Power flow density is too complex, since the phase and angle relationship of E and H changes with the radiation direction. Besides, a certain amount of energy is not absorbed by the receiver but is stored by the transmitter antenna. Hence, the energy oscillates in this region. The boundary of this region [92] is given by

$$R < 0.62 \sqrt{\frac{D^3}{\lambda}} \tag{3.2.3}$$

where, R, D and λ are the reactive near field, maximum dimension of antenna, and wavelength.

In the radiating near field, the energy oscillation becomes progressively weak and the radiation field starts to radiate along the radiation distance. However, the radiation field also changes with the radiation direction. The boundary of the radiating near field [92] is given by:

$$0.62 \sqrt{\frac{D^3}{\lambda}} < R < \frac{2D^2}{\lambda} \tag{3.2.4}$$

where, R, D and λ are the radiating near field, maximum dimension of antenna, and wavelength.

In the far field, the radiation pattern does not change with radiation distance and can be approximated as a plane wave or spherical wave. The E field and H field are orthogonal to each other. The boundary of the far field region [92] is given by:

$$\begin{cases} R > \frac{2D^2}{\lambda} \\ R \gg D \\ R \gg \lambda \end{cases} \tag{3.2.5}$$

where R, D and λ are the radiating near field, maximum dimension of antenna, and wavelength.

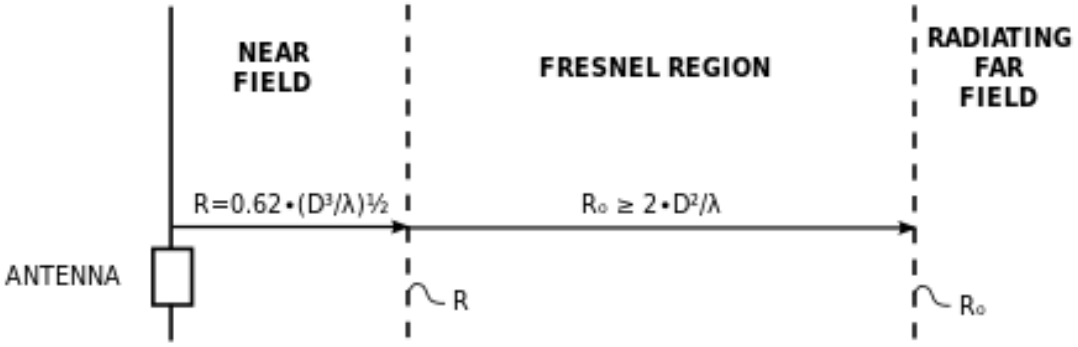

Fig 3.2 Reactive near field, radiating near field and far field. [105]

3.2.4 Half Energy Beam Width (HEBW)

The power flow density represents the radiated power from the antenna front middle in the near-field [93]. To gain insight into the power flow density, we illustrate the power flow density quantitatively using Half Energy Beam Width (HEBW). The HEBW is defined as a plane perpendicular to the radiation direction. The HEBW is

described in the Y-Z plane, with the corresponding distance being between the antenna and the evaluation points in the X-axis. The X-axis, Y-axis and Z-axis are described using notations $HEBW_X$ (mm), $HEBW_Y$ (mm) and $HEBW_Z$ (mm) respectively. The enclosed area of the $HEBW_Y$ (mm) and $HEBW_Z$ (mm) is described using the notation $HEBW_{YZ}$ (mm^2), as shown in Fig 3.3.

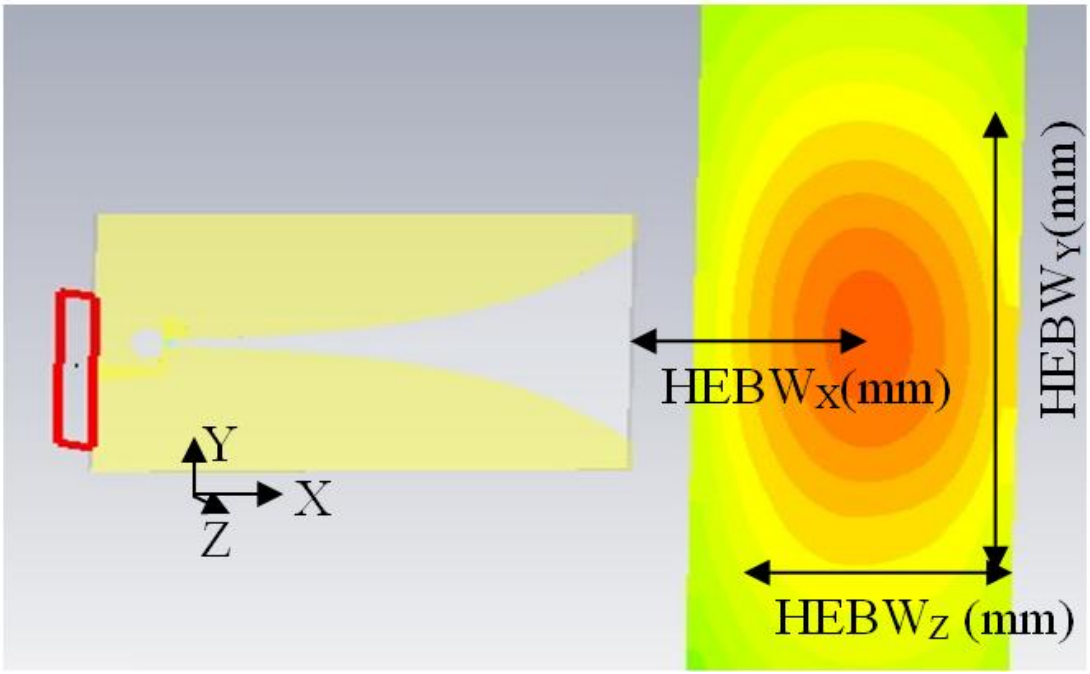

Fig 3.3 Half Energy Beam Width (HEBW).

3.2.5 Directivity and Gain

Directivity is a parameter used for measuring the maximum direction of radiation. It is defined as the ratio of maximum radiation intensity of the measured antenna to

that of a reference antenna radiating the same amount of power. The reference antenna is an isotropic antenna and the directivity is given by [92]:

$$D = \frac{4\pi U_{max}(\theta,\varphi)}{P_{tot}} \tag{3.2.6}$$

where $U_{max}(\theta,\varphi)$, P_{tot} are the maximum radiation intensity of the measured antenna and total radiated power.

Gain is given by

$$D = \frac{4\pi U_{max}(\theta,\varphi)}{P_{in}} \tag{3.2.7}$$

where P_{in} is the input power of the antenna. The main difference between the directivity and gain is that the gain takes into account the thermal losses in the antenna.

3.2.6 Radiation pattern

Radiation pattern is a representation of the radiated power by an antenna as a function of angle [92]. The radiation pattern can be specified as isotopic, directional or omni-directional. Isotopic radiation has been mentioned above, and is used as a reference. Directional radiation means that the radiation has the strongest radiation intensity in one direction, as shown in Fig 3.4. The strongest radiation is known as the main lobe. The width of the main lobe is calculated from its half-power point (-3 db),

and is known as half power beam width (HPBW). The omni-directional radiation pattern has a non-directional radiation pattern in all directions. It is worth noting that HPBW is defined in the far-field while the half energy beam width (HEBW) is defined in the near-field.

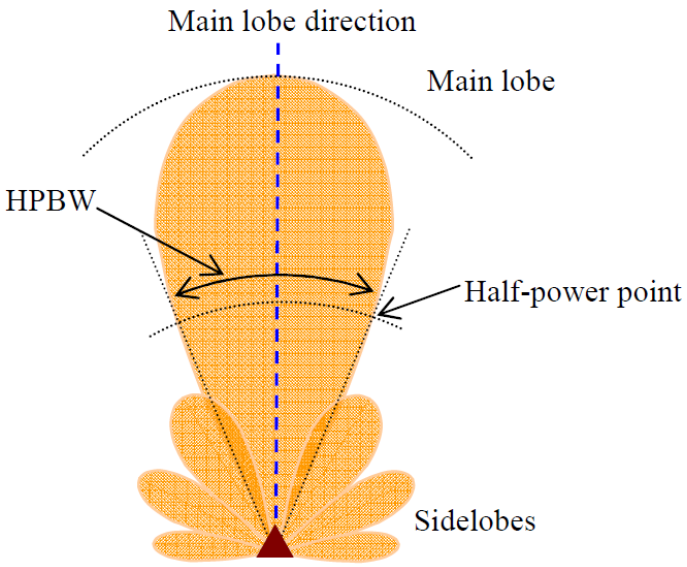

Fig 3.4 The radiation pattern. [92]

3.2.7 Polarization

Polarisation describes the **E** field orientation of the electromagnetic wave. [92] Normally, the polarisation can be specified as circular and linear polarisation, as shown in Fig 3.5. In the circular polarisation, the direction of the **E** field changes rotationally, but with a steady intensity. In the linear polarisation, the direction of the **E** field is along a line.

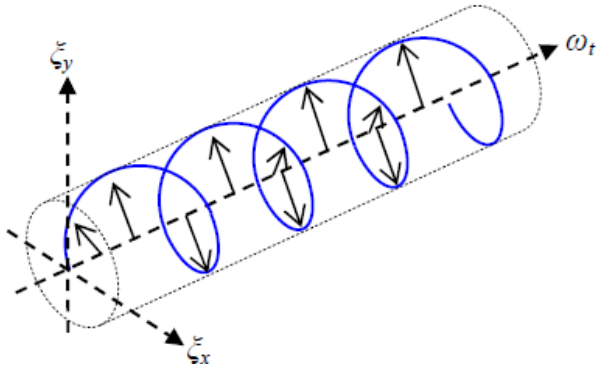

(a)

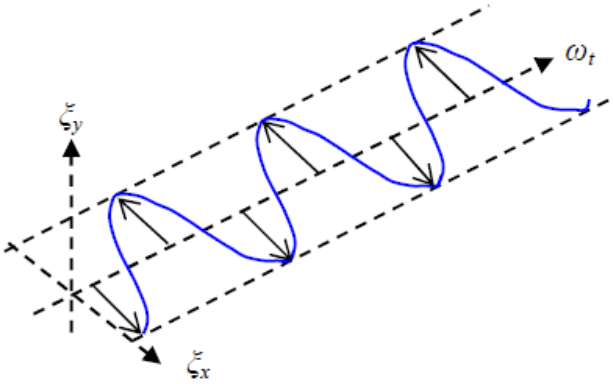

(b)

Fig 3.5 The (a) circular and (b) linear polarization. [92]

3.3 Review of the Vivaldi Antenna

3.3.1 Ultra-wideband Antenna

The definition of the UWB bandwidth follows that of the Federal Communications Commission (FCC): [90]

$$\text{bw} = 2\frac{f_H - f_L}{f_H + f_L} \geq 0.2 \qquad (3.3.1)$$

where bw, f_H and f_L are the bandwidth and highest and lowest frequencies, respectively.

Most UWB antenna prototypes are of the planar type. This planar topology is a good candidate for radar based microwave imaging for breast cancer detection, due to its relatively small dimensions. Hence, most researchers have chosen the microstrip antenna as the prototype which has the advantages of simple fabrication and easy integration. Fabrication of microstrip antenna is based on a printed circuit board (PCB), which offers high precision and extremely low cost. Furthermore, the microstrip antenna can be easily integrated into a PCB board with the whole microwave imaging system based on photo-etching technology, which increases system integration and reduces costs.

Non-planar UWB antennas such as the horn antenna and the log period antenna use resistive loading to expand the bandwidth, but this, results in low efficiency. Planar antennas such as the monopole antenna, bowtie antenna and stacked patch antenna have also been studied [76, 89]. Most of these except for the horn antenna are used in the multi-static radar systems due to its physical large dimensions.

In this thesis, the mono-static radar is selected as the prototype for the proposed imaging system. As mentioned above, mono-static radar uses a single antenna or a pair of antenna to mechanically scan the breast. Hence, the dimensions of the antenna are not a critical issue. In our study, the Vivaldi antenna is selected as the prototype for breast cancer detection.

3.3.2 The Fundamental Description of the Vivaldi Antenna

The Vivaldi antenna was first proposed in 1970 [94], with its significant advantages being wide bandwidth, high directivity and simple structure. Fig 3.6 shows three

kinds of tapered slot antennas (TSAs) [95]. The exponentially tapered slot is the basic profile of the Vivaldi antenna. The other two TSAs are a linearly tapered slot antenna (LTSA) and a constant width slot antenna (CWSA).

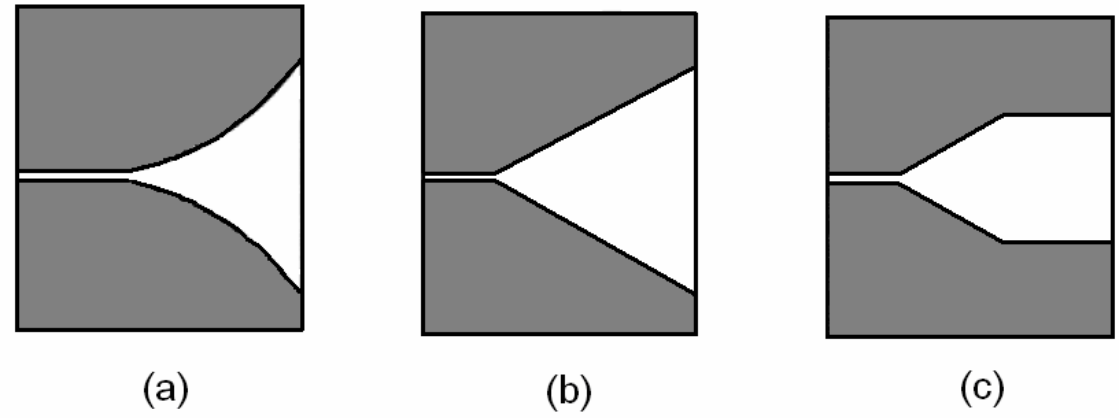

Fig 3.6 Types of TSA: (a) exponentially tapered (Vivaldi); (b) linearly tapered (LTSA); and (c) constant width slot antenna (CWSA). [95]

The Vivaldi antenna is a kind of travelling wave antenna. A travelling wave antenna is defined as one whose current has the same amplitude but different phases [92]. The Vivaldi antenna has an exponential tapered slotline which can be described using an exponential function. This exponential tapered slotline is also known as a radiation section since the wave is radiated along this slotline. Fig 3.7 illustrates the fundamental geometry of a Vivaldi antenna. The slotline is excited in the narrowest part of the slotline. Exciting methods used can be Directly Coupled Transitions [96] or Electromagnetically Coupled Transitions [97], as described below. The separation between the slotline starts to expand from the exciting point, and the separation distance determines the bandwidth of the Vivaldi antenna. The largest separation of the slotline is equivalent to half of the wavelength of the lowest working frequency, while the smallest slotline separation corresponds to the highest working frequency.

As discussed above, the slotline of the Vivaldi antenna is known as the radiation part. The wave travels down the slotline from the narrow part to the largest part. During this process, the energy is tightly bound to the slotline in the narrowest part and starts to radiate due to the increase of slotline separation. The energy starts to radiate into the air when the separation of the slotline is close to one-half of the wavelength.

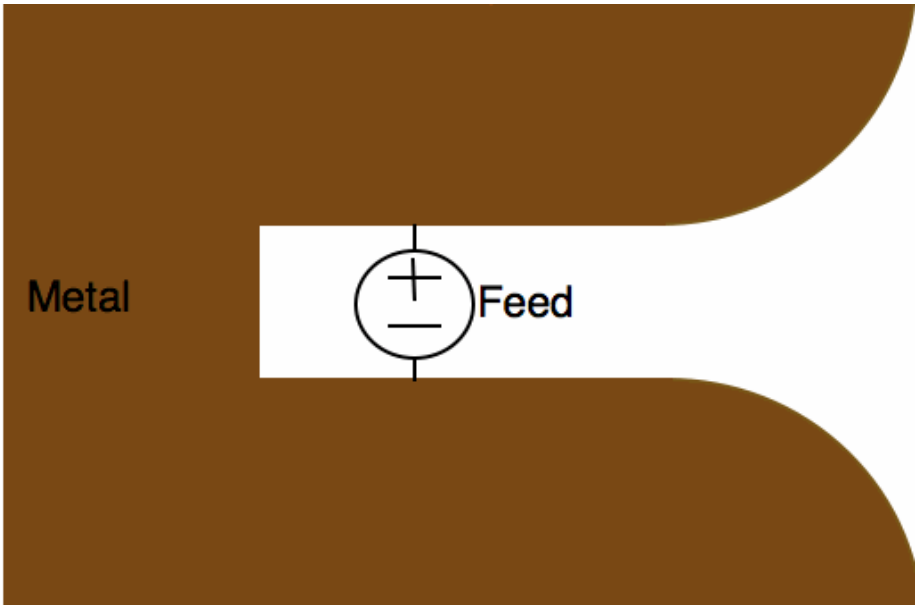

Fig 3.7 Fundamental geometry of Vivaldi antenna. [104]

3.3.3 Feeding Methods

The fundamental structure and operating principles of Vivaldi antenna are now discussed. The exciting point is located in the narrowest part of the slotline, and there are two types of feeding approaches known as directly feeding and electromagnetically feeding.

- Directly feeding

In directly feeding, energy is coupled to the slotline directly using a coaxial line. A coaxial probe is soldered to the Vivaldi antenna, with the inner conductor connected to one side of the slotline and the outer conductor soldered to the other side of the slotline as the ground.

- Electromagnetically Coupled Transitions

Unlike directly feeding, the energy to the slotline can be based on the electromagnetic coupling, of which microstrip coupling and stripline coupling are the best known types [97]. Fig 3.8 shows the microstrip coupling transition. [97] The microstrip and the slotline are etched on each side of the substrate. The microstrip and slotline cross by one quarter of a wavelength with each other. The quarter part of the microstrip acts as a short circuit when crossing with the slotline, while the quarter part of the slotline acts as an open circuit. Electromagnetic coupling is based on these 'short circuit' and 'open circuit'.

Fig 3.9 shows stripline coupling. A stripline is located on the centre of the substrate, while slotlines are etched on both sides of the substrate. The stripline and slotline still cross by one quarter of a wavelength with each other as in the microstrip coupling transition mechanism. A stub can be added to both the microstrip/stripline and the slotline to match the impendence, and this therefore increases the bandwidth of the Vivaldi antenna, as shown in Fig 3.10.

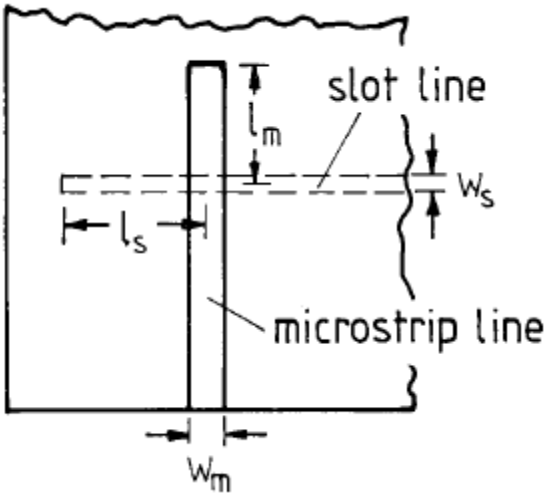

Fig 3.8 Microstrip based Electromagnetically Coupled Transitions. [97]

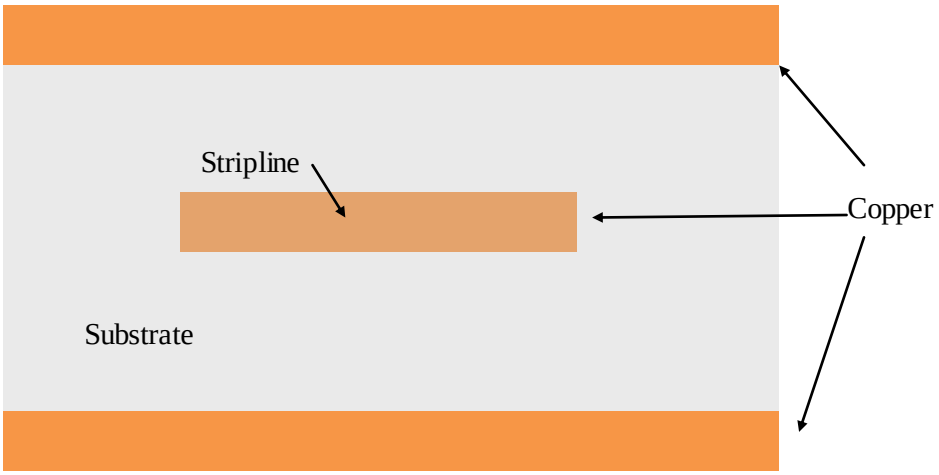

Fig 3.9 Stripline based Electromagnetically Coupled Transitions.

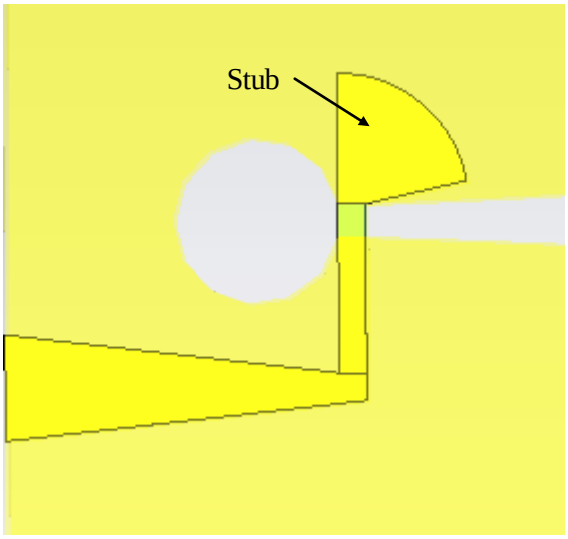

Fig 3.10 Adding a stub to increase the bandwidth of the Vivaldi antenna.

3.4 The Design of Vivaldi Antenna for Breast Cancer Detection

3.4.1 Geometrical Parameters of the Vivaldi Antenna

The Vivaldi antenna is a kind of travelling wave antenna and the operating principle can be summarized as follows. The exciting point is located in the narrowest part of the slotline and the microwave starts to radiate due to the increase in slotline separation. The energy starts to radiate into the air when the separation of the slotline is close to the half wavelength. The feeding methods can be directly feeding and electromagnetically feeding. Microstrip and stripline coupling are the best known types of electromagnetic coupling. In this thesis, microstrip feeding is chosen due to its excellent performance in terms of bandwidth and beamwidth. The proposed

Vivaldi antenna model is shown in Fig 3.11, which also illustrates its parameters. These parameters are analyzed as follows.

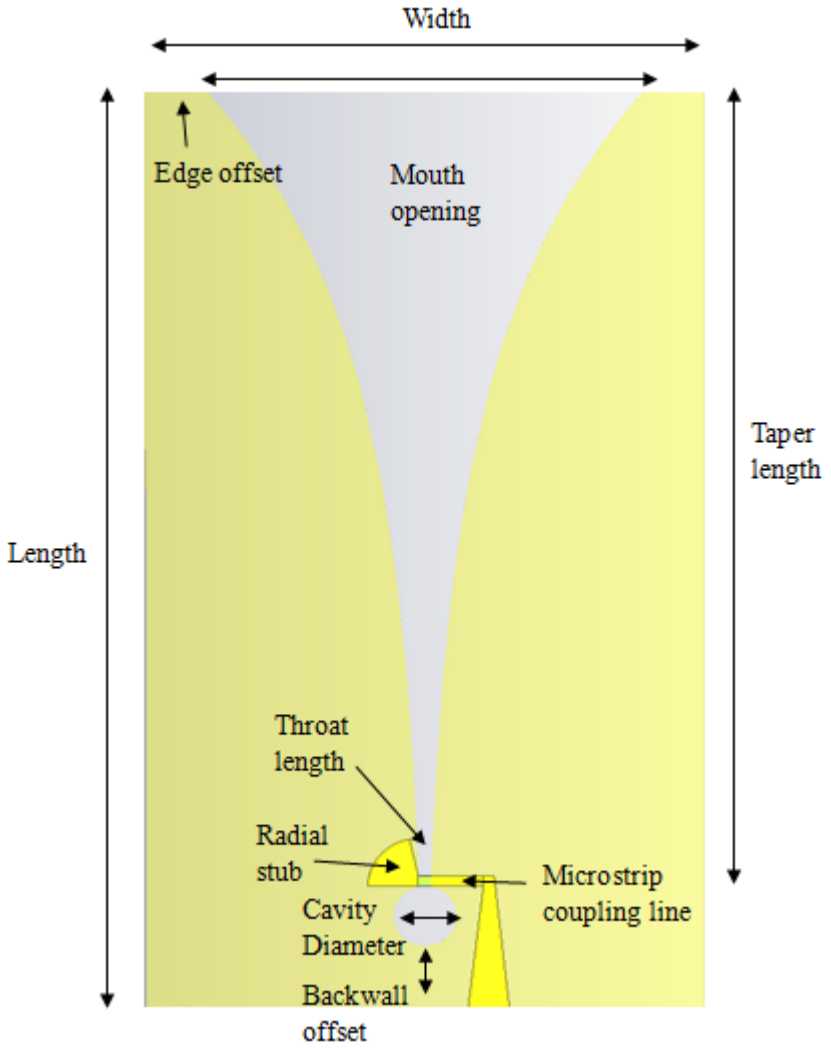

Fig 3.11 The proposed Vivaldi antenna model.

3.4.1.1 The Equivalent Circuit Model of the Vivaldi Antenna

An equivalent circuit schematic of the Vivaldi antenna is shown in Fig 3.12[98]. Here, Z_m and Z_s indicate the characteristic impedance of the microstrip line and the slotline respectively. L_m and C_s show the equivalent inductor and capacitor of the

microstrip line and the slotline respectively. X_m and X_s denote the input reactance of the microstrip line and the slotline respectively. Z_{ant} indicates the impedance of the cross-section of the slotline and microstrip line.

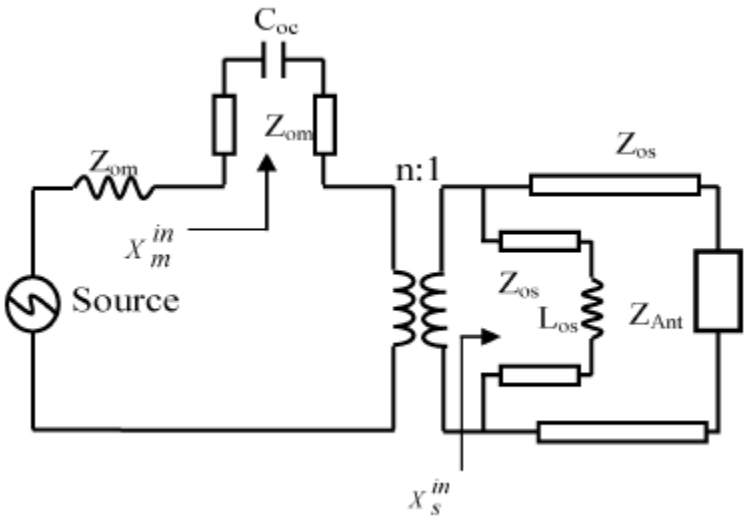

Fig 3.12 The equivalent circuit model of the Vivaldi antenna. [98]

3.4.1.2 Substrate

The design of the substrate can be considered in terms of its dielectric constant and thickness. The use of higher dielectric constant substrate shrinks the antenna dimensions. Besides, the use of a substrate with a lower dielectric constant provides wider bandwidth. The trade-off between dielectric constant, dimensions and bandwidth needs careful consideration.

The thickness of the substrate is the other important design parameter. Normally, the use of a thicker substrate improves antenna performance in terms of gain and main beamwidth due to the decrease in antenna reactance.

In this thesis, a FR4 substrate (relative permittivity is 4.3, dissipation factor is 0.017) is used whose thickness is 1.6mm and having 35µm copper on both sides. This

substrate is also the most commonly used PCB board which is cheap and easily fabricated.

3.4.1.3 Antenna Length

The length of the Vivaldi antenna should be longer than one wavelength of the lowest working frequency of the design [94]. An increase in length provides wider bandwidth. These requirements of the Vivaldi antenna guarantee excellent performance in terms of gain, directivity and beamwidth. In this study, the required bandwidth ranges from 5 to 10 GHz and the corresponding wavelengths range from 30 mm to 60 mm. Thus, the minimum length is initially set at 60 mm first. However, achieve a desirable bandwidth is only one of the design targets. Gain and beamwidth can also be affected by antenna width.

3.4.1.4 Antenna Width

The width of the Vivaldi antenna should be longer than half of the wavelength of the lowest working frequency [94]. A decrease in antenna width provides a wider bandwidth. In this study, the initial width is set at 30 mm.

3.4.1.5 Mouth opening

The mouth opening is the maximum open size of the tapered slotline, as shown in Fig 3.13. The exciting point is in the narrowest part of the slotline. The radiation propagates through the increasing of slotline width and the energy starts to radiate

into the air when the separation of the slotline is close to the half wavelength. Thus, the mouth opening should be larger than the half wavelength [94], which is 30 mm in our case. An increase in the mouth opening results in a decrease in the lowest working frequency, and this, increases the overall bandwidth. 28 mm is chosen as the initial mouth opening.

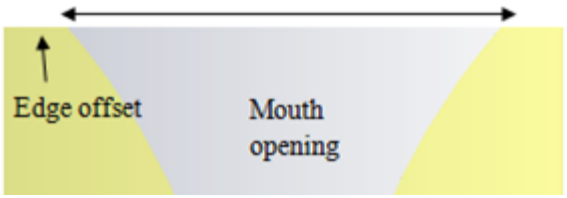

Fig 3.13 The mouth opening.

3.4.1.6 Throat Length

Throat length is the slotline conductor separation distance, which is also the electromagnetic coupling point as shown in Fig 3.14. The microstrip and the slotline are etched on each side of the substrate and cross one quarter of a wavelength with each other at the throat. The quarter part of the microstrip acts as a short circuit when crossing with the slotline, while the quarter part of the slotline acts as an open circuit. The electromagnetic coupling is based on these 'short circuit' and 'open circuit'. A change in throat length could result in a dramatic degradation of return loss [98-99].

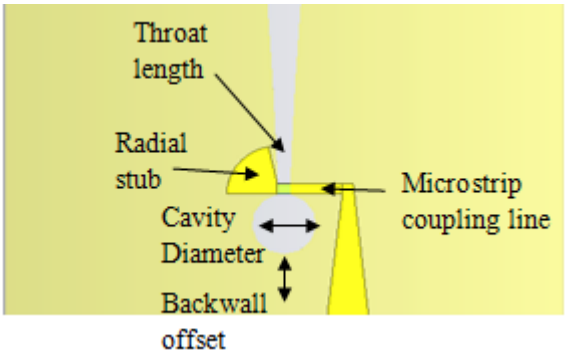

Fig 3.14 The throat length.

3.4.1.7 Edge offset

The edge offset is the extent of the extra metallization at the mouth opening, as shown in Fig 3.15. An increase or decrease in edge offset results in a change of the return loss and the radiation pattern [100]. Two approaches are proposed here to optimize edge offset. The first approach is to keep the mouth opening constant and increases or decreases the width of the Vivaldi antenna. The second approach maintains the width of the Vivaldi antenna while changing the mouth opening. The initial edge offset is set at 4 mm.

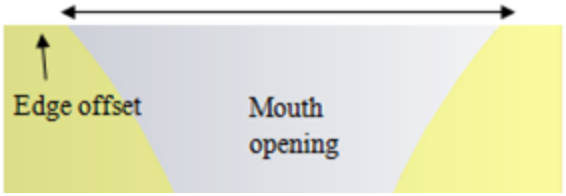

Fig 3.15 The edge offset.

3.4.1.8 Cavity Diameter

A circular cavity is added to the end of the slotline, as shown in Fig 3.16. The use of the cavity offers the freedom to tune the impedance matching [100], and this, affects the bandwidth of the Vivaldi antenna. In this study, the initial diameter is set at 4 mm.

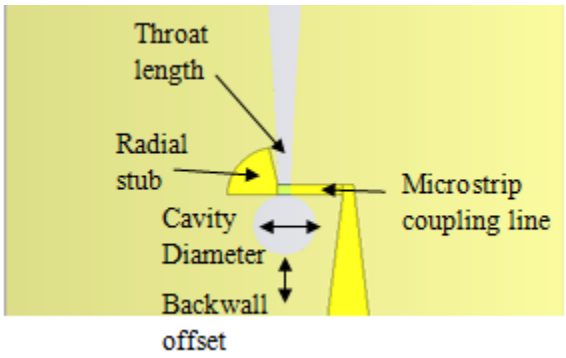

Fig 3.16 The cavity diameter and backwall offset.

3.4.1.9 Taper

Taper design is based on two parameters: taper length and taper rate. The taper length should be on the order of one wavelength in the lowest working frequency [100]. Besides, the taper length is also dependent on the cavity diameter and antenna length. An increase in the taper length improves the bandwidth. The initial taper length is set at 60 mm.

The taper rate can be defined by an exponential function:

$$X = C_1 e^{Ry} + C_2$$

$$C_1 = \frac{x_2 - x_1}{e^{Ry_2} - e^{Ry_1}} \qquad (3.4.1)$$

$$C_2 = \frac{x_1 e^{Ry_2} - x_2 e^{Ry_1}}{e^{Ry_2} - e^{Ry_1}}$$

where R is the taper rate, x_1, x_2, y_1 and y_2 indicate the slotline start and end points. In this study, the initial taper rate is 0.05.

3.4.1.10 Backwall Offset

The backwall offset is the extension metallization between the cavity and the edge of the antenna, as shown in **Fig 3.16**. The use of the backwall offset prevents the abrupt end of the current flow, and this, offers the freedom to tune the bandwidth. In this study, the initial backwall offset is 5 mm.

3.4.1.11 Microstrip Coupling Line

Microstrip width is an important parameter in calculating the antenna impedance. In [102], the solution for calculating the characteristic impedance of the microstrip line is presented in Equation 3.4.1, where the substrate thickness is much smaller than the wavelength (h<<λ):

$$Z_0 = \begin{cases} \frac{60}{\sqrt{\varepsilon_e}} \ln\left(\frac{8h}{w_m} + \frac{w_m}{4h}\right) & \frac{w_m}{h} \leq 1 \\ \frac{120\pi}{\sqrt{\varepsilon_e}\left[{}^{w_m}/_{h} + 1.393 + 0.667 \ln\left({}^{w_m}/_{h} + 1.444\right)\right]} & \frac{w_m}{h} > 1 \end{cases} \quad (3.4.2)$$

where w_m and h indicates the width of the microstrip line and the thickness of the substrate respectively. ε_e represents the effective dielectric constant:

$$\varepsilon_e = \frac{\varepsilon_r + 1}{2} + \frac{\varepsilon_r - 1}{2 \times \sqrt{1 + 12h/w_m}} \quad (3.4.3)$$

where ε_r is the relative permittivity of the substrate.

Normally, a SMA connector is used as the feeding for the Vivaldi antenna, with a characteristic impedance of 50 Ohm. Based on Equation 3.4.1, the characteristic

impedance of the microstrip feeding line can be calculated, with the target being 50 Ohm. The parameters are: h= 1.6 mm, ε_e = 4.6. The calculated results are: Z_0 = 50.36 Ohm, w_m = 3mm. However, the width of the microstrip coupling line is 1mm, with the corresponding impedance being 95 Ohm. A taper is required to match the impedances (50.36 and 95 Ohm). This taper uses a trapezoidal microstrip line, with the bases being 3 mm and 1 mm respectively, as shown in Fig 3.17. The 3mm base corresponds to approximate 50 Ohm impedance, while the other base corresponds to the width of the microstrip coupling line, being 95 Ohm.

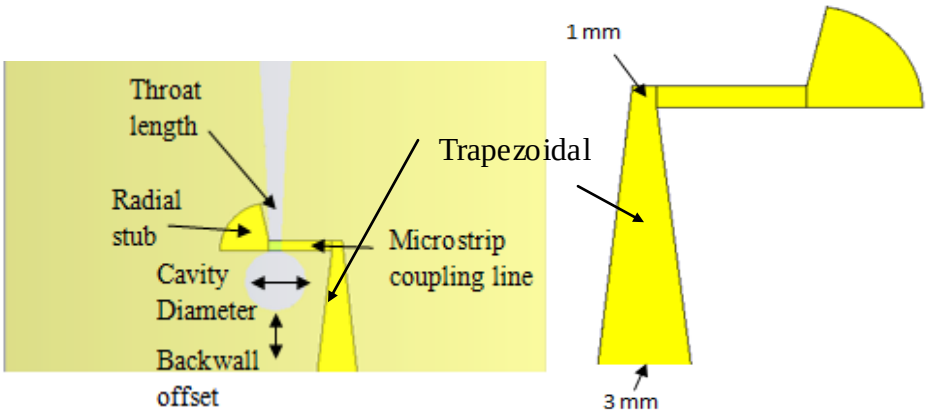

Fig 3.17 The microstrip coupling line and radial stub.

3.4.1.12 Radial stub

A radial stub is connected to the end of the microstrip coupling line, as shown in Fig 3.4.6. The radial stub reflects the incident energy to the microstrip coupling line, which increases the bandwidth. The radius and angle of the stub produce an effect on the working frequency, but this is not as significant as varying the antenna length and width. However, the variation in the radius and angle of the stub provides the freedom to tune the impedance and bandwidth. The impedance of the radial stub provides

effective compensation for the microstrip line impedance [103]. In this study, the initial radius and angle are 4 mm and 90° respectively.

3.4.2 The final design of Vivaldi Antenna

3.4.2.1 Design Flow

The design flow is proposed in the flow diagram, shown in Fig 3.18. The starting point is the selection of the substrate and the dimensions of the antenna. Each of the parameters has been analyzed and simulated. The final design of the Vivaldi antenna is shown in the next section.

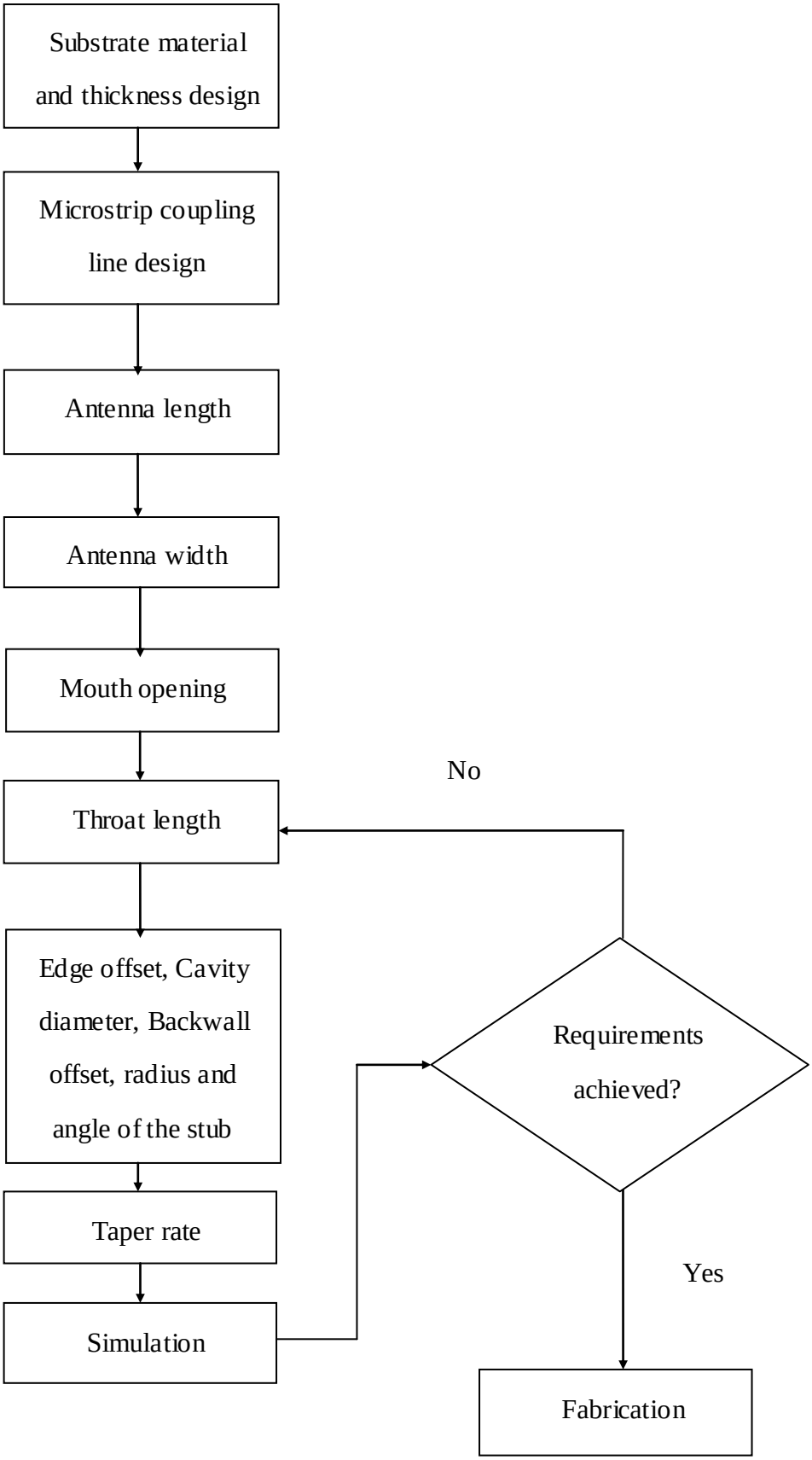

Fig 3.18 The Vivaldi antenna design flow diagram.

3.4.2.2 Final design

The final design of the fabricated Vivaldi antenna is shown in Fig 3.19, with each of the parameters given in Table 3.1.

Table 3.1 The Parameters of the Vivaldi Antenna

Parameters	**Value**
Substrate Material	FR4
Substrate Thickness	1.6 mm
Antenna Length	73.4 mm
Antenna Width	42 mm
Mouth Opening	33 mm
Throat Width	0.95 mm
Edge Offset	4.5 mm
Cavity Diameter	5 mm
Taper Length	63 mm
Taper Rate	0.05
Backwall Offset	5 mm
Microstrip Width	0.8 mm
The Radius of the Stub	3.78 mm
The Angle of the Stub	90°

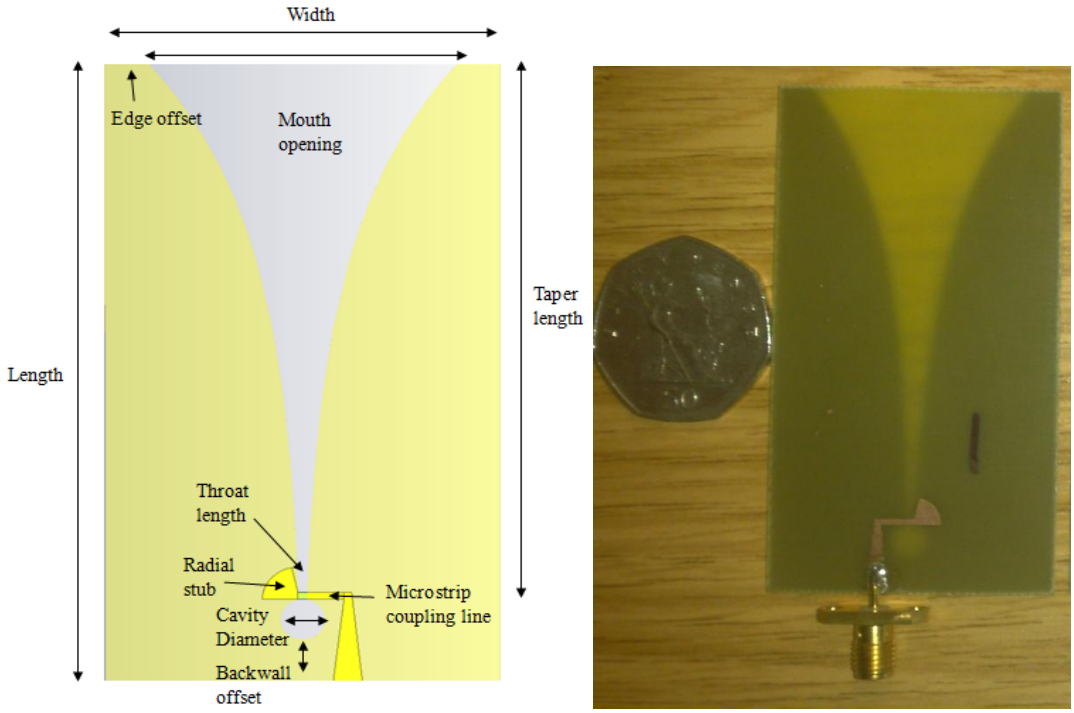

Fig 3.19 The (a) designed and (b) fabricated Vivaldi antenna.

3.4.3 Antenna performance

The Vivaldi antenna is simulated using the CST 2011, based on the Finite-difference time-domain (FDTD) method. For the measurement, an HP 8510B Vector Network Analyser (VNA) is used to measure the S parameters of the Vivaldi antenna. This VNA is capable of measuring from 0 to 20 GHz. An HP 8341B synthesized sweeper is used to generate signal ranges from 45 MHz to 20 GHz, and connected to the VNA.

3.4.3.1 Scatter parameters

Fig 3.20 shows the simulated and measured S_{11} and S_{21} parameters, with good agreement between 5 and 10 GHz, although there is some discrepancy around 6GHz. The simulated and measured S_{21} shows acceptable agreement between 5 and 9 GHz. Besides, the simulated and measured profiles of the S_{21} are very flat from 5 to 9GHz, and this, provides minimal distortion. The discrepancy can be concluded by two aspects. Firstly, the fabricated Vivaldi antenna has some errors whose dimension cannot be exactly the same as the simulated antenna. Fig 3.19 shows the simulated and fabricated antenna. The S_{11} in 10 GHz corresponds to the throat length while the S_{11} in 5 GHz corresponds to the mouth opening part in the antenna. Hence, any fabrication error or even some small uneven could cause discrepancy. The solution is to fabricate the antenna more precisely. Secondly, the S_{11} and S_{21} parameters are measured in the lab using the VNA. The environmental influence for the measurement results is also significant. In the lab, electronic equipments, chair, table, human or even a cup of tea could cause impact on the measurement results. In order to avoid the environmental influence, the measurement should undertake in the anechoic chamber which will reduce the environment influence. Currently, microwave imaging based cancer detection is quite novel, and the quantitative evidence or specified certification to describe the scatter parameters is still studying. Here the words such as good agreements or acceptable agreement are based on our experimental experience, since the scatter parameters are closely related to the imaging quality. In the future, specified certification for the scatter parameters will be studied.

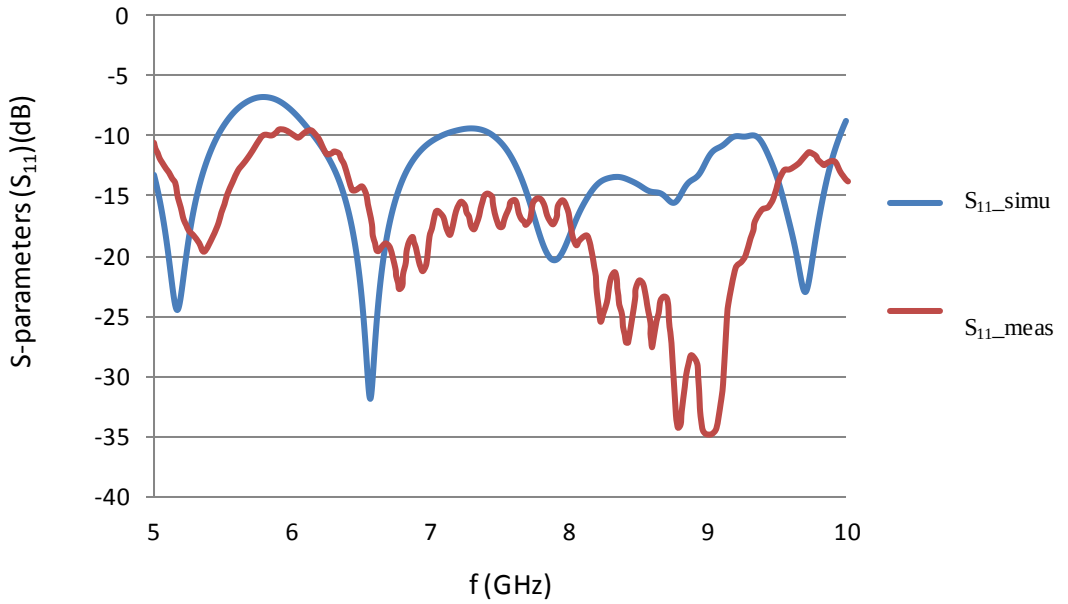

(a)

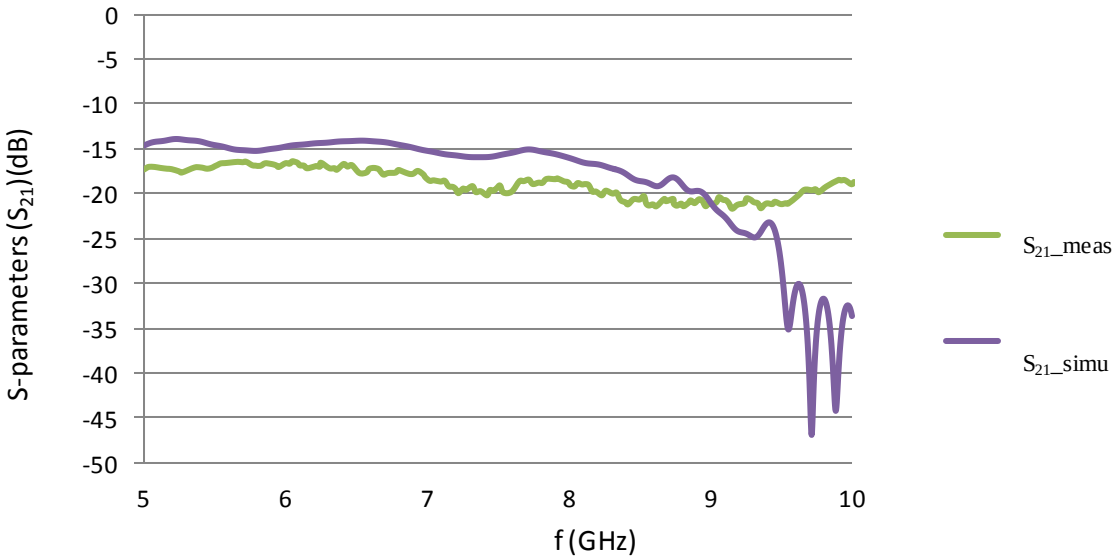

(b)

Fig 3.20 The (a) simulated and measured S_{11} and the (b) simulated and measured S_{21}.

3.4.3.2 Farfield radiation pattern and gain

Fig 3.21 shows the Farfield radiation pattern for 5, 6, 7, 8, 9 and 10 GHz. It is observed that the radiation pattern becomes slimmer with increasing working frequency. The gain increases from 5 to 9 GHz, but then drops dramatically at 10 GHz as shown in Fig 3.22.

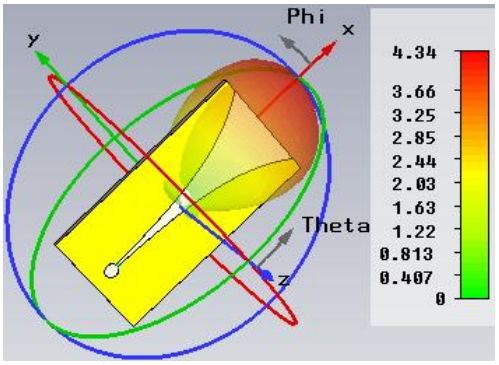

5 GHz

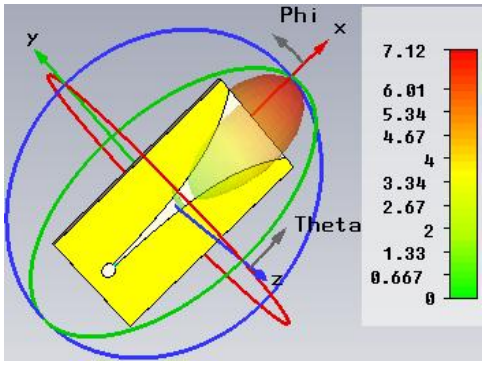

6 GHz

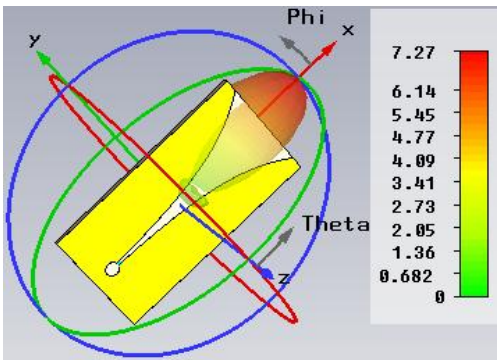

7 GHz

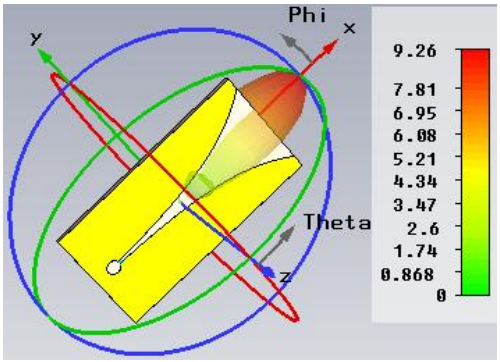

8 GHz

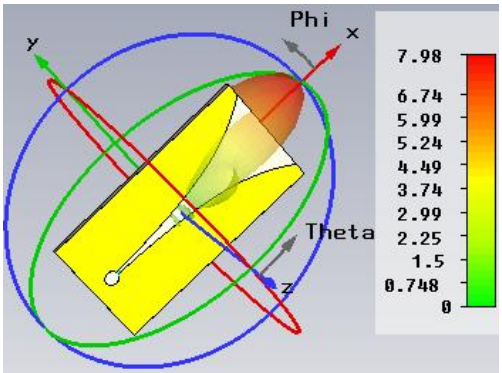

9 GHz

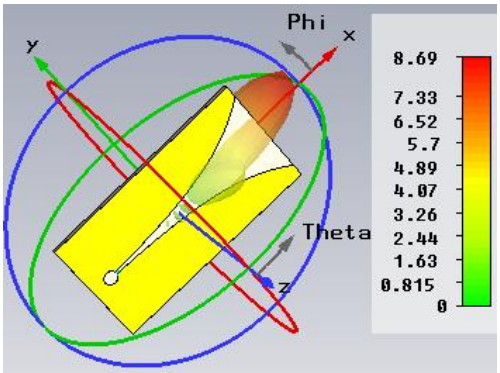

10 GHz

Fig 3.21 The radiation pattern from 5 to 10 GHz.

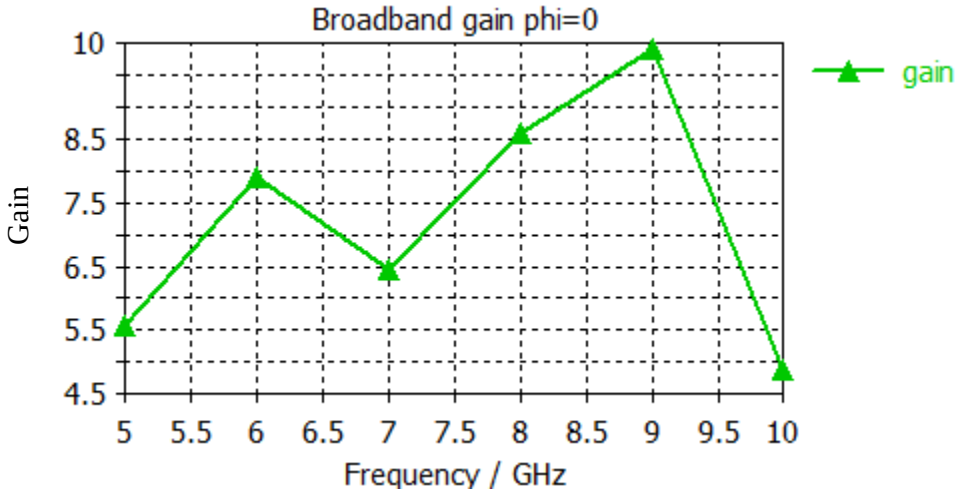

Fig 3.22 The gain from 5 to 10 GHz.

3.4.3.3 Power Flow Density and Half Energy Beam Width (HEBW)

The power flow density and HEBW have been introduced previously. The HEBW is described in the Y-Z plane, with the corresponding distance being between the antenna and the evaluation points in the X-axis. The X-axis, Y-axis and Z-axis are described using the notation $HEBW_X$ (mm), $HEBW_Y$ (mm) and $HEBW_Z$ (mm) respectively. The enclosed area of $HEBW_Y$ (mm) and $HEBW_Z$ (mm) is described using notation $HEBW_{YZ}$ (mm^2), as shown in Fig 3.23 and Fig 3.24. The $HEBW_Y$ (mm), $HEBW_Z$ (mm) and $HEBW_{YZ}$ at 5, 6, 7, 8, 9 and 10 GHz are calculated at different value of the $HEBW_X$ (mm) = 10mm, 20 mm, 30 mm and 40 mm, respectively. Table 3.2 shows the calculated value of the HEBW. It is worth noting that the $HEBW_Y$ (mm), $HEBW_Z$ (mm) and $HEBW_{YZ}$ are all calculated at the half-power point (-3 db).

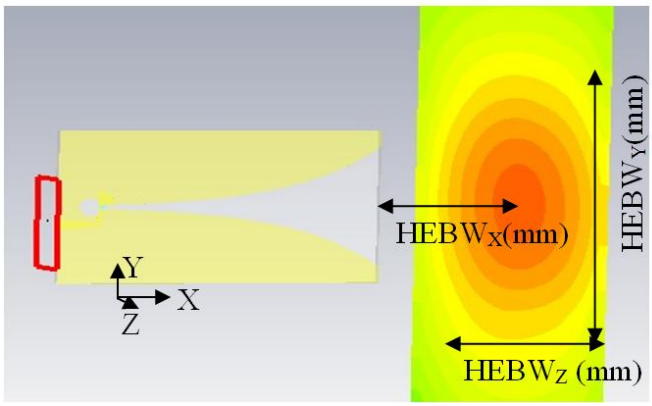

Fig 3.23 The HEBW of the designed Vivaldi antenna.

The $HEBW_{YZ}$ (mm^2) for $HEBW_X$ at 10mm is reduced with increasing the operation frequency. Furthermore, the $HEBW_Y$ increases progressively while the $HEBW_Z$ decreases gradually with an increase in operating frequency. A similar phenomenon also appears in different $HEBW_X$ corresponded $HEBW_Y$ and $HEBW_Z$. Based on these observations, it can be concluded that the HEBW decreases with increasing the working frequency. A similar phenomenon is also observed in the far field radiation pattern. Besides, the peak power starts moving to the front edge of the antenna. Another observation is that the $HEBW_Y$, $HEBW_Z$ and $HEBW_{YZ}$ increase with the increasing $HEBW_X$. The reason for this is that the energy starts to radiate in different directions. The quantitative HEBW shows a clear presentation of near-field power flow density.

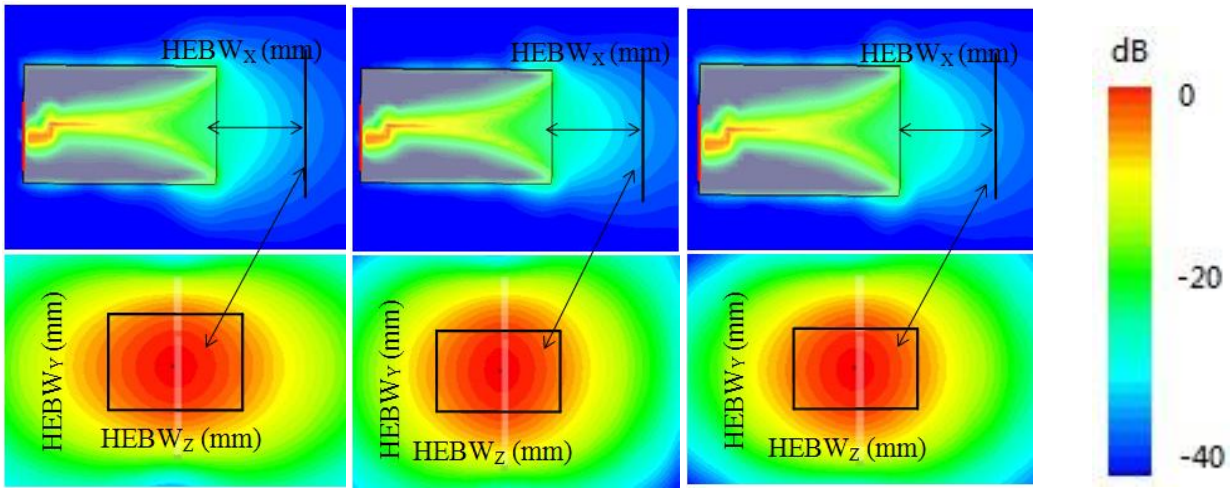

5Ghz **6GHz** **7GHz**

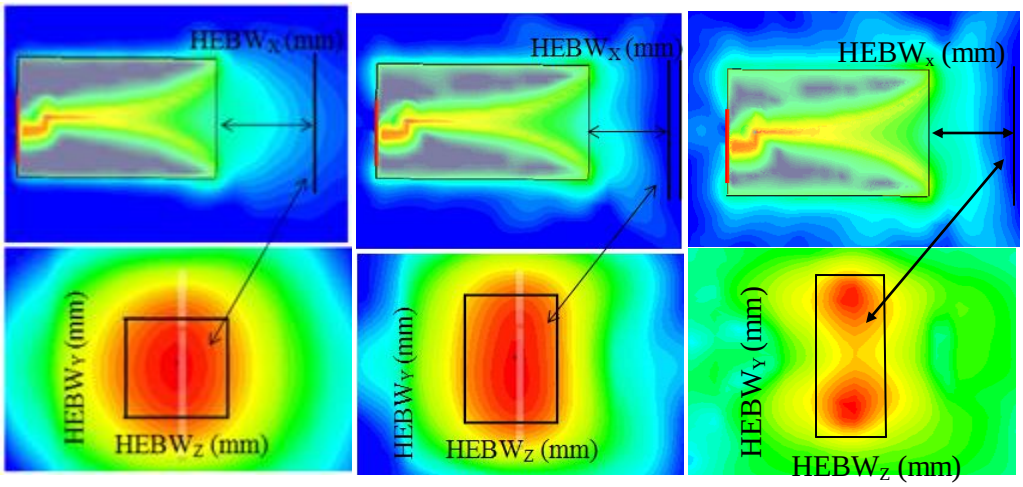

8Ghz **9GHz** **10GHz**

Fig 3.24 The HEBW of the designed Vivaldi antenna from 5 to 10 GHz.

Table 3.2 A Comparison of the HEBW at 5, 6, 7, 8, 9 and 10 GHz

f (GHz)		$HEBW_X$ (mm) (-3 db)			
		10	20	30	40
5 GHz	$HEBW_Y$ (mm) (-3 db)	39	50	70	90
	$HEBW_Z$ (mm) (-3 db)	55	74	93	103
	$HEBW_{YZ}$ (mm2) (-3 db)	2145	3700	6510	9270
6 GHz	$HEBW_Y$ (mm) (-3 db)	40	49	62	80
	$HEBW_Z$ (mm) (-3 db)	50	68	86	100
	$HEBW_{YZ}$ (mm2) (-3 db)	2000	3332	5332	8000
7 GHz	$HEBW_Y$ (mm) (-3 db)	38	47	61	78
	$HEBW_Z$ (mm) (-3 db)	43	62	82	99
	$HEBW_{YZ}$ (mm2) (-3 db)	1634	2914	5002	7722
8 GHz	$HEBW_Y$ (mm) (-3 db)	42	48	60	76
	$HEBW_Z$ (mm) (-3 db)	38	60	83	99
	$HEBW_{YZ}$ (mm2) (-3 db)	1596	2880	4980	7524
9 GHz	$HEBW_Y$ (mm) (-3 db)	42	48	56	77
	$HEBW_Z$ (mm) (-3 db)	32	58	88	96
	$HEBW_{YZ}$ (mm2) (-3 db)	1344	2784	4928	7392
10 GHz	$HEBW_Y$ (mm) (-3 db)	51	59	64	83
	$HEBW_Z$ (mm) (-3 db)	28	46	80	85
	$HEBW_{YZ}$ (mm2) (-3 db)	1428	3304	5120	7055

3.5 The Modified Slot Vivaldi Antenna

The designed Vivaldi antenna provides an ultra-wideband working frequency ranging from 5 to 10 GHz. The directional radiation pattern and high gain also meet the requirements for breast cancer detection. This section investigates the improvement of the Vivaldi antenna.

The improvement focuses on bandwidth, radiation pattern and gain. Generally, the first aim is to increase the antenna bandwidth, which will provide deeper penetration ability. The directional radiation pattern and high gain should be maintained or even improved. The most convenient method of extending bandwidth is to increase the dimension of the antenna, which will provide a lower working frequency band. However, this method will increase the difficult for the breast scanning due to the large dimension of the antenna. Therefore the design target is to increase bandwidth while maintaining antenna dimensions.

3.5.1 Optimizing the Vivaldi Antenna using the Equivalent Circuit Method

The equivalent circuit schematic of the Vivaldi antenna is rewritten here, as shown in Fig 3.25 [98]. Z_m and Z_s indicate the characteristic impedance of the microstrip line and slotline respectively. L_m and C_s show the equivalent inductor and capacitor of the microstrip line and the slotline respectively. X_m and X_s denote the input reactance of the microstrip line and the slotline respectively. Z_{ant} indicates the impedance of the cross-section of the slotline and microstrip line.

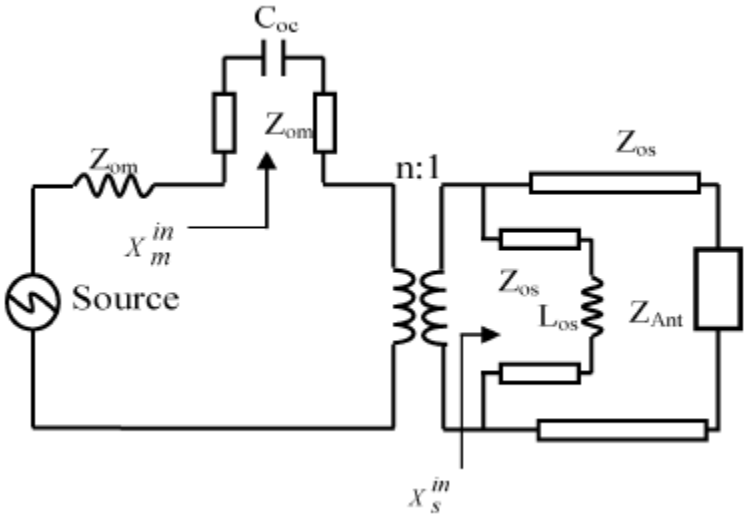

Fig 3.25 The equivalent circuit model of the Vivaldi antenna [98].

The microstrip is inductive and the slotline is capacitive, and the bandwidth is increased to achieve impedance matching at more frequency bands. Hence, the design focuses on the changing of the reactance of the micrstrip line or the slotline.

The widths of the microstrip and slotline have been optimized in previous sections. Hence, slight changes in the microstrip and slotline could result in significant changes in overall antenna performance. Another approach is to change the ground of the Vivaldi antenna.

Based on design experience and the equivalent circuit schematic of the Vivaldi antenna, one or more slots can be added to the ground could generate capacitor, and this will increase slotline reactance X_s.

The first step is to monitor the current density of the Vivaldi antenna. Fig 3.26 shows the current density along the edge of the ground. This Vivaldi antenna is a standing wave antenna whose current has the same amplitude but different phases. Fig 3.26 clearly shows the current density distribution. In order to maximum the capacitance of the slot, its position can be located at the edge between the positive and

negative peak of the current flow. The use of this optimization method based on equivalent circuit schematic provides a theoretical basis for optimizing the antenna rather than scanning parameters aimlessly, which therefore increases the design efficiency.

The second step is to add a slot to the ground of the Vivaldi antenna. However, the dimensions and location of the slot can be varied to obtain different capacitance. The use of the parameter sweep function in CST provides the optimization approaches. Fig 3.27 (a) shows the single and multiple slot configurations. The length, width and location of the single and multiple slots are set as parameters to be swept in CST, with the results shown in Fig 3.27 (b).

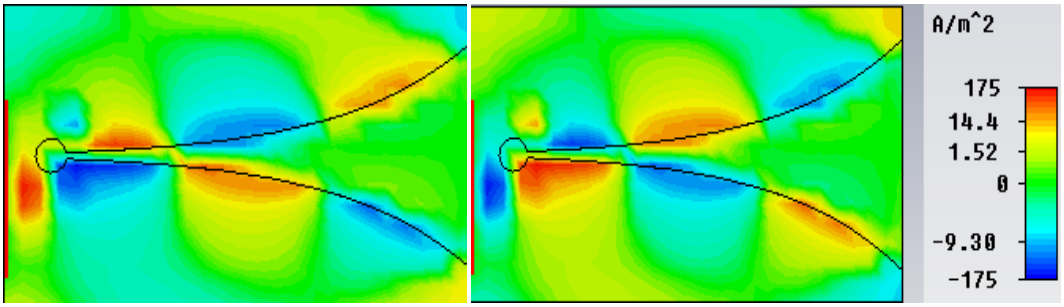

(a) **(b)**

Fig 3.26 The current density with the phase of (a) 0 and (b) 180 degree.

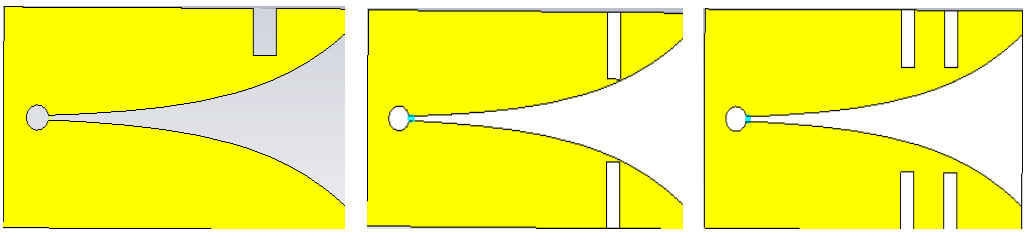

(a)

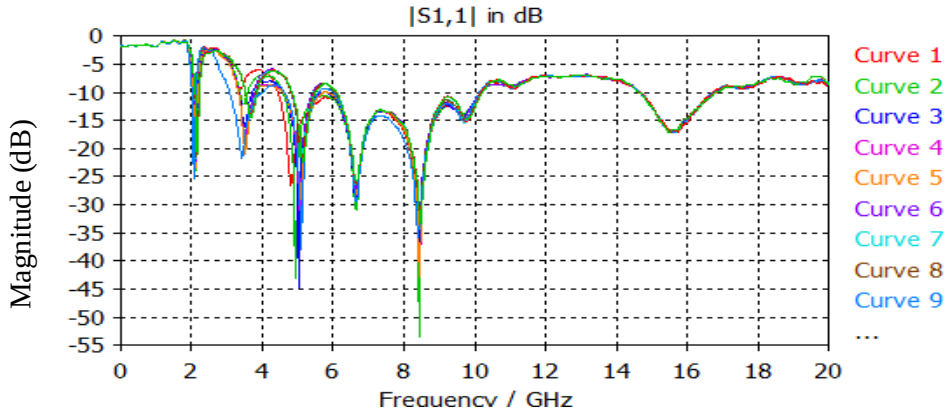

(b)

Fig 3.27 (a) the single and multiply slot configurations and (b) the simulated S_{11}.

3.5.2 The Final Design, Simulation and Measurement Results

3.5.2.1 The final design and scattering parameters

Fig 3.28 shows the simulated and fabricated slot Vivaldi antenna, with the slot dimensions being 10 *3 mm. The simulated and measured S_{11} and S_{21} are shown in Fig 3.29. As seen, the working frequency of the slot Vivaldi antenna ranges from 3 to 10 GHz which is wider than that of the original Vivaldi antenna (5-10 GHz), and this, indicates that the modified slot Vivaldi antenna not only maintains the original

dimensions but also has a better impedance matching in 3 to 5 GHz. The simulated and measured S_{11} parameters show good agreement between 3 and 10 GHz, although there is some discrepancy around 5GHz. Besides, the simulated and measured S_{21} also show acceptable agreement between 3 and 10 GHz. Similarly, here we use the words good or acceptable agreements since there are no specified certifications for the scatter parameters. The fabrication process error and the environmental influence all contribute to the discrepancy around 5GHz, which has been analyzed in Section 3.4.3.1.

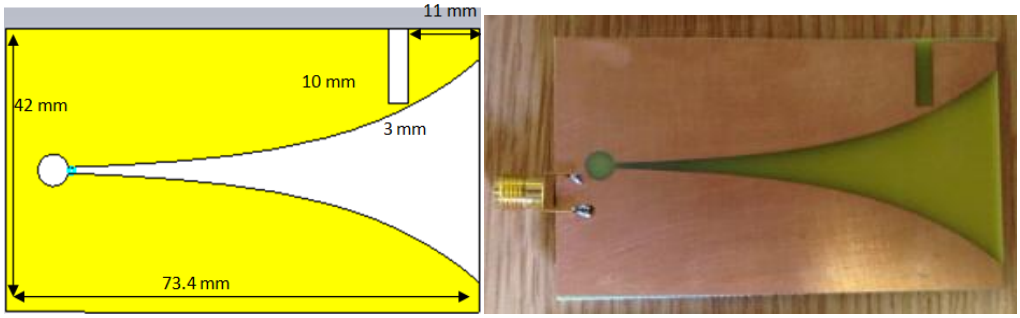

(a) **(b)**

Fig 3.28 The (a) designed and (b) fabricated slot Vivaldi antenna.

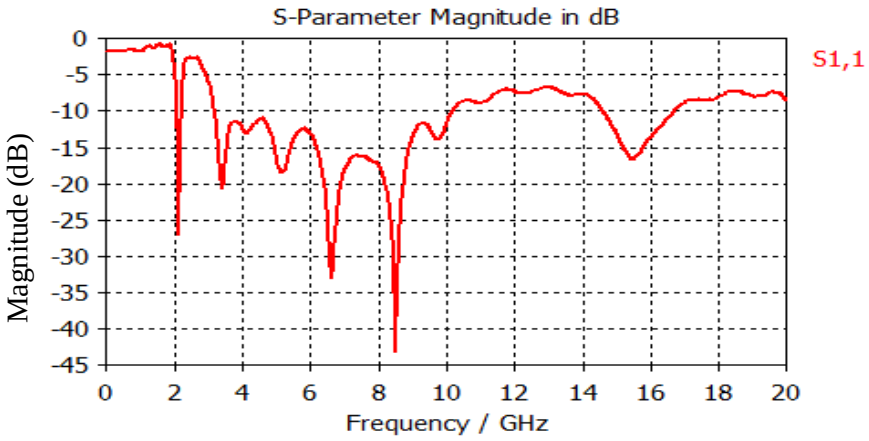

(a)

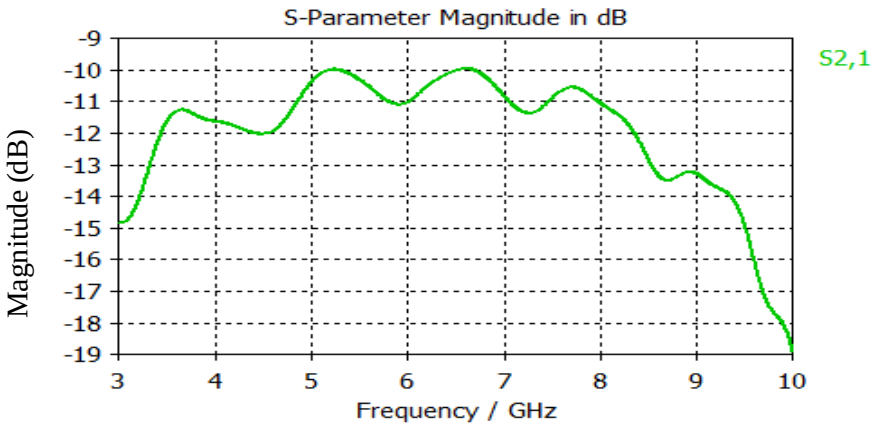
S-Parameter Magnitude in dB
Magnitude (dB)
-9
-10
-11
-12
-13
-14
-15
-16
-17
-18
-19
3
4
5
6
7
8
9
10
Frequency / GHz
S2,1

(b)

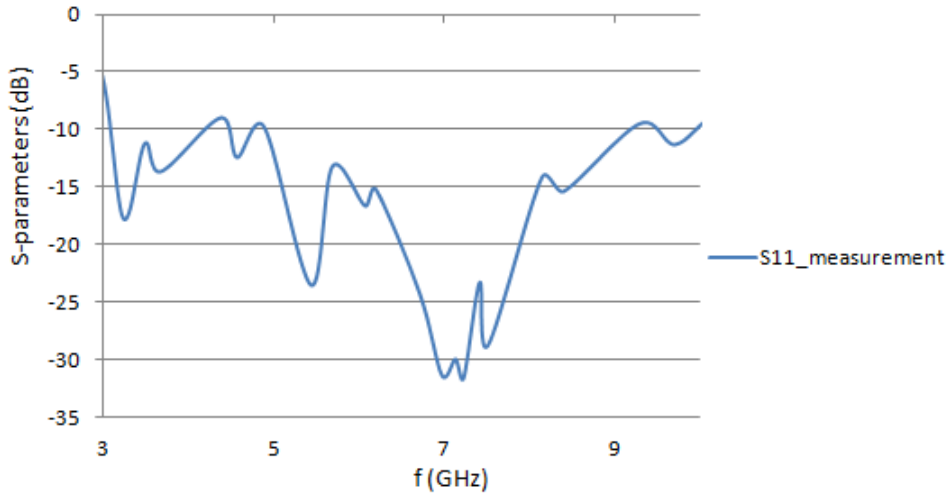
S-parameters(dB)
0
-5
-10
-15
-20
-25
-30
-35
3
5
7
9
f (GHz)
S11_measurement

(c)

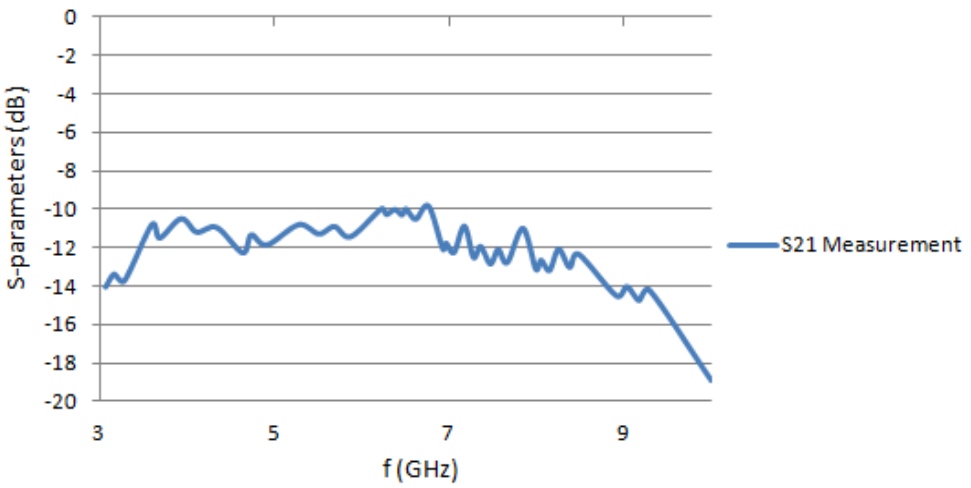

(d)

Fig 3.29 The (a) simulated and (b) measured S_{11} and the (c) simulated and (d) measured S_{21}

3.5.2.2 The current flow density

The current flow density is shown in Fig 3.30. As seen, the slot is located at the boundary between the maximum and minimum current density, which generates maximum capacitance to match the impedance. Besides, the positive and negative amplitudes are in the LHS and RHS of the slot at 0 degrees phase, while the opponent current density is observed at 180 degrees phase. This phenomenon can be observed from 3 to 7 GHz. From 8 to 10 GHz, the wavelength is too short compared with the slot. Hence, the peak current density only covers part of the slot edge.

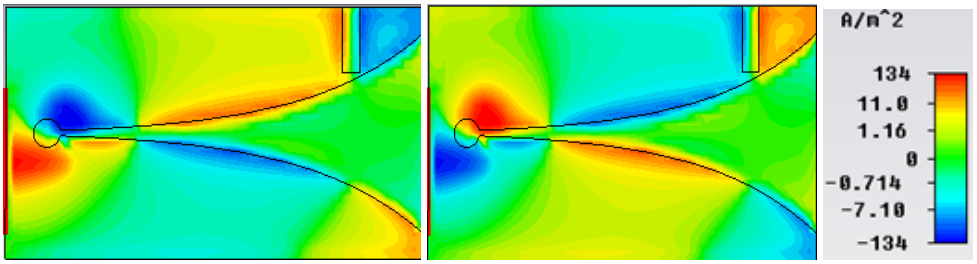

3 GHz, 0 degrees **3 GHz, 180 degrees**

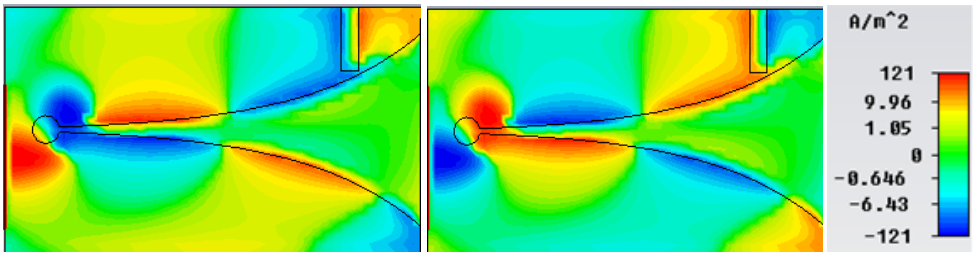

4 GHz, 0 degrees **4 GHz, 180 degrees**

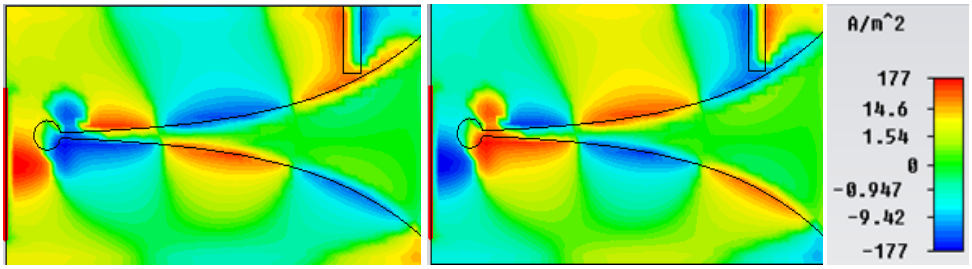

5 GHz, 0 degrees **5 GHz, 180 degrees**

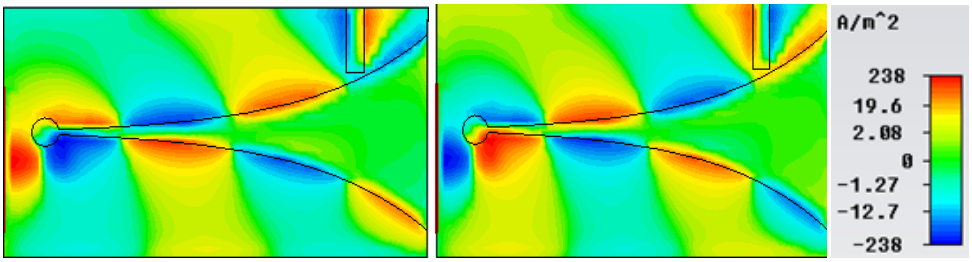

6 GHz, 0 degrees **6 GHz, 180 degrees**

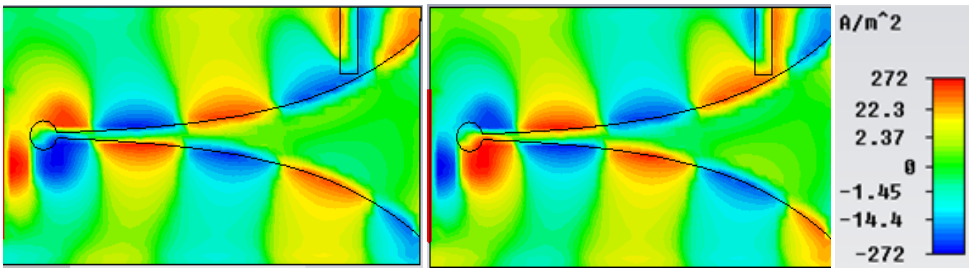

7 GHz, 0 degrees **7 GHz, 180 degrees**

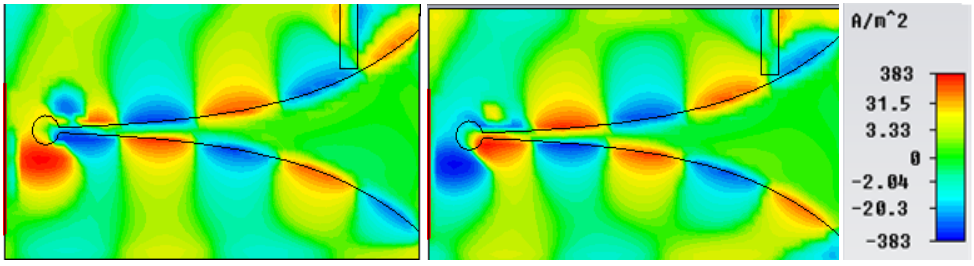

8 GHz, 0 degrees **8 GHz, 180 degrees**

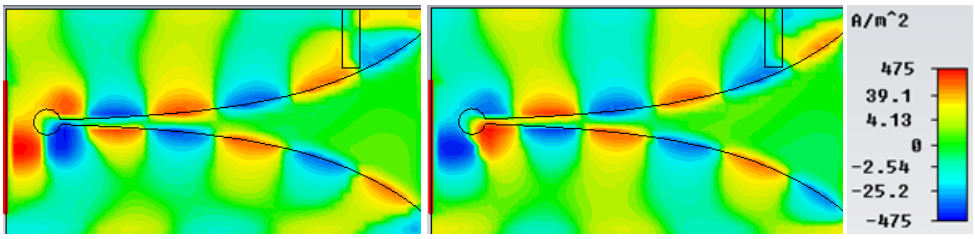

9 GHz, 0 degrees **9 GHz, 180 degrees**

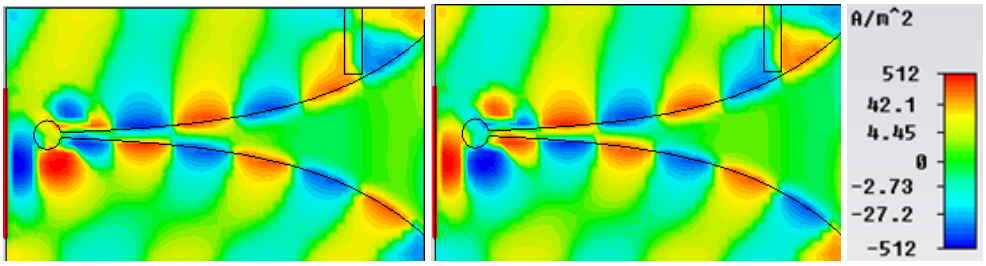

10 GHz, 0 degrees **10 GHz, 180 degrees**

Fig 3.30 Current density with the phases at 0 and 180 degrees from 3 to 10 GHz.

3.5.2.3 The radiation pattern and gain

The radiation pattern and gain are also simulated, with the results of radiation pattern shown in Fig 3.31. As seen, the designed slot Vivaldi antenna also has a directional radiation pattern along all working frequencies. Besides, the gains of the Vivaldi and slot Vivaldi antenna are also simulated, with the results shown in Fig 3.32. As seen, the gain in 3 GHz is close to 2.5. From 4 to 10 GHz, the gains of these two Vivaldi antennas are quite close, which shows that the slot Vivaldi antenna expands the working frequency while maintaining high gain.

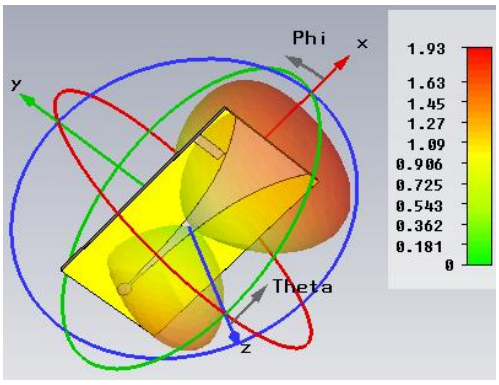

3 GHz

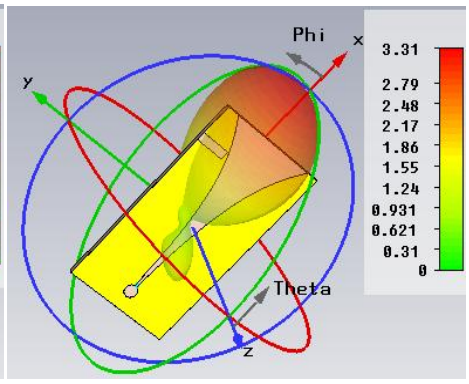

4 GHz

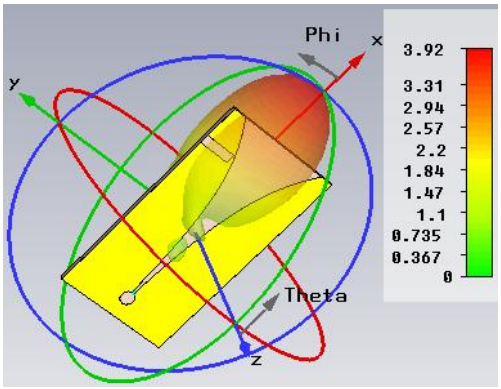

5GHz

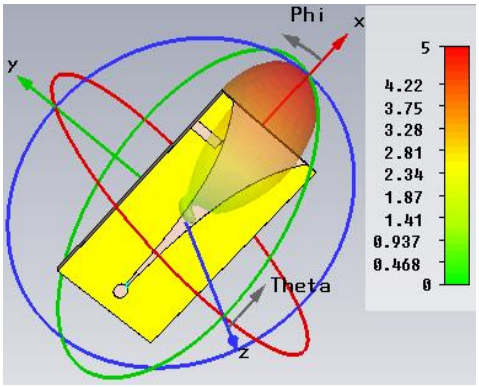

6 GHz

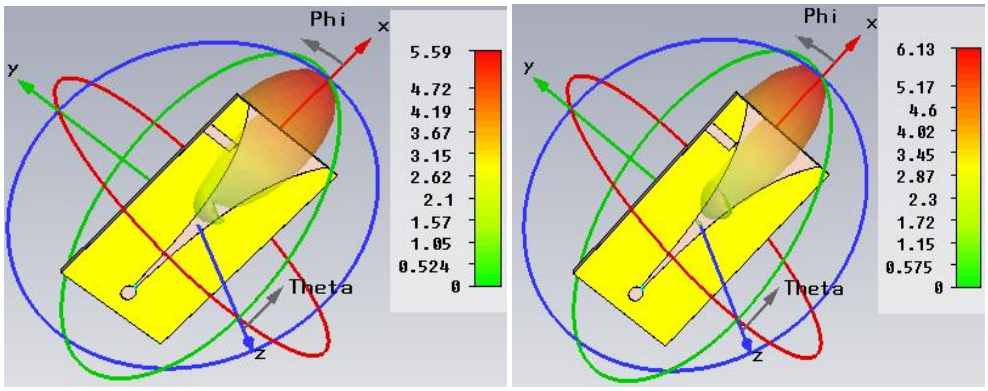

7 GHz **8 GHz**

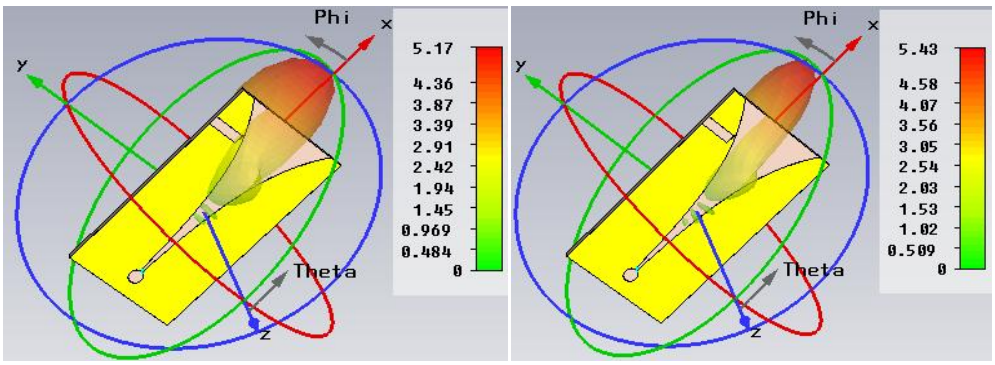

9 GHz **10 GHz**

Fig 3.31 The radiation pattern from 3 to 10 GHz.

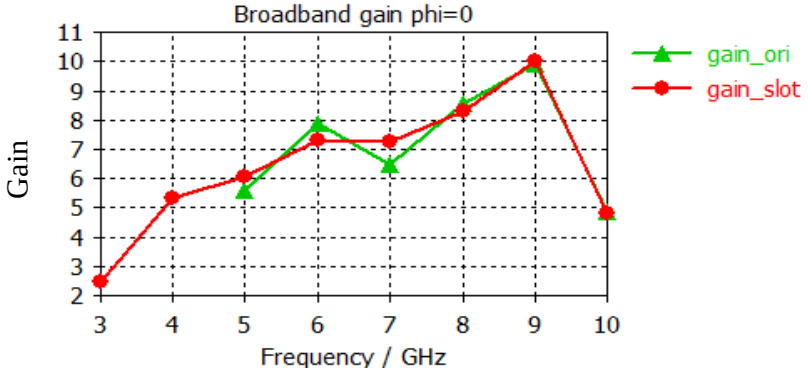

Fig 3.32 The gain of the original designed Vivaldi and the slot Vivaldi antenna from 3 to 10 GHz.

3.5.2.4 The near-field power flow density

The near-field power flow density is also simulated, with the results shown in Fig 3.33. It is observed that the energy gathers in the centre front of the antenna from 3 to 9 GHz. However, at 10 GHz the peak power starts to disperse with the increasing working frequency, acting as a bidirectional antenna, with the two radiation points being at the front edge of the Vivaldi antenna.

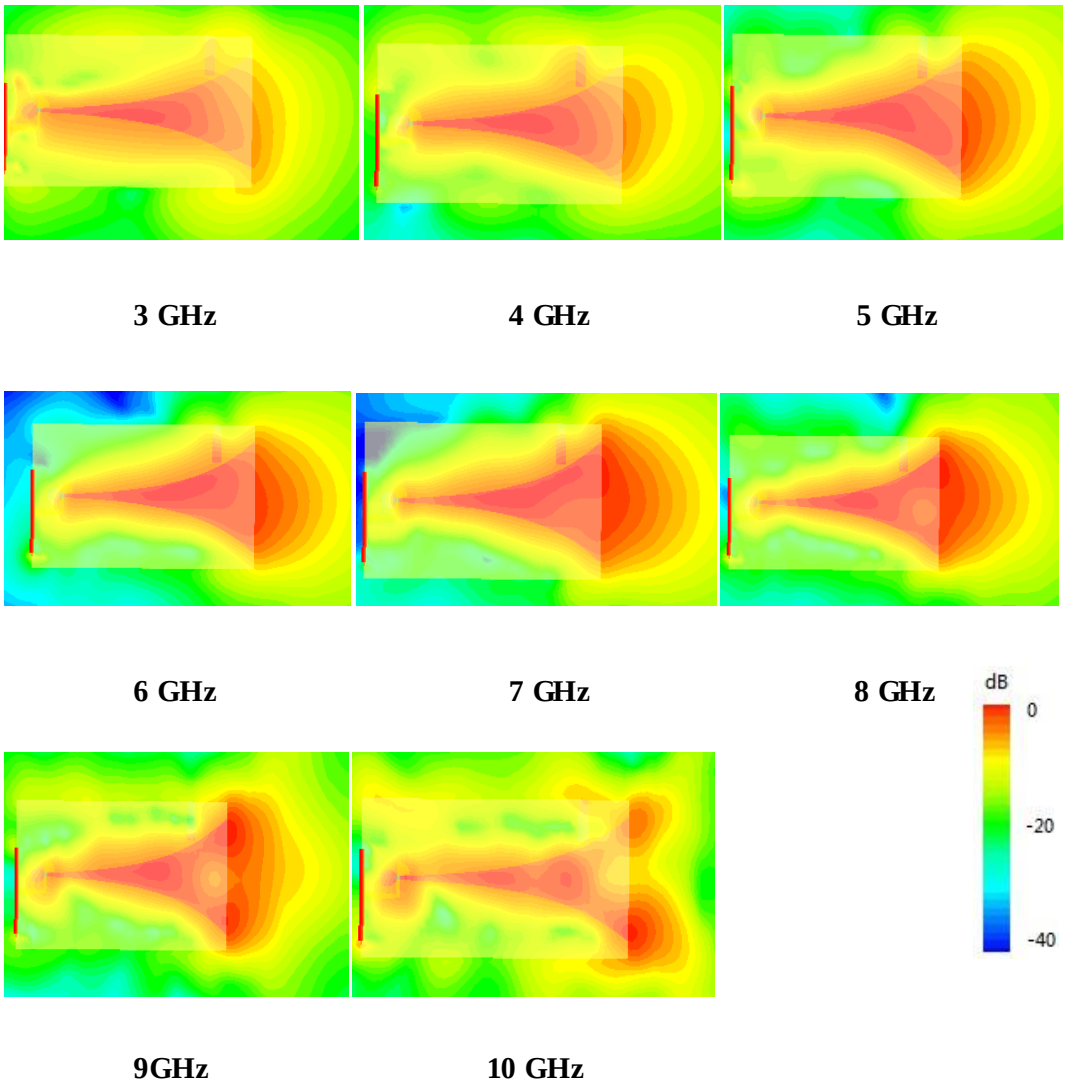

Fig 3.33 The near-field power flow density from 3 to 10 GHz.

3.6 Summary

In this chapter, an ultra-wideband Vivaldi antenna and its modified version as a slot Vivaldi antenna have been proposed for use in cancer detection. The desired antenna performance in terms of bandwidth, working frequency, gain, radiation pattern and beam width are achieved by manipulating the structural parameters of the Vivaldi antenna.

The proposed Vivaldi antenna exhibits an ultra-wideband working frequency ranging from 5 to 10 GHz. The transmission coefficients S_{21} show a very flat profile which will provide a minimal distortion. Besides, the designed Vivaldi antenna has been fabricated, and the scatter parameters measured using VNA. The simulated and experimental results show good agreement. The gains ranging from 5 to 10 GHz achieve 3.613, 6.151, 4.476, 7.207, 9.625 and 3.067 respectively. Furthermore, the desired directional radiation patterns are also achieved from 5 to 10 GHz.

A modified slot Vivaldi antenna is also proposed in order to achieve a better performance while maintaining the total dimensions of the Vivaldi antenna. An optimization method based on the equivalent circuit schematic is proposed for the modification of the Vivaldi antenna. A slot is added to the ground of the Vivaldi antenna in order to increase capacitance, and this, will increase the impedance matching. The final design achieves 3-10 GHz bandwidth while maintaining the directional radiation pattern. The gains ranging from 3 to 10 GHz achieve 2.5, 5.1, 6, 7.2, 7.1, 8.1, 10, and 4.8, respectively. The increase in bandwidth provides stronger penetration ability for the detection of deeply buried tumours.

Chapter 4 Breast Phantom Design and Experimental Measurement

4.1 Introduction

This chapter discusses the design of the breast phantom, including a simulation using the CST and the fabrication of the breast phantom based on tissue-mimicking method. The mono-static radar based microwave imaging system is then introduced. The breast phantom is measured using this imaging system, with the scatter parameters recorded in the time and frequency domains. In chapter 6, the received signals will be processed to create 3-D microwave images to indicate tumour position. This chapter only focuses on phantom design, experimental setup and signal collection.

4.2 Breast phantom

4.2.1 Simulated Breast phantom

The phantom design for the UWB transmission can be simplified in an approximation as a multi-layer model, with each layer corresponding to a particular tissue layer [106-108]. For example, the human head can be modelled as a combination of skin, fat, bone, grey matter and white matter layers. The breast can

also be modelled as skin and fat layers. Tumours and glands can then be fabricated and inserted into these special layers. Several parameters indicate the properties of layers, with the most important parameters being each layer's dielectric constant $\varepsilon_r(f)$, which is frequency dependent.

The dielectric constant $\varepsilon_r(f)$ in bio-layers can be derived by the Cole-Cole model given in Equation (4.2.1) [107-108]. The equation shows that the dielectric reduces as working frequency increases:

$$\varepsilon_\omega = \varepsilon_\infty + \frac{\varepsilon_s - \varepsilon_\infty}{1+(i\omega\tau)^{1-\alpha}} \qquad (4.2.1)$$

where, ω and α are the angular frequency and exponent parameter, ε_∞ and τ are the static frequency permittivity constants and time constant. ε_ω and ε_s are its static and infinite frequency permittivity constants.

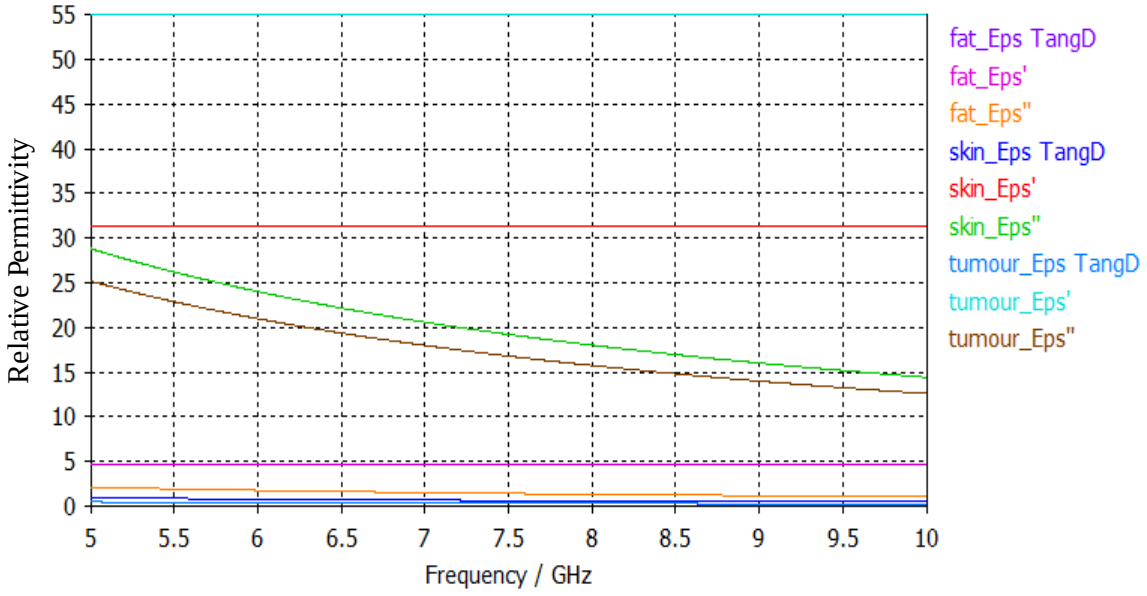

Fig 4.1 The relative permittivity of the skin, fat and tumour in the CST library. Eps', Eps'' and Eps TangD are the real, imaginary part and their tangent value.

Based on this theory, the breast phantom is simulated in the CST Microwave Studio software using the FDTD method. In the CST, a library consisting of a range of materials is available for the design of the microwave devices as well as bio-organs. A phantom simulation of a bio-organ such as the human head is used for the measurement of Specific Absorption Rate (SAR). Furthermore, the bio-organ phantoms can be customized for different applications. **Fig 4.1** shows the real and imaginary parts of the relative permittivity of skin, fat and tumour, as provided in the CST library. In this work, a cancerous breast phantom is designed for breast cancer detection, using these available materials such as skin, fat and tumour. For the study, two kinds of breast phantoms are proposed. One is a planar phantom and the other is a hemi-sphere phantom. The design of the planar phantom is concluded for the purposes of simplifying the working progress, whereas the hemi-sphere breast phantom provides a more realistic model.

4.2.1.1 Planar breast phantom

Fig 4.2 shows the designed planar breast phantom. The dimensions of the breast phantom is 148mm×86mm×37mm. A spherical tumour with a radius of 5 mm is embedded in the phantom, at a depth of 25 mm.

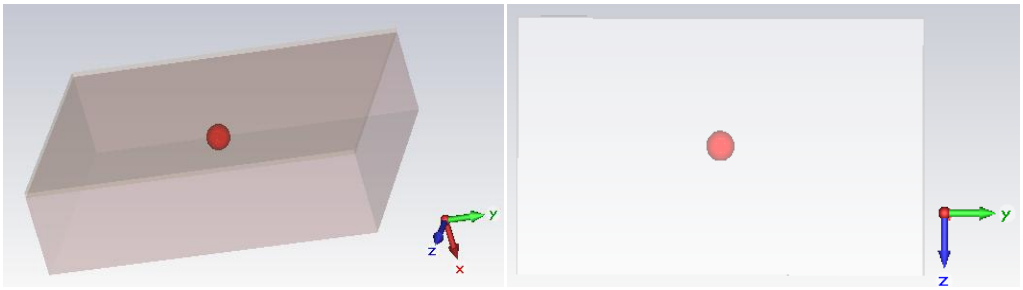

(a) **(b)**

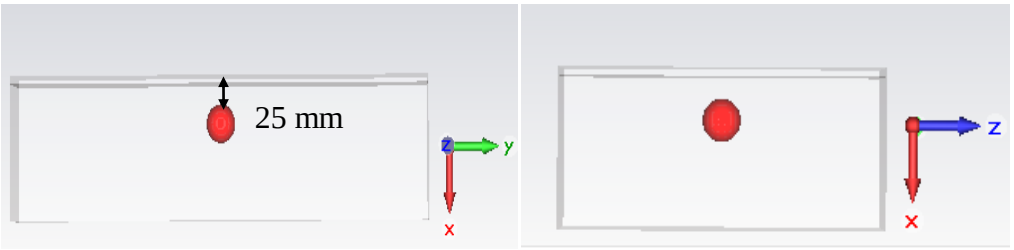

(c) **(d)**

Fig 4.2 (a) The planar cancerous breast phantom and the phantom in the view of (b) y-z axis (c) x-y axis and (d) x-z axis.

4.2.1.2 Hemi-sphere breast phantom

The designed hemi-sphere breast phantom is shown in Fig 4.3. This hemi-sphere breast phantom consists of a skin layer (thickness = 2mm), a fat layer (thickness = 68 mm), with a spherical tumour (radius = 5mm) embedded in the fat layer. The tumour is at a depth of 25 mm.

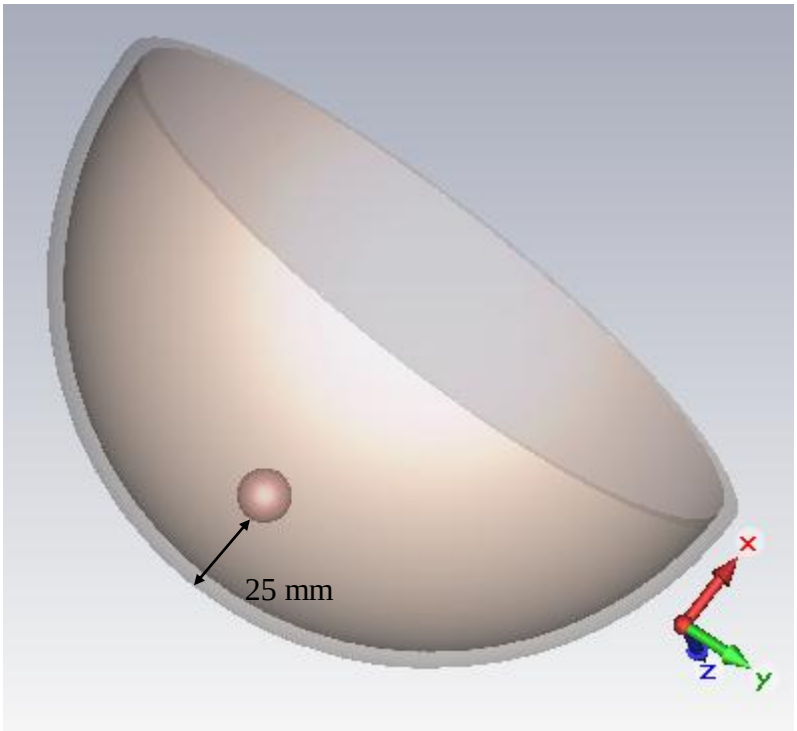

Fig 4.3 The hemi-sphere breast phantom.

4.2.2 Tissue Mimic Breast Phantom

Electromagnetic based technology works at microwave frequency. Therefore, the growing interest in the interaction of microwave with bio-tissues has led researchers to design bio-phantoms which mimic the electrical properties of real tissue in the microwave frequency.

4.2.2.1 Fabrication Method

Several tissue mimicking (TM) methods have been proposed [109-112]. The most attractive TM method is based on gelatine-oil. This method has advantages such as stable mechanical properties, low cost and easy fabrication. A gelatine-oil based TM

method has been proposed for UWB with working frequency ranging from 500MHz to 20 GHz [110-111]. The detailed fabrication method is as follows.

1) Mix p-toluic acid into n-propanol in a beaker, and then heat until the p-toluic dissolves. The heating source should be controlled very carefully to avoid the over-heating.
2) Mix (1) into deionized water which is at room temperature.
3) Pour while stirring dry mass gelatine into (2). This procedure should be in room temperature and the gelatine must be dry.
4) Cover the beaker using a film, heat and stir (3) using the water heating in order to prevent overheating. The heating should finish when the mixture become transparent with no air bubbles exist.
5) Continue to stir the mixture until all air bubbles disappear and the mixture is uniform.
6) Immerse the backer into cool water, stirring and wait the mixture to 50℃.
7) Pour safflower oil into (6) while stirring. The safflower oil should be 50℃ as well.
8) Add Ultra Ivory detergent into (7) while stirring. This mixture should become while colour and very uniform. Cool the mixture until 40℃ by immersing the baker in cool water while continuing steering.
9) Add formadldehyde solution into (8) while stirring. Cool the mixture until 34℃ and then pour into a mould to produce phantom.
10) Wait more than 5 days for the gelatine to become stable.

It is worth noting that the fabrication procedures do not specify the used volumes of the chemical material. For the fabrication of each layer, the amounts of ingredients are given in Table 4.1. [110]

Table 4.1 The Amount of Chemicals for Each Layer.

	Chemical Amount		
	Skin	Fat	Tumour
p-toluic acid (g)	0.294	0.133	0.346
n-propanol (mL)	28.69	6.96	17.00
Deionized water (mL)	279.5	132.7	328.0
200 Bloom gelatine (g)	50.02	24.32	58.67
Formaldehyde (g)	1.53	3.33	3.72
Oil (mL)	265.6	98.6	38.4
Ultra Ivory detergent (mL)	12	5.86	2.00

4.2.2.2 TM Planar breast phantom

In this work, the two-layer phantom is modelled as a cuboid, which consists of a skin layer 1 mm thick and a fat layer 35 mm thick. The dimensions of this breast phantom are 145mm× 86 mm × 45 mm. The chemical mixture for the skin layer is mixed and poured into a cuboid container. This skin layer mixture should then be allowed to rest for 2-3 days to become solid. Then the fat layer mixture can be poured into the same container to cover the skin layer. The solid skin layer is flexible, firm and off-white in colour. However, the solid fat layer is a slightly flaccid and a pale yellow colour. This colour difference is due to the fat layer containing more oil but less gelatine. The fabricated planar breast phantom is shown in **Fig 4.4**.

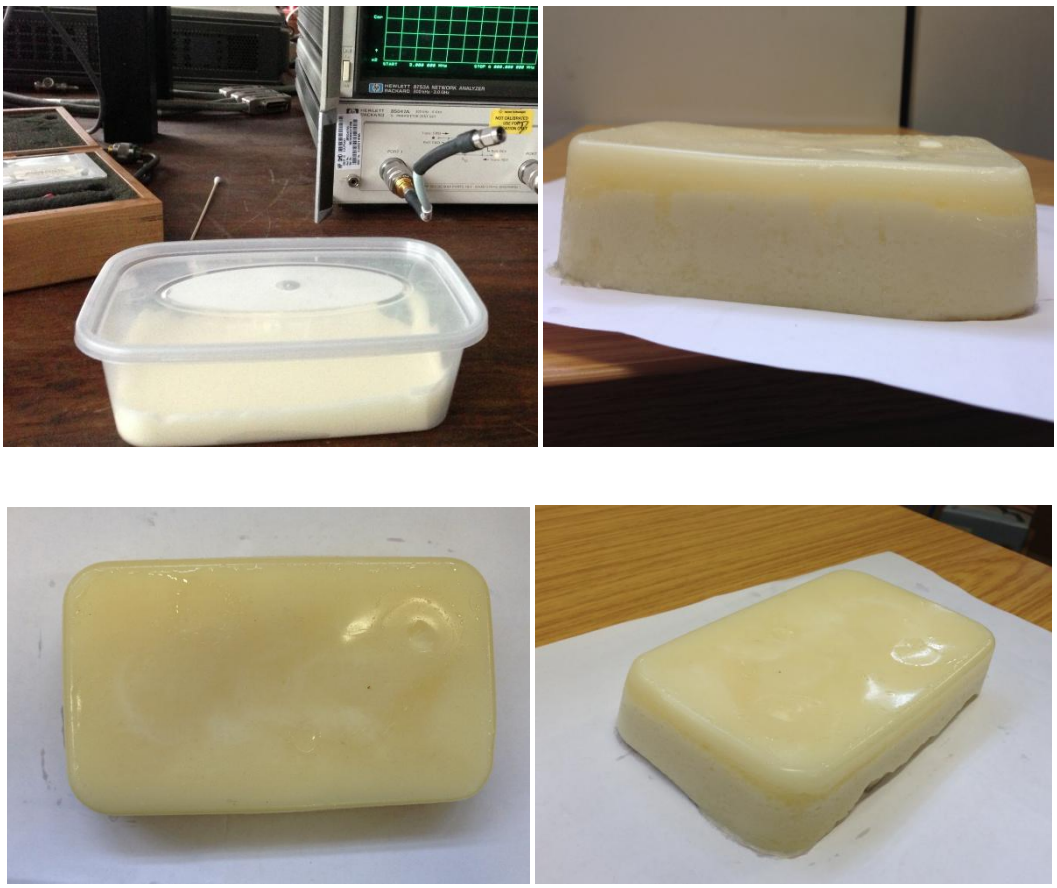

Fig 4.4 The TM planar breast phantom.

4.2.2.3 TM Hemi-sphere Breast Phantom

The TM planar breast phantom has been fabricated to provide a simple prototype for preliminary study. However, a more realistic TM model is also required. The fabrication procedure for the TM hemi-sphere breast phantom is quite similar to that of the planar one. The only difference is the mould used. The mould for the planar breast phantom is a simple cuboid container. However, the mould for the TM hemi-sphere breast phantom is much more complicated, and the most difficult part is the fabrication of the skin layer.

Fig 4.5 shows the mould for the TM hemi-sphere breast phantom. This mould has a cover and a base, with inner radius being 69 and 70 mm, respectively. The skin layer tissue can be fed into this 1 mm gap. The detailed fabrication procedure is as follows:

1) Fabricate the skin layer tissue using the list of ingredients and amounts given in Table 4.1.
2) Feed (1) into the base before the mixture becomes solid.
3) Place the cover onto the base.
4) Wait for 2 days for the skin layer to solidify
5) Remove the cover. This procedure must be conducted very careful since the skin layer is very thin and easily damaged.
6) Fabricate the tumour mixture and cut it down to a 5mm sphere.
7) Leave the skin layer in the base and feed the fat tissue onto the skin layer.
8) Place the tumour in the desired position before the fat layer solidifies.

These 8 steps describe the fabrication procedure of the cancerous breast phantom. However, some challenges need to concern. In steps 3), the procedure of placing the cover to the base could easily produce air bubbles. The air bubbles could easily break the skin layer. In step 5) when remove the cover it is very easy to tear the skin layer. To avoid such problems, the trick is to compress and remove the cover slowly and carefully. Besides, the cover must be in the centre of the base and always maintain the horizontal to the base. However, even though we carefully carry out these steps, the skin layer is still easily broken since the skin layer is too thin (1 mm). The solution is to repeat the fabrication steps until successful. For our experimental work, we repeat this fabrication procedure 5 times to obtain a complete skin layer. **Fig 4.6** shows the fabricated TM hemi-sphere breast phantom. In [110], the author uses two bowls to compress the mixture to produce the skin layer. The problem is that these two bowls are too light, which require compressing these two bowls using hand. This procedure is very difficult to carry out since it is very easy to use unequal pressure. The

thickness of the resulting skin layer could be unequal. However, in our experiment, a heavy plastic cover is used as the cover. The skin layer can be produced using the own weight of the cover to achieve the equal pressure.

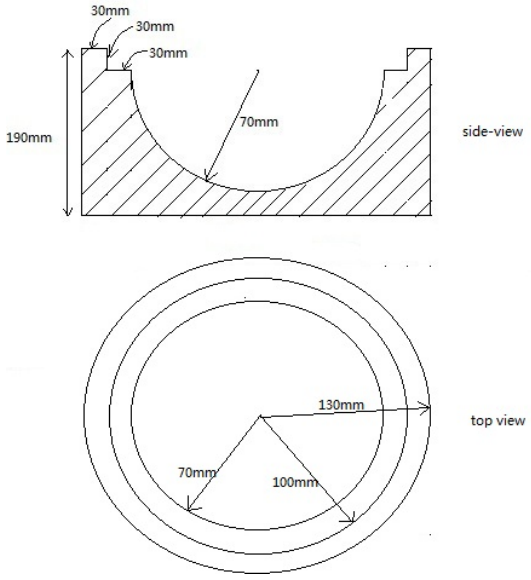

(a)

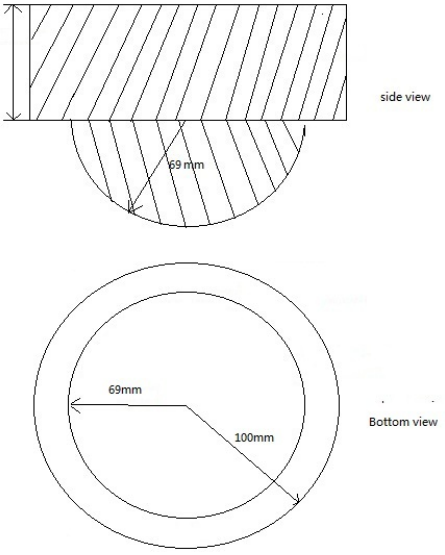

(b)

Fig 4.5 The mould for the TM hemi-sphere breast phantom, (a) the base and (b) the cover.

Fig 4.6 The TM hemi-sphere breast phantom.

4.3 Experimental Study of Planar breast phantom

The breast phantom has been simulated and fabricated based on the CST and TM methods, respectively. This section describes the measurement of breast phantom using the designed Vivaldi antenna. The planar and semi-sphere breast phantoms are discussed separately, and the scatter parameters are measured using single antenna or an antenna pair in different configurations. However, in this chapter the microwave images are not presented. The scatter parameters obtained are analyzed and processed in the next chapter and then used to create the microwave images.

4.3.1 Simulation

The planar breast phantom has been simulated in the CST. Two antenna configurations, a single antenna and an antenna pair, are proposed and used to measure the breast phantom, with the scattering parameters recorded.

4.3.1.1 Single Antenna

- ***Frequency Domain Signals***

The single antenna configuration is shown in **Fig 4.7**. The Vivaldi antenna is placed on the top of the breast phantom, with the distance to the skin layer being 30 mm. The front middle of the antenna is located towards the tumour. This antenna is then moved to scan different locations in the steps of 10 mm. The dimensions of this breast phantom are 145mm× 86 mm × 45 mm. Hence, a total of 112 (14 × 8) sets of scatter parameters are obtained by this antenna scanning, as shown in **Fig 4.8**. However, these scatter parameters have very close profiles and overlap with each other. It is very difficult to distinguish between them. Hence, only three sets of typical antenna locations are selected, with the notation of X_1, X_2, and X_3 shown in **Fig 4.7**.

These three sets of S_{11} are located 0, 35, 70 mm away from the tumour in the Y-axis to provide a comparison of the sensitivity of the cancerous and healthy tissues to the antenna pulse.

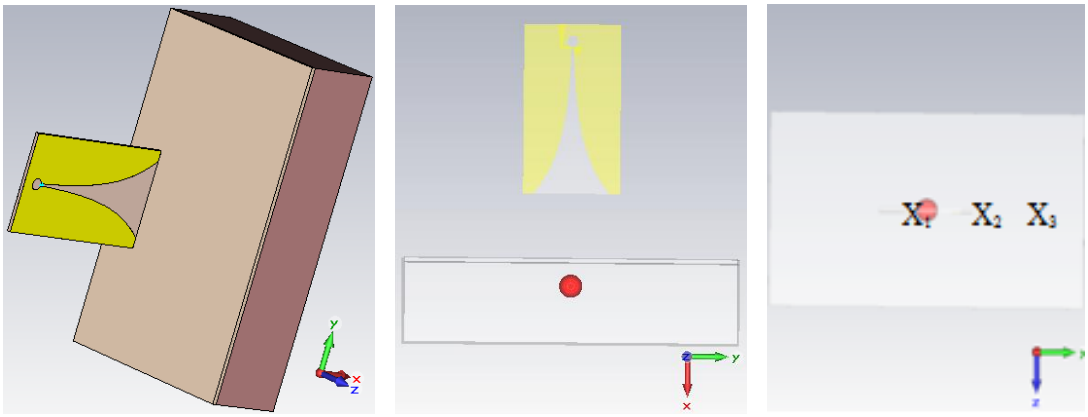

Fig 4.7 The single antenna configuration.

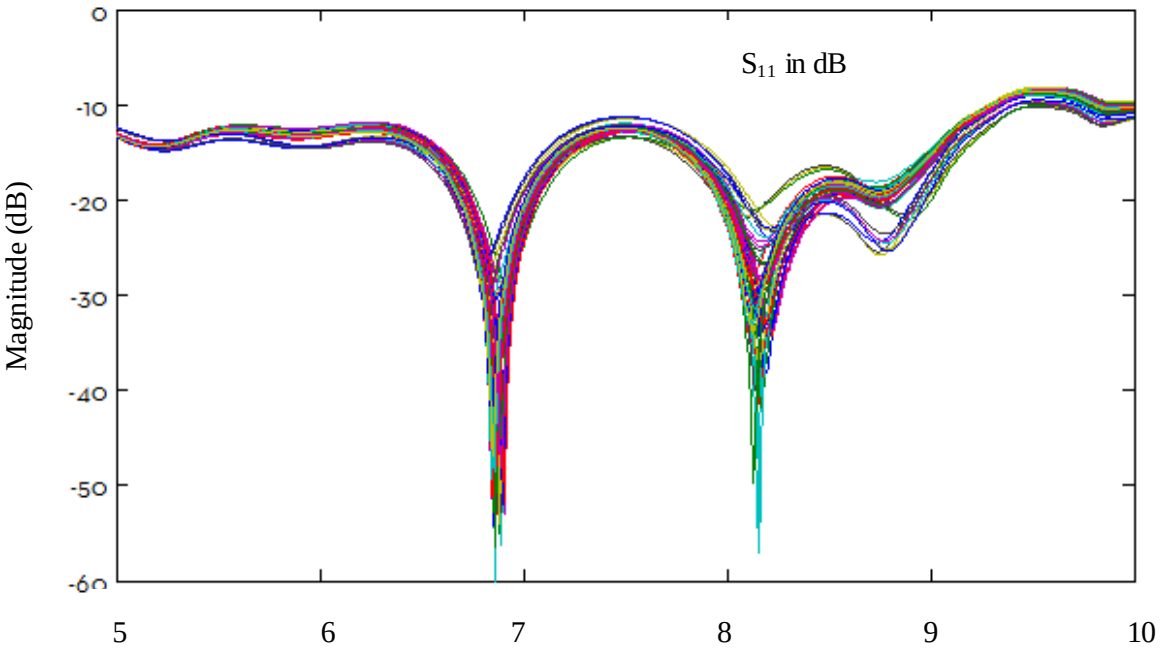

(a)

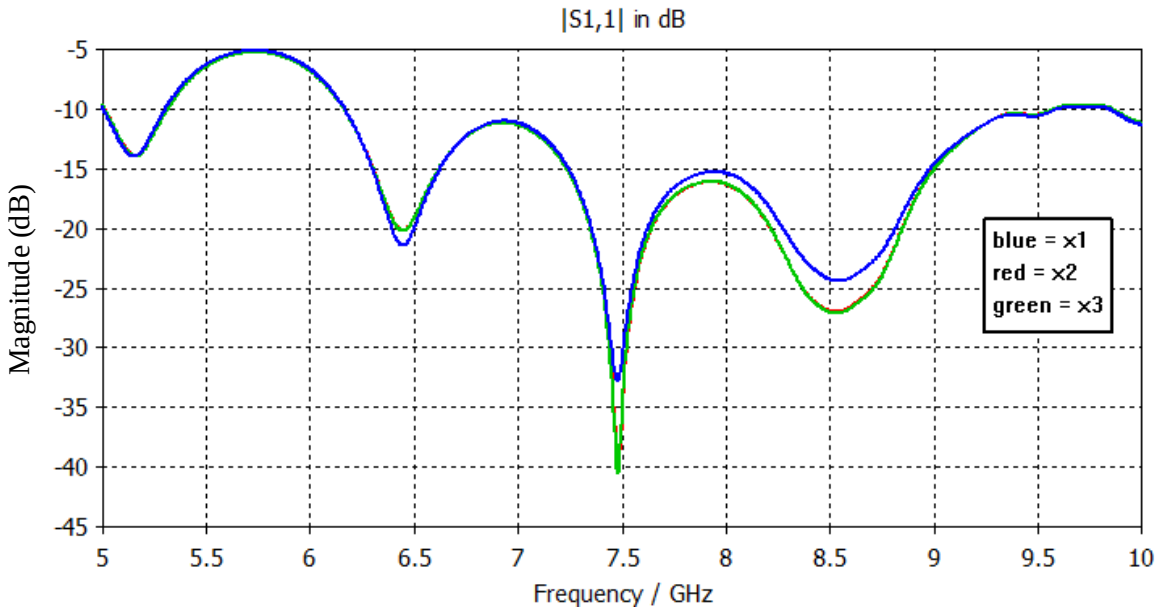

(b)

Fig 4.8 Results for (a) all sets of S_{11} parameters and (b) selected S_{11} parameters.

The term 'sensitive' here refers to the scatter parameter S_{11} which represents the reflected energy from the tissue. **Fig 4.8** (b) shows that the X_1 is higher than both X_2 and X_3 in all working frequencies except 6.4 GHz. Besides, the X_2 and X_3 almost completely overlap with each other. Based on the collected $S_{11,}$ it can be concluded that the reflected energy (S_{11}) increases when the antenna moves close to the tumour; otherwise, it is reduced when the antenna moves away from the tumour. This is the basic principle which can be used to create the microwave images to indicate the tumour position. However, the creation of the microwave image is not simple, since the received signals have to be processed first. Based on electromagnetic theory, the discontinuity of a boundary will cause a strong reflection of the incident electromagnetic wave. The reflection level is highly dependent on the dielectric constant difference. Hence, the strong reflection from the tumour is due to the high difference in relative permittivity between cancerous and healthy tissues. Furthermore,

the pencil radiation property of the Vivaldi antenna not only ensures that enough energy penetrates the phantom but also reduces the region of illumination, and this, increases the resolution of the microwave image.

- ***Time Domain Signals***

In addition to the frequency domain scatter parameters, time domain signals are also measured. The simulated time domain signals O_{11} are presented in **Fig 4.9**. Similarly, the time domain signals in X_1, X_2, and X_3 are also collected. An insert picture is also presented to indicate the very weak tumour response.

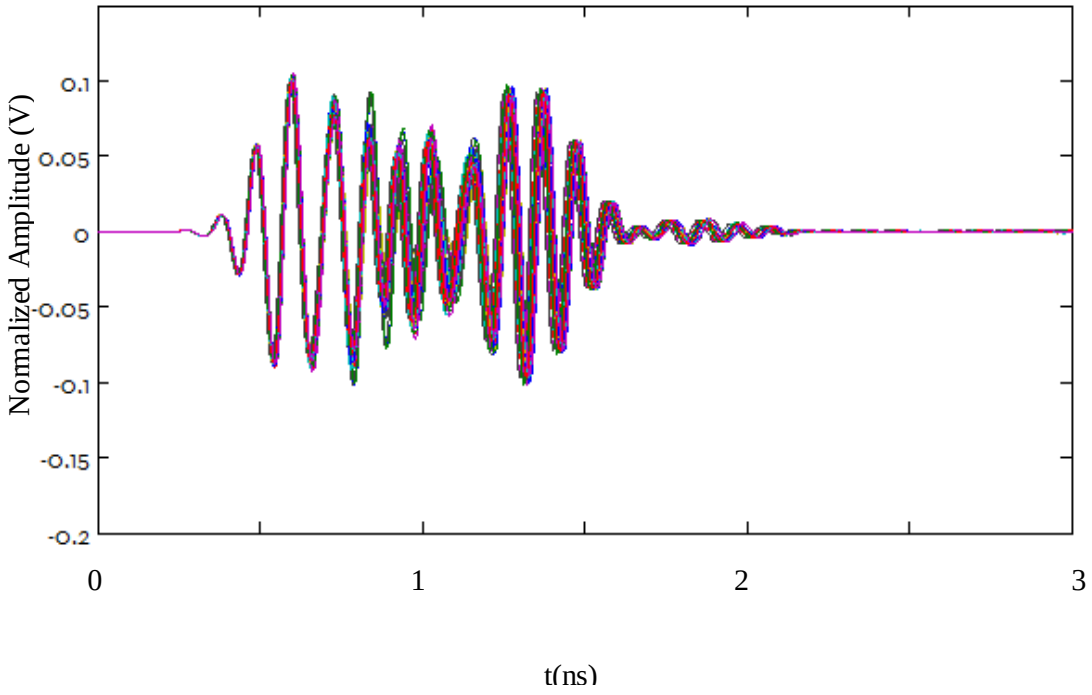

(a)

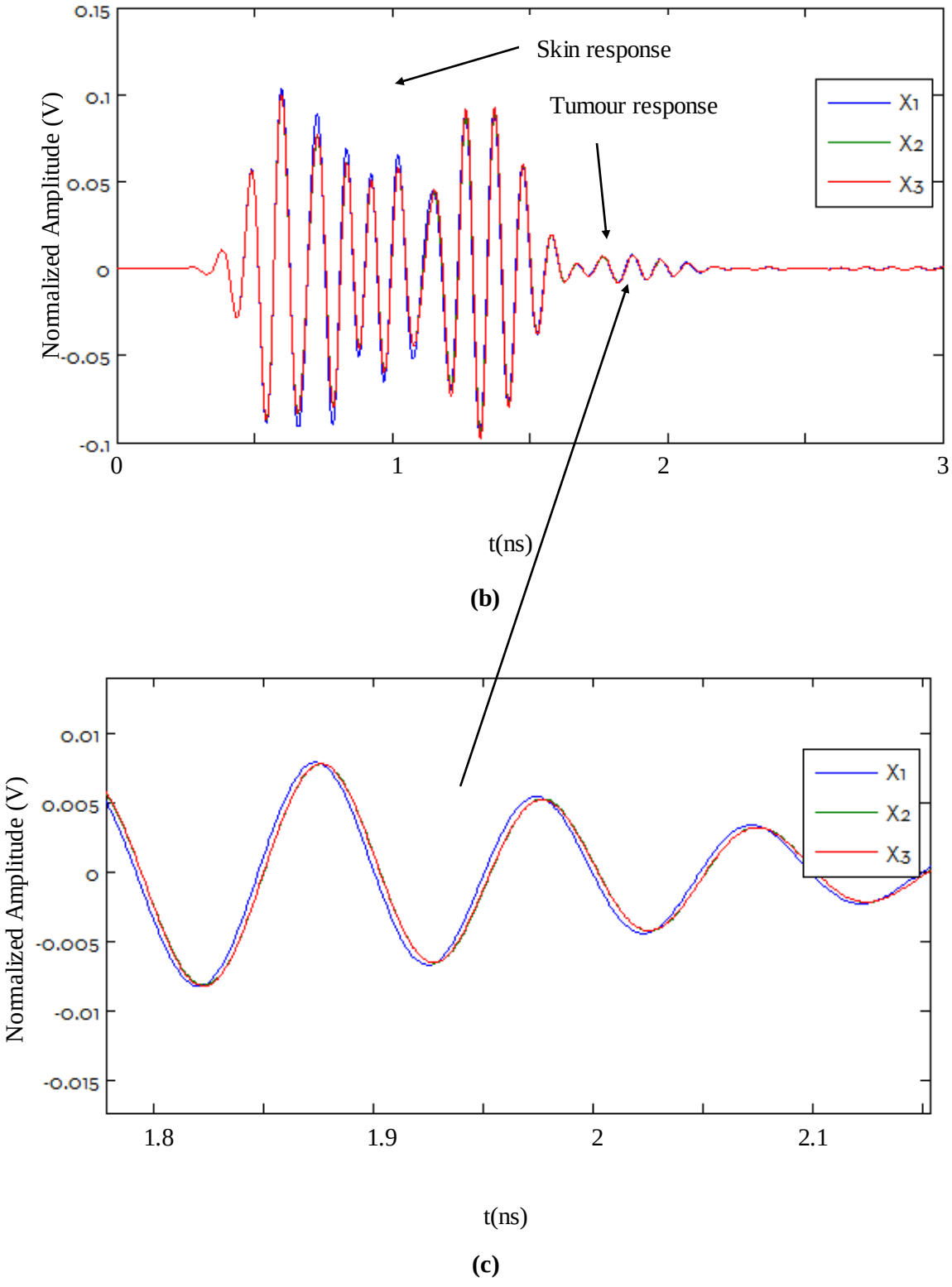

Fig 4.9 Results of (a) all sets of O_{11} parameters, (b) selected O_{11} parameters and (c) the enlarged part.

Fig 4.9 shows that the received signals have very similar profiles and the tumour response is very weak due to the most energy being reflected by the skin layer. The same conclusion can also be drawn based on the time domain signal, where the strongest tumour response can be received when the antenna moves close to the tumour.

The use of the time domain signals allows for the identification of the different tissue response (skin and tumour responses) in the time sequence. The microwave propagation speed in different tissues can be calculated based on their relative permittivity:

$$v_m = \frac{c_0}{\mathrm{Re}\left[\sqrt{\varepsilon_r(f)}\right]} \tag{4.3.1}$$

where v_m is the microwave wave propagation speed in different tissues, ε_r is the relative permittivity of the tissue and c_0 is the wave propagation speed in vacuum. Hence, the propagation time to the different layers (skin, fat and tumour) can be estimated using distance/speed. However, a more accurate method for the estimation of response time is introduced in the next chapter.

In addition to the identification of the different tissues in the time sequence, another advantage is that the use of time domain signals provides a better average description over the whole working frequency range rather than just focusing on certain working frequencies. The incident wave uses an UWB signal ranging from 5 to 10 GHz. The low frequency component provides high penetration ability to detect relatively deeply buried tumours while the high working frequency component lacks penetrating ability but offers higher resolution to detect relatively small tumours. The time domain signals contain the high and low frequency components which can be used to comprehensively describe the tumour properties.

4.3.1.2 Antenna pair I

- ***Frequency Domain Signals***

In this section, an experimental setup using the antenna pair is proposed. Unlike in the single antenna configuration, two Vivaldi antennas are used. One is the transmitting antenna and the other is the receiving antenna. The spatial relationship between the two antennas is clearly illustrated in **Fig 4.10**. The distance between these two antennas is larger than $\lambda/2$ which significantly reduces the mutual coupling. This antenna pair also moves to scan the breast phantom, as in the single antenna configuration. The forward transmission coefficient S_{21} is recorded instead of S_{11}. Here, for $S_{21,}$ the notation 1 and 2 refers to the transmitting and receiving antennas respectively. The working principle is similar to that of the single antenna configuration. The transmitting antenna transmits the incident wave to the breast phantom, and the reflected wave is received by the receiving antenna.

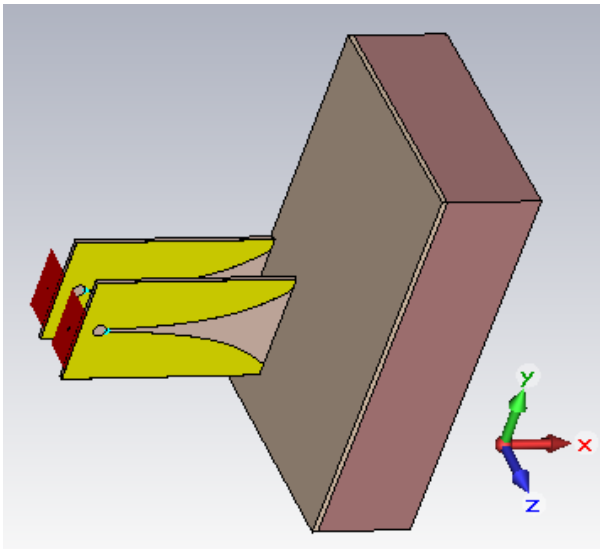

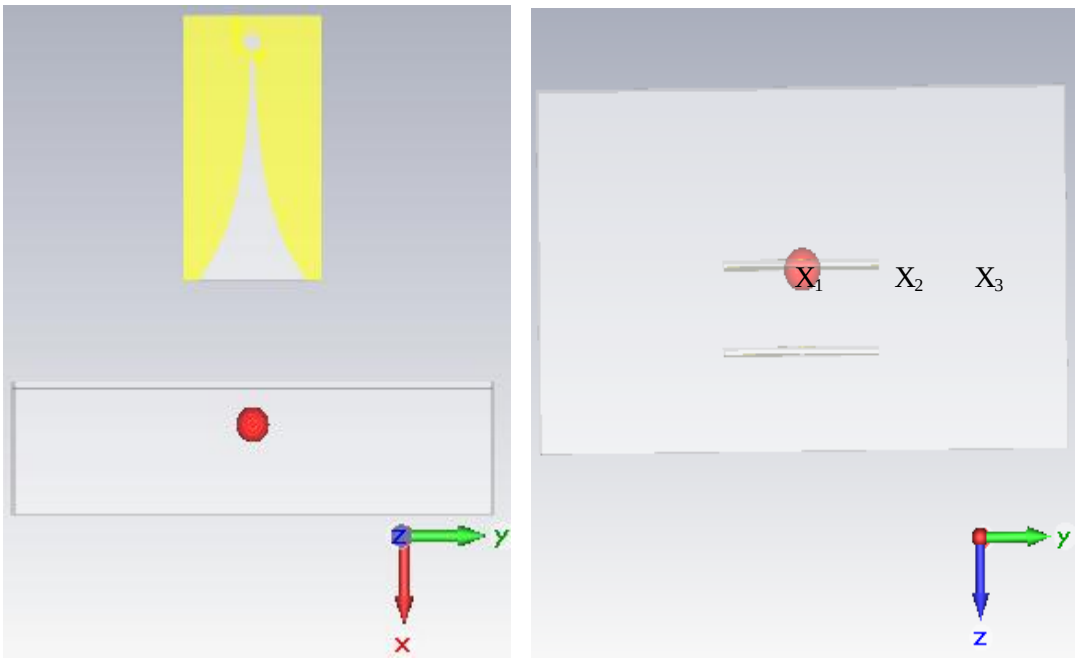

Fig 4.10 The antenna pair I configuration.

In the study of mono-static radar based imaging systems, the antenna pair is the most commonly used configuration. The transmitting and receiving antennas are connected to the transmitter and receiver, respectively. The use of the single antenna configuration requires a high speed switcher in order to switch the antenna to the transmitter and receiver in a very short duration. Firstly, the single antenna transmits a pulse to the breast and then the antenna should be connected to the receiver before the reflected wave is received. However, in this work, the antenna is connected to the Vector Network Analyzer (VNA). The scattering parameters can be directed measured and displayed using the VNA. The focus here is the investigation of breast cancer detection rather than transmitter and receiver design. Hence, based on the VNA, all of the signal and antenna pair configurations are acceptable.

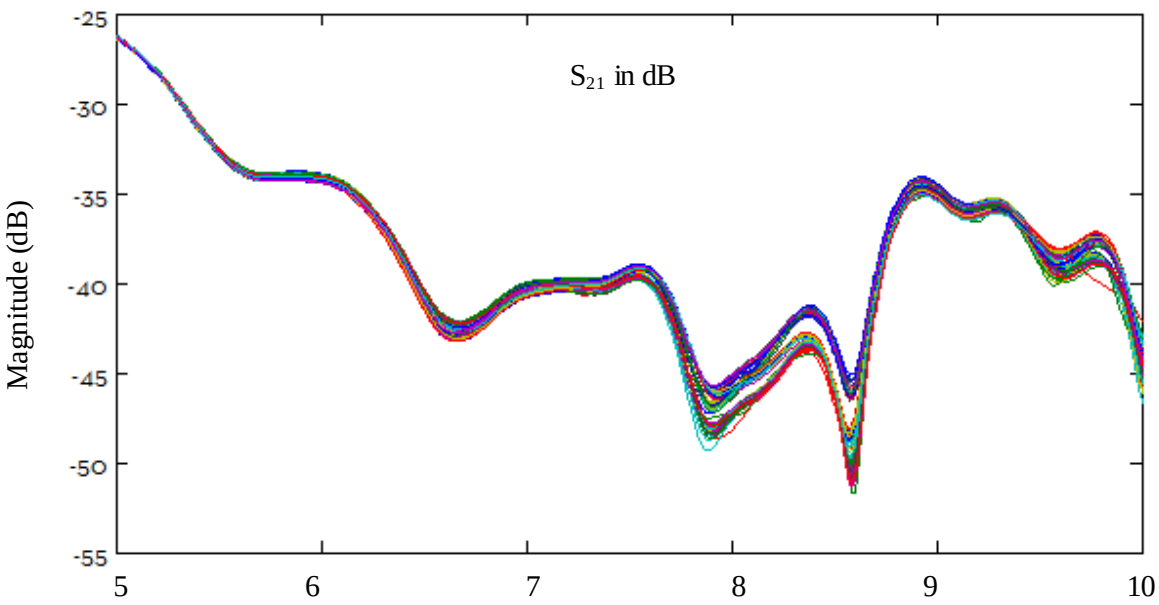

(a)

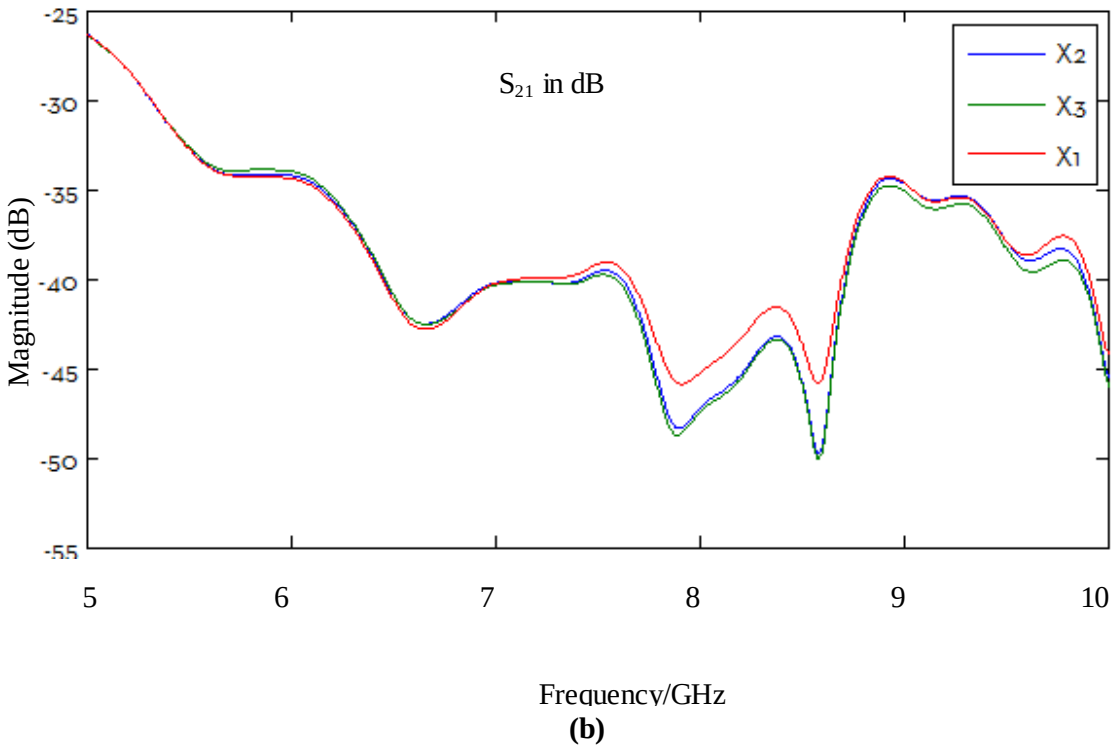

(b)

Fig 4.11 Results of (a) all sets of S_{21} parameters and (b) selected S_{21} parameters.

Fig 4.11 shows the received and selected S_{21}.The antenna pair moves together to scan the breast phantom. The selected S_{21} parameters correspond to three measurement locations X_1, X_2 and X_3, shown in **Fig 4.10**. The received S_{21} parameters also show that the reflected energy increases when the transmitting antenna moves close to the tumour; otherwise, the reflected energy is reduced when the transmitting antenna moves away from the tumour. This conclusion is quite similar to that of the single antenna configuration. The difference between the single antenna and the antenna pair configurations is that the latter uses one antenna to transmit the signal and the other as the receiving antenna to receive the signal. The single antenna configuration uses the single antenna to both transmit and receive the signal.

- ***Time domain signals***

In addition to the frequency domain scatter parameters, time domain scattering signals are also collected. **Fig 4.12** shows the received time domain signals O_{21} and three selected signals.

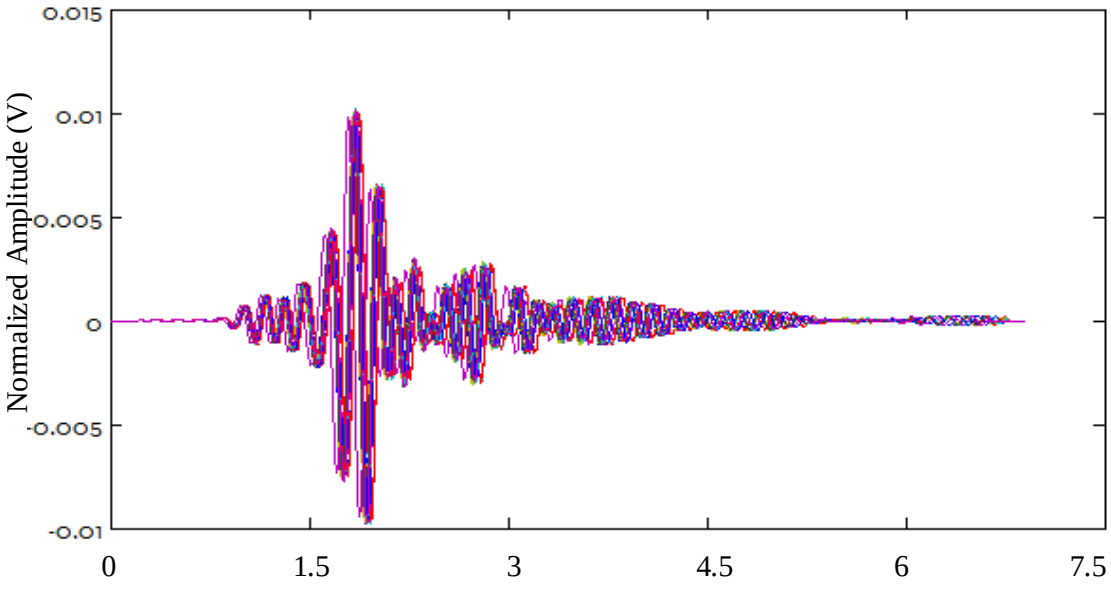

(a)

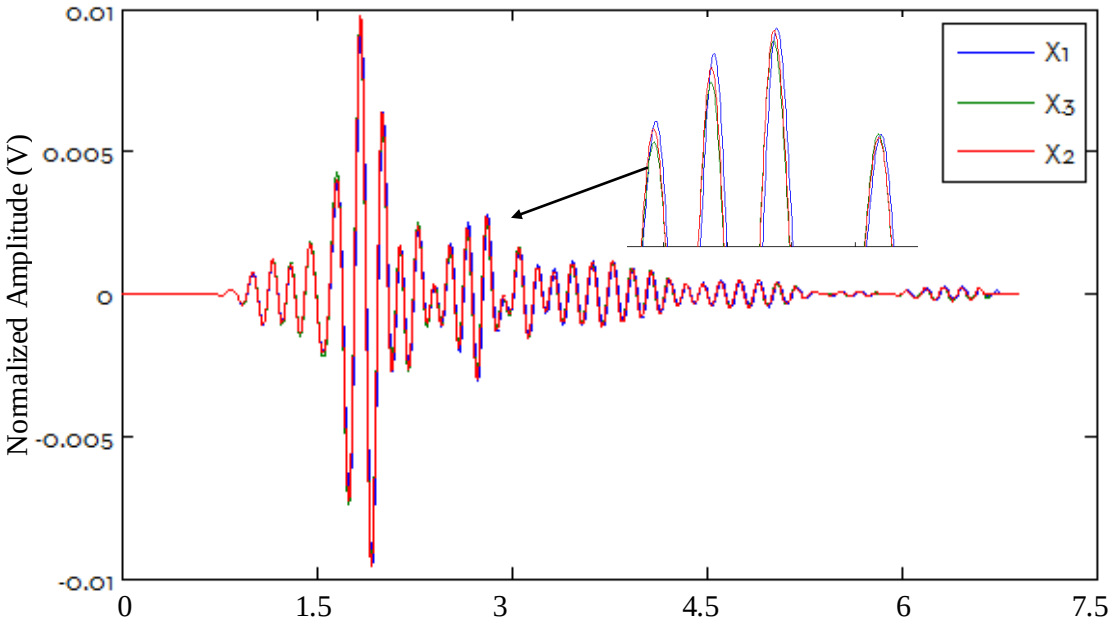

(b)

Fig 4.12 The measured (a) all sets of O_{21} parameters, (b) selected O_{21} parameter.

The same conclusion can also be drawn from the time domain signals that the highest tumour response can be received when the transmitting antenna moves closer to the tumour. The skin layer reflection is also significant compared to the tumour response. However, these received time domain signals cannot be directly used to create microwave images and the signal processing methods used are introduced in the next chapter.

4.3.1.3 Antenna pair II

- ***Frequency domain signals***

The experimental setup for the antenna pair was introduced above. This configuration places the transmitting and receiving antenna together and moves to scan the breast phantom. Compared with the single antenna configuration, the antenna pair configuration uses one antenna to transmit the signal and the other as the receiving antenna to receive the signal.

This section introduces another antenna pair configuration. **Fig 4.13** shows the antenna pair II configuration. Compared with the antenna pair I configuration, one antenna faces now the breast phantom and the other is on the opposite side of the phantom. The antenna pair moves together to scan the breast phantom. In practice, this configuration cannot be applied due to the complex physiological structure of the human body. But multiple bio-layer transmission in UWB can be investigated using this antenna configuration.

Similarly, the reflection coefficients $S_{11,}$ S_{22} and transmission coefficients $S_{21,}$ S_{12} are measured. Here, the notation 1 and 2 refers to the antennas in the LHS and RHS of the breast phantom, respectively. The transmitting antenna transmits the incident wave to the breast phantom, and the transmitted microwave through the breast phantom received by the receiving antenna, as shown in **Fig 4.13**.

The experimental set up is as follows. Firstly, the phantom is removed and the S_{11} and S_{21} are measured using only the two Vivaldi antennas. Secondly, the phantom is placed between the two antennas and the skin layer faces the transmitting antenna (LHS Vivaldi antenna), and the reflection and transmission coefficients are measured as S_{11} and S_{21}. Then, S_{22} and S_{12} are measured, which means that the RHS Vivaldi antenna is used as the transmitting antenna and the LHS Vivaldi antenna is used as the receiving antenna.

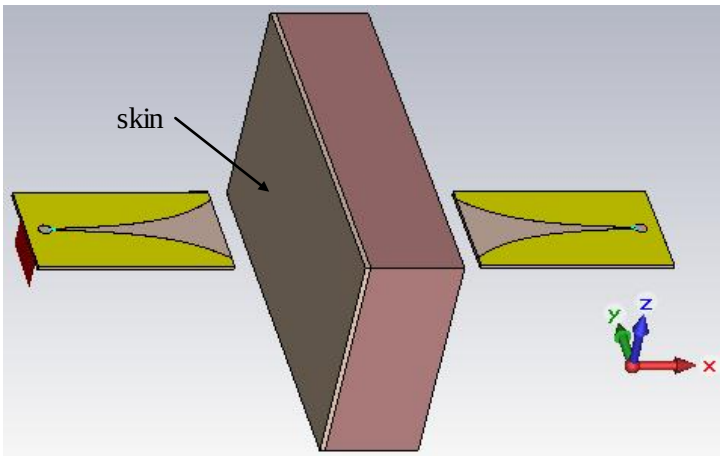

(a)

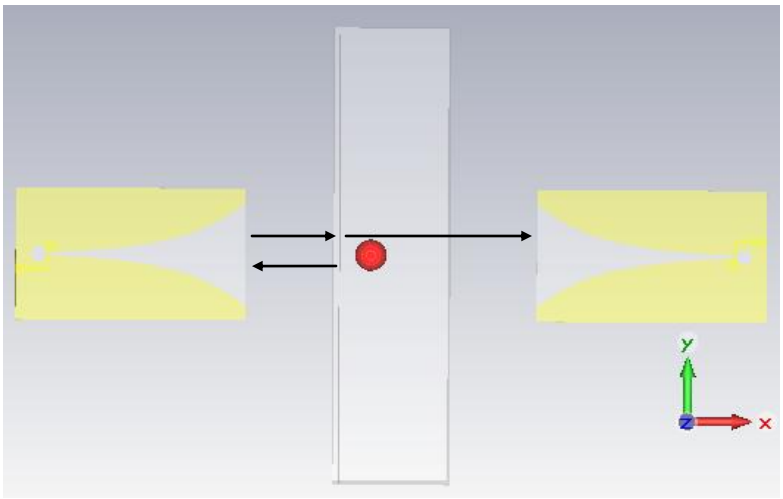

(b)

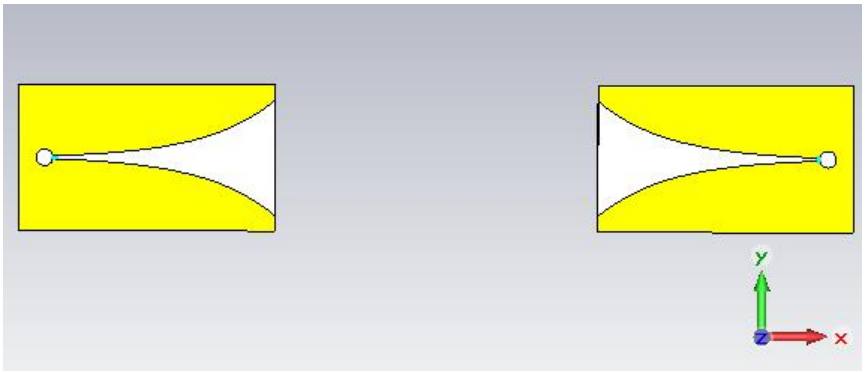

(c)

Fig 4.13 (a) and (b)The antenna pair II configuration and (c) remove the phantom.

Fig 4.14 (a) shows the simulated S_{11} and S_{22} when the breast phantom is removed. It is observed that the -10dB working region extends from 5 to 10 GHz, although there is some discrepancy around 6 GHz. As shown in [112], a wider bandwidth will provide the highest resolution. Besides, the magnitude of the transmission coefficient should be as flat as possible across the whole working frequency in order to achieve minimal distortion when the pulse radiates into the bio-layers. The transmission coefficients S_{12} and S_{21} are shown in **Fig 4.14** (a). The simulated $S_{12,}$ S_{21} are very flat, which is benefited from the high gain and pencil-beam radiation pattern of the Vivaldi antenna. It is worth noting that S_{11} and $S_{22,}$ S_{12} and S_{21} are exactly the same since both transmitting and receiving antennas are the Vivaldi antenna.

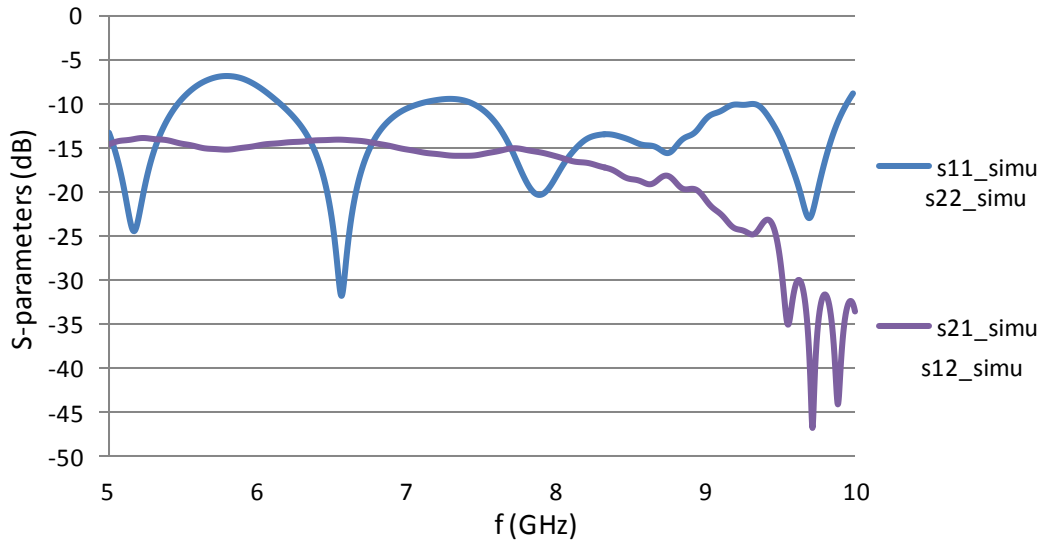

Frequency

(a)

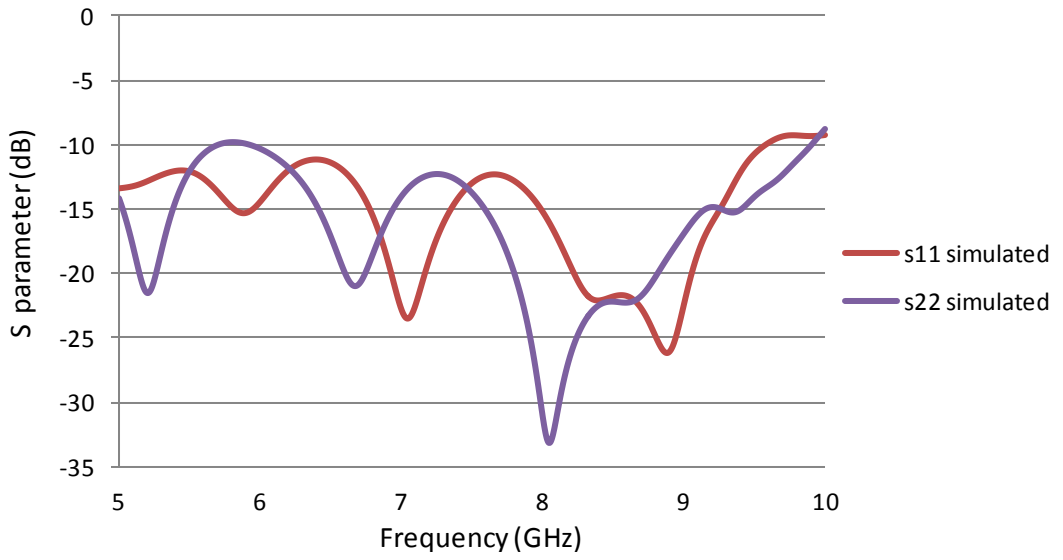

(b)

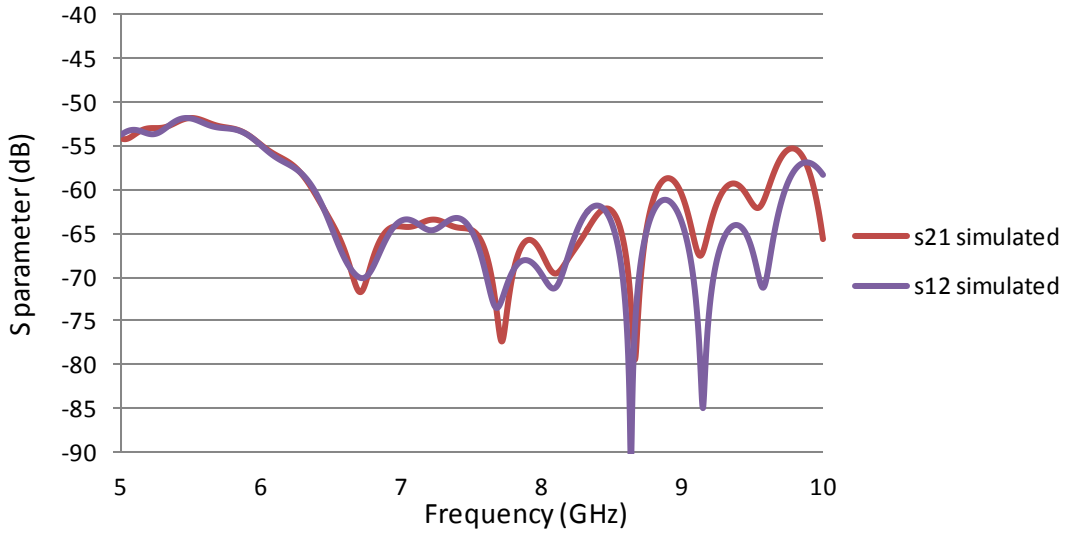

(c)

Fig 4.14 (a) Simulated reflection (S_{11}, S_{22}) and transmission (S_{12}, S_{21}) coefficients without the phantom and the simulated (b) reflection (S_{11}, S_{22}) and (c) transmission (S_{12}, S_{21}) coefficients with the breast phantom.

Fig 4.14 (b) shows that the reflection coefficients S_{11} and S_{22} will rise when the phantom is placed between the middle of the antennas. This is due to part of the UWB signal being reflected by the phantom, but with some of the signal being transmitted through the phantom and detected by the receiver.

In **Fig 4.14** (c), the S_{12} has a profile very close to that of the S_{21} from 5 to 7.5 GHz. However, S_{21} is also slightly higher than S_{12} from 7.5 to 10 GHz. The close profile in the lower frequency band (5 to 7.5 GHz) is due to the relative large wavelength (λ = 60 mm to 40 mm) compared to the thickness of the breast phantom (λ = 37 mm). However, in the higher working frequency band (7.5 to 10 GHz), the wavelength (40 to 30 mm) is less than the thickness of the breast phantom. The electromagnetic properties such as refraction and scattering will affect the propagation even with a small boundary difference in the propagation path.

Another simulation is then carried out, in which the antenna pair is moved to scan the breast phantom. This simulation is similar to the previous simulations with the single antenna and the antenna pair I configurations. However, in this simulation, the antenna pair is focused only on the tumour (X_1), and then it is moved to the healthy region (X_2) since we have the prior knowledge of the tumour location.

Fig 4.15 (a) shows the received reflection coefficients in X_1 and X_2. As seen, both S_{11} and S_{22} have stronger intensity in the X_1 position, which means that the reflected energy increases when the antenna pair moves close to the tumour due to the high difference in relative permittivity between the tumour and the healthy tissues. The same conclusion has been drawn for the single and antenna pair I configurations.

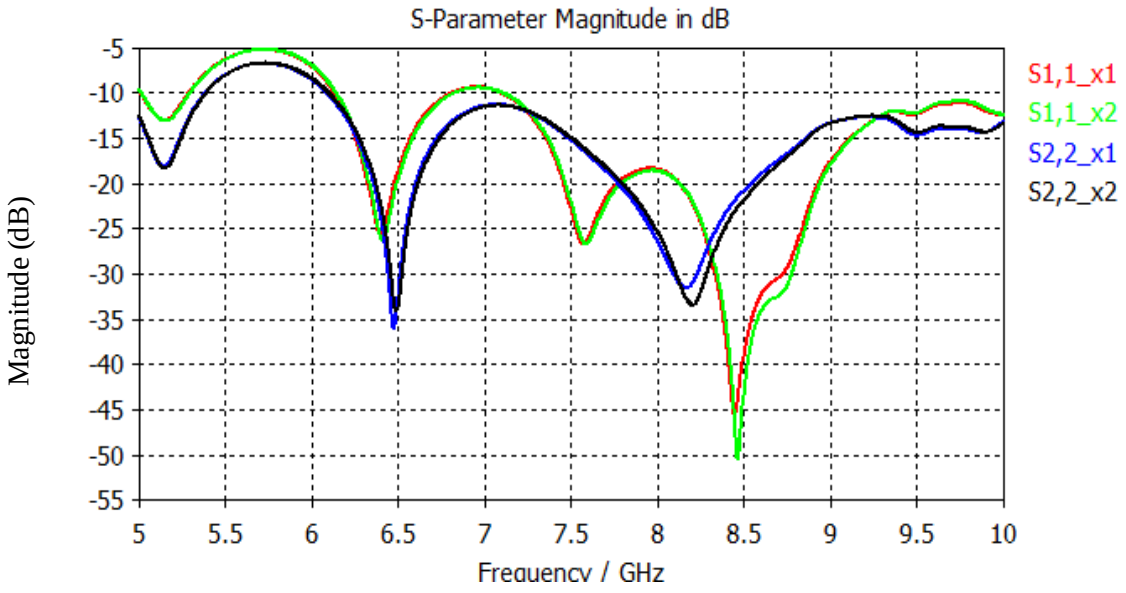

(a)

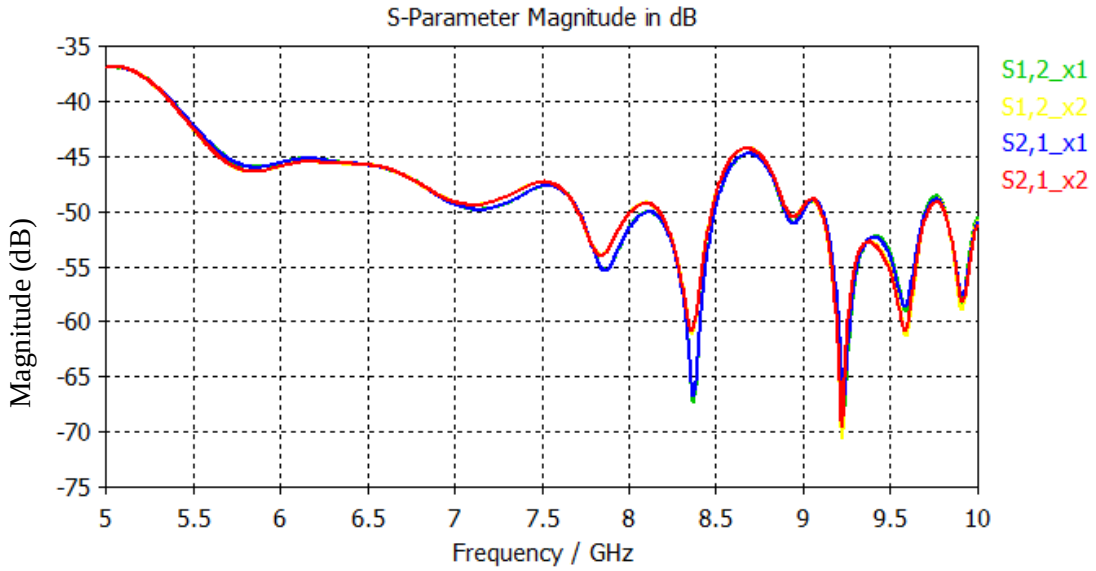

(b)

Fig 4.15 (a) Simulated reflection (S_{11}, S_{22}) and (b) transmission (S_{12}, S_{21}) coefficients in X_1 and X_2 positions.

Fig 4.15 (b) shows the transmission coefficients S_{12} and S_{21}. Take S_{21} for example, X_2 has stronger amplitude than X_1, which means that the transmitted energy is blocked or reflected by the tumour in the X_2 position. Also, S_{12} and S_{21} have very close profiles since the energy transmission rate is very low. Furthermore, both S_{12} and S_{21} in X_1 and X_2 are reduced with increasing working frequency due to the high attenuation rate in the high frequency band.

- ***Time Domain signals***

The simulated time domain signals O_{11}, O_{22} and O_{21}, O_{12} are shown in **Fig 4.16**. The O_{11} and O_{22} are the reflection coefficients when the transmitting and receiving antennas respectively face the skin layer. As seen, the skin layer reflects more energy than the fat layer. The O_{21} and O_{12} are the transmission coefficients when transmitting and receiving antenna face the skin layer, respectively. Their profiles are very close due to the high attenuation effect of the breast phantom. Hence, the difference between the reflections caused by the skin and fat layer is too small compared with the breast phantom attenuation.

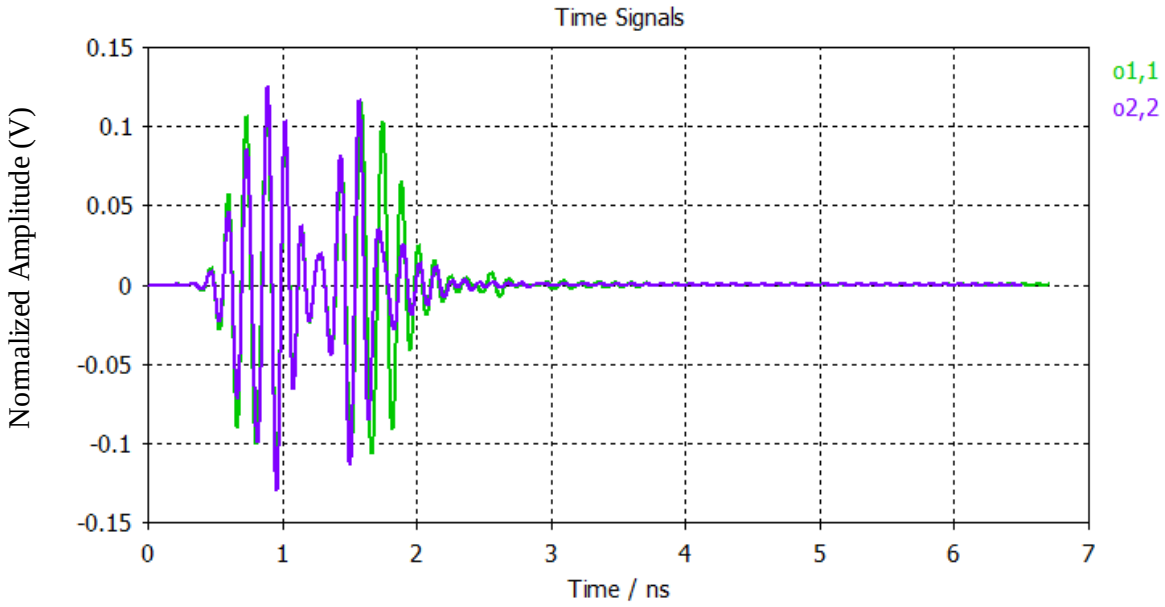

(a)

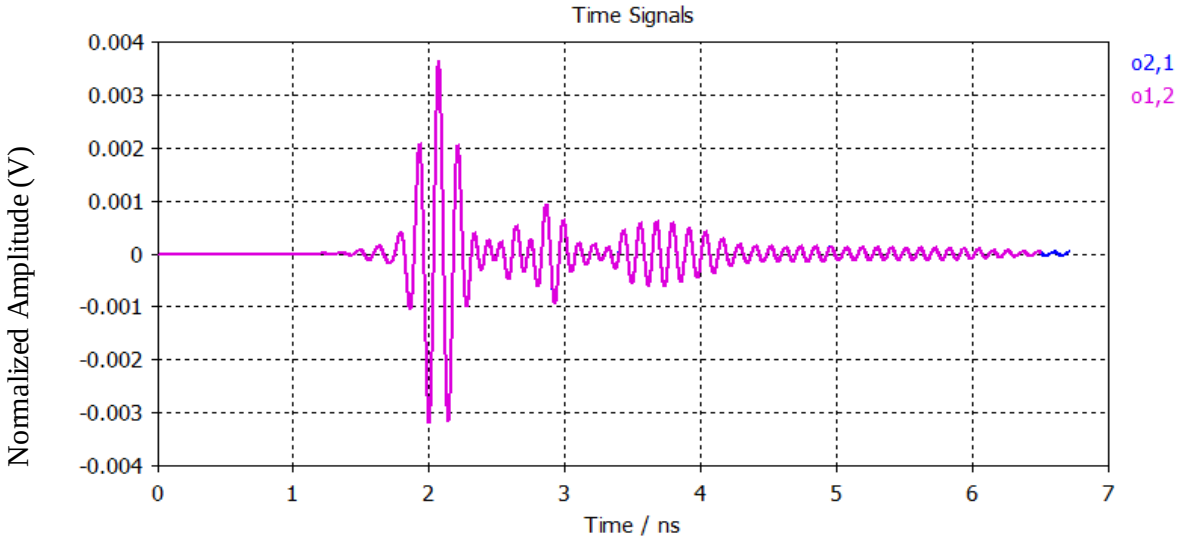

(b)

Fig 4.16 The simulated (a) reflection (O_{11}, O_{22}) and (b) transmission (O_{12}, O_{21}) coefficients with the breast phantom.

Another simulation in which the antenna pair is moved to X_1 and X_2 positions is also carried out in the time domain, as shown in **Fig 4.17**. The observed results in the time domain are similar to those in the frequency domain. Firstly, the skin layer reflects more energy than the fat layer. Secondly, the tumour reflects more energy than the healthy tissues. Thirdly, the tumour blocks and reflects the transmitted energy. Fourthly, the transmission coefficients have very close profiles due to the high attenuation effect of the breast phantom.

The simulations based on the planar breast phantom have been discussed above, and three antenna configurations have been introduced. The following conclusions can be drawn based on the simulation results:

1) The skin layer reflects more energy than the fat layer since the former has a higher relative permittivity.
2) More energy will be reflected when the antenna moves close to the tumour, since the tumour has higher relative permittivity than the surrounding fat layer.
3) Based on (1) and (2) it is concluded that the higher relativity permittivity tissue reflects more energy.
4) The attenuation effect in the high working frequency is very significant, and this, is the reason why the lower frequency microwave penetrates more deeply than the high frequency microwave.
5) It is better to use the reflection coefficients (S_{11}, S_{22}, O_{11}, O_{22}) than the transmission coefficients (S_{12}, S_{21}, O_{12}, O_{21}) since the latter could be too low to be drowned out in noise.

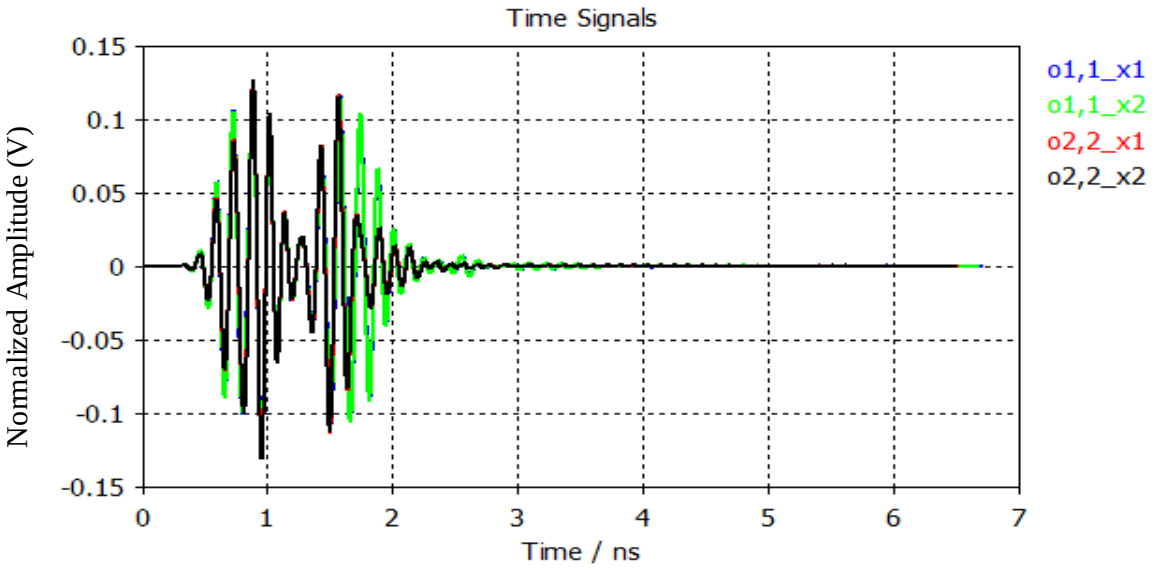
Time Signals
Normalized Amplitude (V)
0.15
0.1
0.05
0
-0.05
-0.1
-0.15
0
1
2
3
4
5
6
7
Time / ns
o1,1_x1
o1,1_x2
o2,2_x1
o2,2_x2

(a)

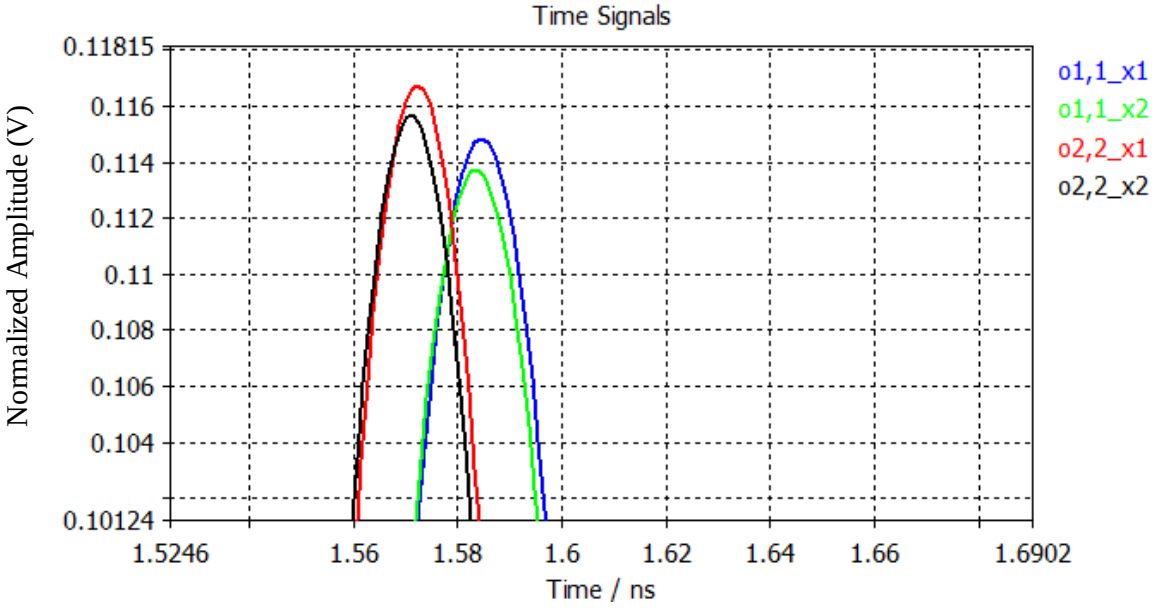
Time Signals
Normalized Amplitude (V)
0.11815
0.116
0.114
0.112
0.11
0.108
0.106
0.104
0.10124
1.5246
1.56
1.58
1.6
1.62
1.64
1.66
1.6902
Time / ns
o1,1_x1
o1,1_x2
o2,2_x1
o2,2_x2

(b)

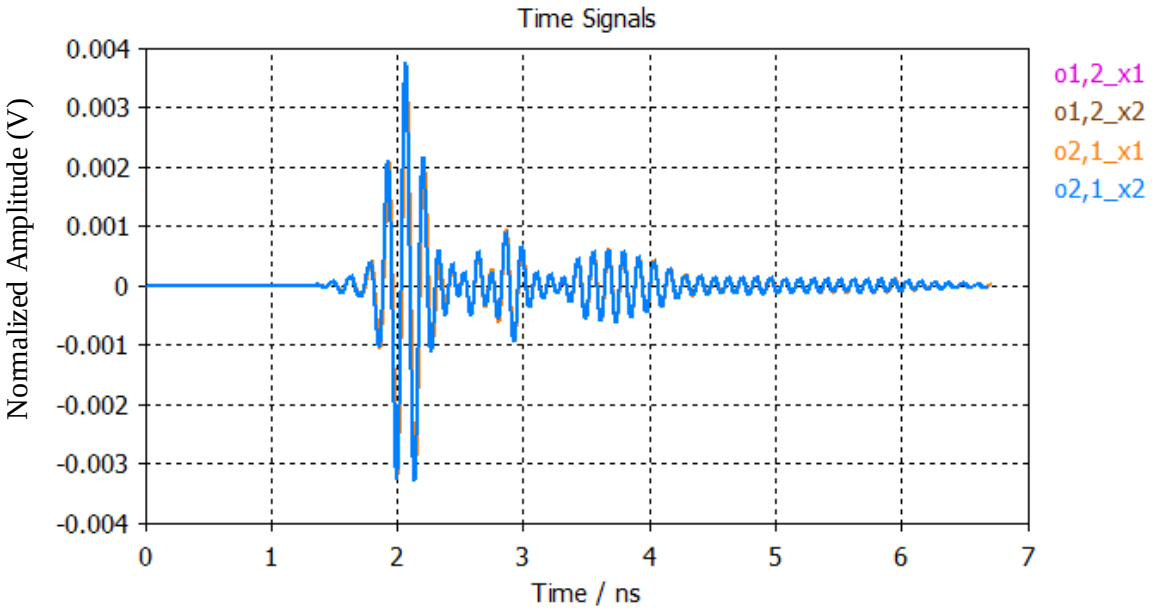

(c)

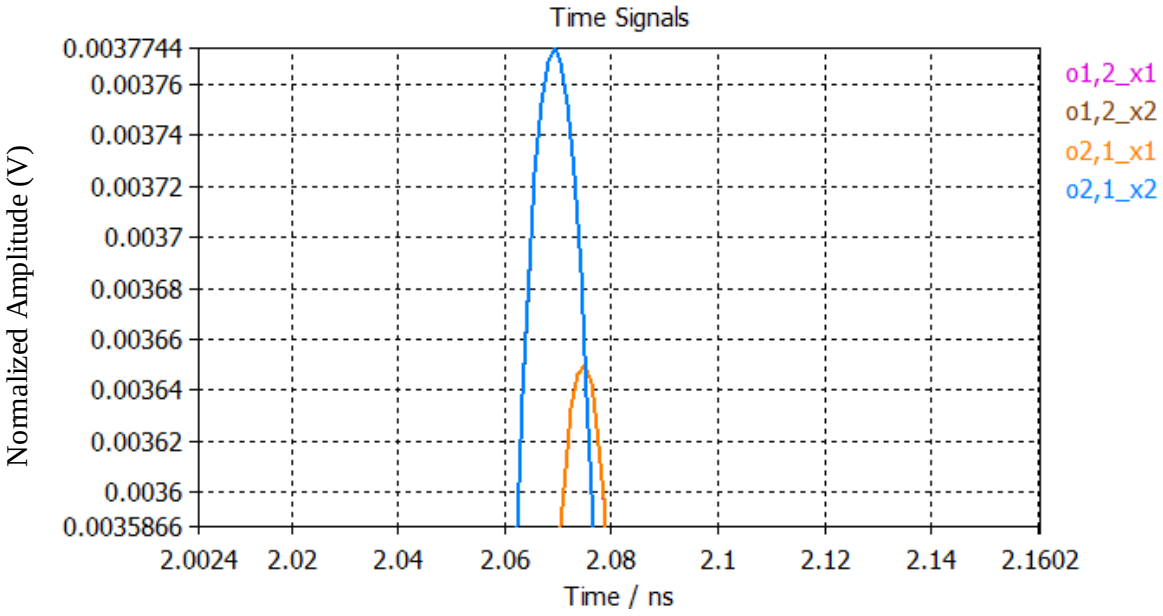

(d)

Fig 4.17 The simulated (a) (b) reflection (O_{11}, O_{22}) and (c) (d) transmission (O_{12}, O_{21}) coefficients with the breast phantom in X_1 and X_2.

4.3.2 Practical Measurement

The simulation results have been presented based on the three antenna configurations of a single antenna and antenna pair I and II. All three are measured in both the frequency and time domains. Based on the simulation results, it is concluded that the reflected energy increases when the antenna moves close to the tumour; otherwise the reflected energy is reduced when the antenna moves away from the tumour.

This section discusses the practical measurements. In the experiment, an HP 8341B synthesized sweeper and an HP 8510B vector network analyzer are used to measure the transmission and reflection coefficients through the breast phantom. **Fig 4.18** shows the experimental setup. The HP 8341B synthesized sweeper can generate signals ranging from 45 MHz to 20 GHz. The working frequency of the Vivaldi antennas ranges from 5-10 GHz, and so, the sweeper is set to that working frequency. The HP 8510B network analyser is connected to the Vivaldi antennas, one of which is connected to port1 (LHS in **Fig 4.18**) as the transmitting antenna. The other antenna is connected to port2 (RHS in **Fig 4.18**) as the receiving antenna. The two Vivaldi antennas are 93 mm apart from each other and fixed by two holders. The phantom is placed in the middle of the two antennas and the pink absorber is placed under the phantom to absorb the scatter from the ground. The skin layer faces the transmitter (LHS antenna in **Fig 4.18**) and the other side of the phantom faces the receiver.

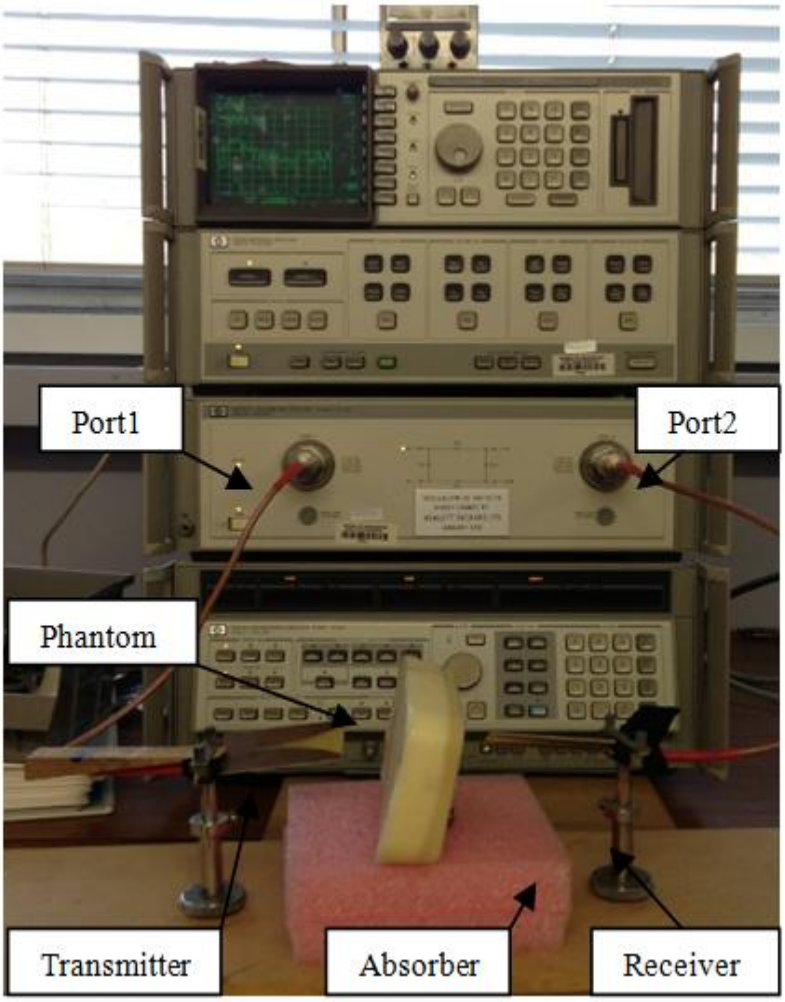

Fig 4.18 Experimental setup.

4.3.2.1 Single antenna

- ***Frequency Domain Signals***

In this practical measurement, the Vivaldi antenna is placed on the top of the breast phantom, with the distance to the skin layer being 30 mm. The front middle of the antenna is located facing towards the tumour. The antenna is moved to scan the breast phantom, with three sets of S_{11} recorded in the locations X_1, X_2, and X_3, as indicated in

Fig 4.19 (a) (b). These three sets of S_{11} are quite representative, which are located 0, 35 and 70 mm away from the tumour in the Y-axis.

Fig 4.19 (c) shows the measurement results. The amplitudes of S_{11} in the location X_1 is stronger than those in the locations X_2 and X_3 at all working frequencies except for 6.3 GHz. Also, the S_{11} at the X_2 and X_3 almost completely overlap. Based on the measured $S_{11,}$ it can also be concluded that the reflected energy increases when the antenna moves close to the tumour, and is reduced when the antenna moves away from the tumour.

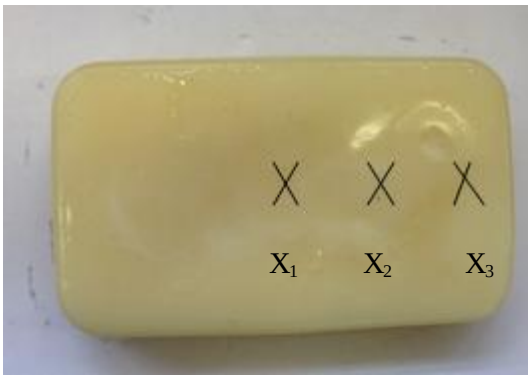

(a)

(b)

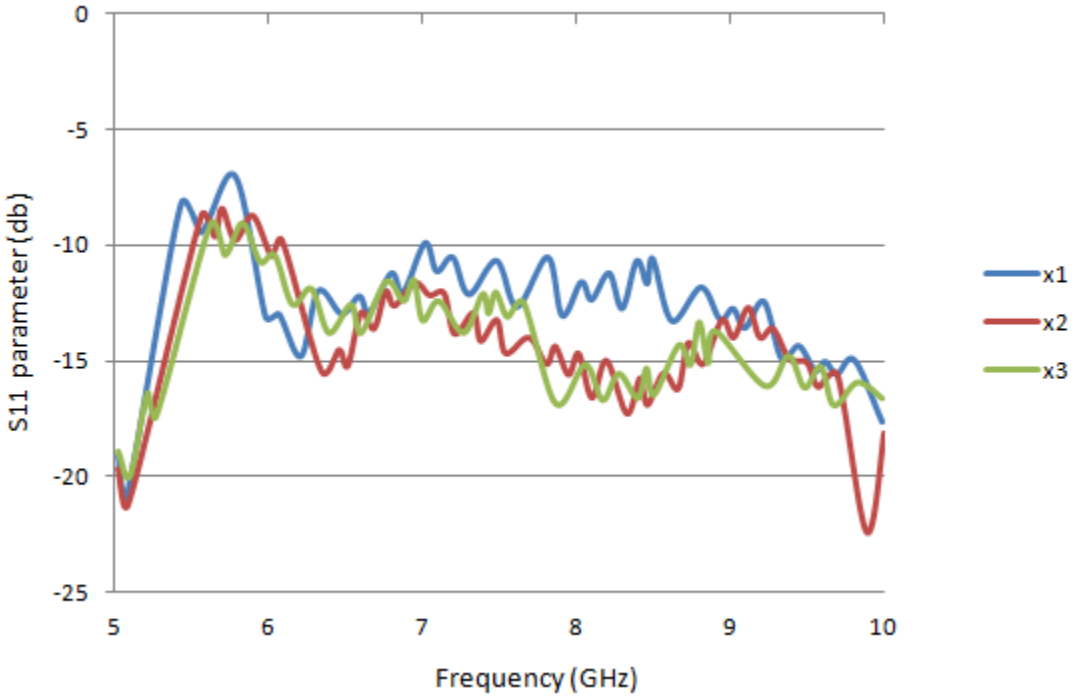

(c)

Fig 4.19 (a)The planar breast phantom and antenna movement locations X_1, X_2, and X_3, (b) the single antenna configuration and (c) the measurement results.

- ***Time Domain Signals***

The HP 8510B vector network analyzer is capable of measuring the scattering parameters in the time domain. The measurement principle is that the VNA first measures the scattering parameters in the frequency domain and then calculates the time domain scattering parameters based on the Chirp-Z Fast Fourier transform in the real-time. **Fig 4.20** shows the received O_{11} in the locations X_1, X_2, and X_3. The peak amplitude around 2 ns is the skin reflection and the peak amplitude around 2.5 ns is the tumour reflection. Similar to the S_{11}, the O_{11} in the location X_1 is higher than that in X_2 and X_3 due to the tumour response. It is worth noting that the O_{11} in X_1, X_2 and X_3 are quite close due to the weak responses of the tumour.

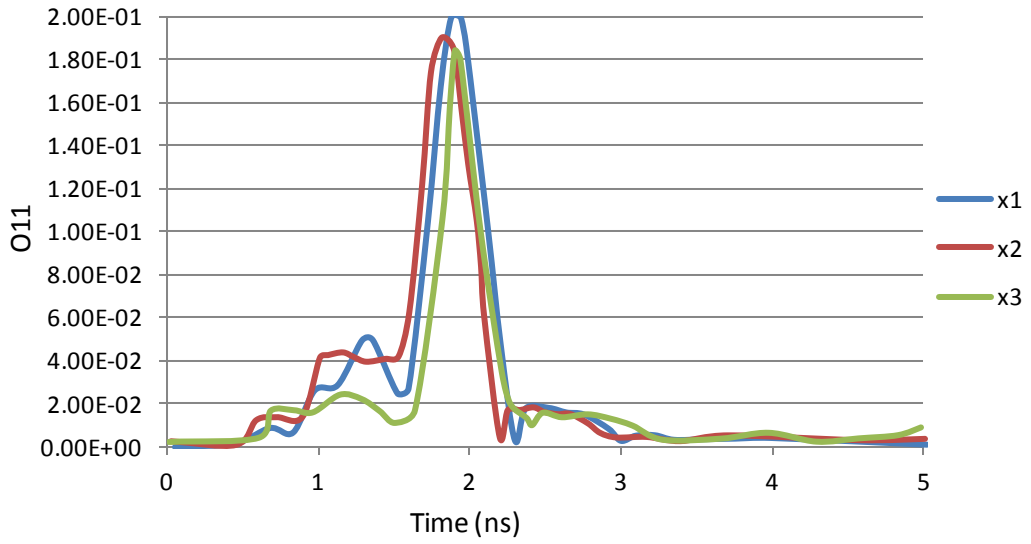

Fig 4.20 The received time domain signals in X_1, X_2, and X_3.

4.3.2.2 Antenna Pair I

- ***Frequency Domain Signals***

This antenna configuration has been introduced in the simulation section. This antenna pair moves to scan the breast phantom with transmission coefficients S_{21} recorded. **Fig 4.21** (a) shows experimental setup for this the antenna pair.

(a)

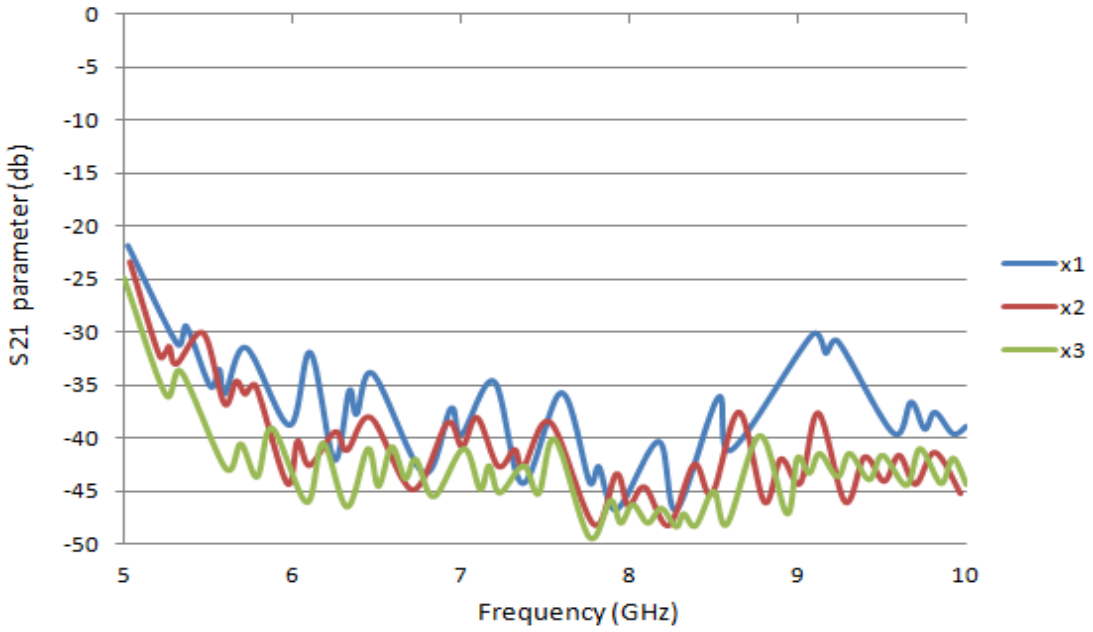

(b)

Fig 4.21 (a)The antenna pair I experimental setup, and (b) the measured S_{21} parameters.

Similar to the simulation, S_{11} in the locations X_1, X_2 and X_3 are recorded. **Fig 4.21** (b) shows the measurement results. The S_{11} at X_1 is higher than those at X_2 and X_3. The simulation results showed that the S_{11} at X_2 is quite close to that at X_3. However, the measured S_{11} in X_2 and X_3 are not close to each other due to the non-planar surface of the breast phantom. However, the tumour still shows a strong response (at X_1 location), which also matches with the simulation results.

- ***Time Domain Signals***

The time domain signal is mathematically transformed from the S parameters based on the Chirp-Z Fast Fourier transform. Similar to the S_{21}, the O_{21} in the location X_1 is higher than that in X_2 and X_3 due to the tumour response. Also, the amplitude of the O_{21} is much smaller than that of the O_{11} due to the strong transmission loss as shown in **Fig 4.22**.

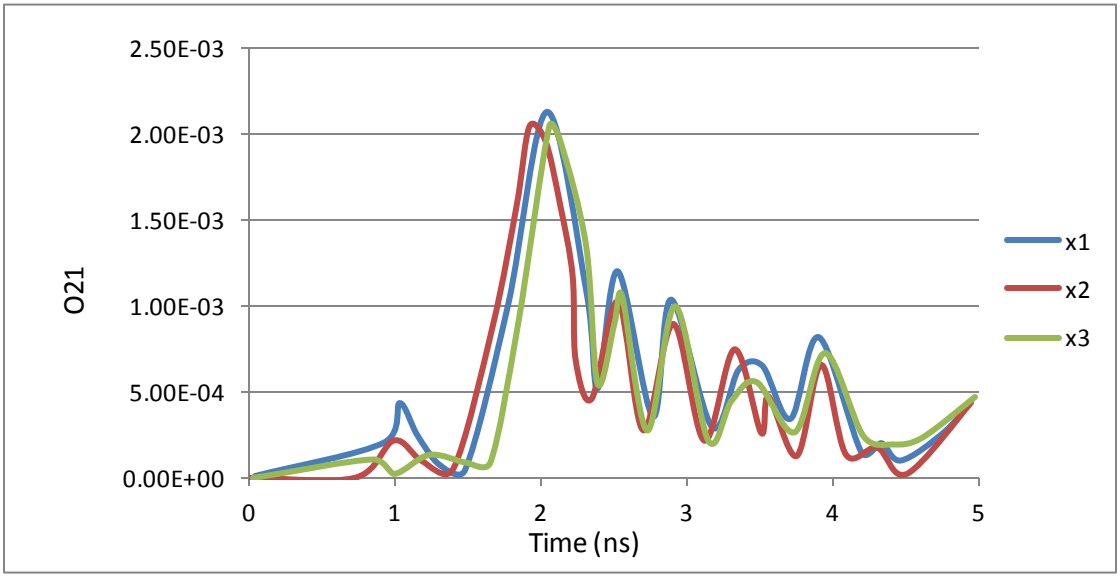

Fig 4.22 The measured O_{21} parameters.

4.3.2.3 Antenna Pair II

- ***Frequency Domain Signals***

For the antenna pair II measurement, one antenna faces the breast phantom and the other is on the opposite side of the phantom. The antenna pair moves together to scan the breast phantom. In practice, this configuration cannot be applied due to the complex physiological structure of the human body. But we can investigate the multiple bio-layer transmission in UWB using this antenna configuration. **Fig 4.23** shows the antenna pair II configuration.

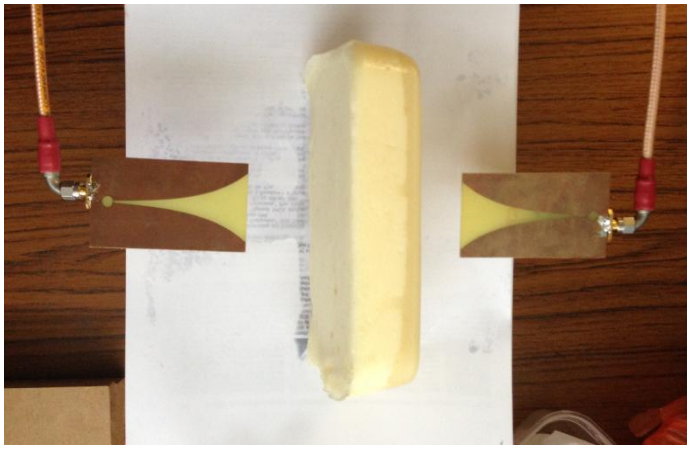

(a)

Fig 4.23 The antenna pair I experimental setup.

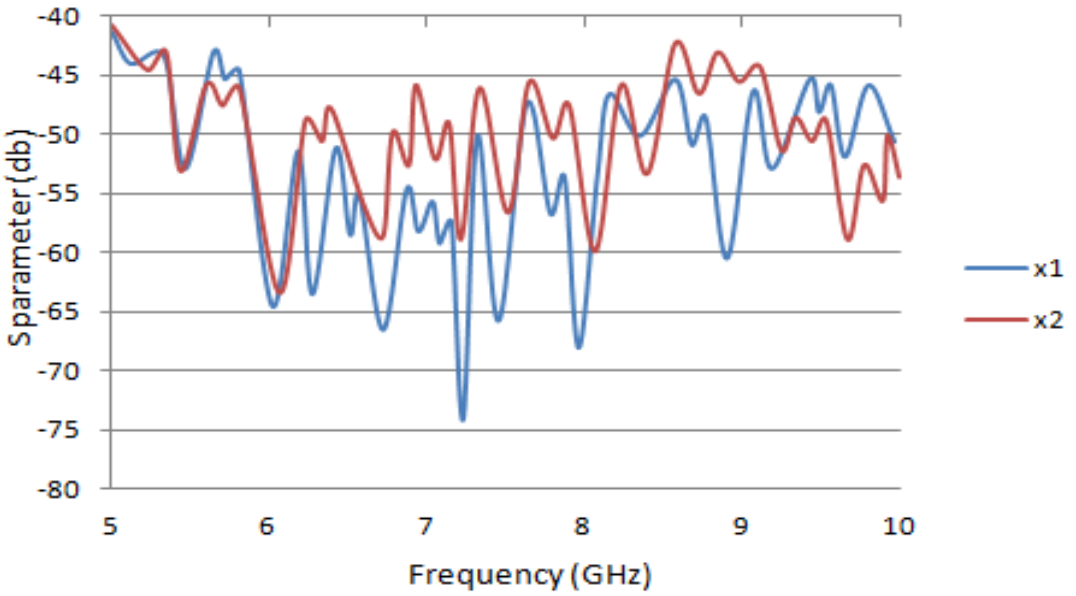

Fig 4.24 The measured S_{21} parameters in the locations X_1 X_2

Fig 4.24 shows the measured S_{21} at the locations X_1 X_2. As seen from the results, the transmission coefficients increase when the antenna pair move away from the tumour since the energy transmitted is blocked or reflected by the tumour at the location X_2. Besides, S_{12} and S_{21} have very close profile due to the low energy transmission rate.

- ***Time domain signals***

The time domain signals are also measured as shown in **Fig 4.25**. The measurement results also show that the transmission coefficients increase when the antenna pairs move away from the tumour.

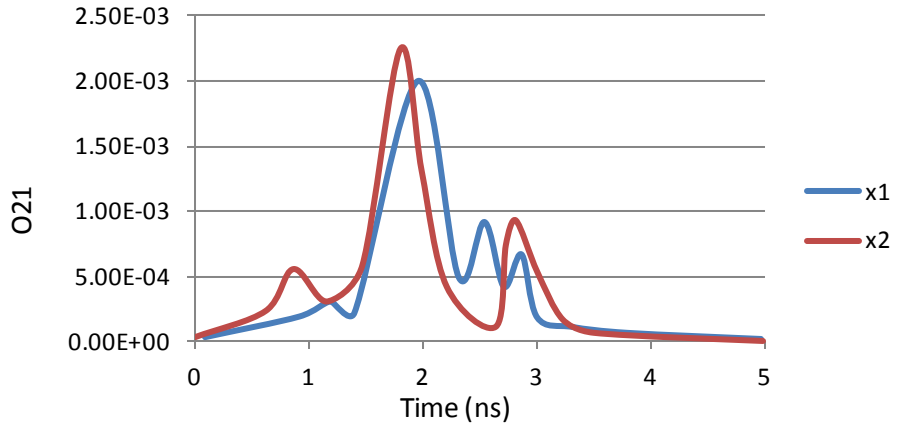

Fig 4.25 The measured S_{21} parameters in locations X_1 X_2

4.4 Hemi-sphere Breast Phantom Experiment

The planar breast phantom has been measured using the designed Vivaldi antenna in the time and frequency domains. This planar breast phantom consists of a skin layer, a fat layer and a tumour, which represents a basic structure of breast. However, a more realistic breast phantom is required in order to acquire more precise measurement results.

The hemi-sphere breast phantom has been proposed, simulated and fabricated. In this section, this hemi-sphere breast phantom is measured using the Vivaldi antenna, with measurement results analyzed.

4.4.1 Simulation

4.4.1.1 Single antenna

The single antenna configuration is used to measure the breast phantom. **Fig 4.26** (a) shows the single antenna configuration. The antenna is first placed at the top centre,

30mm away from the breast phantom. The Vivaldi antenna is then rotated along the surface of the breast phantom to transmit and receive the signals. **Fig 4.26** (b) shows the rotation tracks and stop points. The Vivaldi antenna rotates and stops at these points, with the scattering parameters measured in the time and frequency domains. During this procedure, the antenna is maintained at the same distance from the surface of the breast phantom being steady.

Based on the planar breast phantom measurement, it is predicted that the reflection coefficients will increase when the antenna moves closer to the tumour due to the high difference in relative permittivity difference between the tumour and fat tissue.

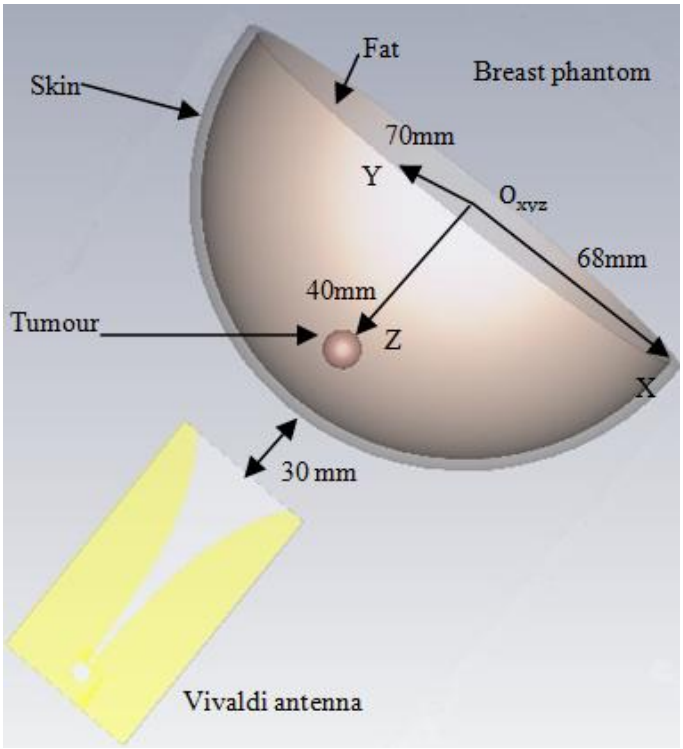

(a)

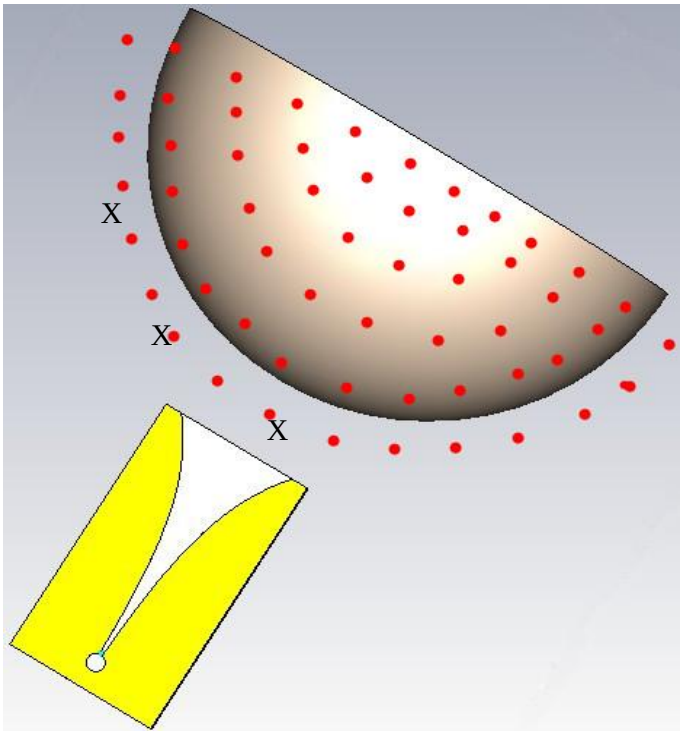

(b)

Fig 4.26 (a) The single antenna based experimental setup of the imaging system using the hemi-sphere breast phantom and (b) the antenna stop positions.

- ***Frequency Domain Signals***

Fig 4.27 shows the received reflection coefficients S_{11} at X_1, X_2 and X_3, which are indicated in **Fig 4.26**. As seen, the tumour response is very significant. The amplitude of X_1 is higher than those of X_2 and X_3 in all working frequencies except 5.2 and 9.5 GHz. Besides, the X_2 and X_3 are very close and the profiles almost completely overlap. These results confirm the prediction that as the antenna moves close to the tumour causes a strong increase in reflection coefficients.

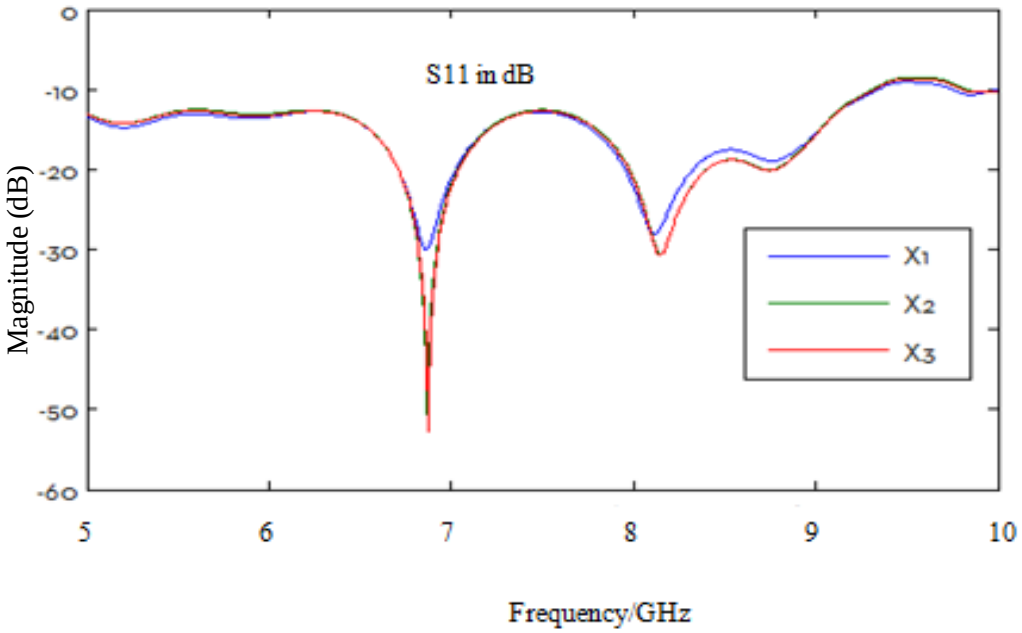

Fig 4.27 The received reflection coefficients S_{11} in the X_1, X_2 and X_3.

- ***Time Domain Signals***

The time domain signals are shown in **Fig 4.28**, showing that the tumour response part is very weak. The O_{11} in X_1 is slightly higher than those in X_2 and X_3. The time domain signal is an average description over the whole working frequency. As seen from **Fig 4.28**, the X_1 is higher than X_2 and X_3 at all working frequencies except for 5.2 and 9.5 GHz. Hence, the amplitude difference in the time domain between the X_1 and X_2, X_3 is not as significant as that in the frequency domain. Besides, the skin layer reflection is very strong and the tumour response is relatively small. It is therefore necessary to further process the tumour response. Furthermore, it is worth analyzing that the discrepancy around 5.2 GHz and 9.5 GHz. As discussed below, when the antenna or antenna array moves to scan the breast phantom, the distance between the skin layer and the antenna must be maintained. Any small change in the distance could cause unpredictable the measurement results. In the simulation work, the breast phantom is very smooth and the distance can be controlled precisely. However, in the

practical work, the antenna movement cannot be controlled as precisely as in the simulation work, which results in the change in the distance. This is the reason why the discrepancies occur.

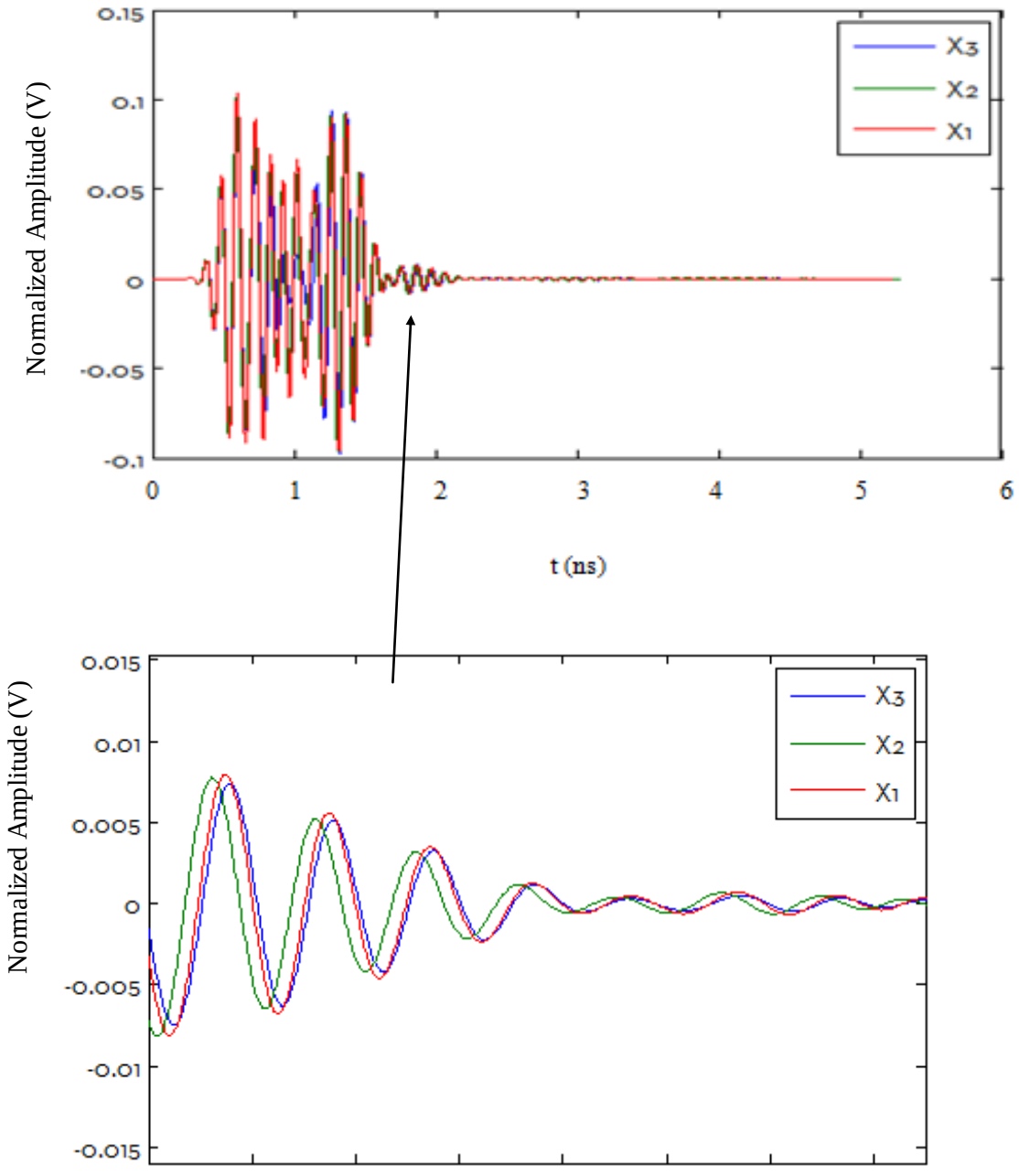

Fig 4.28 The received reflection coefficients O_{11} in the X_1, X_2 and X_3.

4.4.1.2 Antenna Pair

The single antenna configuration has been discussed above. This section considers the antenna pairs where one antenna is used one as the transmitting antenna and the other one as the receiving antenna. The distance between these two antennas is 30 mm, which is greater than λ/2, and this, significantly reduces their mutual coupling of the antennas. This antenna pair moves along the surface of the breast phantom to scan the breast while keeping their spatial relationship constant, as shown in **Fig 4.29**. The transmitting antenna transmits the incident wave to the breast phantom, and the reflected wave is received by the receiving antenna. The transmission coefficients are recorded in both the frequency and time domains.

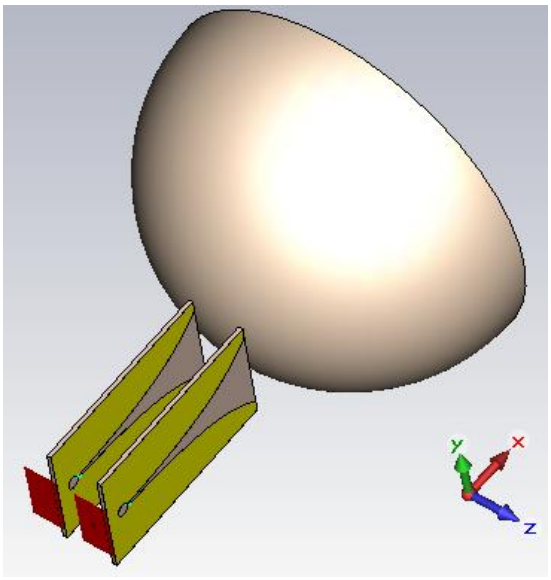

Fig 4.29 The antenna pair based experimental setup of the imaging system using the hemi-sphere breast phantom.

- ***Frequency Domain Signals***

As before, the antenna pair moves to scan the breast phantom, with the received transmission coefficients S_{21} recorded in X_1, X_2 and X_3. **Fig 4.30** shows the received S_{21} in X_1, X_2 and X_3. The X_1 is higher than X_2 and X_3 in all working frequencies except 6.8 and 9.5 GHz. Also, the X_2 and X_3 are very close and almost completely overlap. Compared with Fig 4.4.2, the transmission coefficients are much lower than the reflection coefficients due to the signal attenuation caused by the multi-path transmission caused

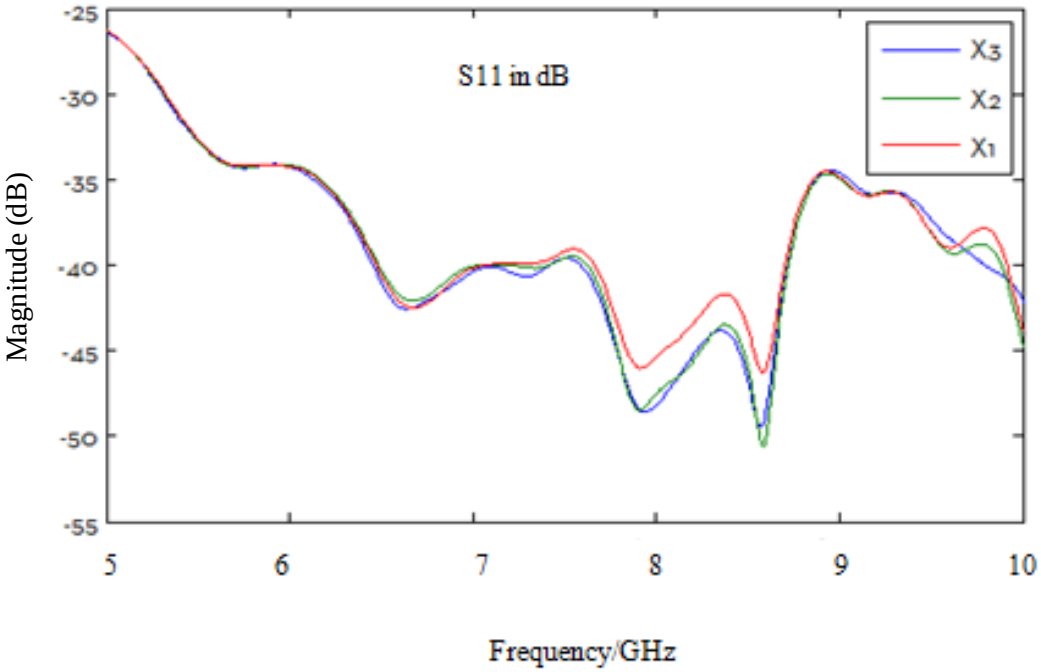

Fig 4.30 The received reflection coefficients S_{21} in the X_1, X_2 and X_3.

- ***Time Domain Signals***

The time domain signals are shown in **Fig 4.31**. As seen, the skin reflection part dominates the whole signal and the tumour response is very weak. Besides, the peak value of the antenna pair based time domain signal (0.01 in Fig 4.4.6) is much weaker than that of the single antenna based time domain signal (0.1 in Fig 4.4.5) due to the

signal attenuation caused by the longer transmission path of the antenna pair configuration.

Furthermore, the amplitude at the X_1 is stronger than those of the X_2 and X_3, which shows that the transmission coefficients increase when the transmitting antenna moves close to the tumour.

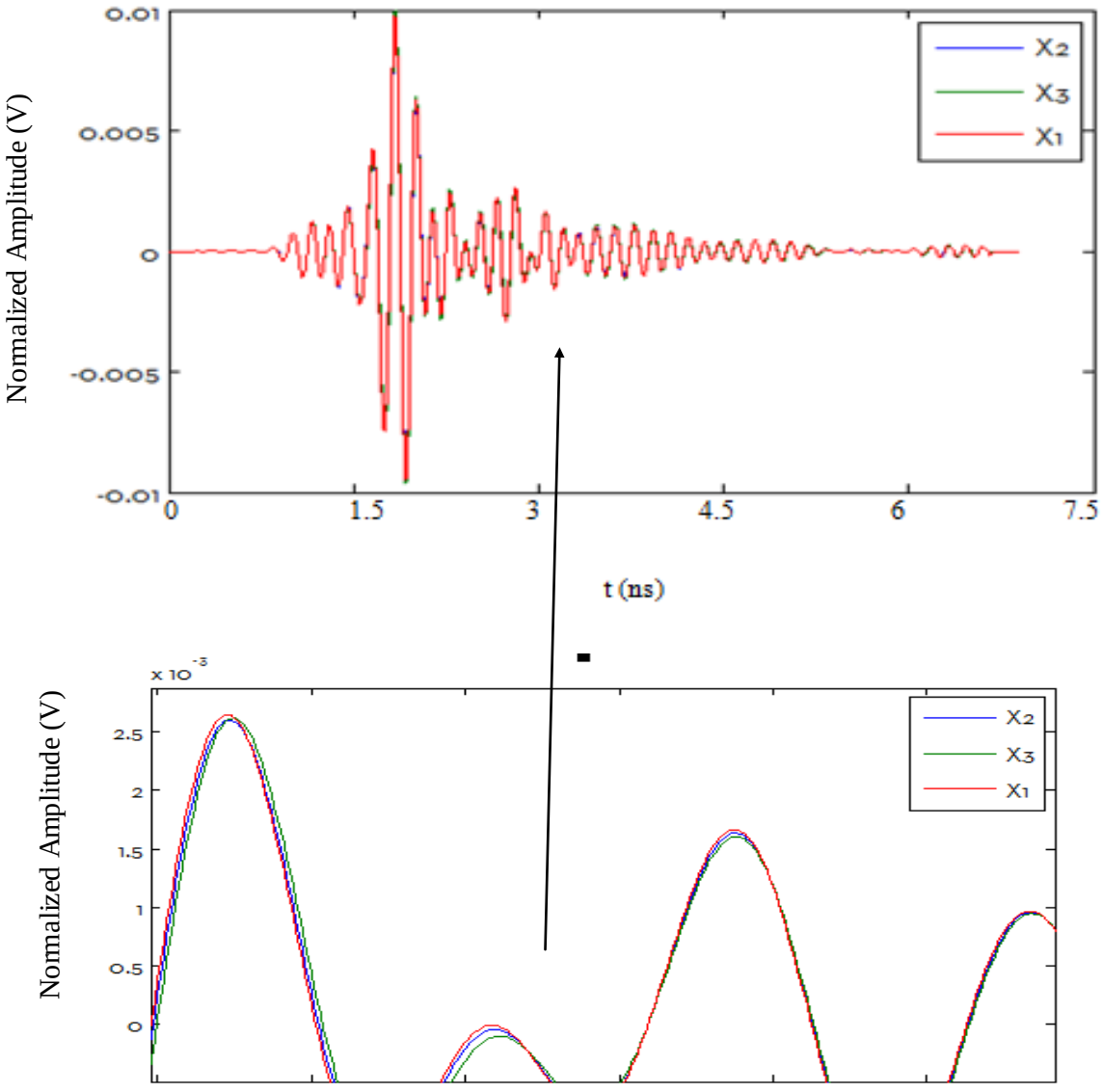

Fig 4.31The received reflection coefficients O_{11} in the X_1, X_2 and X_3.

4.4.2 Practical Measurement

4.4.2.1 Single Antenna

- ***Frequency Domain Signals***

The hemi-sphere breast phantom is also measured experimentally using the HP 8510B vector network analyser. The experimental setup is as introduced earlier for the single antenna configuration. For this measurement, the only difference is that the planar phantom is replaced by the hemi-sphere breast phantom. This breast phantom is placed on the top of the pink absorber, as indicated in **Fig 4.32** (a). The single antenna is placed at the top centre of the breast phantom with 30 mm away and moved to scan the phantom, with the reflected coefficients recorded. Similarly, the S_{11} at X_1, X_2 and X_3 are shown in **Fig 4.32** (b).

Fig 4.32 (b) shows the measurement results. The S_{11} at the location X_1 is higher than those at X_2 and X_3 at all working frequencies except 6.8 GHz. The measurement results confirm that the antenna which moves close to the tumour will obtain higher amplitude. Similarly, the measurement results also indicate that some discrepancies occur at 6.8 GHz. As we have discussed in Section 4.4.1.1, the discrepancies are due to the unsmooth surface of the fabricated phantom. The measurement results are very sensitive to the distance between the antenna and the phantom surface. The unsmooth surface will result in the discrepancies of the measurement results. The unpredictable measurement results could occur in different frequency band due to the unpredictable phantom surface. The discrepancies of the measurement result in the next several sections can be explained by discussed below.

(a)

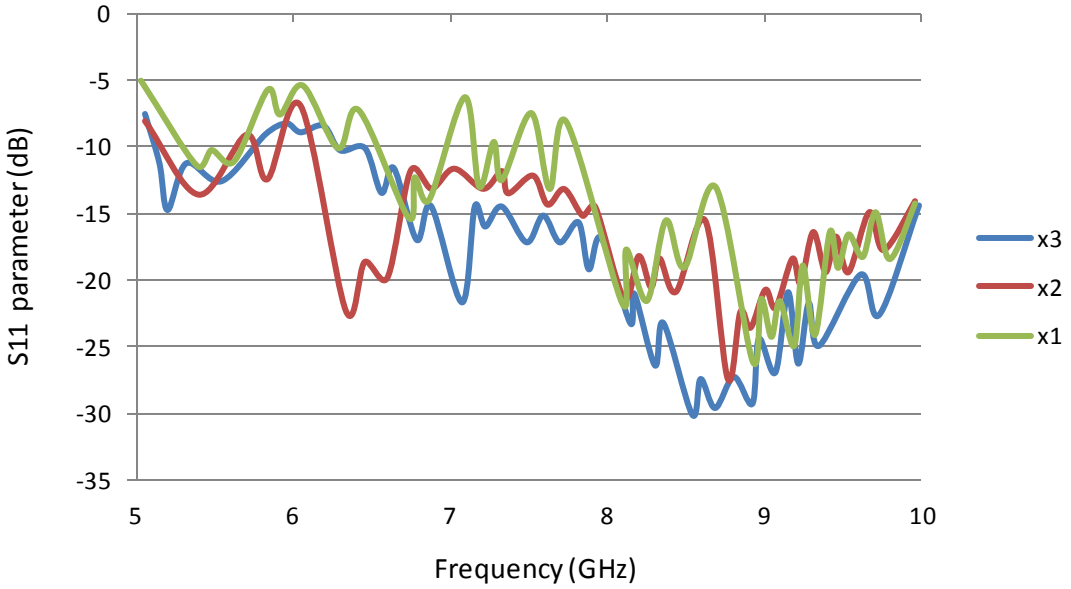

(b)

Fig 4.32 (a)The hemi-sphere breast phantom and antenna movement locations X_1, X_2, and X_3 and (b) the measurement results.

- ***Time Domain Signals***

The measured time domain signals O_{11} are shown in **Fig 4.33**. As seen, the amplitude at X_1 is higher than those at of X_2 and X_3. The skin reflection is around 2 ns and the tumour response is around 2.5 ns. The tumour response is also very significant. It is worth noting that the tumour and coarse surface contribute to the tumour response together. This is the reason why the amplitude difference of the measured X_1, X_2 and X_3 is stronger than that of the simulated X_1, X_2 and X_3. Similar to the S_{11}, the O_{11} at the location X_1 is higher than that in X_2 and X_3due to the tumour response.

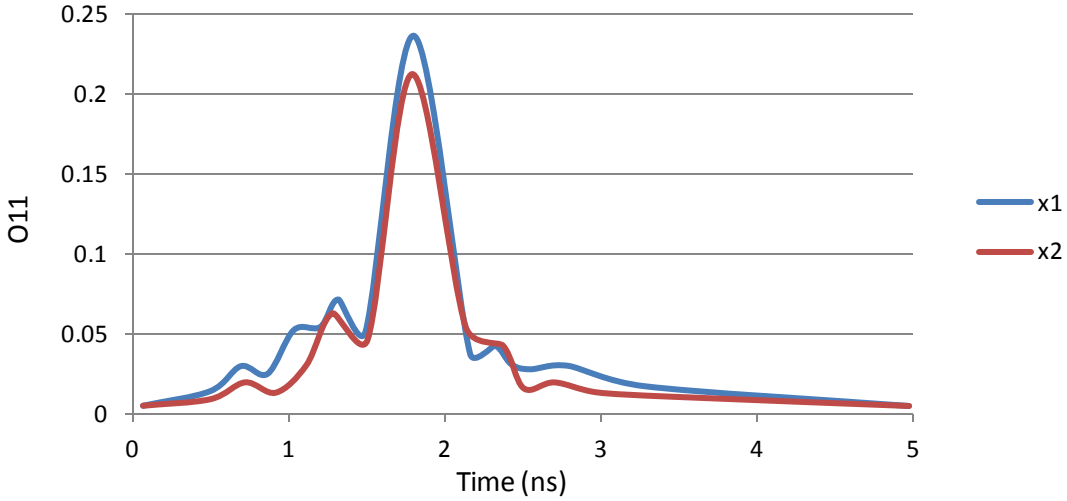

Fig 4.33 The received time domain signals in X_1, X_2, and X_3.

4.4.2.2 Antenna Pair

- ***Frequency Domain Signals***

Fig 4.34 (a) shows experimental setup for the antenna pair which is placed 30 mm away from the top centre of the breast phantom and then moved to scan the breast phantom, with the S_{21} recorded at X_1, X_2 and X_3.

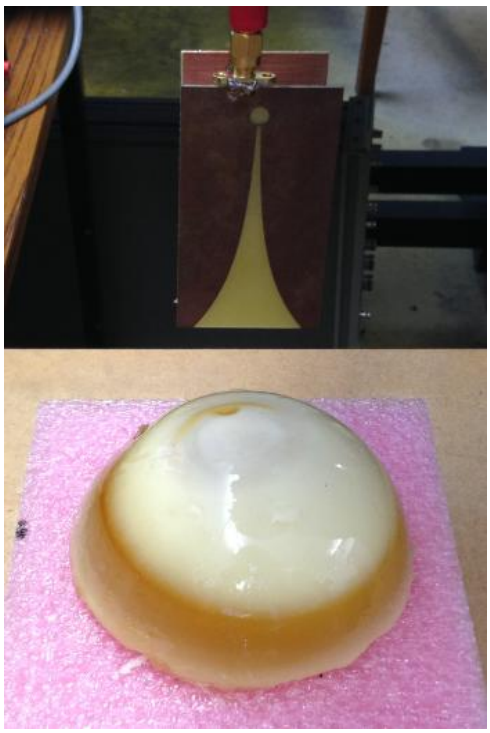

(a)

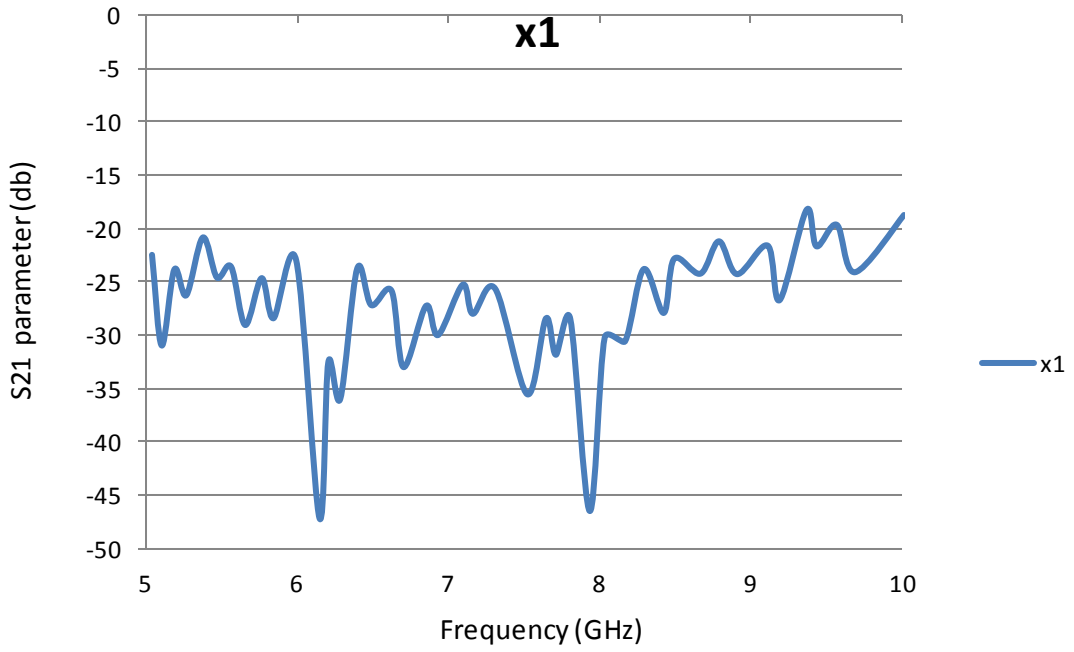

(b)

Fig 4.34 (a)The antenna pair I experimental setup, and (b) the measured S_{21} parameters.

Fig 4.34 (b) shows the measurement results. The S_{21} at X_1 is higher than those at X_2 and X_3 at all working frequencies. However, the S_{21} in X_1 and X_2 are much stronger than that in X_3 since in X_3 the antenna is quite close to the pink absorber, and this, reduces the reflection from the breast phantom.

- ***Time Domain Signals***

The measured time domain signals are also shown in **Fig 4.35**. Firstly, the measured transmission coefficient O_{21} at X_1 is stronger than those in X_2 and X_3. Also, the phase delay between the X_1, X_2 and X_3 is significant due to the different microwave transmission path.

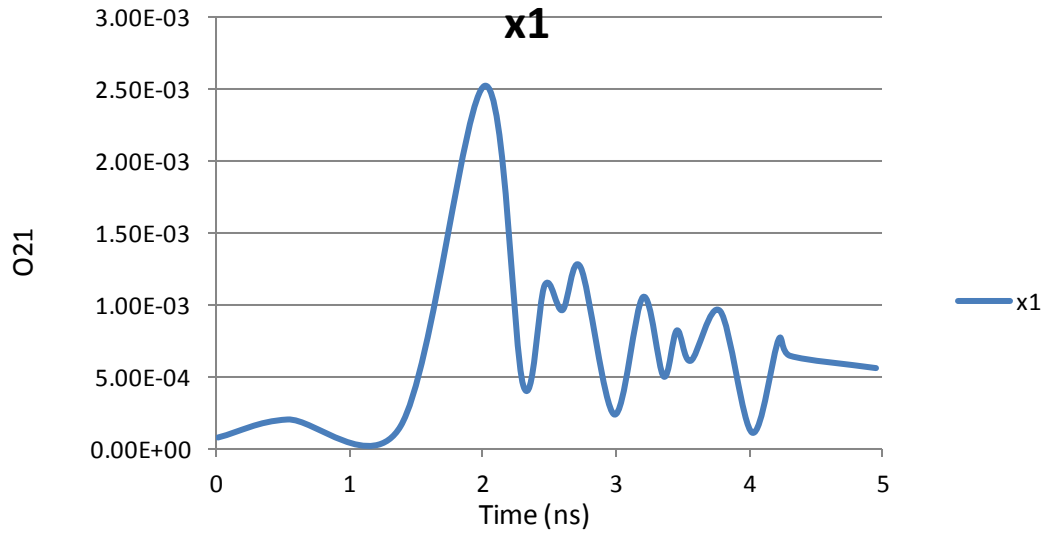

Fig 4.35 The measured O_{21} parameters.

4.5 The Slot Vivaldi Antenna Measurements

The Vivaldi antenna has been used to measure the breast phantom in the time and frequency domains. The measured results indicate that the discontinuity of the boundary between the tumour and healthy tissue causes a strong reflection of the incident electromagnetic wave. This strong reflection can be observed from the scattering signals.

The slot Vivaldi antenna has been proposed in the previous chapter. This has a wider bandwidth (3-10 GHz) compared to the original Vivaldi antenna (5-10 GHz) while maintaining the same dimensions. In this section, the slot Vivaldi antenna is used to measure the hemi-sphere breast phantom.

4.5.1 The Hemi-sphere Breast Phantom Measurement

The hemi-sphere breast phantom has been measured using the Vivaldi antenna. In this section, the slot Vivaldi antenna pair configuration is applied, with the scattering parameters measured in the time and frequency domains. **Fig 4.36** shows the slot Vivaldi antenna configuration. The antenna pair is first located at the top of the breast phantom (X_1) and is then moved to the position (X_2).

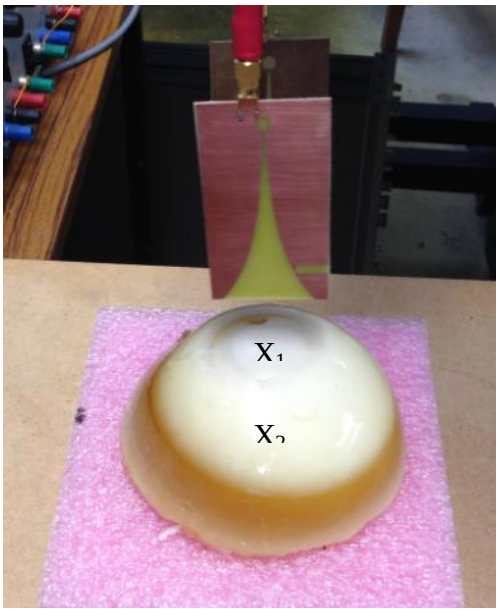

Fig 4.36 The slot Vivaldi antenna pair configuration.

This scan method has been discussed in previous sections, and the measurement results are presented in **Fig 4.37**. As seen, the amplitude at the X_1 is stronger than that at the $X_{2,}$ which shows that the reflection (S_{11}, O_{11}) and transmission coefficients (S_{21}, O_{21}) increase when the transmitting antenna moves close to the tumour. This phenomenon has also been observed using the original designed Vivaldi antenna.

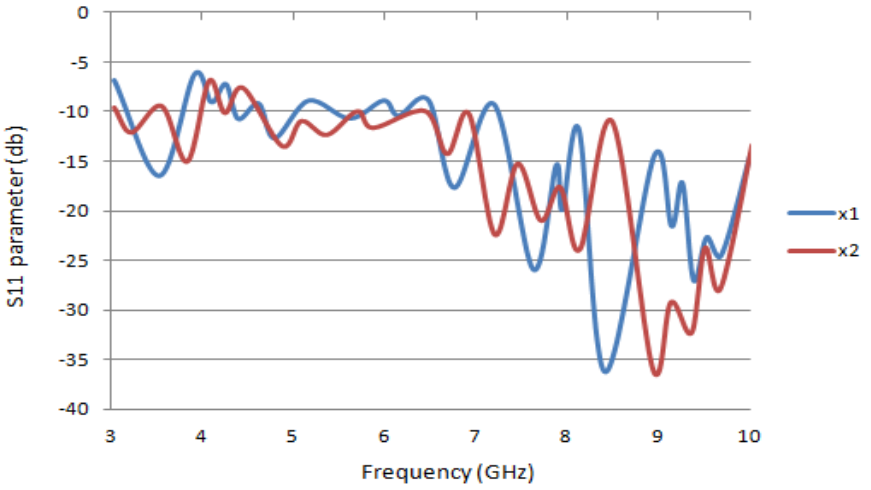

(a)

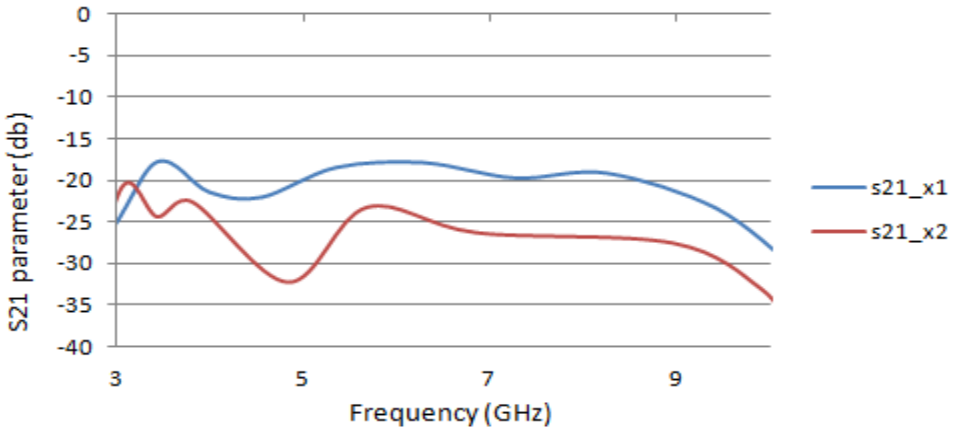

(b)

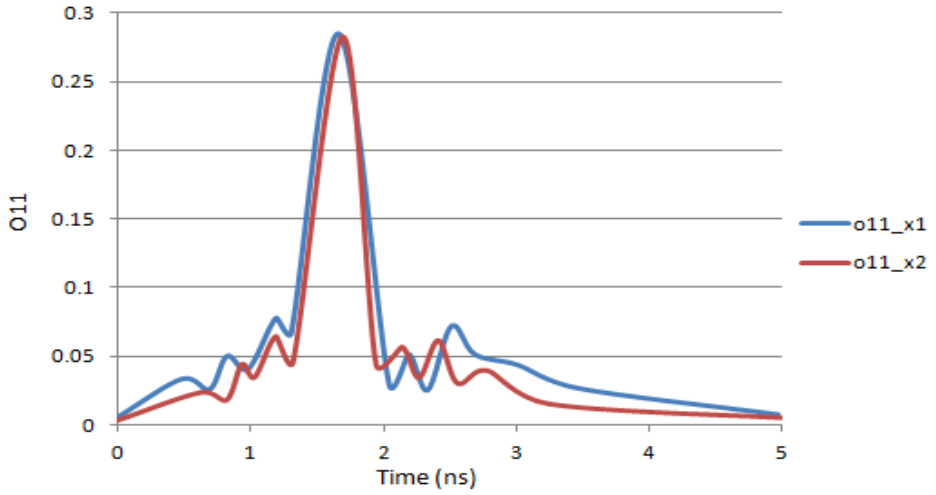

(c)

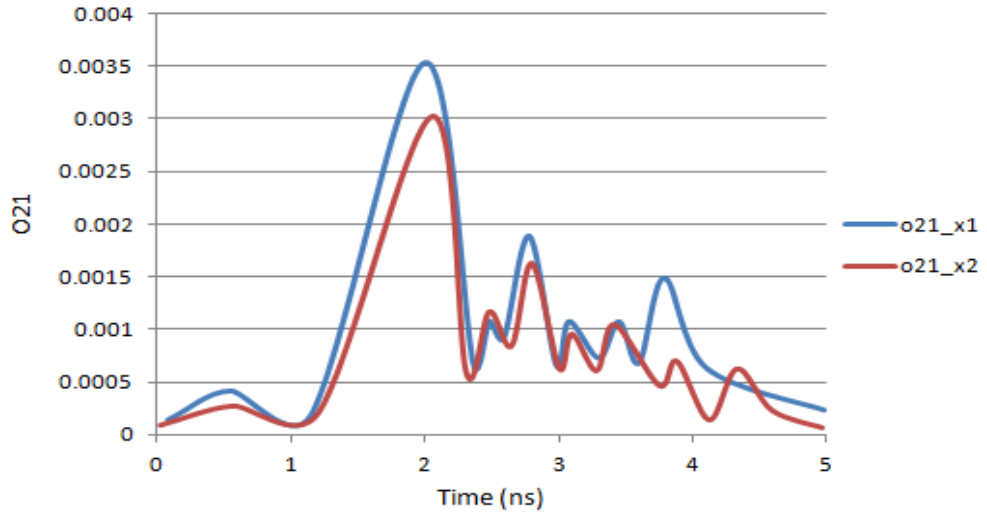

(d)

Fig 4.37 The slot Vivaldi antenna pair configuration.

4.5.2 The Detection of Deeply Buried Tumour

The slot Vivaldi antenna provides a wider bandwidth (3-10 GHz) compared with the non-slot Vivaldi antenna (5-10 GHz). The lower working frequency provides a stronger penetration ability. Hence, the use of the slot Vivaldi antenna could have the advantage being able to detect deeply buried tumours. Hence, a multiple bio-layer phantom which contains skin and fat layers and has two tumours (T_1 and T_2) buried at different depths is proposed, as shown in **Fig 4.38**.

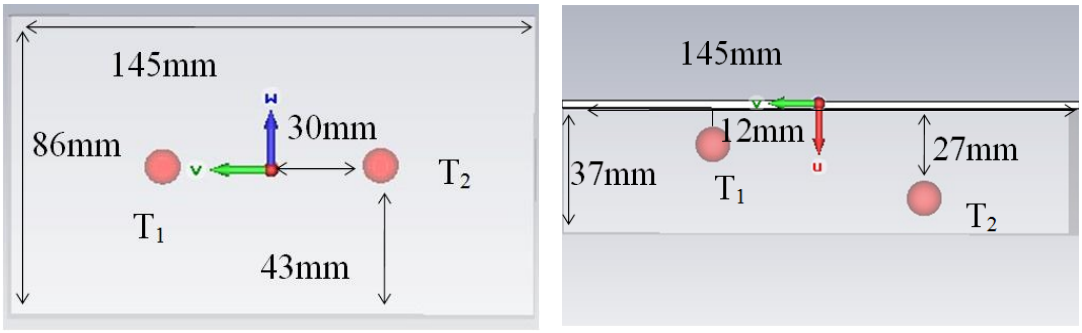

Fig 4.38 The simulated breast phantom with two tumours embedded in different depth.

The slot-Vivaldi antenna is used to measure these two tumours. The single slot Vivaldi antenna is moved to T_1 and T_2, with scatter parameters recorded in the frequency and time domains, as shown in Fig 4.39. It is observed that the depth difference caused amplitude difference is very weak. However, the enlarged signal part between 3.5 to 5GHz indicates that the shallow buried tumour reflects more energy than the deeply buried tumour, although the amplitude difference is quite small. The time domain signals at around 2 ns also show the same phenomenon.

The simulation results show that the use of the slot-Vivaldi antenna increases the penetration ability. However, the problem is that the difference between the shallow and deeply buried tumour responses is too weak to be detected.

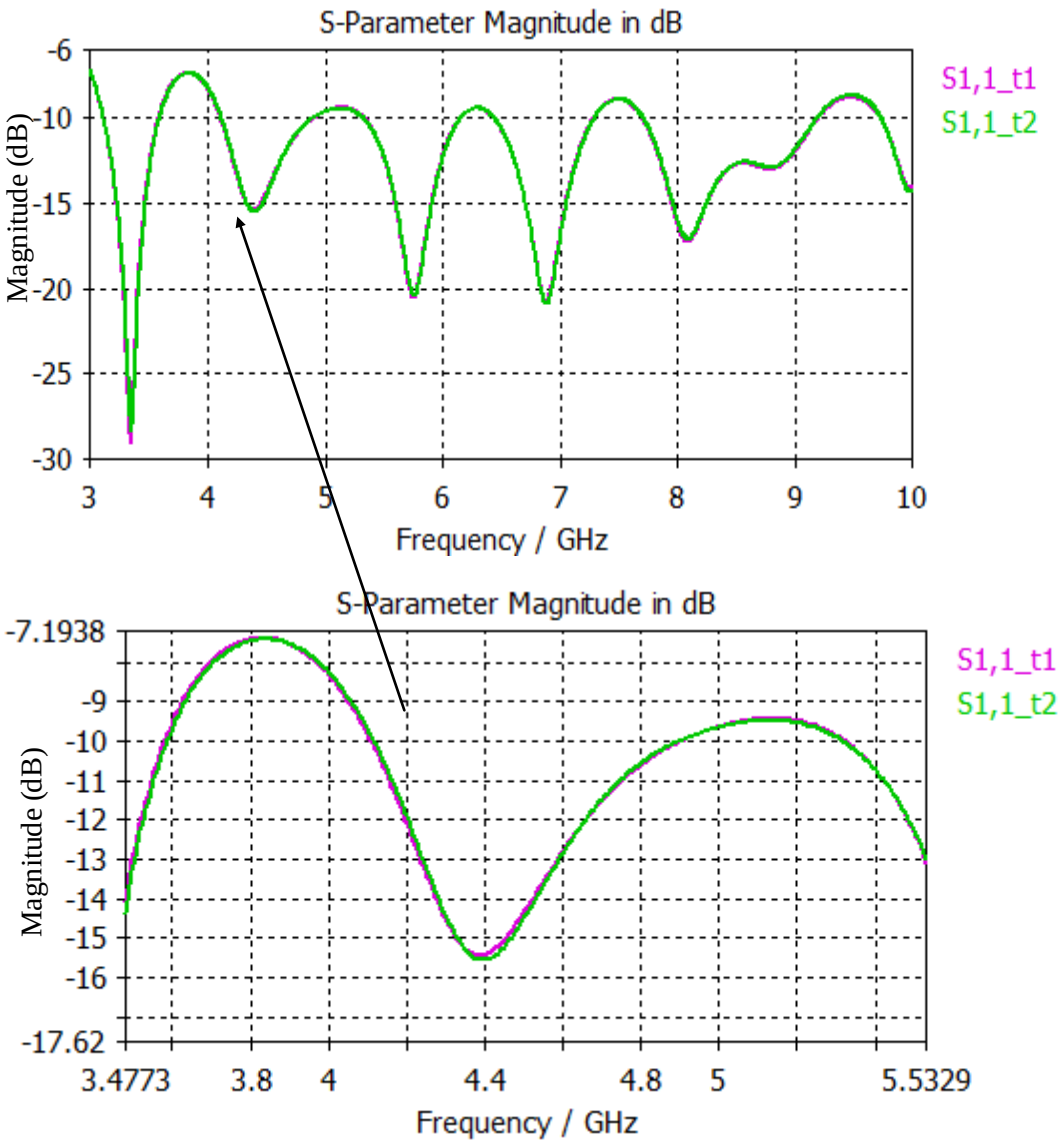

(a)

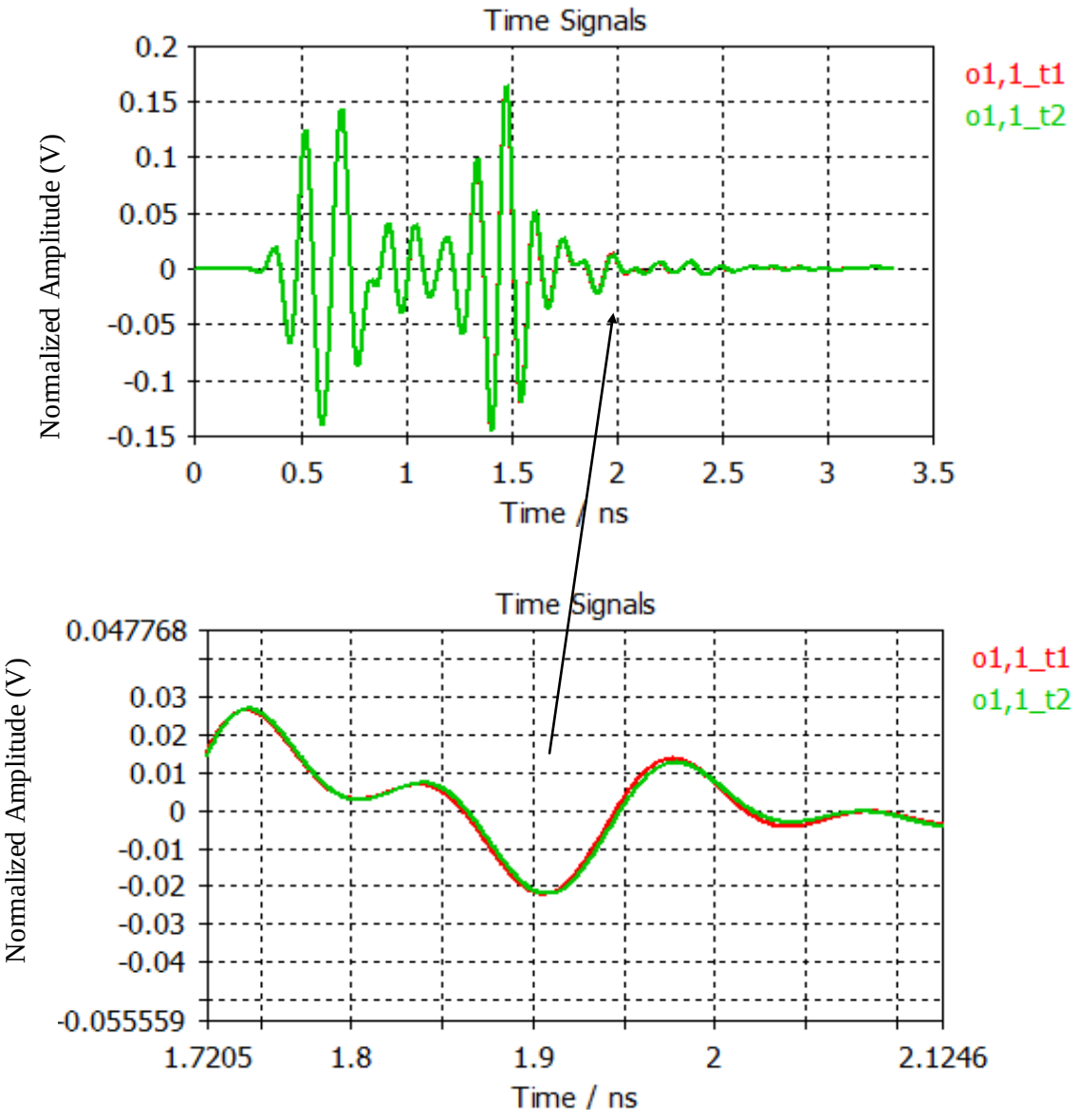

(b)

Fig 4.39 (a) The S_{11} at T1 and T2 and (b) The O_{11} at T1 and T2.

Besides, we can also confirm the correctness of received time domain signal, as shown in Fig 4.39 (b). The microwave propagation velocity in the fat layer is v= 1.3984e+008 m/s. Assume the distance between t1 and t2 is d= 0.01m, the phase difference in Fig 4.39 (b) can be calculated as t= d/v = 7.151e-11 s = 7.151e-2 ns, which confirms that Fig 4.39 (b) is correct.

4.6 Summary

In this chapter, the planar breast phantom and hemi-sphere breast phantom have been proposed. The breast phantom is simulated and fabricated using the CST and tissue-mimicking materials, respectively. The mono-static radar systems based on single antenna configuration and antenna pair configuration are then proposed. These two imaging systems are used to measure the planar breast phantom and hemi-sphere breast phantom respectively, with the reflection coefficients and the transmission coefficients recorded in the time and frequency domains. Based on the measurement results, it is concluded that the reflected energy increases when the antenna moves close to the tumour; otherwise, the reflected energy reduces when the antenna moves away from the tumour. This is the basic principle which is used to create the microwave images to indicate the tumour position.

Furthermore, the multi bio-layer phantom which contains a skin and fat layer with two tumours buried at different depths is also proposed. The slot-Vivaldi antenna is used to measure these two tumours. The results indicate that shallow buried tumour response is stronger than the deeply buried tumour. However, the difference in response is quite weak.

In the next chapter, these measured scattering signals will be processed to create the microwave images used to indicate tumour position.

Chapter 5 Signal Processing for the Received Scattering Signals

The antenna and breast phantom designs and experimental setup have been introduced. Based on the time and frequency domain signals collected and discussed in Chapter 4, it is concluded that the reflected energy increases when the antenna moves close to the tumour; otherwise, the reflected energy is reduced when the antenna moves away from the tumour. This is the basic principle which is used to create the microwave images to indicate the tumour position.

However, the collected signals contain strong skin reflections and environmental noise. Besides, the tumour response is quite weak, which could easily be drowned out in the noise. Hence, the signal and image processing is required in order to obtain diagnosis images with high resolution and low noise.

Before applying signal processing methods, it is necessary to study the transient signal based electromagnetic scattering theory. In this chapter, the fundamentals of the electromagnetic scattering mechanism are analyzed first. The Singularity Expansion Method (SEM) is then investigated. The SEM is used to extract the complex natural responses (CNRs) of the illuminated object (tumour) in order to determine the morphology of the tumour. The morphology of the tumours are an important factor in discriminating between the benign and malignant tumour.

Previous radar based cancer detection research has assumed the tumour has a uniform shape such as a sphere or ellipsoid [113-122]. Actually, as discussed in

the Chapter 2, tumours can be classified as benign or malignant tumours. Different tumour corresponds to different diagnosis methods. Hence, the discrimination between the benign and malignant tumours is also very important. The use of the SEM provides a mathematical approach to discriminate the benign and malignant tumours, and this, has the potential to complement the current radar based cancer detection.

5.1 The Electromagnetic Scattering Mechanism

A typical radar system contains a transmitter and a receiver. The signal is transmitted by the transmitter and then scattered by the object. The scattering signal is then received by the receiver.

For the electromagnetic scattering mechanism research, these devices such as transmitter and receiver are all ignored. The transmitter is replaced by an incident wave while the receiver is replaced as an observation point. The incident wave and scattering wave are represented using electric field $\vec{E^i}$ and $\vec{E^s}$. The induced current of the object after being illuminated is represented by $\vec{J}$. Fig 5.1 shows the electromagnetic scattering mechanism. Based on these assumptions, an incident wave illuminates on an object, the scattered wave in the frequency domain can be represented as [123-125]

$$\vec{E^s}(\bar{r}, s) = \int_{v'} \bar{\bar{G}}(\bar{r}, \bar{r}', s) \cdot \vec{J}(\bar{r}', s)\, dv' \qquad (5.1.1)$$

where $\bar{\bar{G}}$ is the dyadic Green function, $\bar{r}$, $\bar{r}'$ are the backscattering wave observation point and one point inside the object , v' is the volume of the object, $\vec{J}(\bar{r}', s)$ is the induced current of the object, $s = jw$ represent the frequency domian.

However, the electromagnetic wave also contains a magnetic component, which is not discussed here. The induced current $\vec{J}(\bar{r}', s)$ depends on the incident wave in terms of polarization, frequency, amplitude, etc as well as the object and the electrical properties of its surrounding medium. $\overline{\overline{G}}$ is the dyadic Green function. In the far field, this function becomes $e^{-\gamma R}/4\pi R$, where $\gamma = \alpha + j\beta$, α is the attenuation factor and β is the phase constant. R is the distance between the observation point and one point in the object volume. In free space, $\alpha = 0$, which means that this is a lossless medium. However, in practice, $\alpha \neq 0$.

The time domain equation of Equation (5.1.1) is [123-125]

$$\vec{E^s}(\bar{r}, t) = \int_{v'} \overline{\overline{G}}(\bar{r}, \bar{r}', t - R/v) \otimes \vec{J}(\bar{r}', t)\, dv' \qquad (5.1.2)$$

where v is the propagation velocity in the medium, and $R = |\bar{r} - \bar{r}'|$ represents the distance between one point in the object and the observation point.

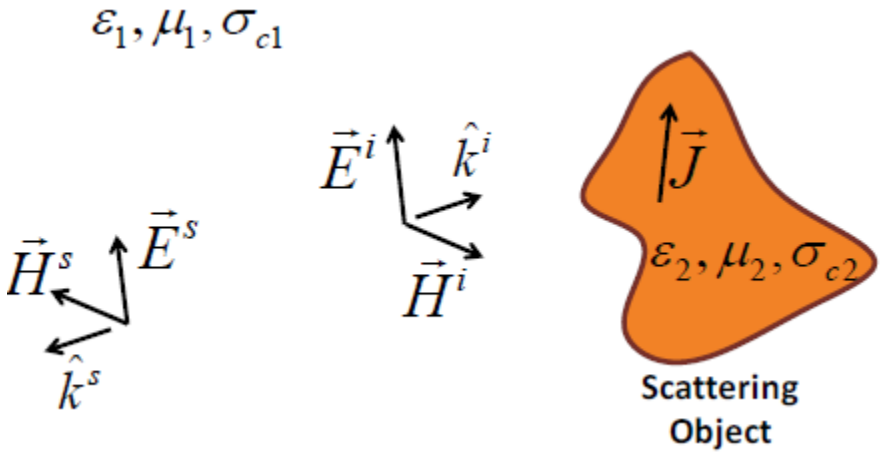

Fig 5.1 The electromagnetic scattering mechanism. [123]

Electromagnetic scattering can be specified by three regions: the Rayleigh region, response region and optical region. The specification of these three regions is based on the ratio of the relative dimensions of the scattering object to the wavelength of the incident electromagnetic wave [126]. Equation (5.1.3) shows the relation between the scattering region and the relative dimensions of the scattering object to the wavelength of the incident microwave

$$\text{Scattering region}=\begin{cases} \frac{D}{\lambda} \ll 1 & \text{Rayleigh region} \\ 0.5 < \frac{D}{\lambda} < 10 & \textit{R}\text{esonance region} \\ \frac{D}{\lambda} > 10 & \textit{O}\text{ptical region} \end{cases} \tag{5.1.3}$$

where D is the dimension of the scattering object, and λ is the incident wavelength of the electromagnetic wave.

Equation (5.1.3) shows the electromagnetic scattering region in free space; however, for the breast cancer detection, the tumour is buried in the breast and the electromagnetic wave propagates in a lossy medium. Hence, Equation (5.1.3) has to be modified. The propagation speed in the lossy medium depends on the relative permittivity of the medium, expressed by Equation (5.1.4): [133]

$$\lambda = \frac{v_m}{f} = \frac{c_0}{f * \mathrm{Re}\left[\sqrt{\varepsilon_r(f)}\right]} \tag{5.1.4}$$

where v_m is the electromagnetic wave propagation speed in the lossy medium, ε_r is the relative permittivity of the lossy medium, and c_0 is the wave propagation speed in free space.

Based on Equation (5.1.4), the wavelength and propagation velocity in different medium can be calculated. Table 5.1 shows the calculated wavelength λ in each layer of the cancerous breast, and the ratio of the scattering object dimension (D) to the wavelength (λ) of the incident microwave, $\frac{D}{\lambda}$ in each layer. The working frequency ranges from 5 to 10 GHz, with the wavelength being from 30 to 60 mm. It is worth noting that for the $\frac{D}{\lambda}$, this λ refers to the wavelength of the incident wave rather than that of the wave in the incident layer. For example, $\frac{D}{\lambda}$ for the skin layer, λ is the wavelength in free space rather than that in the skin layer since λ refer to the incident wave. Likewise, $\frac{D}{\lambda}$ for the fat and tumour layers, λ are the wavelength in the skin and fat layers, respectively. D is the dimension of each layer.

Based on Table 5.1 and Equation (5.1.4), it can be concluded that the skin layer propagation mechanism involves in the optical regions, while the fat and tumour propagation mechanism involves the optical and resonance regions, respectively.

Table 5.1 The Minimum and Maximum Wavelength in Different Layers of Breast.

	Vacuum	Skin	Fat	Tumour
Min (λ) mm	30	10	26	8
Max (λ) mm	60	11	28	9
D	N/A	440	427	31
Min(D/λ)	N/A	7	39	1.1
Max(D/λ)	N/A	15	43	1.2

The classification of three scattering regions has been discussed quantitatively. As seen from Equation (5.1.4), the optical scattering region is due to the wavelength of incident wave being much smaller than the object dimension. Most scattering waves are due to the specular reflection from the object surface. In the optical region, the theories of Geometrical Optics (GO) or Physical Optics (PO) can be used to solve the scattering problem [127, 134].

The Rayleigh region is due to the wavelength of the incident wave being much larger than the object dimension. Hence, the object is too small to affect the incident wave.

Resonance region scattering is of interest due to the tumour scattering mechanism being in this region. When the incident electromagnetic wave illuminates the object, an induced current surrounding the object will be excited. The generated electric field is opposite to the electric field of the incident wave.

Fig 5.2 illustrates the electromagnetic scattering mechanism [123]. The object is assumed to be a perfect conducting sphere (PCS). This PCS is illuminated by an incident wave which is then followed by two scattering stages: early time response (ETR) and late time response (LTR). Part of the incident wave is directly reflected by the PCS, which is also called specular reflection. Another part of the incident wave propagates around the PCS until reaching the specular point. This part of the incident wave is also called the travelling wave. The travelling wave combines with the specular reflection wave constructively or destructively to generate a combined reflection wave which is also called the creeping wave. This reflection process is the so called ETR. As seen, the early time response is caused only by the incident wave. However, the late time response (LTR) is generated by the induced wave. As discussed, when the incident wave illuminates the object, an induced current and electric field surrounding the object will be excited. The excited and incident electric field have the opposite direction, which means that the induced electric wave resists

the incident wave. This induced electric field is called the resonant response, or late time response (LTR). It is worth noting that for the PCS based scattering mechanism, the creeping wave only travels along the surface of the PCS since there is no electric field inside the PCS. However, for an object in a lossy medium, an electric field is also generated inside the object. Hence, the creeping waves are generated on the surface of the object in the lossy medium as well as in the interior of this object.

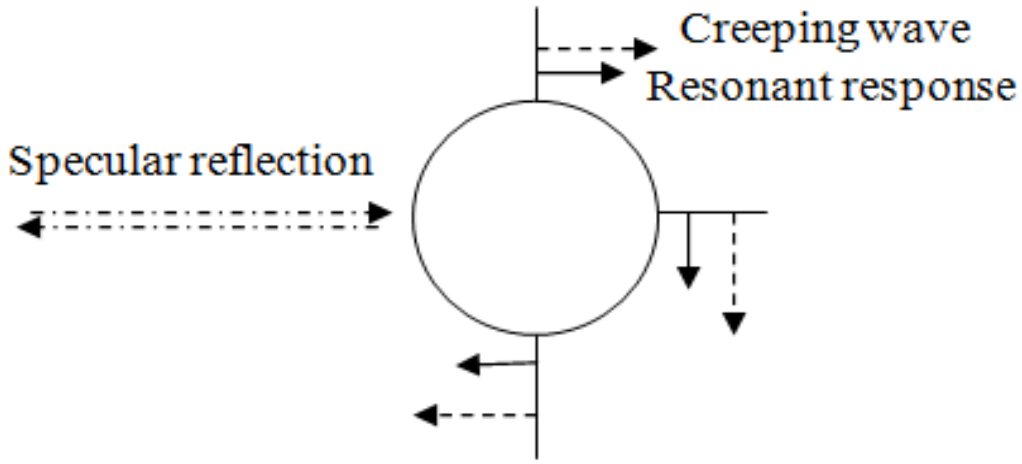

Fig 5.2 The resonant response.

The reflected wave is the combination of ETR and LTR. The basic electromagnetic scattering mechanism discussed above can be applied to any object. However, the properties of object in terms of its material, relative permittivity and conductivity as well as the propagation environment could affect the transient response of the object. For electromagnetic scattering in breast cancer detection, the problem is considered as a lossy object (tumour) scattering in a lossy propagation medium. The lossy propagation medium is composed of air, skin and fat layer. As seen from Table 5.1, the scattering in skin and fat layer involves the optical region and the tumour

reflection involves in the resonance region. In other words, the skin and fat layer reflection is the early time response and the tumour reflection is the late time response. This unique feature provides the basis of the mathematical analysis in next section.

5.2 Singularity Expansion Method

The transient scattering discussed above can also be mathematically represented using singularity expansion method (SEM). The SEM was introduced by Baum [124-125] from the observation that the electromagnetic scattering response is dominated by exponentially damped sinusoids functions.

The SEM based mathematical representation is developed by expanding the Laplace domain singularity such as poles and residues. Assuming a perfect conducting sphere (PCS) is illuminated by an electromagnetic wave, an induced current on the surface of the PCS can be expressed by: [123-125]

$$\vec{J}\ (\bar{r}', s) = \sum_{n=1} \frac{E^i(s_n)\eta_n(\hat{k}^i,\hat{e}^i)v_n(\bar{r}')}{s-s_n}\ e^{-(s-s_n)t_L} + \bar{F}\ (\hat{k}^i,\hat{e}^i,s) \qquad (5.2.1)$$

where $\vec{J}$ is the induced current on the surface of the PCS, E^i is the electric field of the incident wave, t_L is the late time response (LTR) turn on time, $s_n = \sigma_n + j\ \omega_n$ is the resonant response in the Laplace domain, $\hat{k}^i$ is the direction of the incident electromagnetic wave while $\hat{e}^i$ is its polarization of the incident electromagnetic wave, σ_n and ω_n are the damping factors and resonant frequencies, η_n is the coupling coefficient which determine the induced strength of the incident wave, $\bar{F}$ is

the early time response (ETR), v_n is the natural mode structure of the resonant response.

The scattering wave can be derived by substituting (5.2.1) into (5.1.1) as [123-125]

$$\overrightarrow{E^s}\ (\bar{r}', s) = \sum_{n=1} \frac{e^{-(s-s_n)t_L} \int_{v'} \bar{\bar{G}}\ (\bar{r},\bar{r}',s) E^i(s_n) \eta_n(\hat{k}^i,\hat{e}^i) v_n(\bar{r}') dv'}{s-s_n} +$$

$$\int_{v'} \bar{\bar{G}}\ (\bar{r},\ \bar{r}',s) \bar{F}\ (\hat{k}^i,\hat{e}^i,s) dv' \qquad (5.2.2)$$

Equation (5.2.2) can be reduced to

$$\overrightarrow{E^s}\ (\bar{r}', s) = \sum_{n=1} \frac{\overline{R_n'}(\hat{k}^i,\hat{e}^i,\bar{r})}{s-s_n}\ e^{-(s-s_n)t_L} + \bar{W}\ (\hat{k}^i,\hat{e}^i,\bar{r},s) \qquad (5.2.3)$$

where $\bar{W}$ is the Early Time Response (ETR) part, $\overline{R_n'}$ is the residue of the pole. The residue here refers to the amplitude of the scattering wave at the resonance frequency, which depends on the direction ($\hat{k}^i$) and polarization ($\hat{e}^i$) of the incident wave and the distance between the scattering point and the observation point ($\bar{r}$).

The time domain of Equation (5.2.4) can be expressed by the Laplace transform: [123-125]

$$\overrightarrow{E^s}\ (\bar{r}, t) = \sum_{n=1} \overline{R_n'}(\hat{k}^i,\hat{e}^i,\bar{r}) e^{s_n t}\ u(t - t_L) + \overline{W_e}\ (\hat{k}^i,\hat{e}^i,\bar{r},t) \qquad (5.2.4)$$

where $e^{s_n t}$ is a sum of exponentially decaying sinusoids function, t_L is the late time response (LTR) Turn On time which indicates the time boundary between the ETR and LTR, $u(t - t_L)$ is the unit step function. The ETR is the combination of the specular reflection from the surface of the PCS and the travelling wave surrounding it. $e^{s_n t}$ represents the rapid decaying of the ETR. After the incident wave has travelled through the PCS, the LTR starts while the PCS acts as a source free oscillator.

As seen from Equation (5.2.3) and (5.2.4), the poles $s_n = \sigma_n + j\,\omega_n$ are independent of the properties of incident wave such as direction, polarization and only is dependent on the object properties such as relative permittivity, conductivity and shape. The residue of the pole $\overline{R'_n}$ represents the amplitude of the scattering wave which depends on the direction ($\hat{k}^i$) and polarization ($\hat{e}^i$) of the incident wave. Based on the expression of the poles s_n and the residue of the pole $\overline{R'_n}$, it can be concluded that the scattering wave has the same poles but different residue. These distinctive features of the poles are very useful. As previously mentioned, the benign and malignant tumour can be distinguished based on their different shapes. A malignant tumour usually has an irregular surface while a benign tumour has smoother surface and roughly spherical morphology. The resolution of the imaging results from the microwave imaging, MRI and CT approaches is not high enough to distinguish between benign and malignant tumours. However, the use of poles analysis method provides the mathematical approaches to distinguish between them.

As previously discussed, the solution for distinguishing between benign and malignant tumours is to extract the poles of the tumour. Recalling Equation (5.2.4), the LTR is (5.2.5): [123]

$$x(t) = \sum_{n=1}^{N} \overline{R_n'}\left(\hat{k}^i, \hat{e}^i, \bar{r}\right) e^{s_n t}\, u(t - t_L) \tag{5.2.5}$$

Equation (5.2.5) can be rewritten as:

$$x(t + t_L) = \sum_{n=1}^{N} \overline{R_n'}\left(\hat{k}^i, \hat{e}^i, \bar{r}\right) e^{s_n t}\, u(t) \tag{5.2.6}$$

The digitized equation (5.2.6) can be expressed as:

$$x(m\Delta_t + t_L) = \sum_{n=1}^{N} \overline{R_n'}\left(\hat{k}^i, \hat{e}^i, \bar{r}\right) e^{s_n m\Delta_t} = \sum_{n=1}^{N} \overline{R_n'} e^{s_n m\Delta_t} \tag{5.2.7}$$

where m = 0, 1, …, M-1, M is the total number of samples, and Δ_t is the sampling interval.

Now the problem is reduced to calculate the pole s_n, or in other words, the damping factor. The mathematical solutions for calculating damping factor have been introduced in [135-139] such as Prony's method, Covariance method and Matrix Pencil Method (MPM).

5.3 The Transient Signal Analysis

5.3.1 The Turn-on Time

The Singularity Expansion Method (SEM) as introduced above provides the mathematical representation of the transient scattering wave. Specifically, the poles are independent of the properties of the incident wave such as direction, polarization and dependent on the object properties such as relative permittivity, conductivity and shape. The residue of the pole represents the amplitude of the scattering wave which depends on the direction and polarization of the incident wave. These unique features provide a mathematical approach for use in distinguishing between benign and malignant tumours. In this section, the received transient signals in Chapter 4 are analyzed based on the SEM.

The electromagnetic scattering mechanism has been discussed in section 5.1. A PCS in free space is considered first and then this is followed by the analysis of a lossy object (tumour) embedded in a lossy medium (skin and fat layers). The skin layer propagation mechanism involves the optical regions, while the fat and tumour propagation mechanism involves the optical and resonance regions, respectively. Hence, when an incident electromagnetic wave illuminates a cancerous breast, the scattering wave contains reflections from the skin, fat and tumour. However, the skin and fat reflections involves the optical region, which means that in the SEM representation these reflections contribute to the ETR. The tumour reflection involves the resonance region and contributes to the LTR. The tumour reflection can be extracted based on this unique feature.

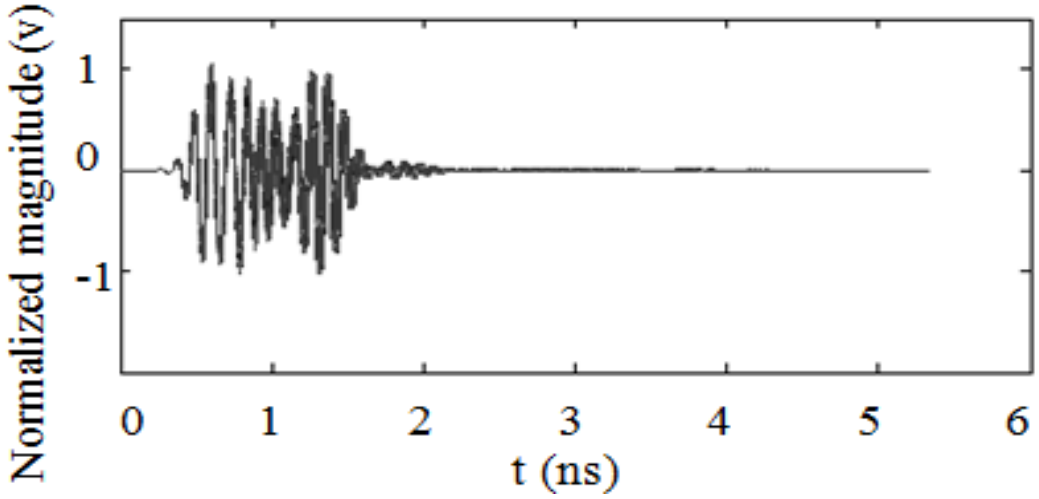

(a)

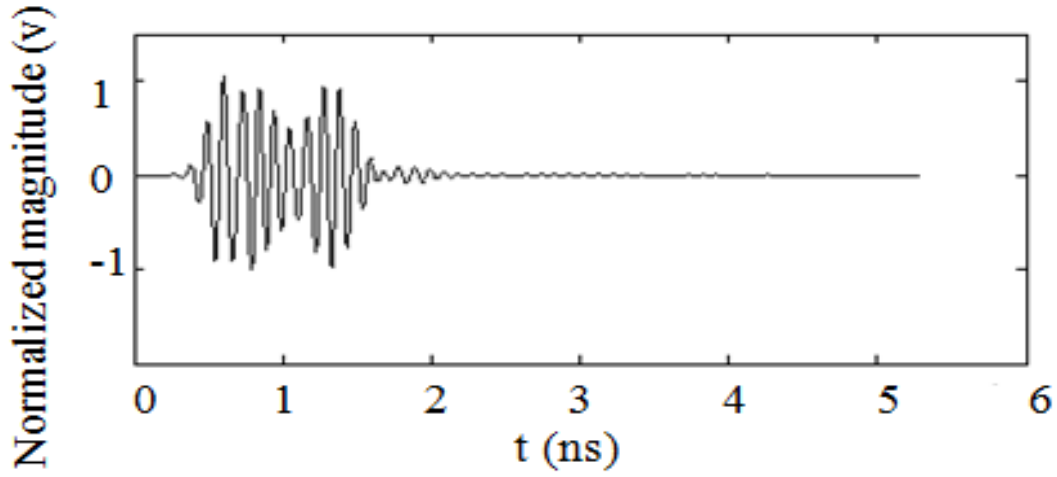

(b)

Fig 5.3 (a) The received transient signals from single antenna configuration and (b) the received signal when the antenna stops at the front centre of the tumour.

Fig 5.3 (a) shows the received transient signals. These signals are obtained from the single antenna configuration, with each signal corresponding to an observation point. The detailed single antenna configuration has been discussed in Chapter 4. Here, the

received signal when the antenna stops at the front of the tumour is chosen as shown in **Fig 5.3** (b).

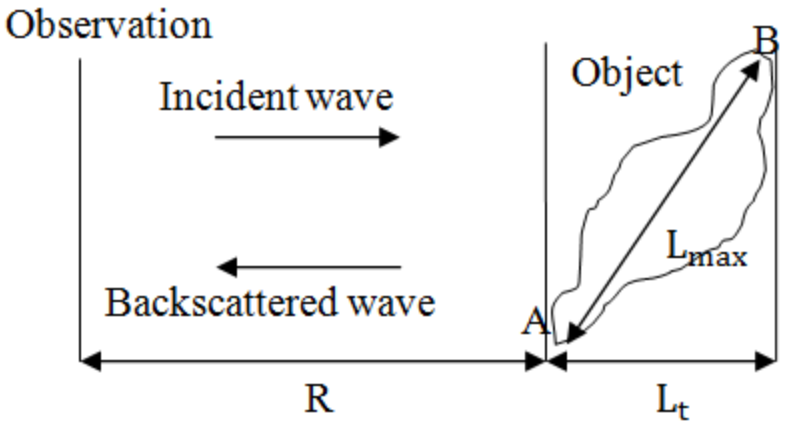

(a)

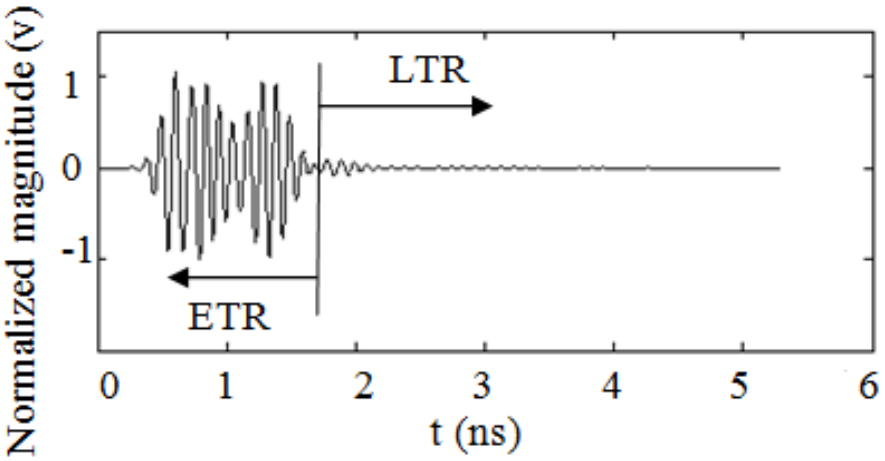

(b)

Fig 5.4 (a) free space scattering configuration [132] and (b) The transient scatter signal of the cancerous breast phantom.

The tumour response involves the LTR. Hence, the first step is to investigate the turn on time of the LTR which means the boundary between the LTR and ETR. In [132], the author suggests that the turn on time is equal to twice the time of the incident electromagnetic wave passing the surface of the object. Assuming the diameter of the object is 2α, the turn on time can be calculated as $t_L = 4\alpha/c$. In [132], the turn on time t_L is considered in free space by using an object with irregular surface, as shown in **Fig 5.4** (a). The turn on time t_L can be calculated as (5.3.1):

$$
\begin{aligned}
t_A &= R/c \\
t_B &= t_A + L_t/c \\
t_{Lmax} &= L_{max}/c \\
t_L &\geq 2t_A + 2t_{Lmax} \geq 2t_B + t_{pw}
\end{aligned}
\tag{5.3.1}
$$

where t_A and t_B are the incident electromagnetic wave propagation time when the incident wave reaches the point A and B. L_t is the object dimension along the wave propagation path, R is the propagation distance from the observation point to the point A. L_{max} is the maximum dimension of the object, t_{pw} is the width of the input pulse, t_L is the turn on time. Equation (5.3.1) provides the scattering model of an irregular surface object in free space. However, considering the breast phantom based scattering mechanism, Equation (5.3.1) has to be modified (5.3.2):

$$t_A = R_v/c + R_s/v_s + R_f/v_f$$

$$t_B = t_A + L_t/c$$

$$t_{Lmax} = L_{max}/ v_f \qquad (5.3.2)$$

$$t_L \geq 2t_A + 2t_{Lmax} \geq 2t_B + t_{pw}$$

where R_f, R_s, R_f show the propagation path in free space, skin and fat layers respectively. v_s and v_f indicate the wave propagation speed in the skin and fat layers, respectively. $L_{max} = L_t$ indicates the diameter of the object (tumour).

Based on Equation (5.3.2), the turn on time t_L can be calculated. **Fig 5.4** (b) shows the ETR, LTR and their boundary t_L. The ETR contains the scattering signals from the skin and fat layers. Specifically, the specular reflection contributes to the ETR. The tumour resonance response mainly involves in the LTR, which is caused by the induced current.

Equations (5.2.5-5.2.7) provide the mathematical method to decompose the LTR. The LTR can be decomposed to the sum of damping sine function. The frequencies of these damping sine functions correspond to the resonance responses of the tumour. These damping factors are expressed in the Laplace domain, which can be used to distinguish between benign and malignant tumours based on their difference in morphology. As discussed above, the damping factors are independent of the properties of the incident wave such as direction and polarization and dependent on the object properties such as relative permittivity, conductivity and shape.

However, based on Equations (5.3.1-5.3.2), the calculation of the turn on time t_L requires the prior knowledge of the object such as its dimensions and the position. For the purpose of research, prior knowledge of the object can be obtained. However, in

clinical practice, prior knowledge of the object is not available. Hence, for radar based microwave cancer detection, the solution can be founded by first creating cross-section images of the breast. Information about the tumour such as its dimensions and location can be estimated based on the microwave images. Based on their information, the turn on time can be calculated from Equations (5.3.1-5.3.2). The LTR part can be extracted using signal processing methods such as applying a time window. The LTR will then be processed to extract the damping factors based on Equations (5.2.5-5.2.7).

5.3.2 The Skin and Clutters Removal Method

Fig 5.3.1(a) shows the received transient signals obtained from the single antenna configuration. The tumour response is too weak due to the strong skin layer reflection. Besides, the amplitudes of the tumour response are quite close to the clutter. Hence, cross-section images of the breast could be quite noisy if the received transient signals are used directly without any processing.

Skin and clutter removal methods have been proposed in many publications [140-141]. A most commonly used method for the removal of unwanted signal is to simulate or measure the reference transient scattering signals using a breast without the presence of tumour. The reference signals contain the skin reflection and clutters and can be used to calibrate the original received signals. The tumour response can be extracted by subtracting the calibration signals. This calibration process can be expressed by Equation (5.3.3)

$$S_{tumour} = S_{rece} - S_{ref} \tag{5.3.3}$$

where S_{rece} and S_{ref} indicate the received scattering and reference signals, respectively. This method is easily applied and able to remove unwanted signals such as skin reflections and clutter. However, the problem is that this method cannot be applied to in clinical practice since the tumour cannot be removed and an identical healthy breast is also not available. To solve this problem, another method is needed to remove the skin reflection and clutter.

The radar based microwave imaging for breast cancer detection uses a single antenna or an antenna array to detect the tumour and the received scattering signals can be expressed as:

$$S^i_{rece} = S^i_{skin} + S^i_{tumour} + S^i_{clutter} \quad (5.3.4)$$

where S^i_{rece} , S^i_{skin}, S^i_{tumour} and $S^i_{clutter}$ indicate the received scattering signal, skin reflection, tumour response and clutters, respectively. The notation i indicates stop positions of single antenna or the antenna array. The target is to remove the S^i_{skin}, $S^i_{clutter}$ and extract the S^i_{tumour}. Instead of measuring the reference scattering signals using a breast without a tumour, it is proposed here that another reference signal is used which can be expressed by:

$$S^i_{ref} = (S^i_{rece} - S^{i+1}_{rece} + S^i_{rece} - S^{i-1}_{rece} + S^i_{rece} - S^{i+2}_{rece} + S^i_{rece} - S^{i-2}_{rece})/4 \quad (5.3.5)$$

where S^{i+1}_{rece}, S^{i-1}_{rece}, S^{i+2}_{rece} and S^{i-2}_{rece} indicate four adjacent antenna stop positions. The mono-static radar based imaging method uses the antenna to scan the breast while maintaining the same distance between the antenna/antenna pair and the breast

surface constant, which means that the skin reflections and clutters can also remains steady. Hence, the received signal is subtracted by its surrounded four received signals and then the average value is taken. This process eliminates the unwanted parts of signal such skin effects and clutter while enhancing the tumour response. This method can also be applied to the frequency domain signals.

5.3.3 The Hilbert Transform and Wavelet De-noising for the Transient Signals

5.3.3.1 Hilbert Transform

The received signals contain the skin, tumour reflection and clutter. The peak of the signals over a time period can represent each of these parts. Taking **Fig 5.5** (a) for example, the signal from 1 to 1.5 ns represents the skin layer reflections while that from 1.5 to 2 ns represents the tumour reflection. The reflection over a time period is due to the multi-reflections between the antenna, skin layer and tumour.

Instead of directly using the received signal s(t), we employ the analytical signal $s^{+}(t)$ which is represented as (5.3.6) [142-144]:

$$s^{+}(t)= s(t)+j\ H\{s(t)\} \tag{5.3.6}$$

where s(t) is the real part of the analytical signal $s^{+}(t)$ and $H\{s(t)\}$ is as the imaginary part which is transformed using the Hilbert Transform (5.3.7):

$$H\{s(t)\} = \frac{1}{\pi} \int_{-\infty}^{+\infty} \frac{s(\tau)}{s(t-\tau)} d(\tau) \quad (5.3.7)$$

The use of the Hilbert transform shift the received signal s(t) by $\pi/2$ rad to create the imaginary part. The real and imaginary parts are orthogonal (5.3.8):

$$\int_{-\infty}^{+\infty} s(t)\, H\{s(t)\} dt = 0 \quad (5.3.8)$$

Fig 5.5 (b-e) shows the received signal s(t), its imaginary part $H\{s(t)\}$ and their envelope signal. This envelope signal is used for further processing since it is the average representation of the skin and tumour reflections. Specifically, the tumour reflection can be represented by a solo peak rather than a multi-peak. This solo peak will be used for the microwave image creation described in the next section.

The next step is to eliminate the unwanted signals using Equation (5.3.5). **Fig 5.5** (f) shows the signal after calibration. The skin effect and the clutter are significantly reduced compared with the original signal.

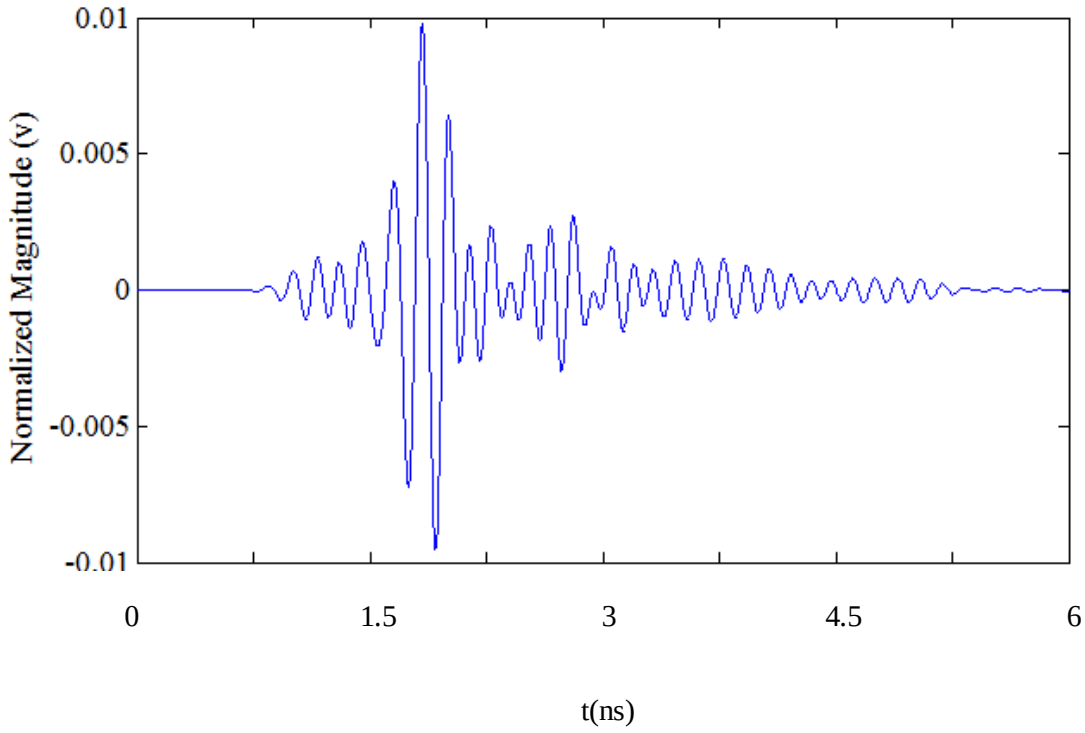
0.01
0.005
0
-0.005
-0.01
Normalized Magnitude (v)
0
1.5
3
4.5
6
t(ns)

(a)

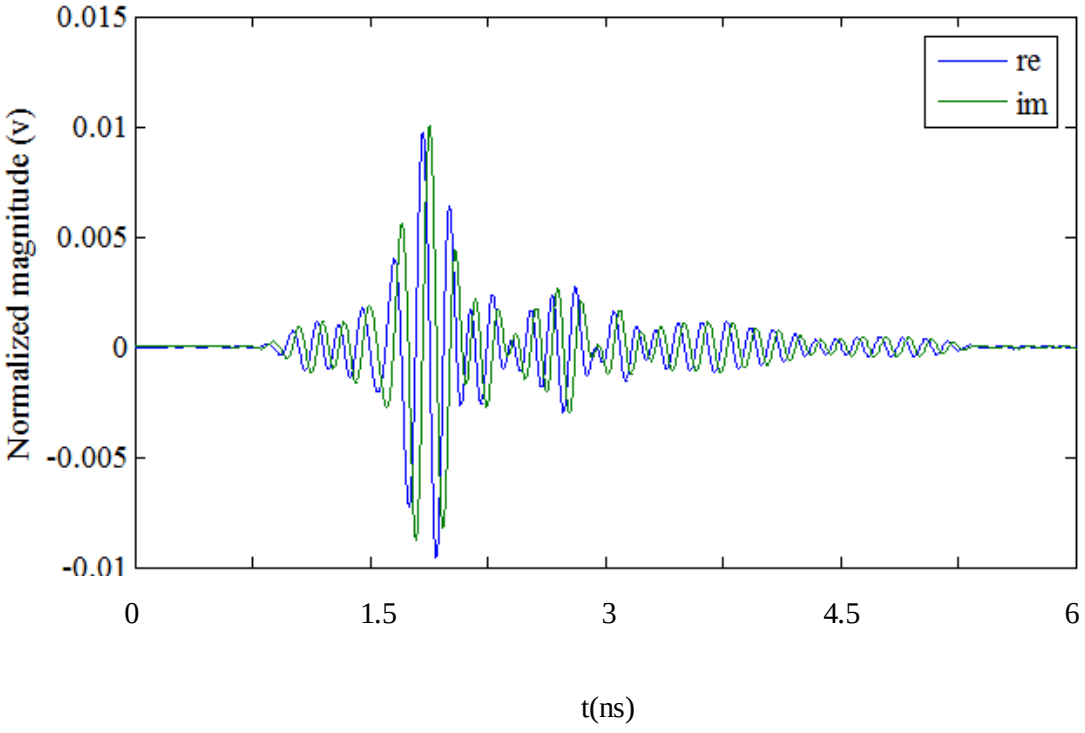
0.015
0.01
0.005
0
-0.005
-0.01
Normalized magnitude (v)
re
im
0
1.5
3
4.5
6
t(ns)

(b)

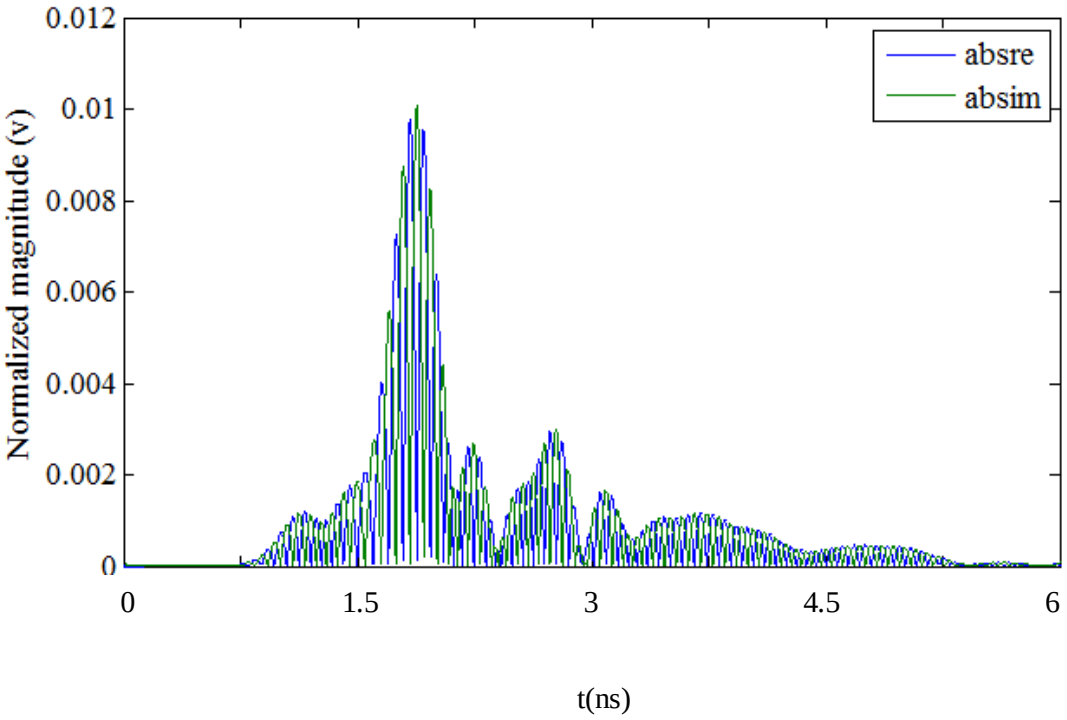
0.012
0.01
0.008
0.006
0.004
0.002
0
Normalized magnitude (v)
absre
absim
0
1.5
3
4.5
6
t(ns)

(c)

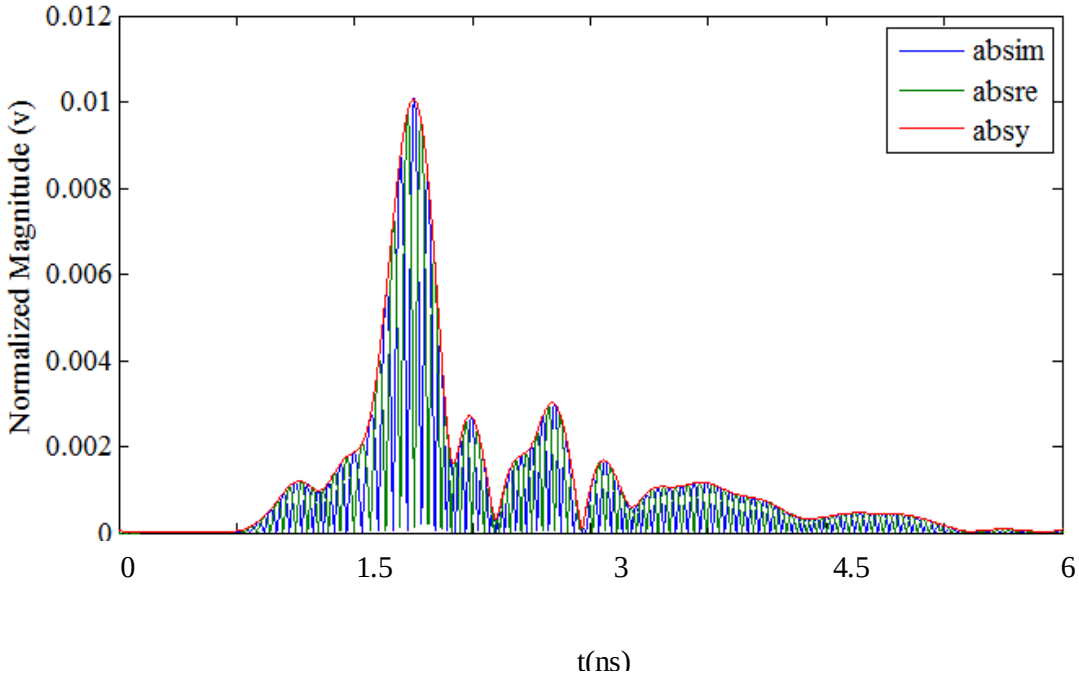
0.012
0.01
0.008
0.006
0.004
0.002
0
Normalized Magnitude (v)
absim
absre
absy
0
1.5
3
4.5
6
t(ns)

(d)

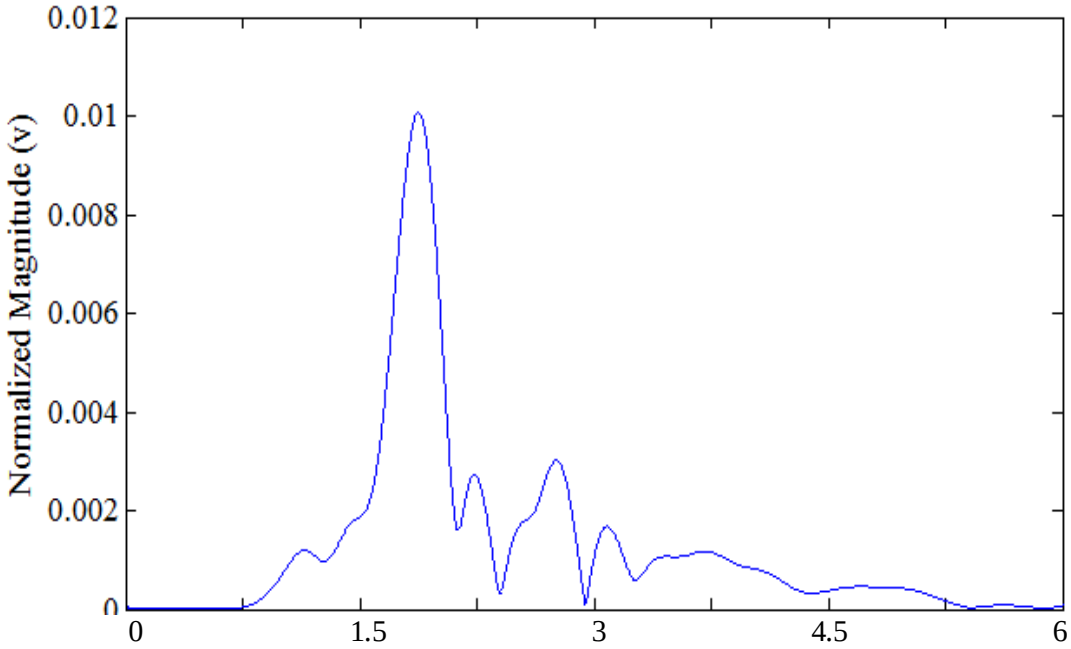

(e)

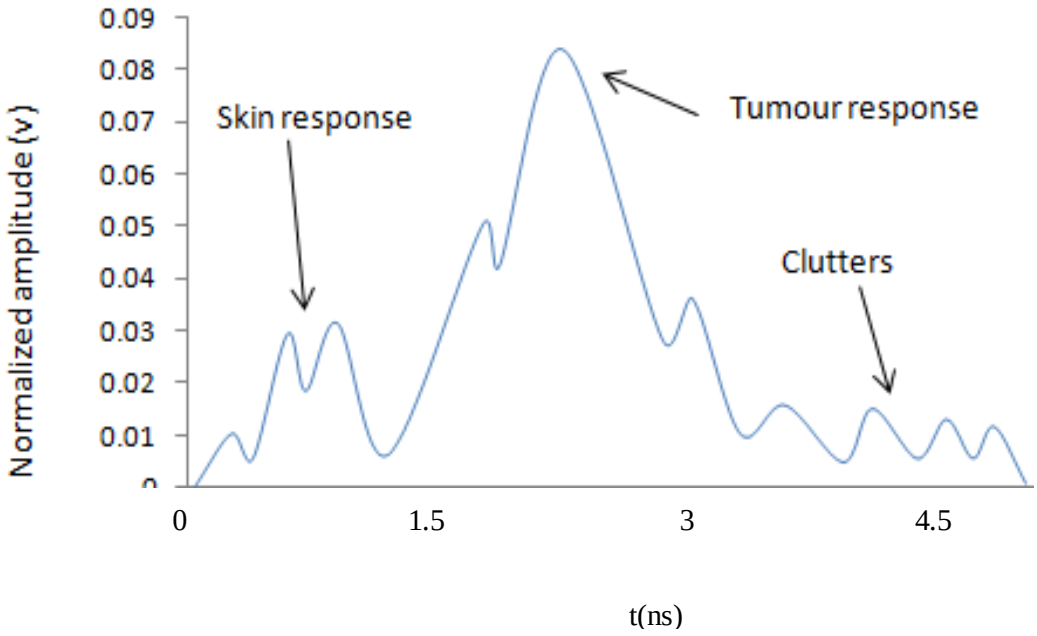

(f)

Fig 5.5 (a) the received signal and (b) the received signal and its Hilbert Transform and (c) the absolute value of the received signal and its Hilbert Transform and (d) the

envelope signal of (c) and (e) the envelope signal and (f) the envelope signal after calibration.

5.3.3.2 wavelet de-noising

A continuous wavelet transform (CWT) function is defined as (5.3.9) [145-146]:

$$W_f\ (a,b)= \frac{1}{\sqrt{a}} \int_{-\infty}^{\infty} f(t)\ \psi^*\ (\frac{t-b}{a})dt \qquad (5.3.9)$$

where $\psi(t)$ is the mother wavelet function and ψ^* is the complex conjugate of $\psi(t)$. $\frac{1}{\sqrt{a}}$ indicates the multiplication to normalize the amplitude. a and b denote the scale and translating coefficients. The selection of the mother wavelet function is dependent on the $f(t)$. In the case of the radar based microwave imaging, the incident wave is a modulated Gaussian pulse. Hence, the Gaussian function is used as the mother wavelet function. The mother wavelet function is expressed as:

$$\psi(t)\ = Cn\ \frac{d^n}{dt^n}(e^{-jt}e^{-t^2}) \qquad (5.3.10)$$

where Cn indicates the normalization coefficient. If n is even, the real part of $\psi(t)$ is also an even function, and the imaginary part is an odd function, and vice versa.

Instead of using CWT, the Discrete Wavelet Transform (DWT) is employed in the signal processing since the discretely sampled signal is more easily processed using a computer [145].

The DWT of the original signal f(m,n) can be expressed as (5.3.11) [145-146]:

$$DWT_\psi f(m,n)= \int_{-\infty}^{\infty} f(t)\ \psi^*_{m,n}\ (t)dt \qquad (5.3.11)$$

where $\psi_{m,n}(t) = 2^{-m}\psi(2^m t - n)$ is the scaling mother wavelet.

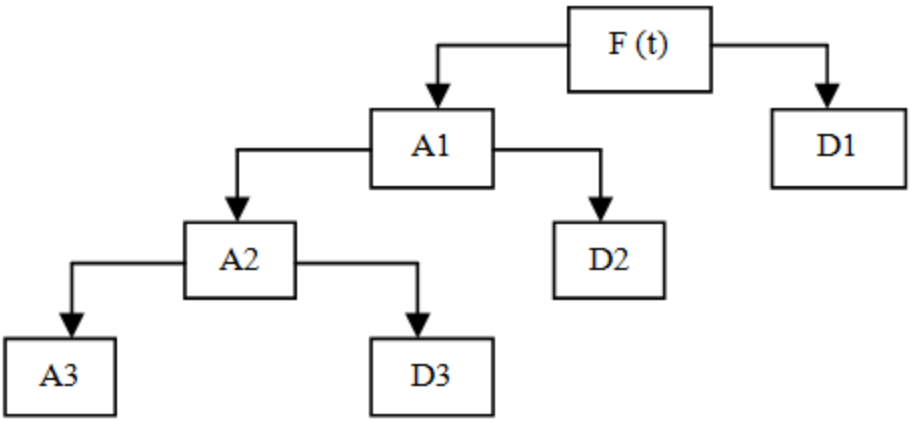

(a)

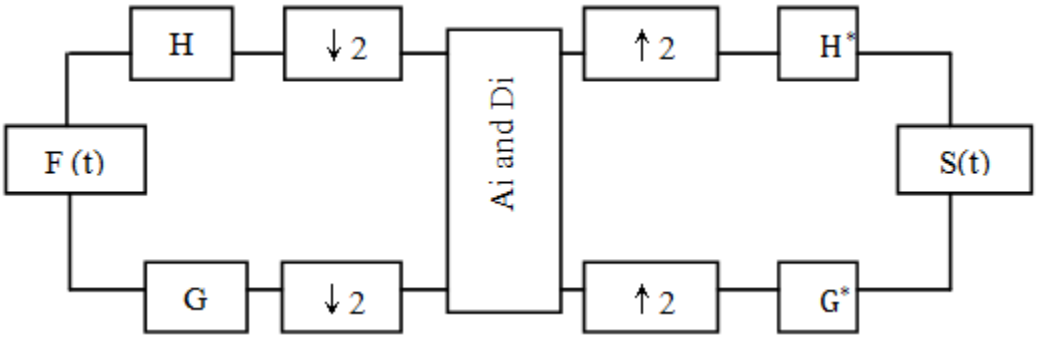

(b)

Fig 5.6 (a) The decomposition of the signal F(t). (b) The chart flow of the decomposition and reconstruction.

The Multi-Resolution Algorithm (MRA) is employed for the DWT to decompose the original signals into frequency and time scales. Fig 5.6 shows the procedure of decomposing signals using the MRA. A signal f(t) can be decomposed by:

$$f(t) = A_1+D_1 = A_2 + D_2 + D_1 = A_3+D_3+D_2+D_1 \quad (5.3.12)$$

where, A_i and D_i are the approximation and detail coefficients at the i level. The signal f(t) contains high and low frequency components which are represented by the approximation coefficient A_i and detail coefficients D_i.

The low frequency components represent the major characteristics of the signal while the high frequency components represent its detailed characteristics. Taking human voice signal for example, the content of the voice signal can be obtained from the low frequency component but this cannot be used to distinguish who is speaking. The high frequency components represent the detailed characteristics of the voice.

This procedure is equivalent to passing the signal f(t) to the high and low pass filter. In Fig 5.7 (b), H and G represent the low pass decomposition filter, the high pass decomposition filter, $\downarrow 2$ and $\uparrow 2$ represent the down-sampling and up-sampling. $H^*$and G^*denote the low and high pass reconstruction filter, respectively.

The signal F(t) is filtered by the high and low pass filter respectively and then sampled. The obtained signal is decomposed into the approximation and detail coefficients by using the MRA. The de-noising method is applied to the approximation and detail coefficients. After de-noising, a reconstruction procedure can be applied to reconstruct the signal. The detailed procedures are as follows:

1) Decompose the signal F(t) into the detail (Ai) and approximation coefficients (Di). The decomposition level depends on desired the signal-to-noise ratio (SNR).
2) After decomposing, an appropriate threshold can be selected to remove noise at each decomposing levels. The threshold can be a hard threshold or a soft threshold.

   The hard threshold can be represented as

$$D_{\varphi}(x) = \begin{cases} D(x), & |D(x)| > \beta \\ 0, & |D(x)| \leq \beta \end{cases} \qquad (5.3.13)$$

   where, β is the hard threshold. $D_{\varphi}(x)$ indicates the detail coefficient after de-noising using the threshold β.

   The soft threshold can be represented as

$$D_{\varphi}(x) = \begin{cases} \text{sign}\big(D(x)\big)(|D(x)| - \beta), & |D(x)| > \beta \\ 0, & |D(x)| \le \beta \end{cases} \quad (5.3.14)$$

where the soft threshold $\beta = \sigma\sqrt{2\log(N)}$, σ and N denote noise at this level and the length of soft threshold coefficients, respectively.

3) After applying steps (1-2), the de-noising procedure is finished. The next step is to reconstruct the signal F (t) using Inverse Wavelet Transform (IWT).

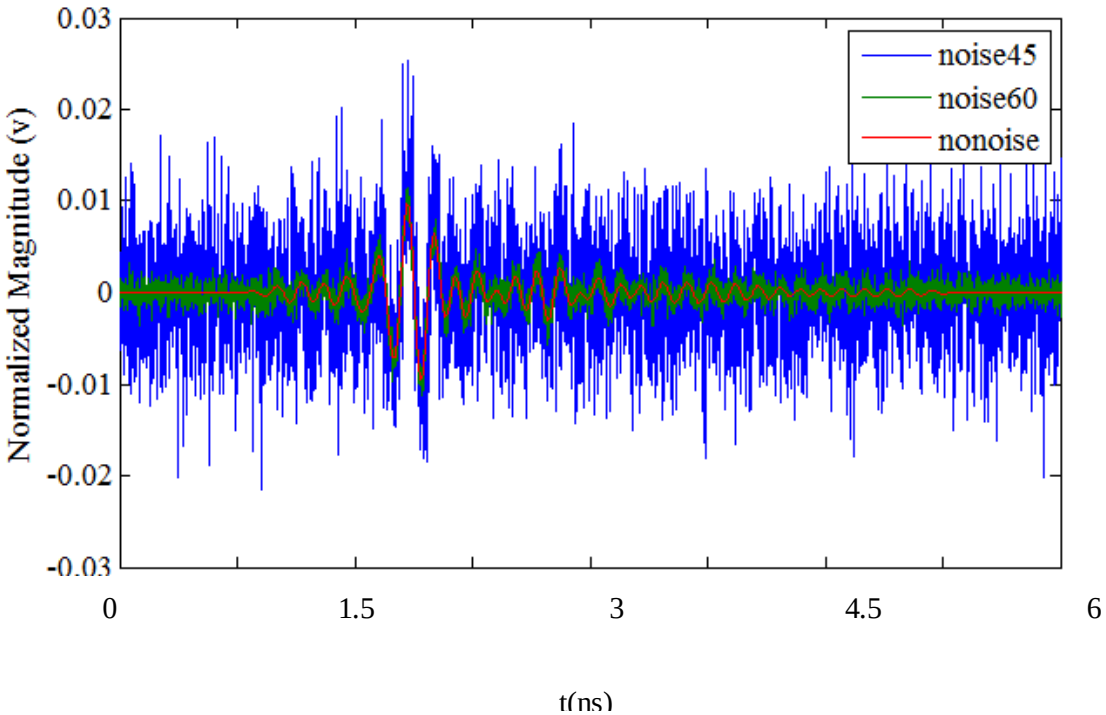

(a)

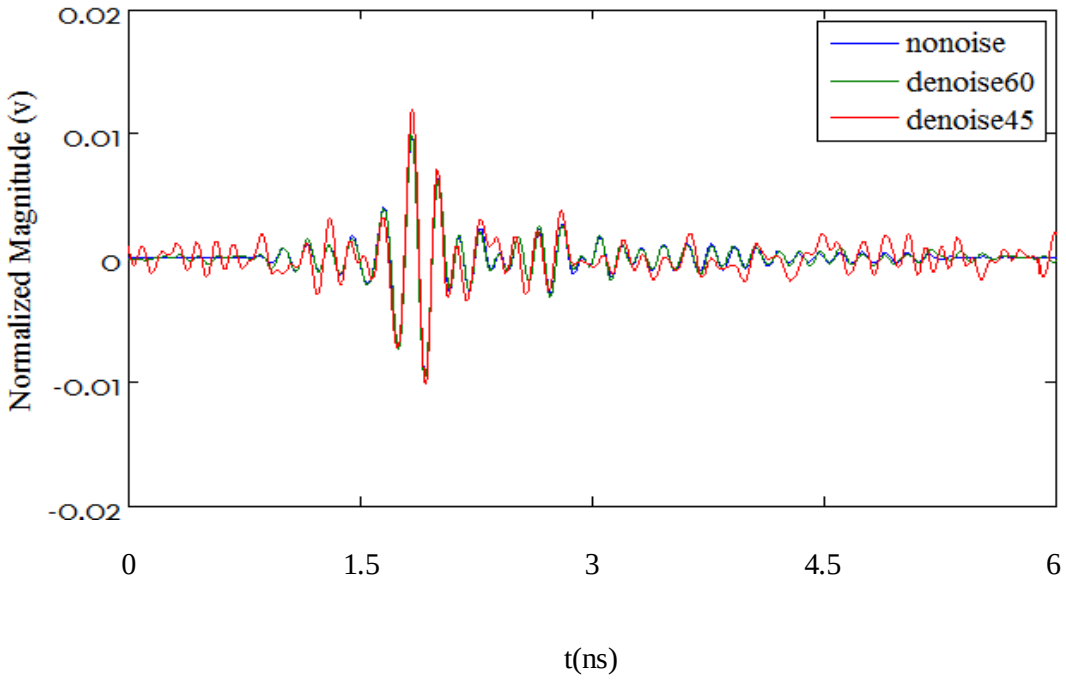

(b)

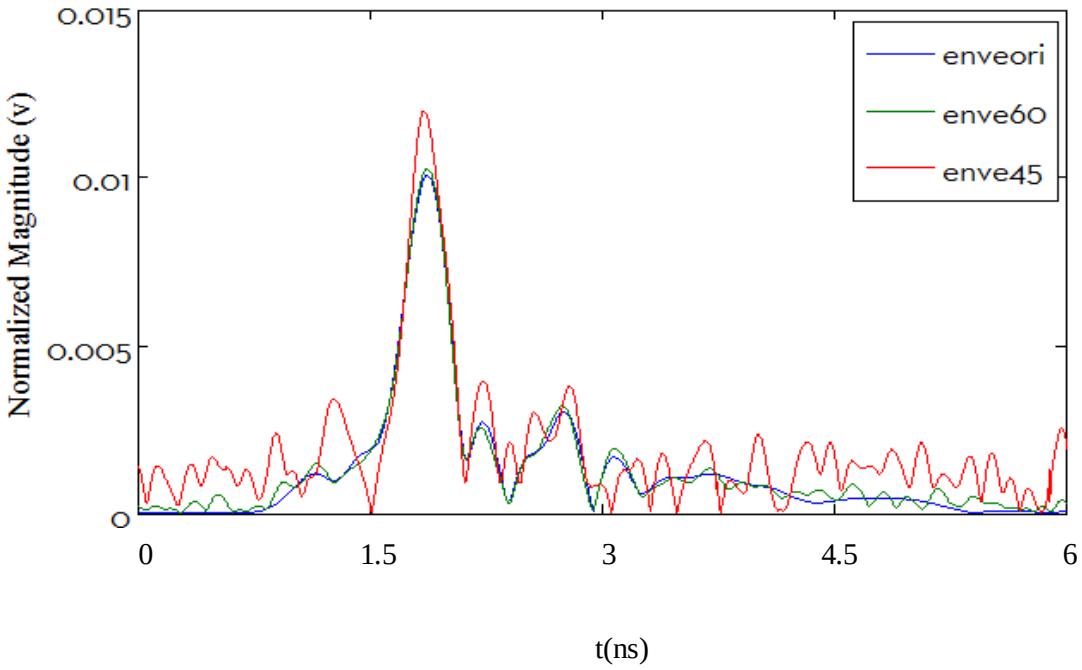

(c)

Fig 5.7 (a) The transient scattering signal (red curve), with noise added such that the SNRs are 60 dB (green curve) and 45 dB (blue curve) and (b) the signals after de-noising and (c) the envelop of the de-noised signals.

The DWT based de-noising method has been discussed and proposed. To verify the effectiveness of the DWT for the breast cancer detection, white Gaussian noise is added to degrade the transient scattering signal such that the SNRs of the signals are 60 dB and 45 dB, as shown in Fig 5.3.5 (a). In levels 1-5, the hard thresholds are setup to be 0.023, 0.022, 0.019, 0.025, and 0.035. Fig 5.3.5 (b-c) shows the signal after de-noising. It can be observed that these three curves have quite close profiles, which verifies the effectiveness of the DWT. However, the red curve (signal with SNR being 45 dB) still contains significant noise which could degrade the microwave images, and this is discussed in the next chapter.

5.4 Summary

The electromagnetic scattering mechanism to be used for the breast cancer detection is discussed. The singularity expansion method (SEM) for the breast cancer is then proposed. The natural response of the object only depends on its properties in terms of surface, material, relative permittivity and conductivity. Malignant and benign tumours have different morphologies, and this, causes different natural responses. This unique feature can be used to discriminate between malignant and benign tumours. The Hilbert Transform and the skin and clutters removal methods are then proposed to extract the tumour response part from the received signals. Finally, the white Gaussian noise is added to the received transient scattering signals. The wavelet de-noising method is proposed and used to de-noise the signals. The de-nosing results present that the wavelet de-noising method is an effective tool for the signal de-noising.

Chapter 6 Microwave imaging Results for Cancer Detection

This chapter considers the creation of the microwave images for the hemi-sphere breast phantom using the received transient signals. Microwave images are created based on the simulation and experimental results using the non-slot Vivaldi antenna and the slot Vivaldi antenna. The tumour buried depth is also studied. A multi bio-layer phantom which contains deeply and shallow buried tumours is simulated and measured using the Vivaldi antenna. A spectrum analysis method is proposed to distinguish between tumour depth differences. Besides, imaging results for the non-slot and slot Vivaldi antenna are also presented. Two cancerous breast phantoms are developed in the CST. One breast phantom contains a benign tumour and the other one contains a malignant tumour. The single antenna configuration is applied to these two phantoms and the microwave images are created first. The Singularity Expansion Method (SEM) for breast cancer detection is then applied to discriminate between benign and malignant tumours. Finally, a preliminary study of brain cancer detection is presented. A cancerous brain phantom is measured and imaged using the Vivaldi antenna, and the wavelet de-noising method is applied to suppress the noise.

6.1 The Microwave Imaging Results

The transient signal processing and signal de-noising have been discussed in Chapter 5. In this chapter, the imaging results based on the received signals are created. Based on the simulation and experimental result in Chapter 4, the conclusions

has drawn that the reflected energy increases when the antenna moves close to the tumour; otherwise, the reflected energy is reduced when the antenna moves away from the tumour. This is the basic principle which is used in this section to create the microwave images. The antenna moves to different locations surrounding the breast, with scattering signals recorded at each stop location. The intensities of the scattering signals are used to create the images.

Based on electromagnetic theory, the discontinuity of a boundary causes a strong reflection of an incident electromagnetic wave. The reflection level is highly dependent on dielectric differences. Hence, the strong reflection from the tumour is due to the high relative permittivity difference between cancerous and healthy tissue.

The microwave image of the breast cancer is an effective, visual method of cancer diagnosis. This section focuses on the creation of the breast cross-section images.

6.1.1 The Hemi-sphere Phantom

6.1.1.1 Single Antenna Configuration

The single antenna configuration has been discussed in Chapter 4. This single antenna configuration is based on a single antenna which moves to scan the breast phantom. The reflected transient signals are measured at each stopping position. The intensities of each reflected signals are used to create the images.

Fig 6.1 shows the single antenna configuration in the simulation and experimental work using the non-slot Vivaldi antenna and the slot Vivaldi antenna, respectively. The simulated images are created using the non-slot (Fig 6.2) and slot Vivaldi antenna (Fig 6.3) respectively, with the tumour being precisely located in x=0, y=0, z=45,

with little noise presented. The experimental imaging results (Fig 6.4 for non-slot Vivaldi antenna and Fig 6.5 for slot Vivaldi antenna) show greater noise due to the environmental interference. Besides, the use of the non-slot Vivaldi antenna provides clearer imaging results compared with the slot Vivaldi antenna in both simulation and experimental results. Overall, the imaging results are clear enough to indicate tumour position.

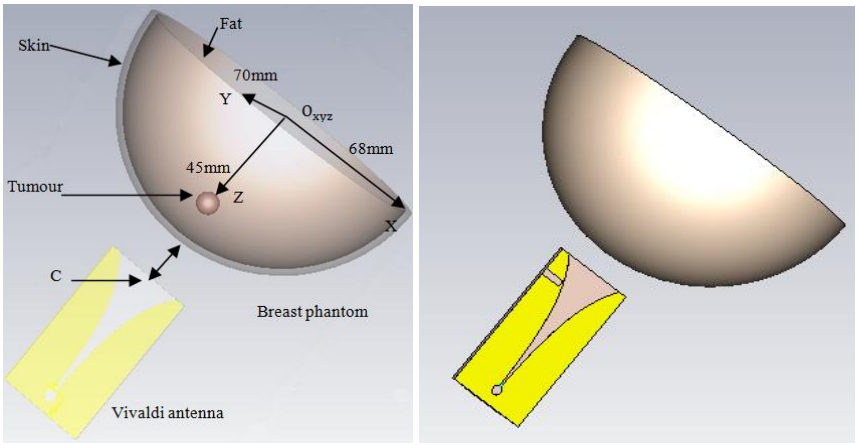

(a)

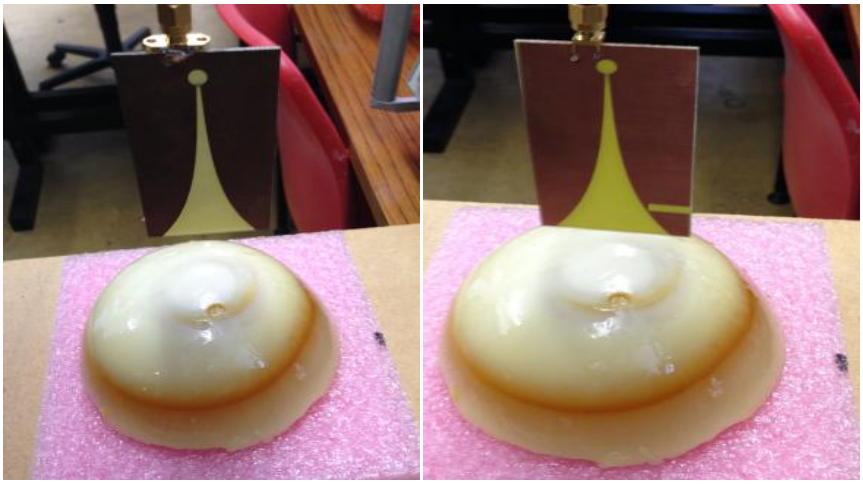

(b)

Fig 6.1 The single antenna configuration of (a) the simulation and (b) experimental work.

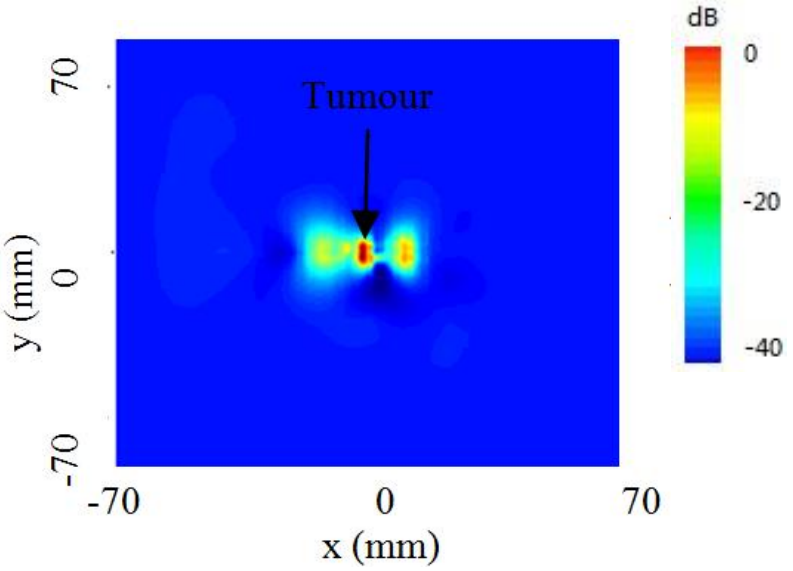
dB
0
-20
-40
Tumour
70
0
-70
y (mm)
-70
0
70
x (mm)

(a)

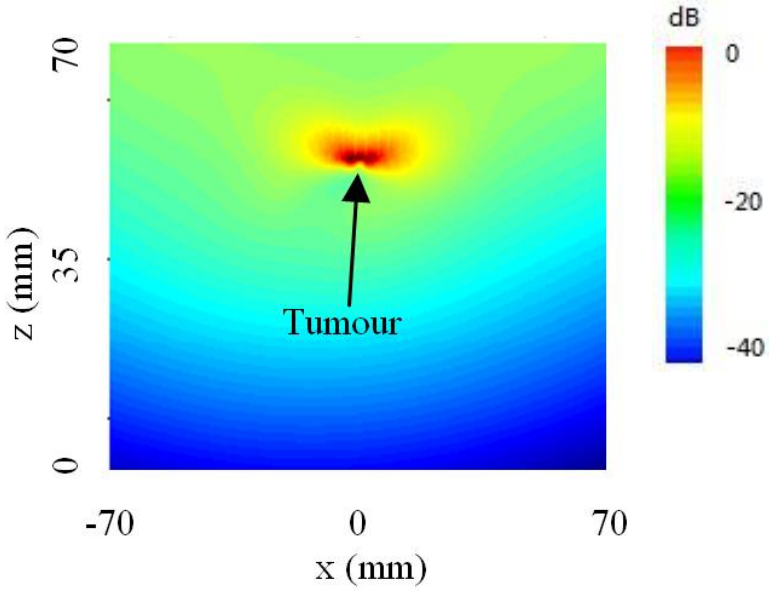
dB
0
-20
-40
Tumour
70
35
0
z (mm)
-70
0
70
x (mm)

(b)

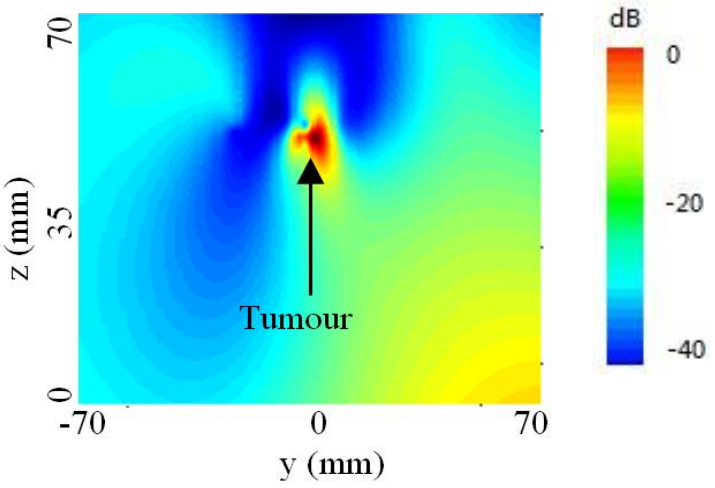

(c)

Fig 6.2 The simulated microwave images of the breast phantom based on the single antenna configuration (using the non-slot Vivaldi antenna) in (a) x-y plane, (b) x-z plane and (c) y-z plane.

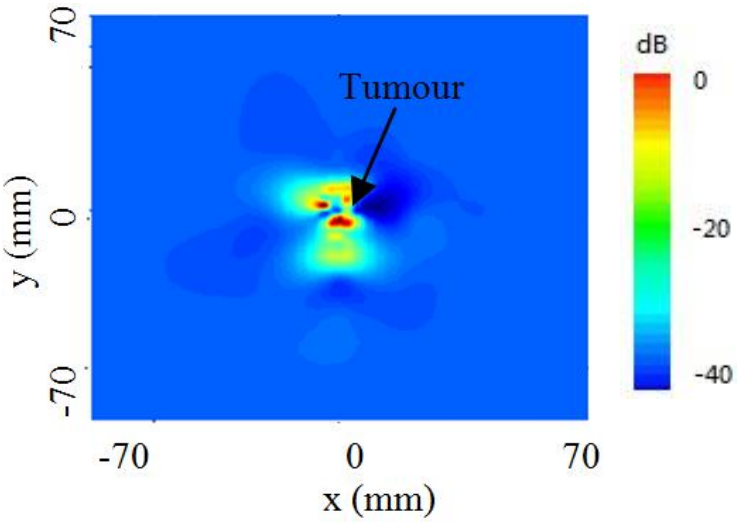

(a)

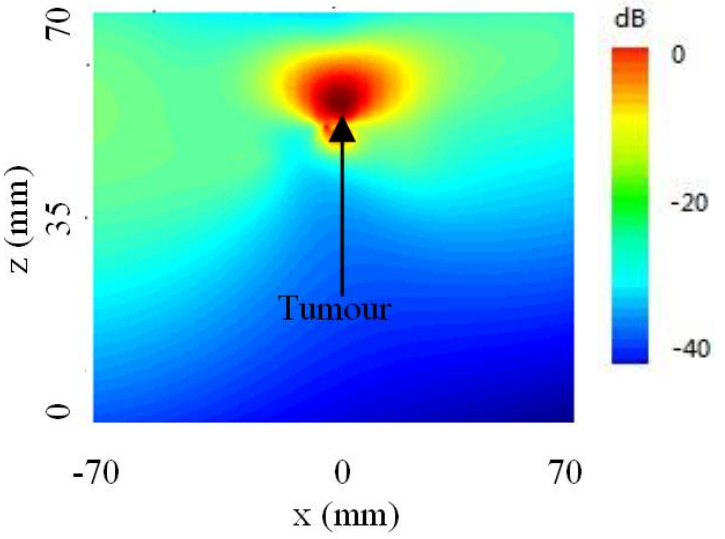

(b)

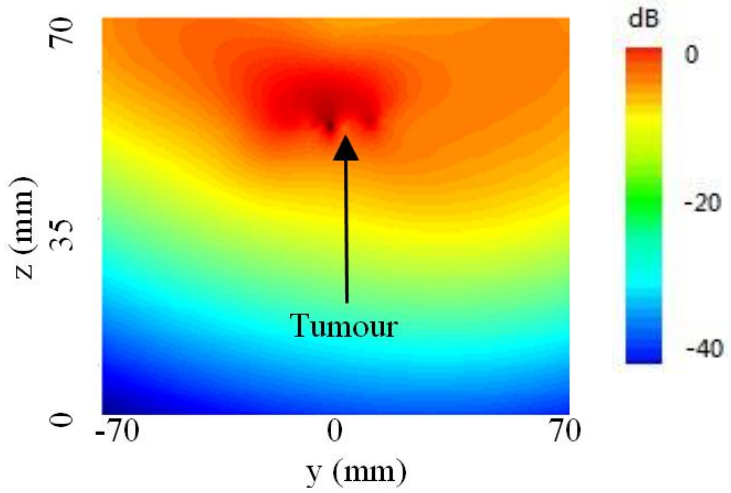

(c)

Fig 6.3 The simulated microwave images of the breast phantom based on the single antenna configuration (using the slot Vivaldi antenna) in (a) x-y plane, (b) x-z plane and (c) y-z plane.

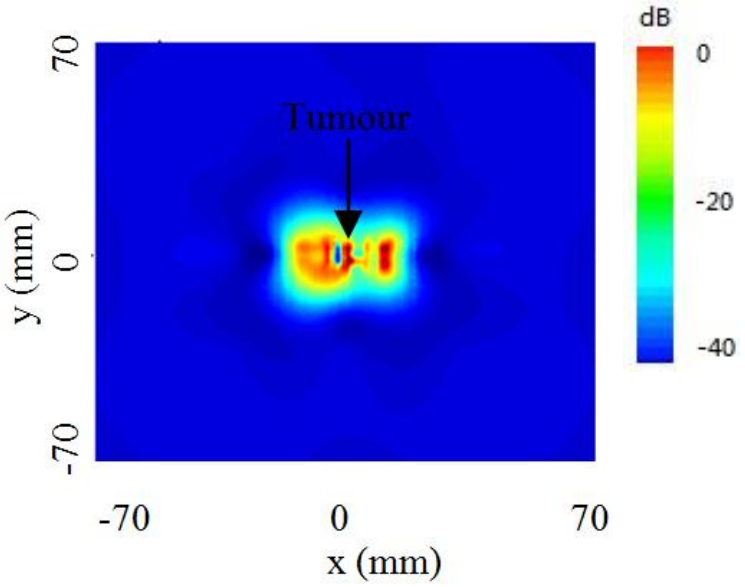
dB
0
-20
-40
Tumour
70
0
-70
y (mm)
-70
0
70
x (mm)

(a)

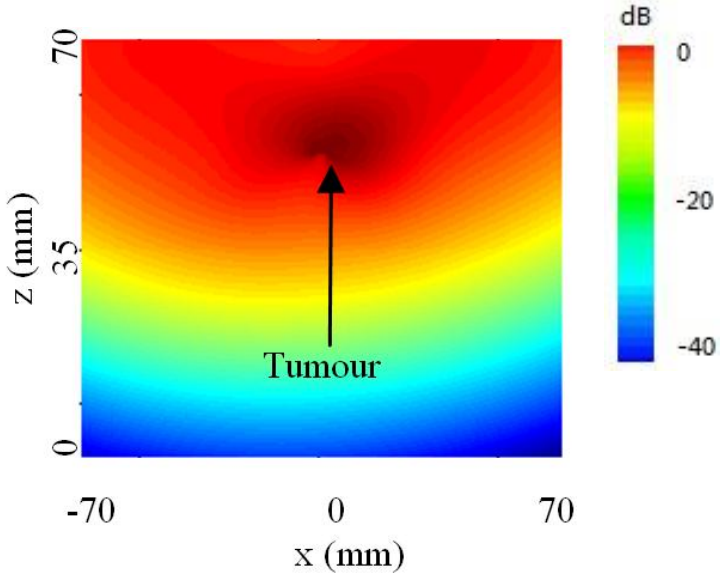
dB
0
-20
-40
Tumour
70
35
0
z (mm)
-70
0
70
x (mm)

(b)

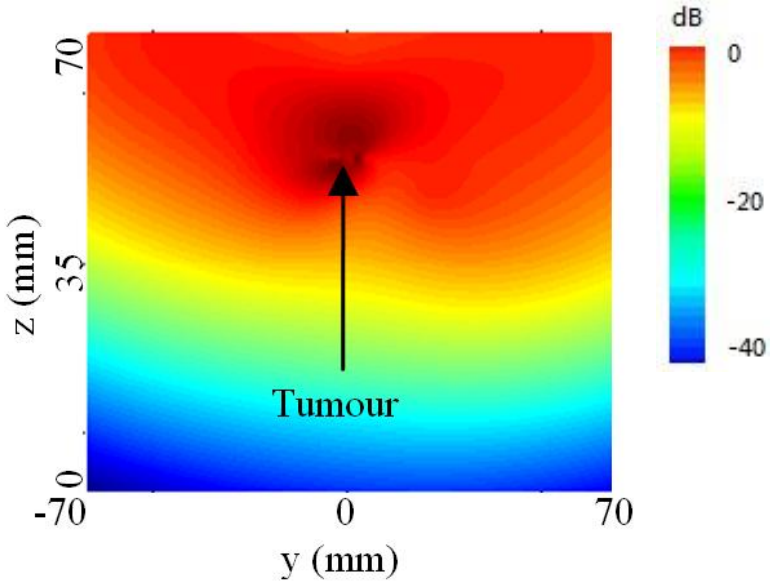

(c)

Fig 6.4 The experimental microwave images of the breast phantom based on the single antenna configuration (using the non-slot Vivaldi antenna) in (a) x-y plane, (b) x-z plane and (c) y-z plane.

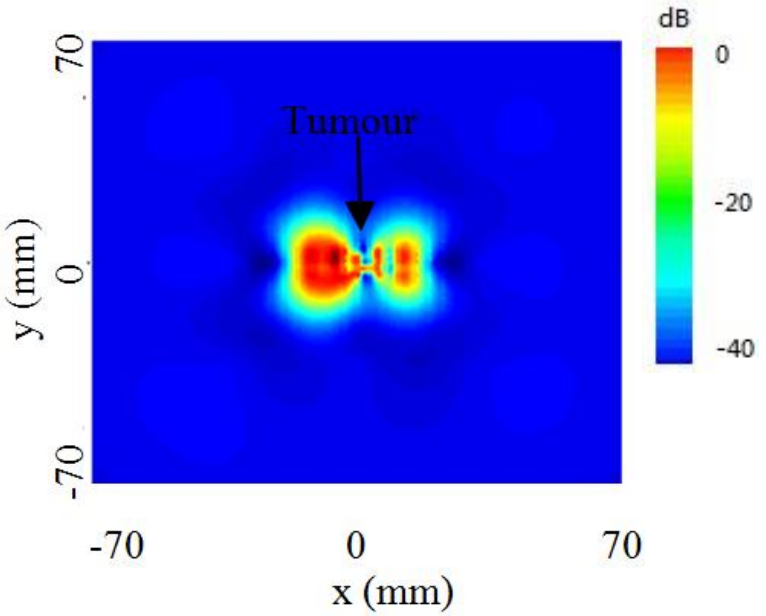

(a)

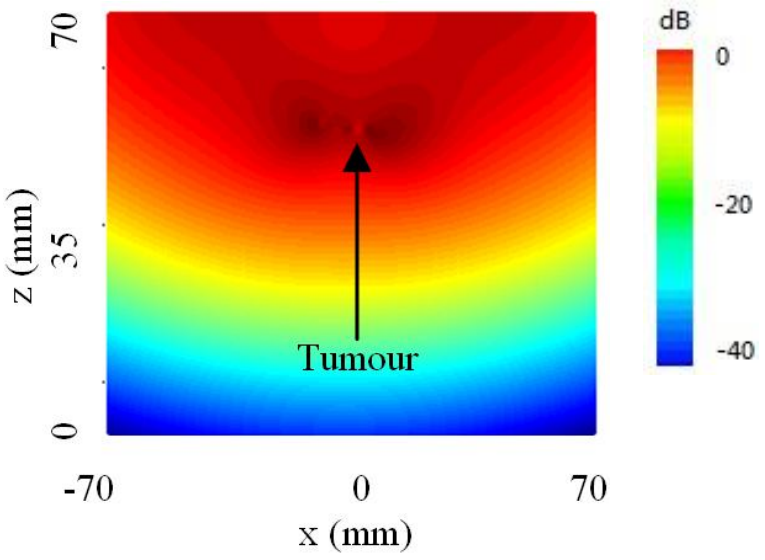

(b)

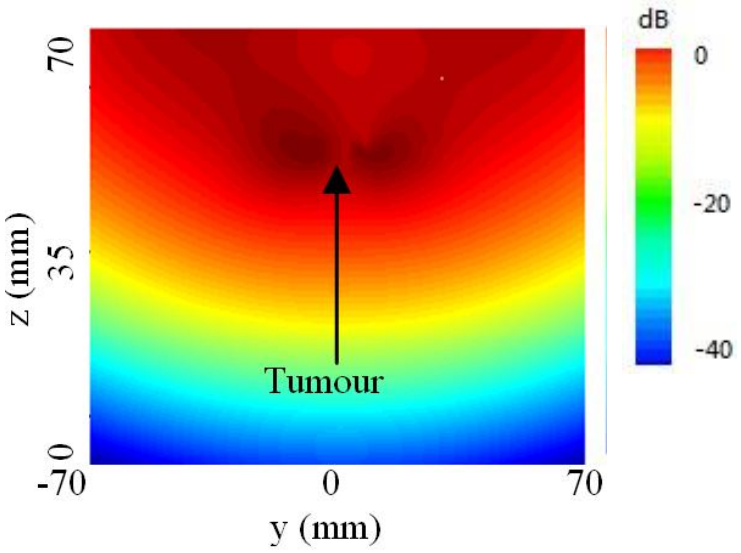

(c)

Fig 6.5 The experimental microwave images of the breast phantom based on the single antenna configuration (using the slot Vivaldi antenna) in (a) x-y plane, (b) x-z plane and (c) y-z plane.

6.1.1.2 Antenna Pair Configuration

The antenna pair configuration is presented in Fig 6.6, Fig 6.7 and Fig 6.8 show the simulated microwave images based on the non-slot and slot Vivaldi antennas. Fig 6.9 and Fig 6.10 show the experimental microwave images based on the non-slot and slot Vivaldi antennas. The simulation images are still clear enough to indicate the position of tumour but more noise gathers surrounding the tumour compared with the images from single antenna configuration (Fig 6.2 - Fig 6.5). The use of the non-slot Vivaldi antenna also provides clearer imaging results than that of the slot Vivaldi antenna. However, the experimental images also show some fake points. The intensities of these fake points are close or even stronger than those of the tumour, which could cause misunderstandings of the real position of the tumour.

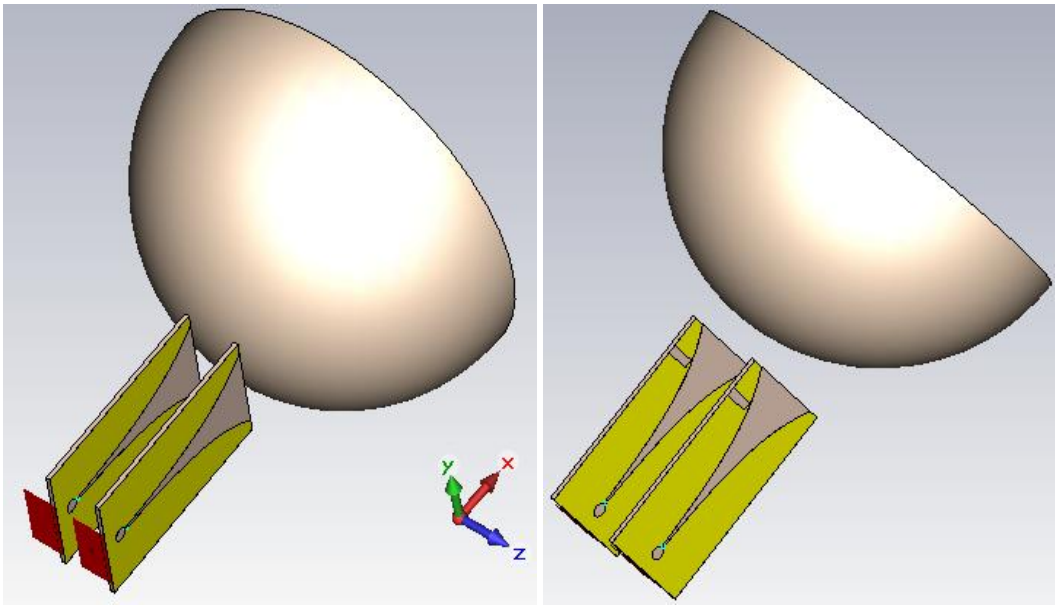

(a)

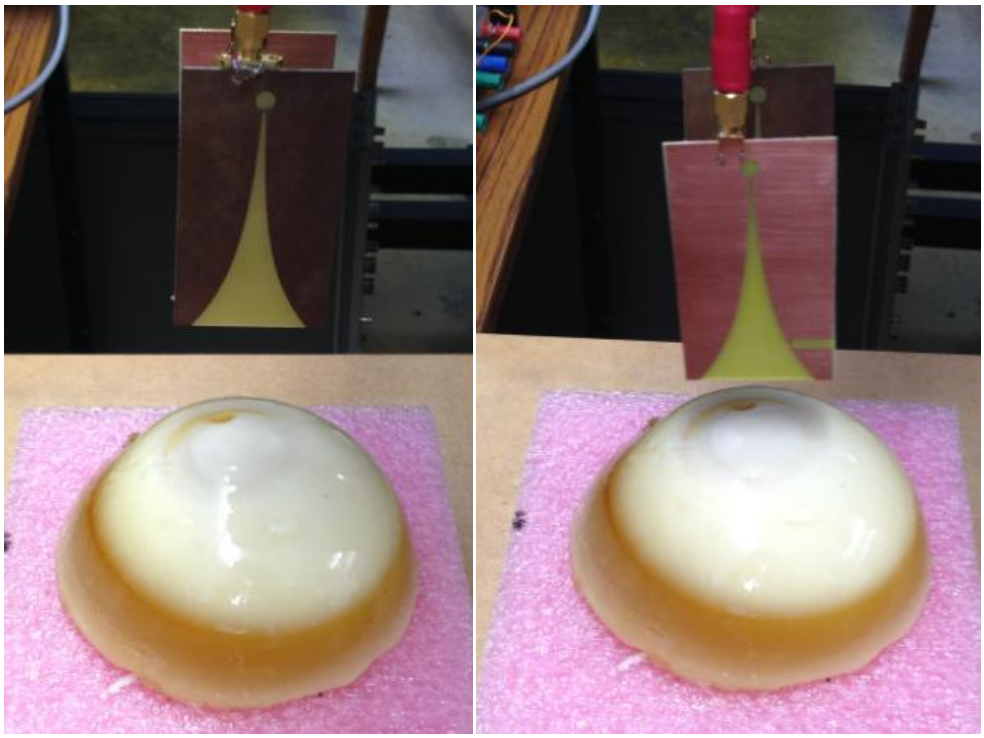

(b)

Fig 6.6 The antenna pair configuration of (a) the simulation and (b) experimental work.

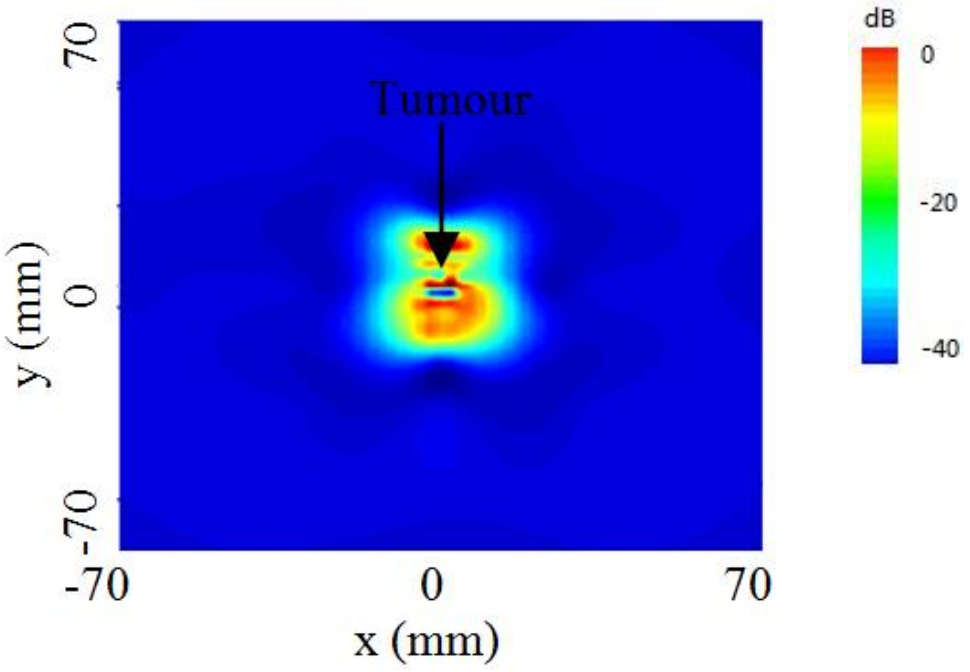
Tumour
70
0
-70
y (mm)
-70
0
70
x (mm)
dB
0
-20
-40

(a)

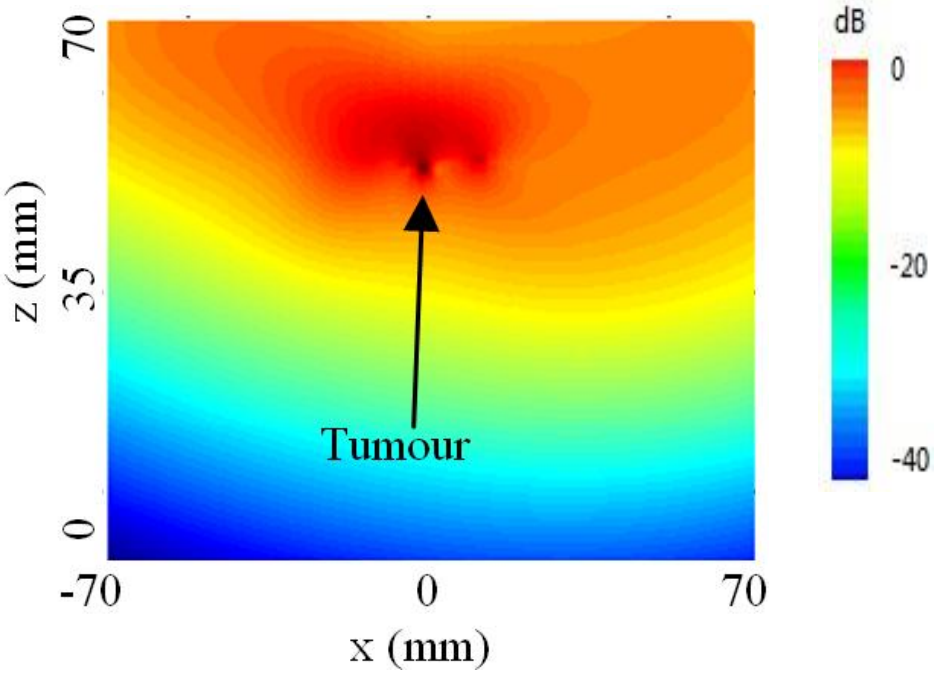
70
35
0
z (mm)
Tumour
-70
0
70
x (mm)
dB
0
-20
-40

(b)

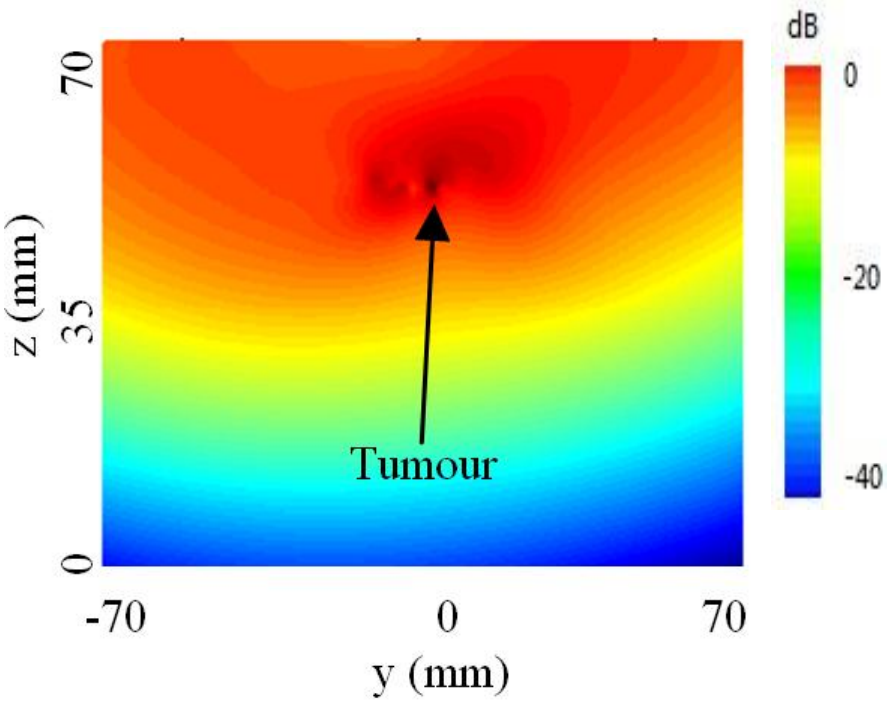

(c)

Fig 6.7 The simulated microwave images of the breast phantom based on the antenna pair configuration (using the non-slot Vivaldi antenna) in (a) x-y plane, (b) x-z plane and (c) y-z plane.

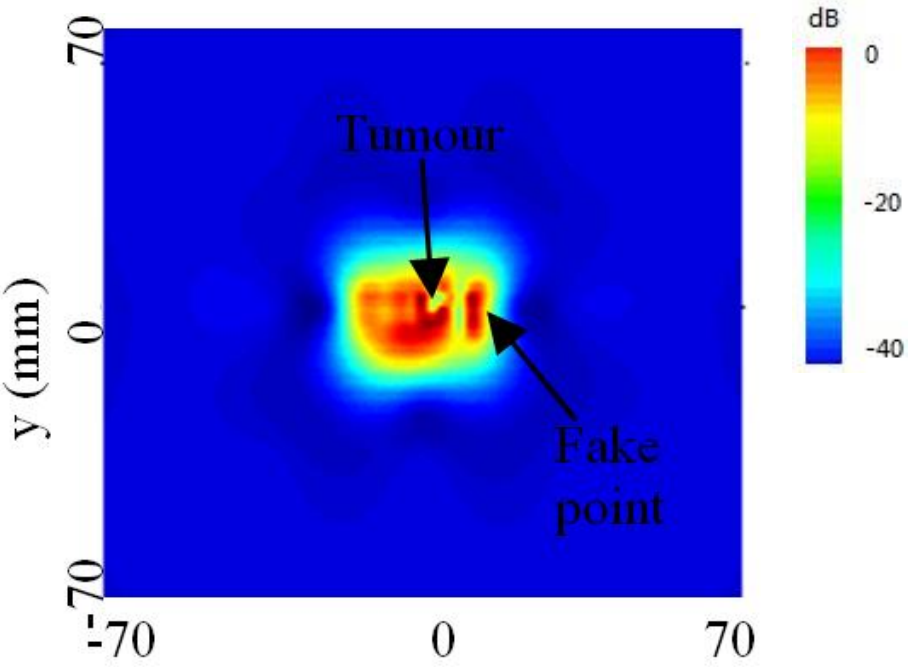
dB
0
-20
-40
Tumour
Fake
point
y (mm)
70
0
-70
-70
0
70

(a)

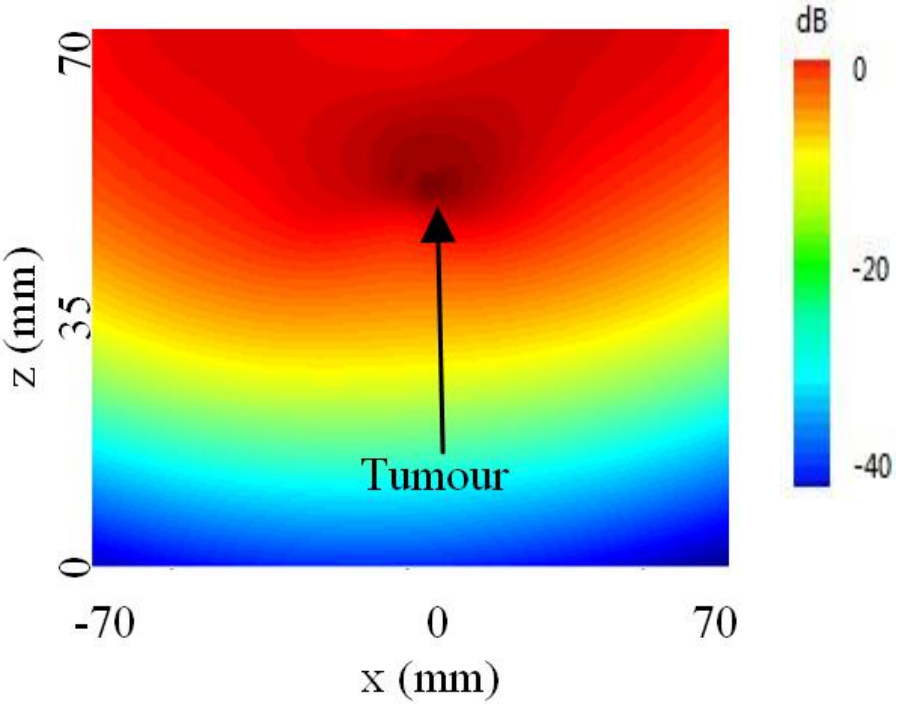
dB
0
-20
-40
Tumour
z (mm)
70
35
0
-70
0
70
x (mm)

(b)

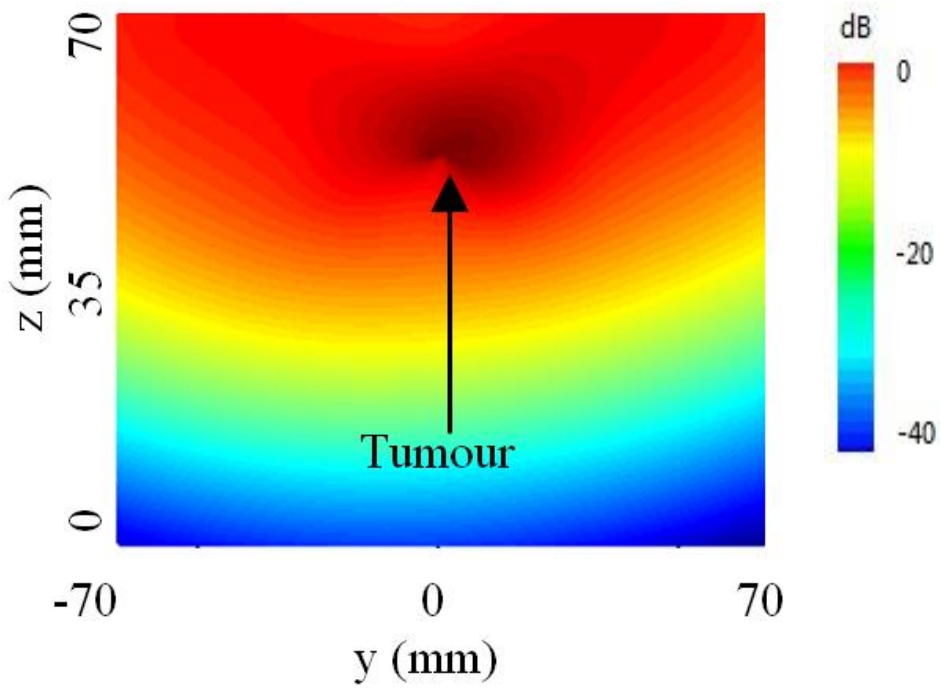

(c)

Fig 6.8 The simulated microwave images of the breast phantom based on the antenna pair configuration (using the slot Vivaldi antenna) in (a) x-y plane, (b) x-z plane and (c) y-z plane.

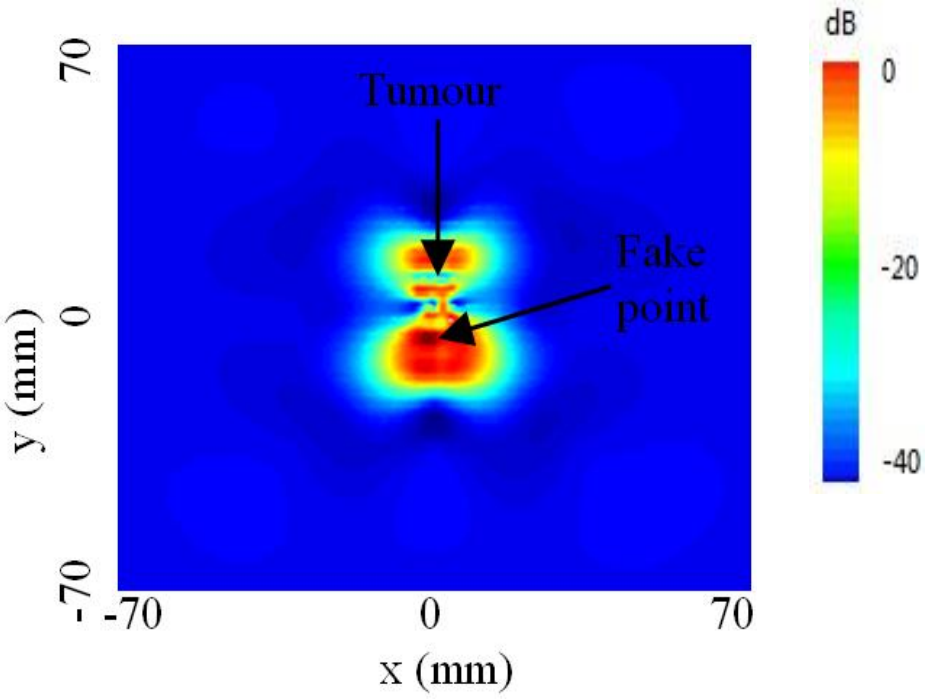
dB
0
-20
-40
Tumour
Fake
point
70
0
-70
y (mm)
-70
0
70
x (mm)

(a)

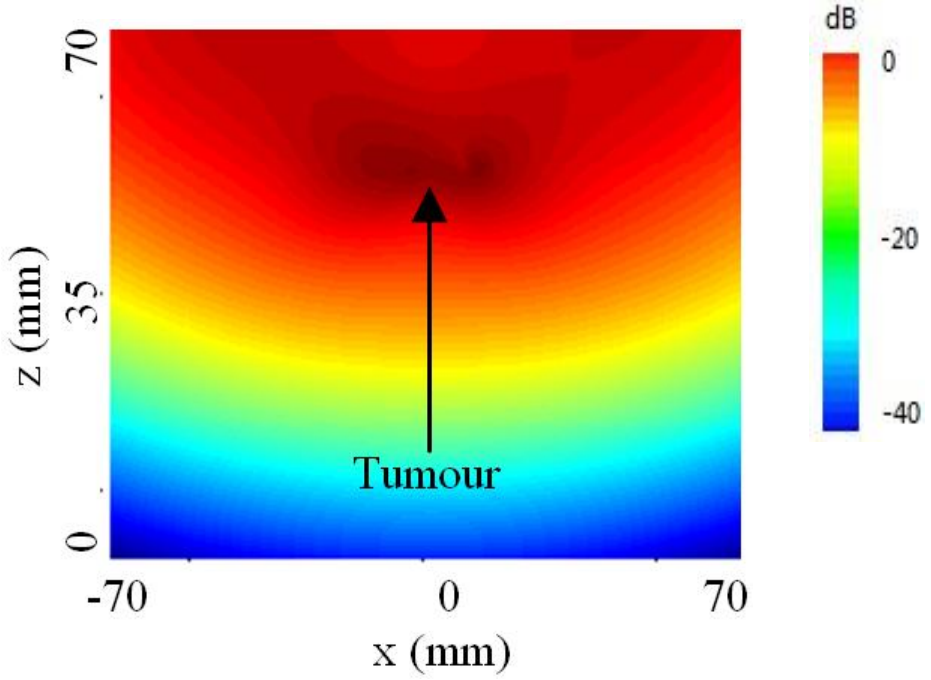
dB
0
-20
-40
70
35
0
z (mm)
Tumour
-70
0
70
x (mm)

(b)

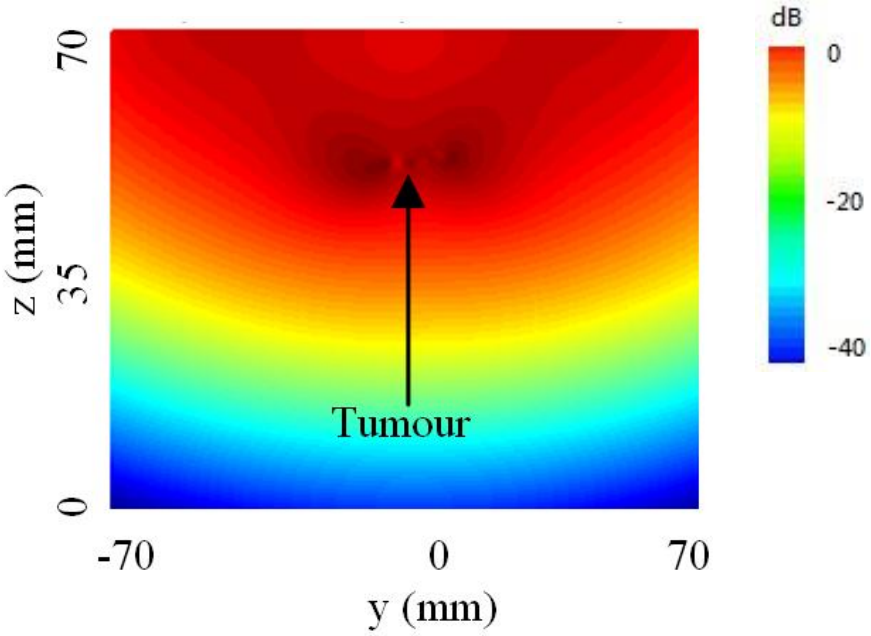

(c)

Fig 6.9 The experimental microwave images of the breast phantom based on the antenna pair configuration (using the non-slot Vivaldi antenna) in (a) x-y plane, (b) x-z plane and (c) y-z plane.

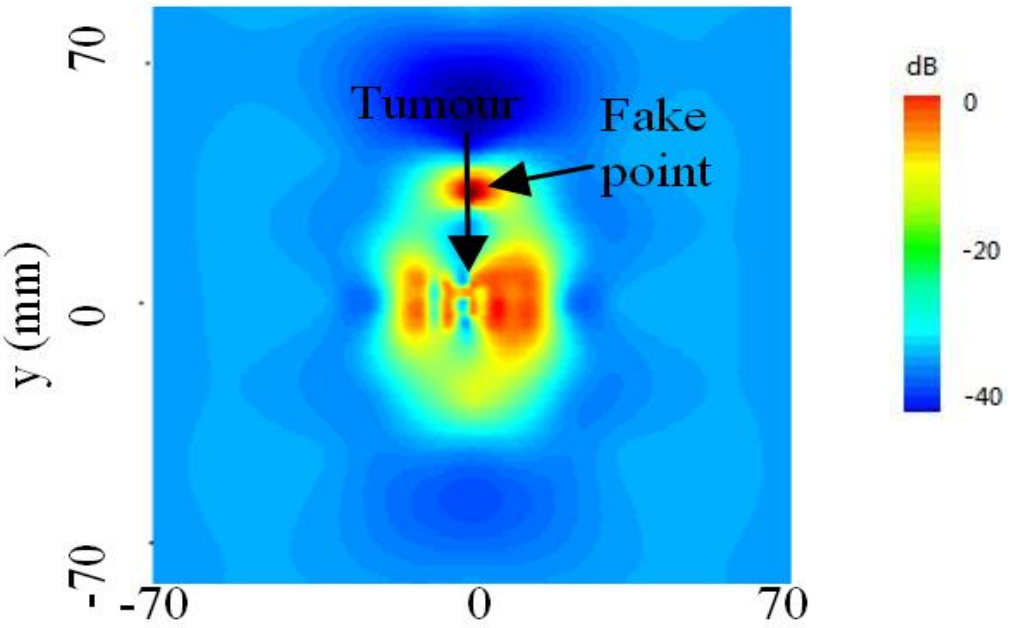
Tumour
Fake
point
dB
0
-20
-40
y (mm)
70
0
-70
-70
0
70

(a)

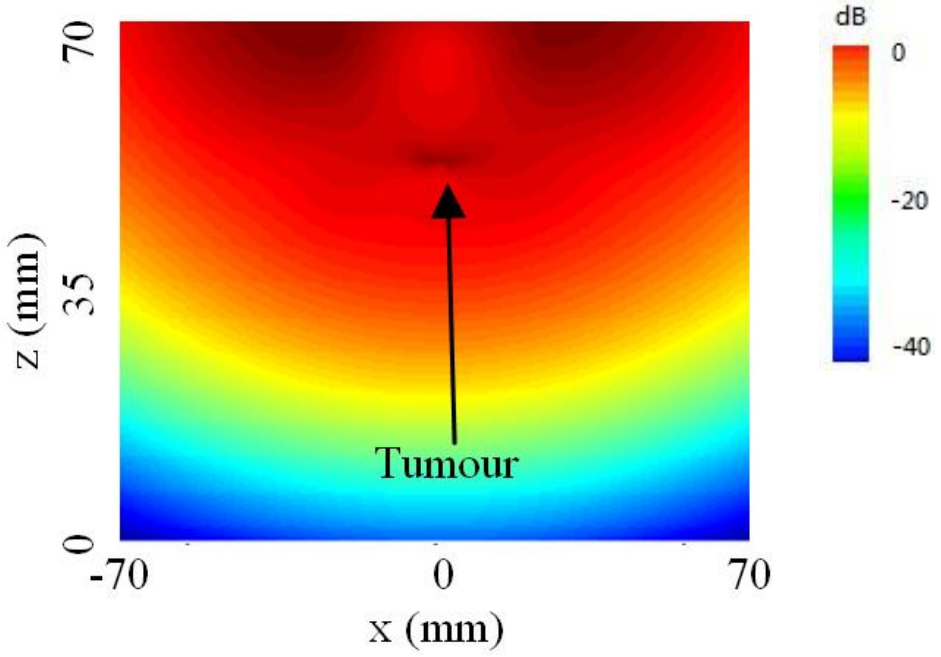
dB
0
-20
-40
z (mm)
70
35
0
Tumour
-70
0
70
x (mm)

(b)

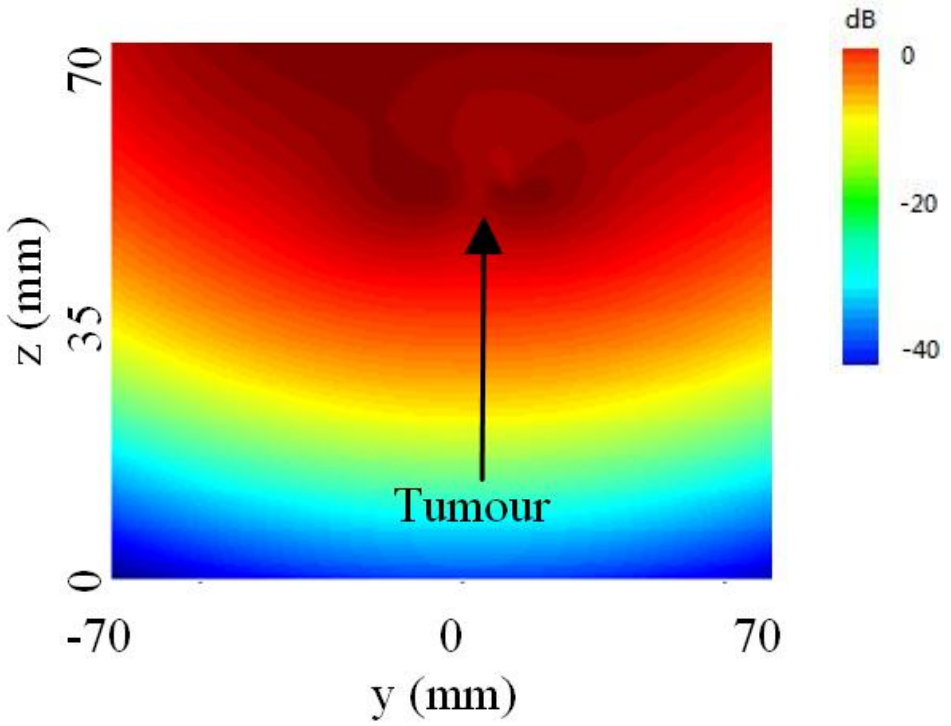

(c)

Fig 6.10 The experimental microwave images of the breast phantom based on the antenna pair configuration (using the slot Vivaldi antenna) in (a) x-y plane, (b) x-z plane and (c) y-z plane.

6.1.1.3 Signal-to-Noise Ratio (SNR) and Discussion

The microwave images are created based on the simulation and experimental work using the non-slot Vivaldi antenna and the slot Vivaldi antenna. Another quantitative measurement of the image quality can be presented using Signal-to-Noise Ratio (SNR) which can be defined as the ratio between the strongest intensity of the tumour to that of the noise. Table 6.1 shows the calculated SNR for the simulated and experimental results using the non-slot Vivaldi and slot Vivaldi antennas. It is worth noting that the presence of fake points is not considered before calculating the SNR.

Table 6.1Signal-to-Noise Ratio (SNR)

Signal-to-Noise Ratio (dB)	Simulated images		Experimental images	
	Non-slot	Slot	Non-slot	Slot
Single antenna	6.8	6.2	1.2	0.9
Antenna pair	5.7	4.3	0.6	0.3

The use of the SNR provides a quantitative description of the imaging quality. It is concluded that the single antenna configuration and the non-slot Vivaldi antenna provide a higher SNR.

6.2 The Study of Tumour Buried Depth

For breast cancer detection, information on the tumour buried depth can be derived from the 3-D images. However, the creation of the 3-D images is based on the particular shape of the breast which can be approximated as a hemi-sphere. In some other cancer detections such as for stomach cancer, pancreatic cancer and lung cancer, the 3-D images are quite difficult to obtain due to the complex structure of human body. Hence, one of the major challenges in UWB based breast cancer detection is the extraction of the tumour depth information (TDI). However, very few studies have been published on the investigation of the TDI. The major challenge is that scatter signals from different depths of tumours are too close to be distinguishable. In this section, we first propose a multi bio-layer phantom. This phantom consists of a skin and fat layer, with two tumours buried at different depths, as shown in **Fig 6.11**. The mono-static radar system using the non-slot Vivaldi antenna is then used to measure

this breast phantom, with scattered signals recorded. These scattered signals are used to create breast cross-section images, with the tumours highlighted. Finally, the TDI is extracted by analysing the frequency spectrum of the scattered signals.

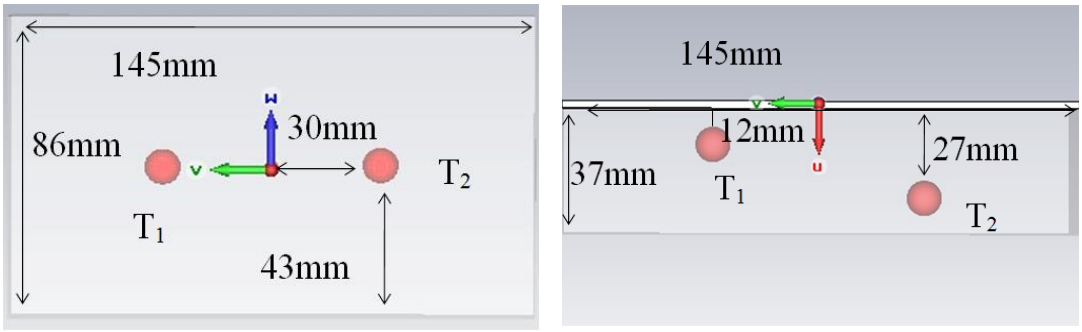

Fig 6.11 The simulated breast phantom with two tumours embedded in different depth.

The Vivaldi antenna is moved to scan this phantom, with 64 sets of scattered time domain signals (O21) recorded. These recorded signals are used to create a 2-D breast phantom cross-section image, with the tumours highlighted. **Fig 6.12** (a) shows the simulated 2-D image, with two tumours highlighted in the correct positions. However, the tumour depth information (TDI) is not available in these 2-D images. Hence, the spectrum information of the tumour reflections can be analysed to determine the TDI. **Fig 6.12** (b) shows the received signals (O1 and O2) when the Vivaldi antenna moves close to these two tumours (T1 and T2). The skin reflections and clutters of these two signals are eliminated first using time windows. However, it is still difficult to distinguish between the amplitude differences of these two tumours due to the weak tumour response, as seen in **Fig 6.12** (c). Hence, the spectrums of the tumour reflection are calculated and shown in **Fig 6.12** (d). As seen, the magnitude of the shallow buried tumour (T1) is stronger than that of the more deeply buried tumour (T2), especially

from 4 to 8 GHz. This is due to the high attenuation ratio in the lossy medium, especially at high working frequency. It is also calculated that the 15 mm depth difference between the two tumours causes a mean change of 0.3 dB in the magnitude of the spectrum, ranging from 4 to 10 GHz. This information can be used as an effective tool for determining tumour depth information.

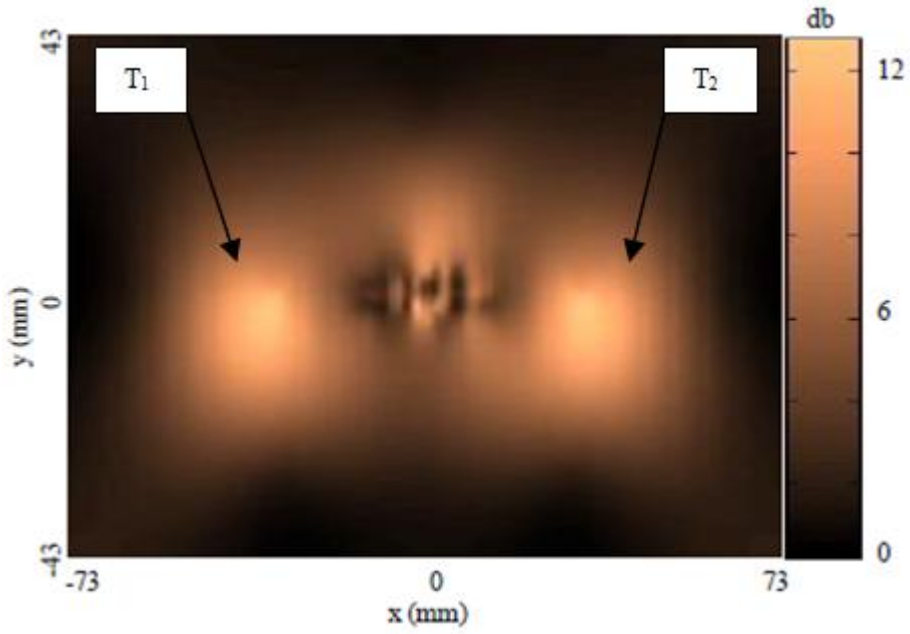

(a)

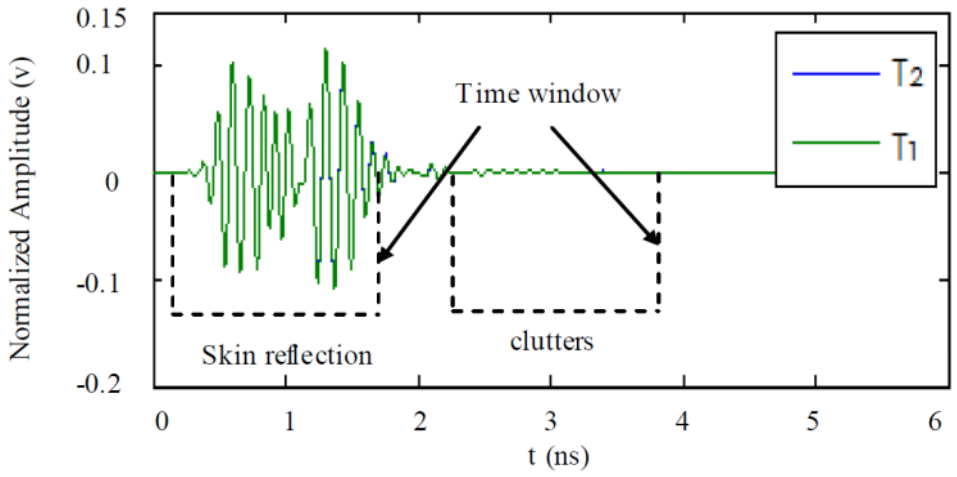

(b)

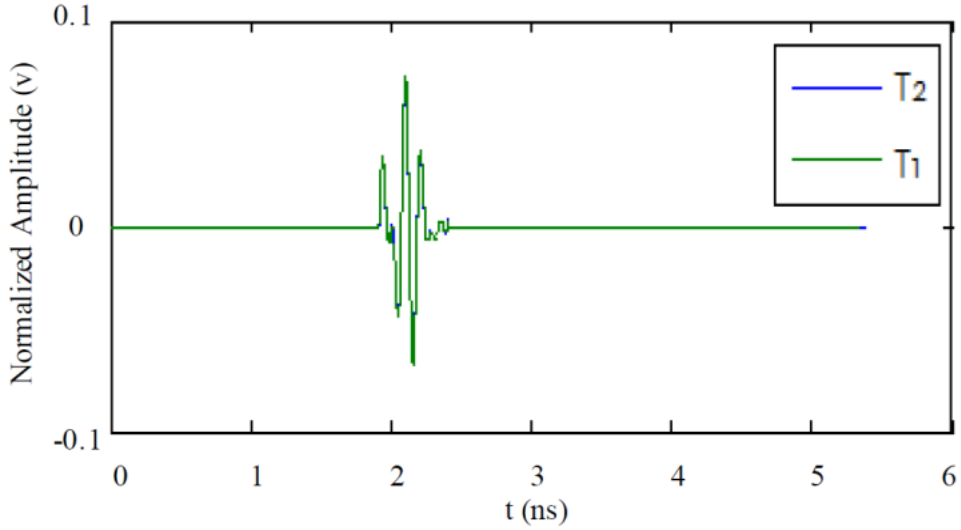

(c)

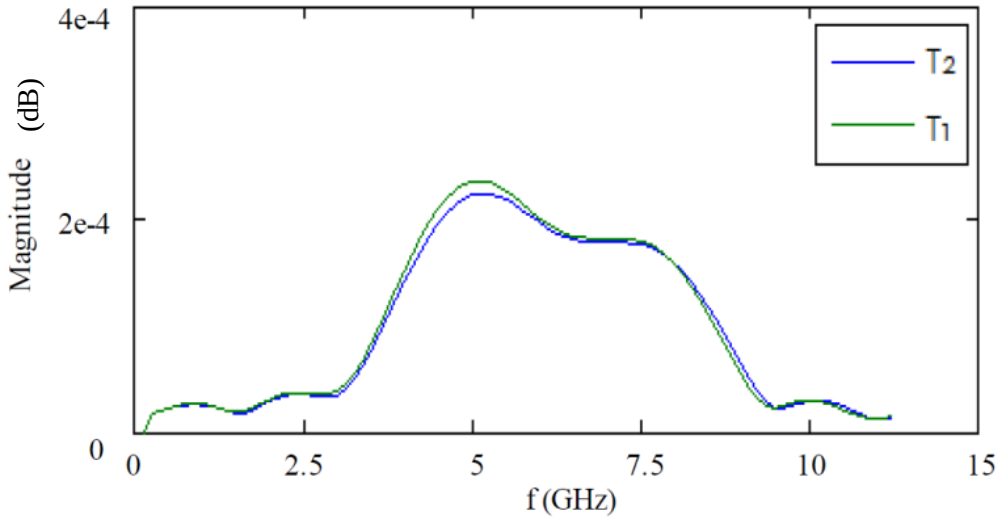

(d)

Fig 6.12 (a) The received signals of the shallow and deeply buried tumours and (b) the tumour scattering responses with skin and clutter eliminated and (c) the spectrum of tumour response.

Another experiment is also carried out based on the non-slot Vivaldi antenna and the slot Vivaldi antenna. The slot Vivaldi antenna provides a wider bandwidth (3-10

GHz) compared with the non-slot Vivaldi antenna (5-10 GHz). Theoretically, the lower frequency component of the electromagnetic wave provides stronger penetrating ability, which means that the use of the slot Vivaldi antenna could have the advantages of being able to detect deeply buried tumours. **Fig 6.13** (a) and (b) show the resulting images based on the non-slot and slot Vivaldi antennas respectively. As seen, the deeply buried tumour is still difficult to distinguish from the images. However, the use of the slot Vivaldi antenna provides an image with lower noise due to the wider bandwidth as well as the lower frequency components. As the imaging results, the use of slot Vivaldi antenna cannot provide a clearer imaging compared with the use of the non-slot Vivaldi antenna. However, the use of the slot Vivaldi antenna provides an image with lower noise when measuring tumours with different depth due to the wider bandwidth as well as the lower frequency components. Hence, the slot Vivaldi antenna can be used when measuring and distinguishing the duo tumours with different depth.

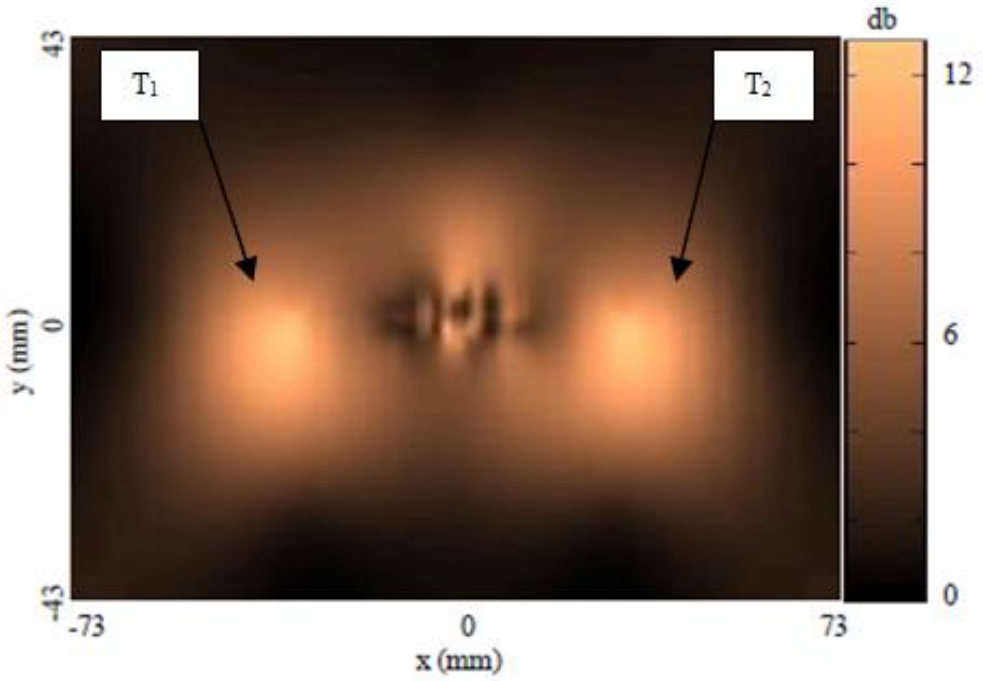

(a)

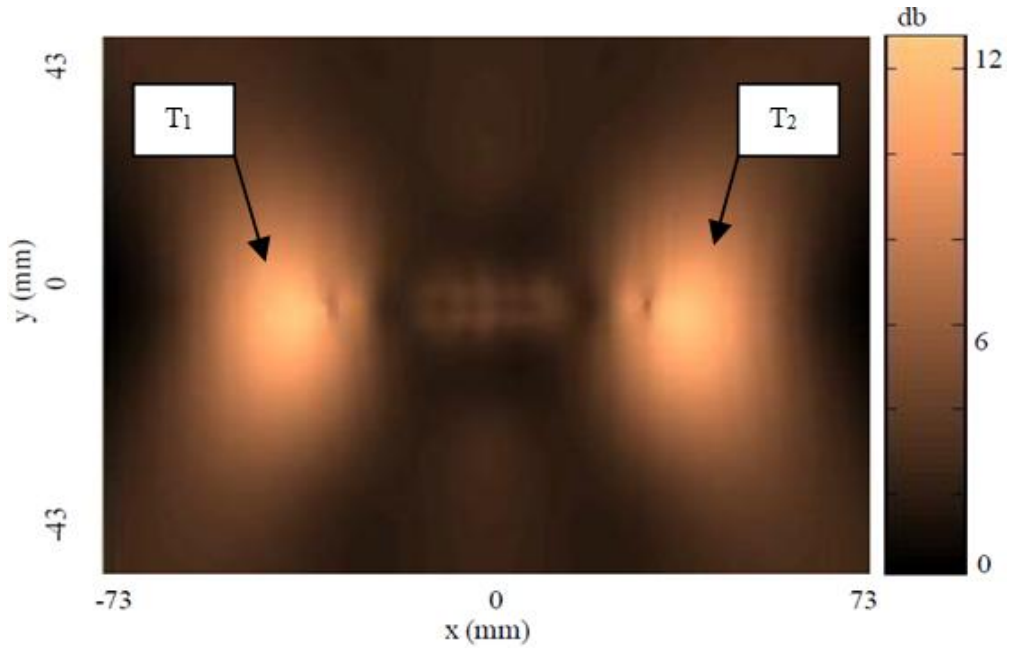

(b)

Fig 6.13 the microwave images based on (a) the non-slot Vivaldi antenna and (b) slot Vivaldi antenna.

6.3 The Discrimination between Benign and Malignant Tumour

In Chapter 5, the Singularity Expansion Method (SEM) has been investigated. The SEM is used to extract the complex natural responses (CNRs) of the illuminated object (tumour) in order to distinguish the morphology of the tumour. The CNRs of the tumour only depends on its properties, such as shape and electrical properties. The morphology of the tumour is an important factor in discriminating between benign and malignant tumours. A malignant tumour usually has a more irregular surface and a benign tumour has a very smooth surface. Hence, the CNRs of benign and malignant tumours can be used to distinguish between them.

Fig 6.14 (a) shows the designed benign and malignant tumour. The benign tumour has a radius of 5mm while the malignant tumour has an irregular surface with an average radius of 5mm. The single antenna configuration shown in **Fig 6.14** (b) is applied to these two phantoms, with microwave images created and shown in **Fig 6.15** (a-f).

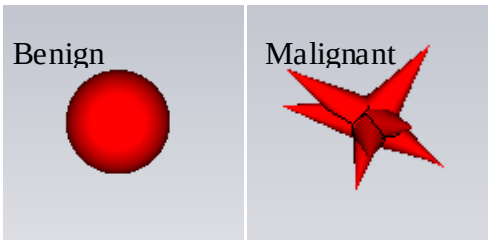

(a)

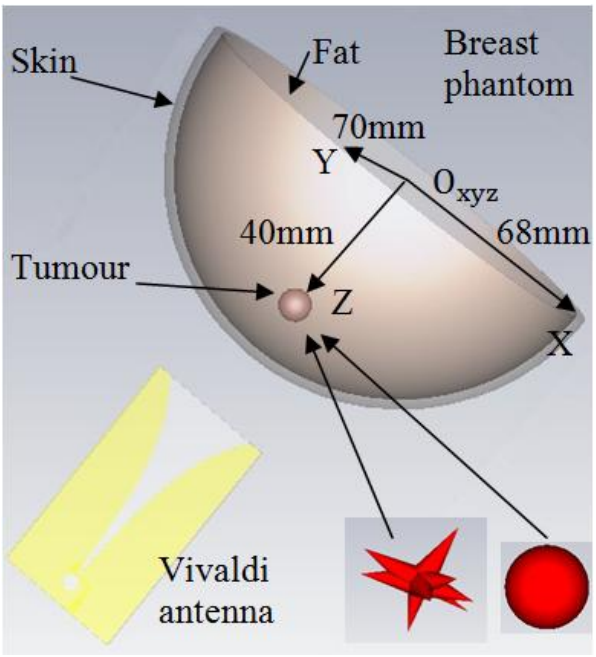

(b)

Fig 6.14 (a) Benign and malignant tumours, (b) the single antenna configuration.

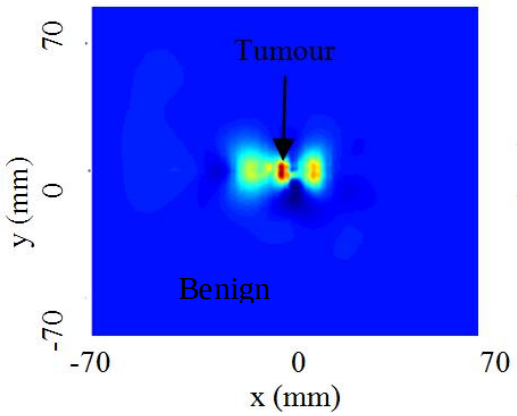
Tumour
Benign
70
0
-70
y (mm)
-70
0
70
x (mm)

(a)

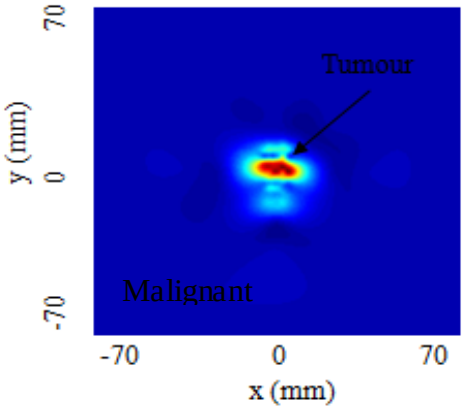
Tumour
Malignant
70
0
-70
y (mm)
-70
0
70
x (mm)

(b)

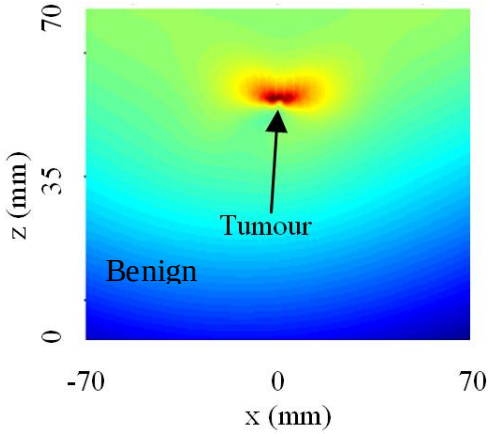
Tumour
Benign
70
35
0
z (mm)
-70
0
70
x (mm)

(c)

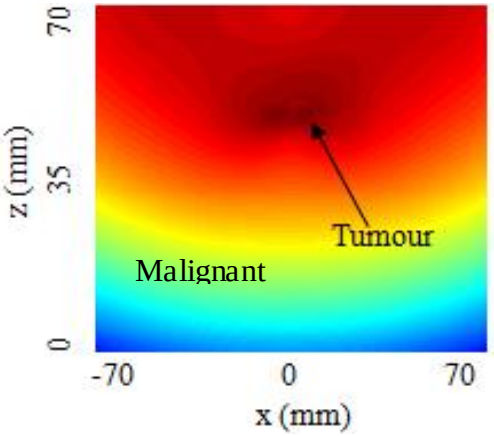
Tumour
Malignant
70
35
0
z (mm)
-70
0
70
x (mm)

(d)

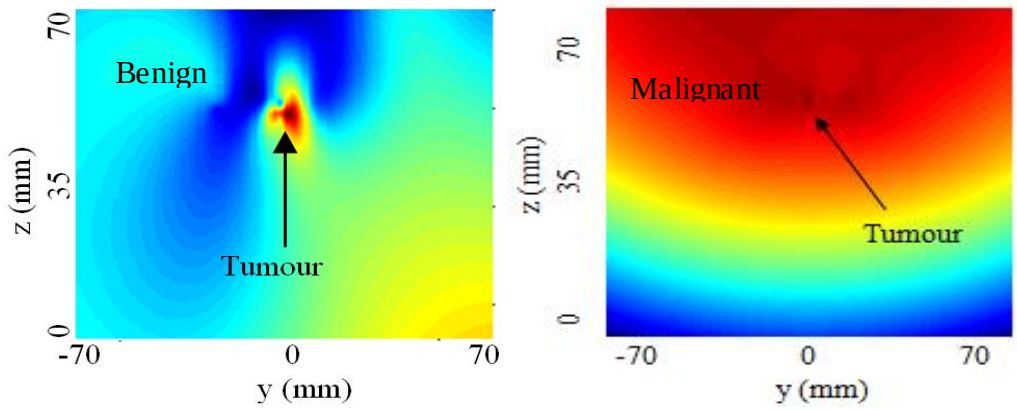

(e) **(f)**

Fig 6.15 The simulated microwave images of the benign and malignant tumours in (a-b) x-y plane, (c-d) x-z plane and (e-f) y-z plane.

The created microwave images show that the malignant and benign tumours can be indicated in the correct positions. However, the malignant and benign tumours cannot be distinguished due to the noise and the vague outline. Hence, the CNRs of the tumours are extracted in order to discriminate between them.

The first step is to determinate the boundary between the ETR and LTR. The boundary can be estimated using Equation (5.3.1), which is shown in **Fig 6.16** (a). A time window is then applied to remove the ETR and the clutter. The remaining signals which represent the tumour responses are shown in **Fig 6.16** (b). The extracted CNRs and the spectrum of the benign and malignant tumours are shown in **Fig 6.16** (c-d)

The results indicate that the damping factors of the benign tumour are lower than those of the malignant tumour. Besides, the damping factors of the malignant and benign tumours increase from 5 to 8 GHz, then falling down until 9 GHz. Also, the spectrum of the malignant tumour response is lower than that of the benign tumour,

ranging from 0 to 25 GHz. Based on the observations from **Fig 6.16** (c-d), these conclusions can be drawn. Firstly, the damping factors and the spectrum can be affected by tumour morphology. The irregular surface of the malignant tumour causes higher damping factors and lower spectrum responses compared with the smoother surface of the benign tumour. This phenomenon is due to the higher microwave scattering caused by the irregular surface of the malignant tumour. The incident wave are scattered to different directions. However, the benign tumour has a smoother surface which reduces the scattering, and this, increases the amplitude of the spectrum and reduces the damping factors.

The use of the CNRs provides a solution to discriminate between the benign and malignant tumour with similar size when the resulting images cannot provide sufficient resolution.

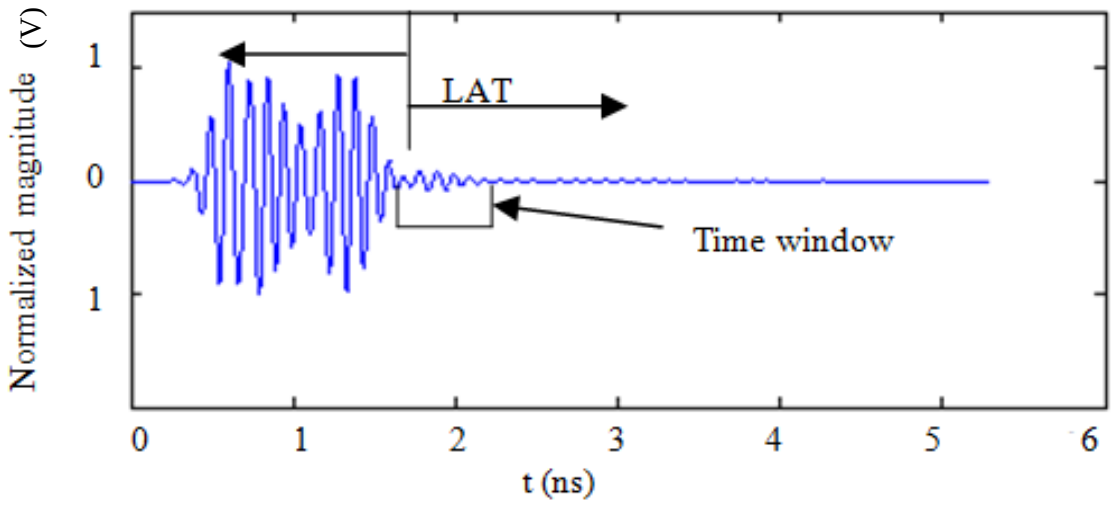

(a)

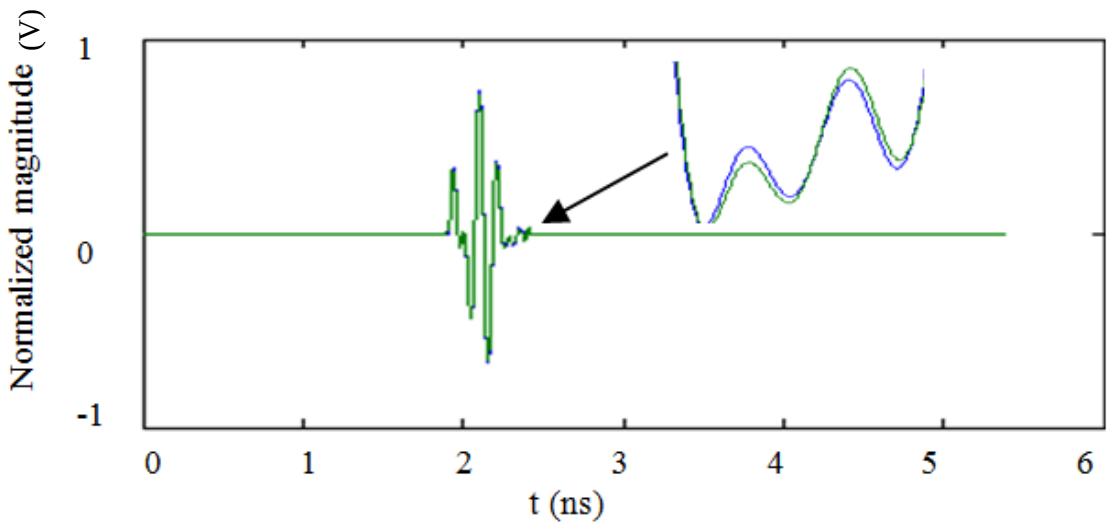
Normalized magnitude (V)
1
0
-1
0
1
2
3
4
5
6
t (ns)

(b)

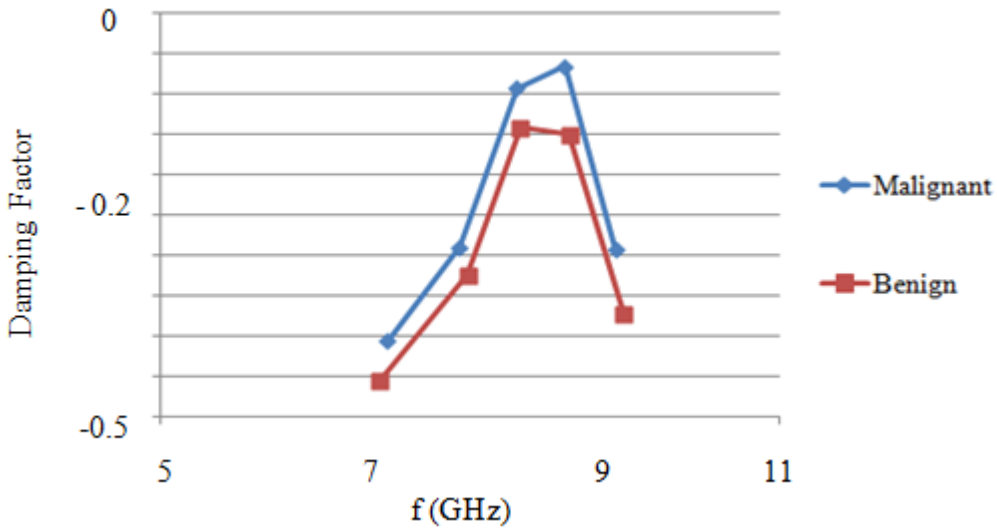
0
-0.2
-0.5
Damping Factor
5
7
9
11
f (GHz)
Malignant
Benign

(c)

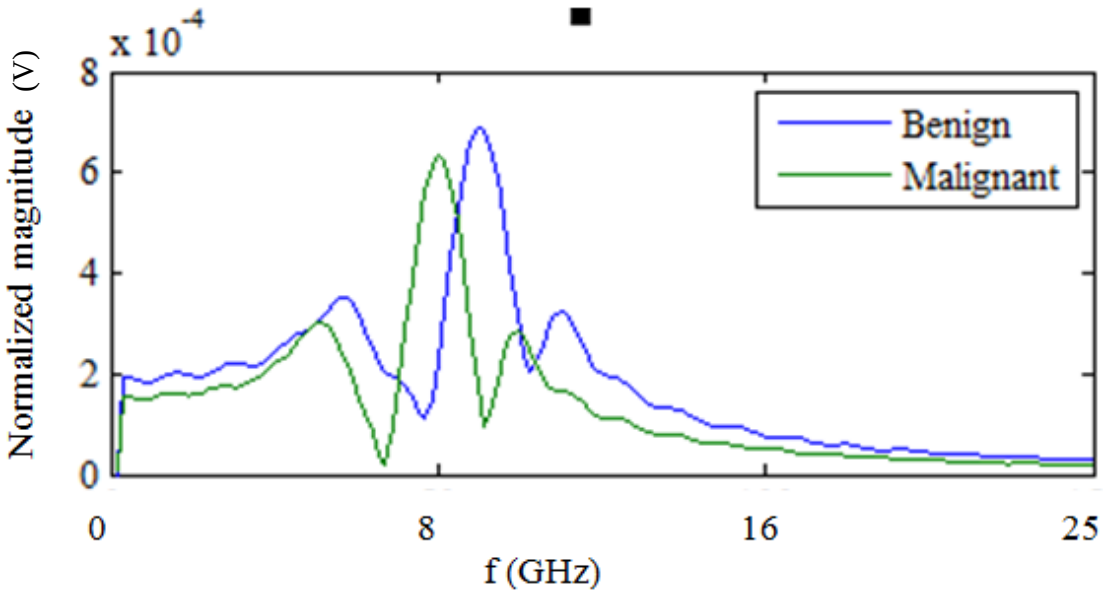

(d)

Fig 6.16 (a) The boundary between the ETR and LTR, (b) tumour response, (c) the damping factor and (d) spectrum of the benign and malignant tumour.

6.4 The Preliminary Study of Brain Cancer Detection

Radar based breast cancer detection has been investigated by many research groups. However, the study of radar based cancer detection for other organs has not been carried out. In our study, the brain cancer detection is considered since the brain has a similar shape compared to the breast. Both of breast and human head have a uniform sphere shape. Besides, they are all composed with different layers. The breast can be

simplified by skin and fat layers, and the human head can be considered as a combination of skin, fat, skull and white matter layers [147].

Based on the electromagnetic theory, the discontinuity of the boundary causes strong reflection of the incident electromagnetic wave. The reflection level is highly dependent on the dielectric difference. For the breast cancer detection, the dielectric difference between the tumour and the fat can achieve 10:1. This significant dielectric difference causes strong reflection from the tumour. For the brain cancer detection, the dielectric difference between the tumour and the white matter can achieve 1.44:1. The dielectric difference of the brain is much smaller than that of the breast.

Besides, the microwave penetrating ability is another important issue. For the breast cancer detection, most of the incident wave is reflected by the skin and only very little energy reaches the tumour. Compared with the breast, the human head has more complex structure (skin, fat and skull) which reflect more energy than the skin layer of the breast [147-148]. This could be the major difficult for the brain cancer detection.

Some challenges and some assumptions for the brain cancer detection have been discussed. In this section, we present the preliminary study of the brain cancer detection in our work, and this, offers valuable further research experience towards the radar based cancer detections for other organs.

6.4.1 The Brain Tumour and its Electrical Properties

6.4.1.1 The Brain Tumour

The brain tumour is a tumour located within the brain and most such tumours lie inside the skull [149]. The tumour is created by abnormally growing cells and could spread to other organs.

Brain cancer is a very serious disease due to the invasive properties of the tumours. Brain tumour can also be divided into benign and malignant tumours. Benign tumour does not invade or destroy surrounding cells or tissues. However, malignant tumour invades and destroys the healthy cells and grows at a high rate.

The signs and symptoms depend on the dimension and the location of the tumour. When symptoms become apparent depends on many factors, with the most important factor being the change from being a benign tumour to a malignant tumour [149].

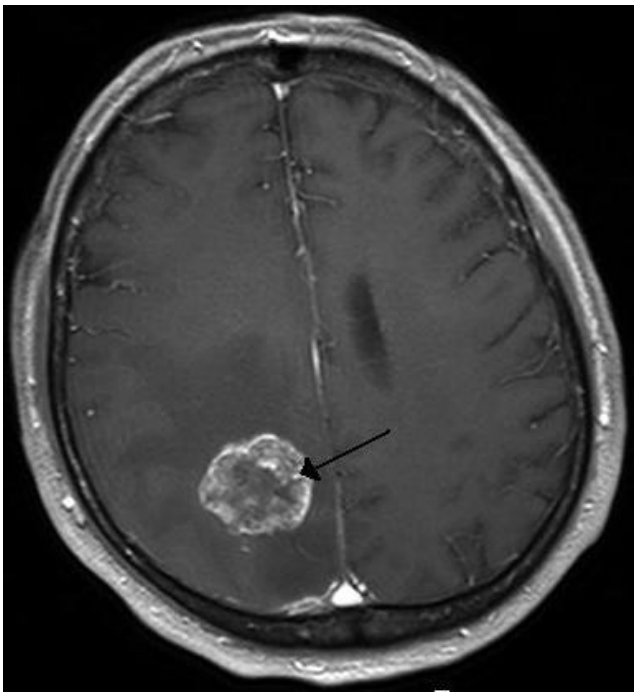

Fig 6.17 The MRI image for brain tumour. [9]

Medical imaging is an important diagnostic method for brain tumour detection. Invasive diagnosis methods such as PEG have been abandoned since it is harmful [149]. Currently, CT and MRI are the most commonly adopted imaging methods. **Fig 6.17** shows a cross-section image of brain tumour based on MRI. It is seen that the

tumour has brighter colour compared with the surrounding tissues. Similarly, CT images also show brain tumour in a brighter colour compared with the surrounding tissues.

The definitive diagnosis of a brain tumour cannot be achieved using the medical images, but can only be confirmed by the histological examination [149]. However, the latter is quite dangerous since most brain tumours are located inside the skull.

6.4.1.2 Electrical Properties

In microwave imaging based cancer detection, the tumour can be detected due to the significant difference in electrical properties between the tumour and its surrounding tissues. The electrical properties of the cancerous breast have been studied in Chapter 2, and in this section, the electrical properties of the cancerous brain are also presented.

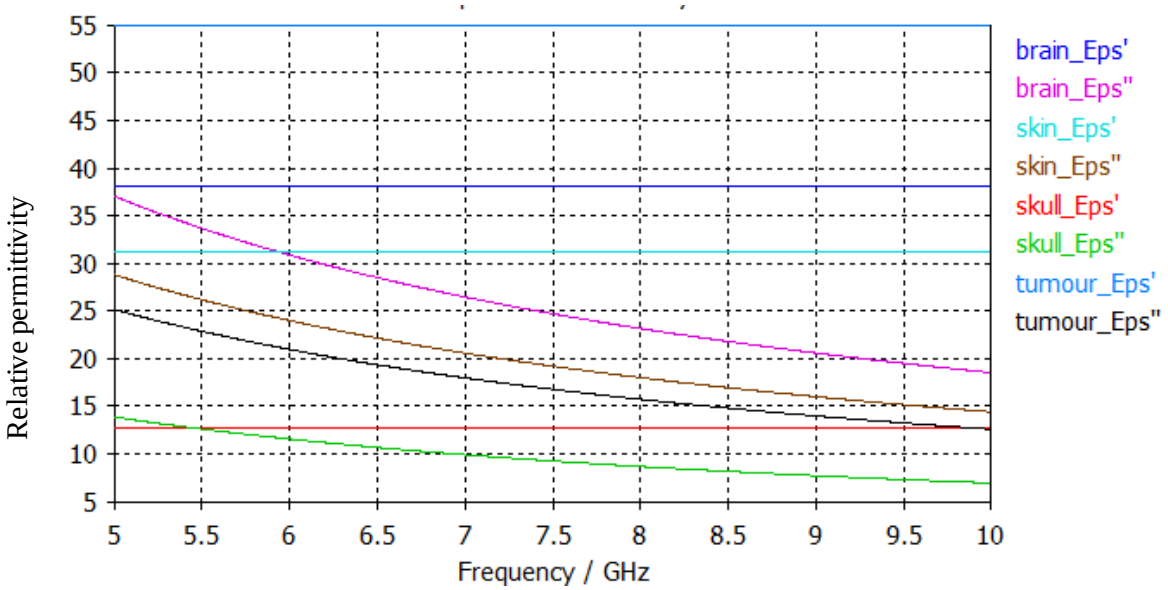

Fig 6.18 The relative permittivity of the skin, fat, skull, brain tissue and tumour in the CST library. Eps', Eps'' are the real, imaginary part of the relative permittivity.

The phantom design for the UWB transmission can be simplified in an approximation as a multi-layer model, with each layer corresponding to a particular layer. The human head can be modelled as a combination of skin, skull, grey matter and white matter layers. The dielectric constant $\varepsilon_r(f)$ in bio-layers can be derived from the Cole-Cole model, given by the equation (6.4.1). This equation shows that the dielectric reduces as the working frequency increases [149]:

$$\varepsilon_\omega = \varepsilon_\infty + \frac{\varepsilon_s - \varepsilon_\infty}{1+(i\omega\tau)^{1-\alpha}} \tag{6.4.1}$$

where ω and α are the angular frequency and exponent parameter, ε_∞ and τ are the static frequency permittivity constants and time constant. ε_ω and ε_s are its static and infinite frequency permittivity constants.

In this work, a cancerous brain phantom is designed for brain cancer detection, using the materials available in the CST. **Fig 6.18** shows the relative permittivity of the skin, fat, skull, brain tissue and tumour in the CST library.

As seen, the ratio of relative permittivity between different layers of the human head can be summarized as follows: skin to skull = 2.46, white matter to skull = 3.02, tumour to white matter = 1.44. Similarly, for the breast cancer detection, the relative permittivity ratio of skin to fat is 6.7. As discussed previously, the discontinuity of the boundary causes a strong wave reflection from the tumour. The reflection level is highly dependent on the dielectric difference. The skin layer reflection in breast cancer detection is due to the high dielectric difference between the air and the skin. The same effect can also occur in the brain tumour detection. However, the human head has many more layers compared to the breast. As seen from the relative permittivity ratios between different layers in human head, the maximum ratio is that of the white matter to the skull (3.02) which is only the half of the skin to the fat ratio (6.7). Based on the ratios between these different layers, it could be predicted that the

energy reflections between head layers (skin and skull layer, skull layer and white layer) could be even smaller than those between breast layers (skin and fat layer). However, another issue is that the ratio of the tumour to the white matter (1.44) is much smaller than that of the tumour to the fat (12), which could reduce the tumour reflection.

This analysis can be verified using the measured reflections, transmission coefficients and microwave images, which are presented in the following sections.

6.4.2 Brain Phantom Design and Measurement Results

6.4.2.1 Cancerous Brain Phantom

The cancerous brain phantom design procedure is similar to that for the cancerous breast phantom. The brain phantom is designed using the CST Microwave Studio. **Fig 6.19** shows the designed cancerous brain phantom, which consists of a skin layer (thickness = 1mm), a skull layer (thickness = 10 mm), a white matter layer (thickness = 60 mm) with a spherical tumour (radius = 5mm) embedded in the white matter layer close to the skull.

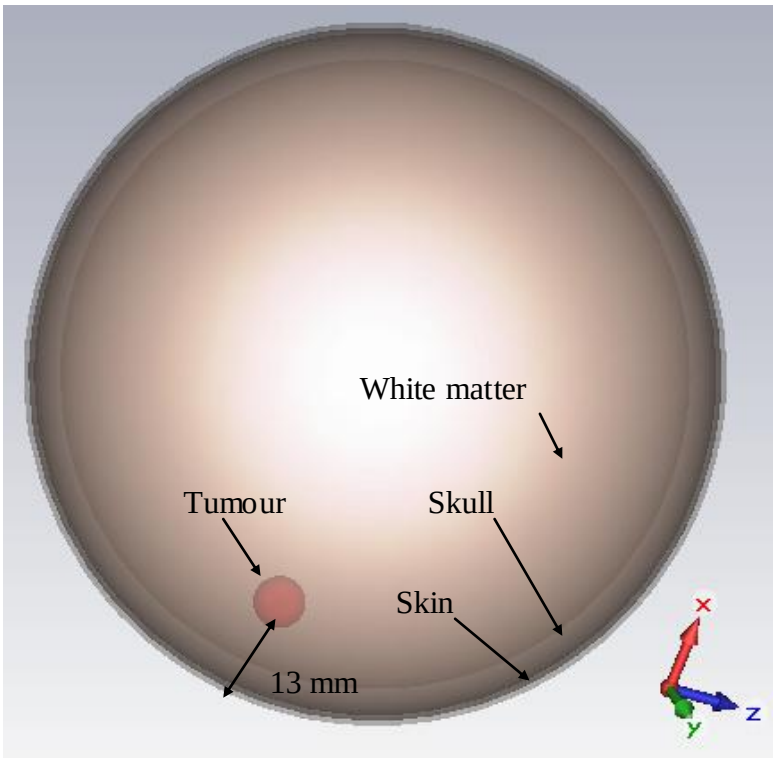

Fig 6.19 The designed cancerous brain phantom.

6.4.2.2 Experimental setup

The antenna pair configuration is used to scan the brain phantom, with the transmission coefficients recorded in the frequency and time domains.

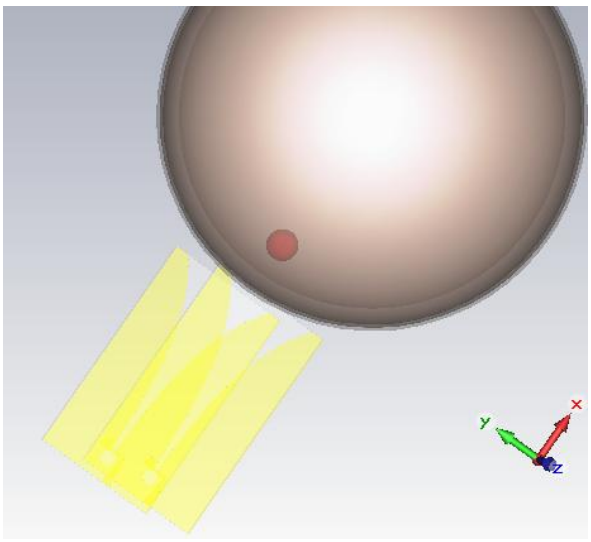

Fig 6.20 The antenna pair configuration for brain cancer detection.

As before, one antenna is used one as the transmitting antenna and the other one as the receiving antenna. The distance between these two antennas is 30 mm, which is greater than λ/2 and this, significantly reduces the mutual coupling of the antennas. This antenna pair moves along the surface of the cancerous brain phantom to scan it while maintaining a constant distance from the skin layer, as shown in **Fig 6.20**. The transmitting antenna transmits the incident wave to the breast phantom, and the reflected wave is received by the receiving antenna. Here the notations O_{xy} and S_{xy} are used to indicate the reflection coefficients and transmission coefficients in the time and the frequency domains, where x indicates the receiving antenna and y indicates the transmitting antenna.

Two experiments are carried out. For the first experiment, two sets of transmission coefficients O_{21} are measured in the time domain, with the measurement results shown in **Fig 6.21**. These two sets of O_{21} are for when the brain phantom is presented with (red curve) and without (blue curve) the tumour embedded. It is seen that the amplitude of the red curve is slight greater than that of the blue curve due to the

tumour reflection. This experiment confirms that the tumour inside the brain is detectable.

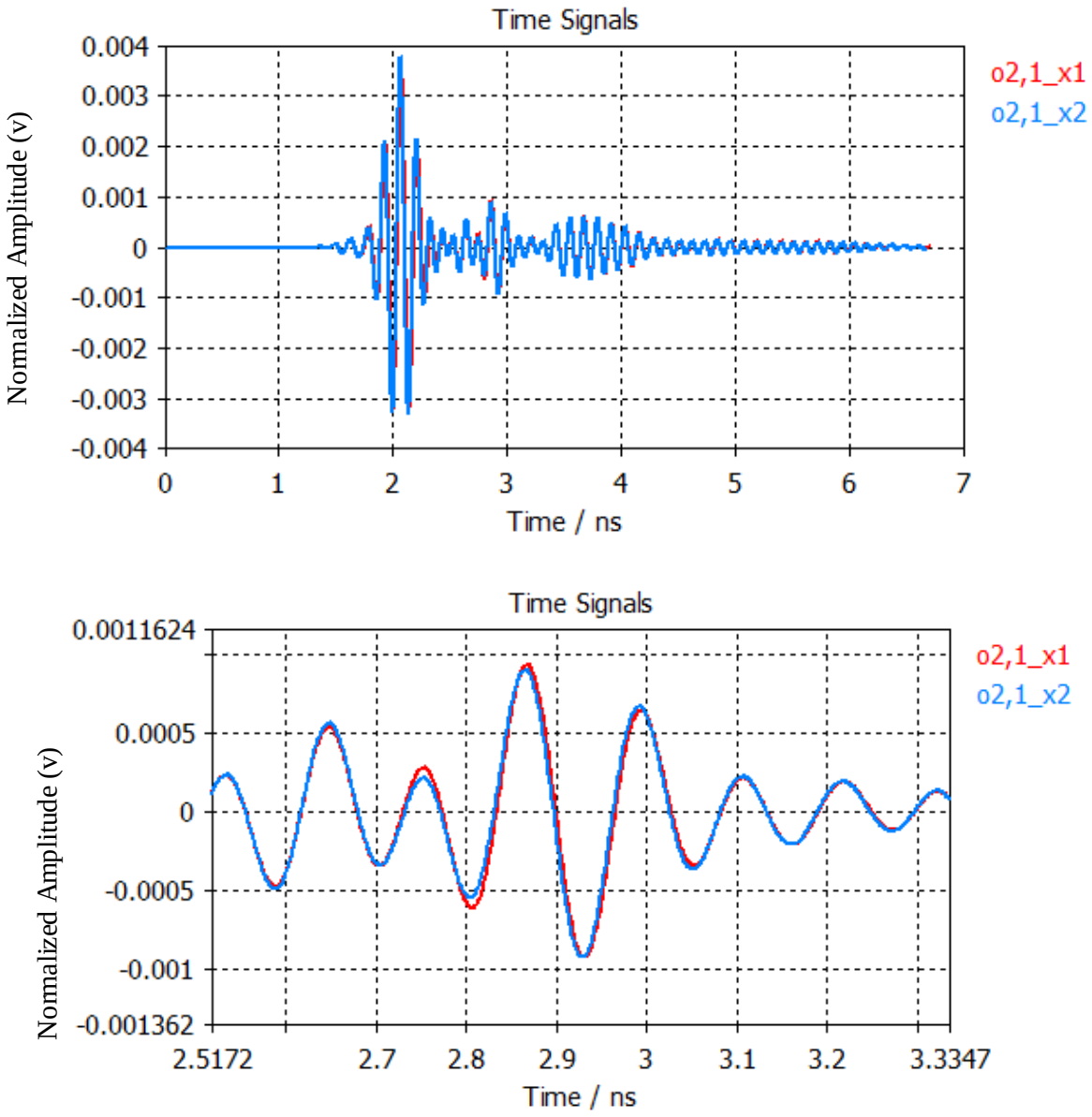

Fig 6.21 The measurement results with and without the tumour presented.

The second experiment is carried out by moving the antenna pair to scan the brain phantom, with received transmission coefficients O_{21} recorded in the positions X_1, X_2 and X_3 as shown in **Fig 6.22**. This experiment is similar to that used for breast cancer detection. **Fig 6.23** shows the measurement results. It is observed that the amplitude of the X_1 is stronger than those of the X_2 and X_3, which shows that the transmission coefficients increase when the transmitting antenna moves close to the tumour due to the strong tumour reflection. Besides, the red and green curves have very close profiles since the X_2 and X_3 are in symmetrical positions.

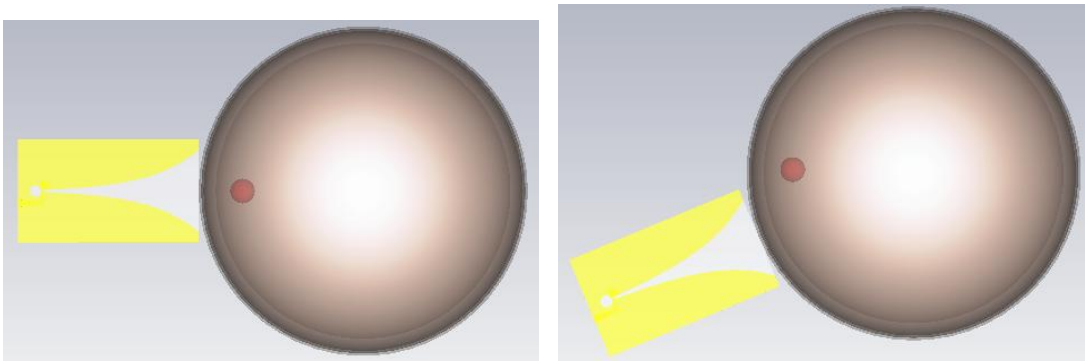

(a) **(b)**

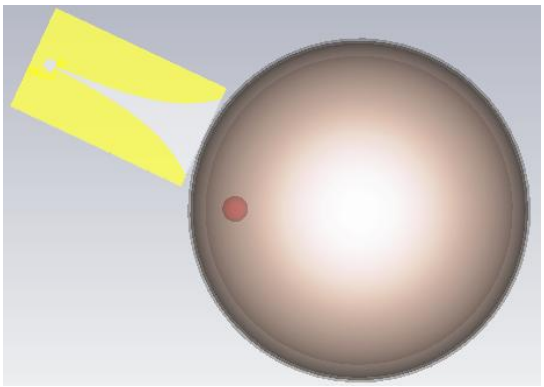

(c)

Fig 6.22 The measurement positions in (a) X_1, (b) X_2 and (c) X_3

Based on these two experiments it can be concluded that the reflected energy increases when the antenna moves close to the tumour; otherwise, the reflected energy is reduced when the antenna moves away from the tumour. This is the basic principle which is used to create the microwave images for the breast cancer detection, and this principle, can also be applied to the brain cancer detection. Besides, although the brain contains more layers than the breast, the microwave energy can still reach the tumour. These important conclusions motivate us to create the microwave images of the cancerous brain.

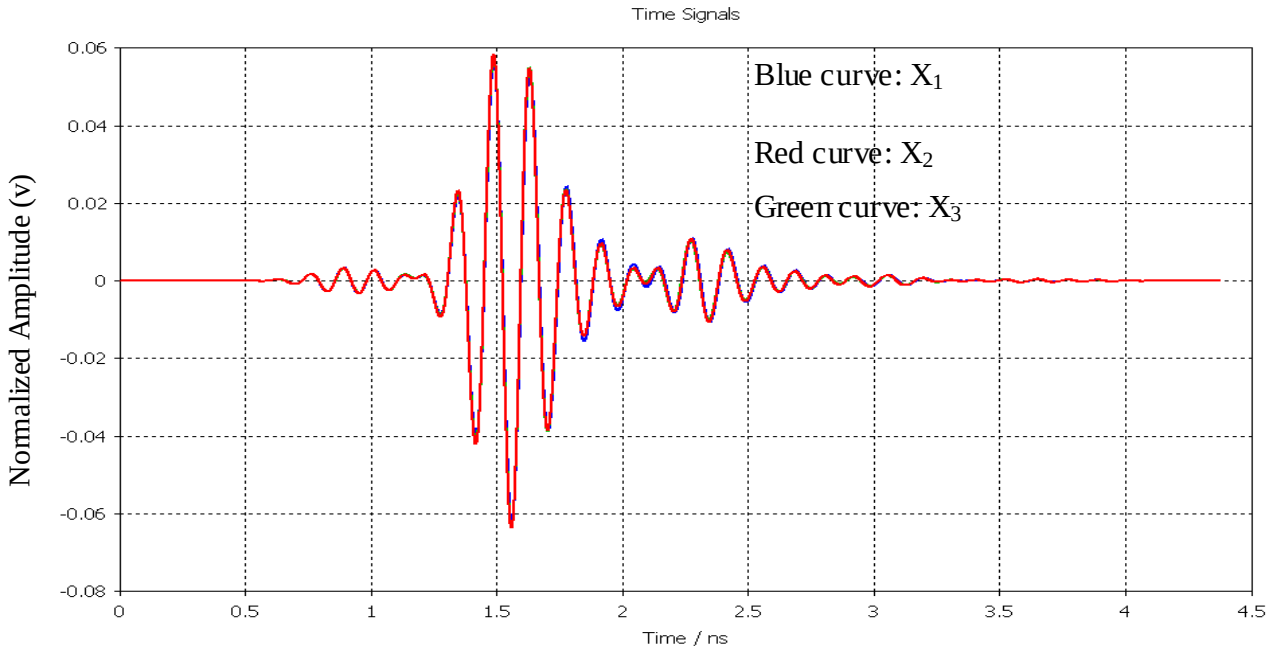

(a)

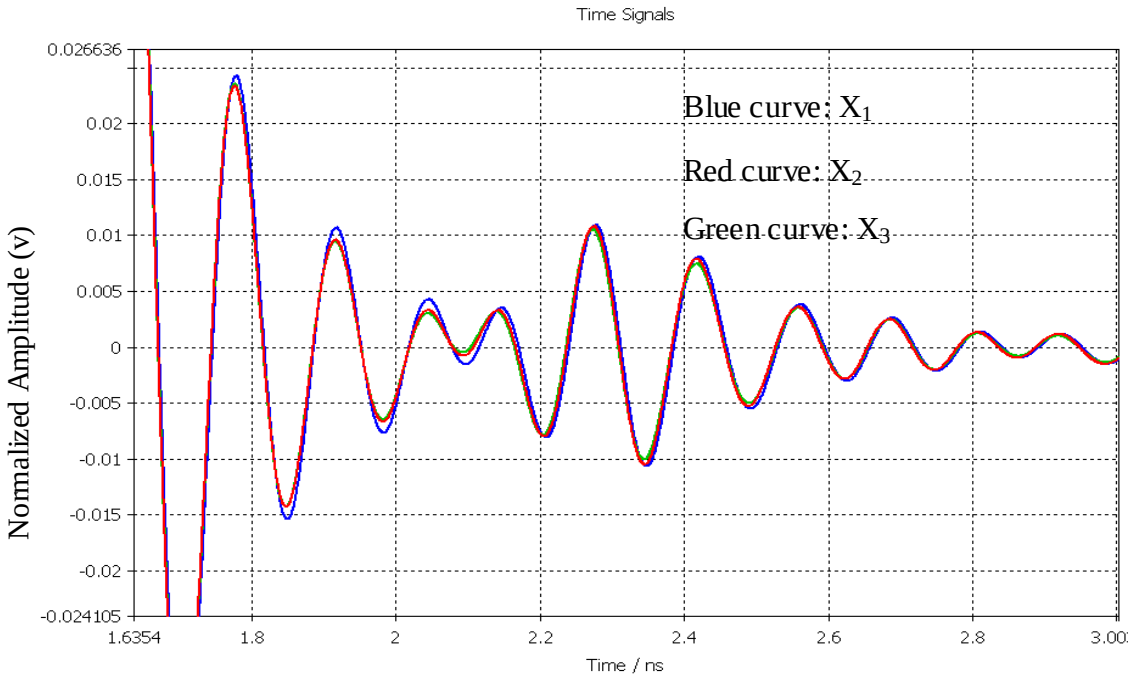

(b)

Fig 6.23 The measurement results in X_1, X_2 and X_3.

6.4.3 Imaging Results for Brain Cancer Detections and the Wavelet De-noising for Resulting Images

6.4.2.3 Microwave images

The measurement results are used to create the microwave images for the cancerous brain. The image creation method is similar to that used in breast cancer detection. Firstly, the received images are processed using the skin and clutters removal method proposed in chapter 5. The extracted tumour response is used to create the microwave images based on the principle that reflected energy increases when the antenna moves

close to the tumour. The intensities of each part of tumour response are used to create the images. **Fig 6.24** shows the microwave images based on the antenna pair configuration. The resulting images are clear enough to indicate the correct tumour position. These resulting images also prove that the radar based microwave imaging can be applied to the brain cancer detection.

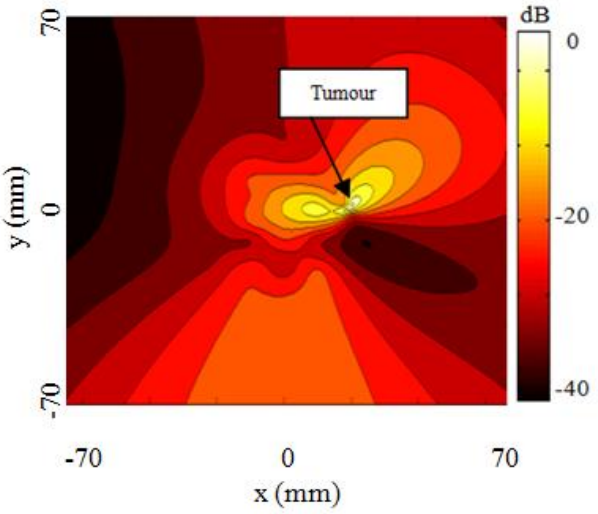

(a)

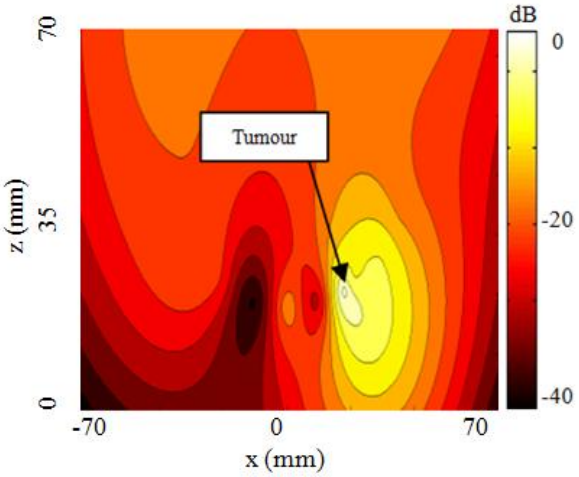

(b)

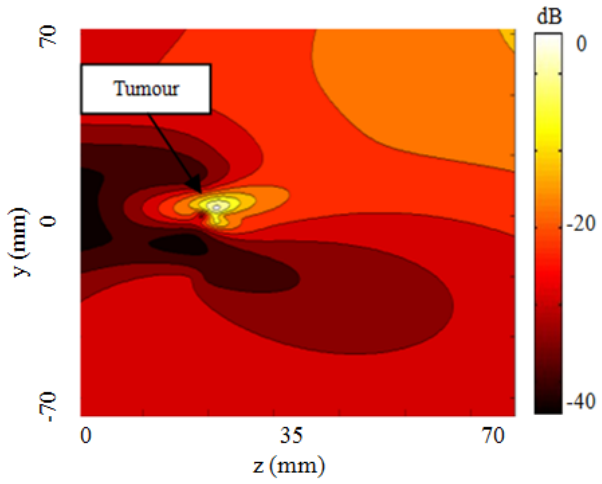

(c)

Fig 6.24 The microwave images created for the brain cancer detection in (a) x-y (b) x-z and (c) y-z.

6.4.2.4 Wavelet De-nosing

The wavelet de-noising method for cancer detection has been proposed in the previous sections. White Gaussian noise is added to degrade the transient scattering signal such that the SNRs of the signals are 60 dB and 45 dB. The use of the wavelet de-noising method greatly suppresses the noise, and the de-noised signals shown in **Fig 6.25**.

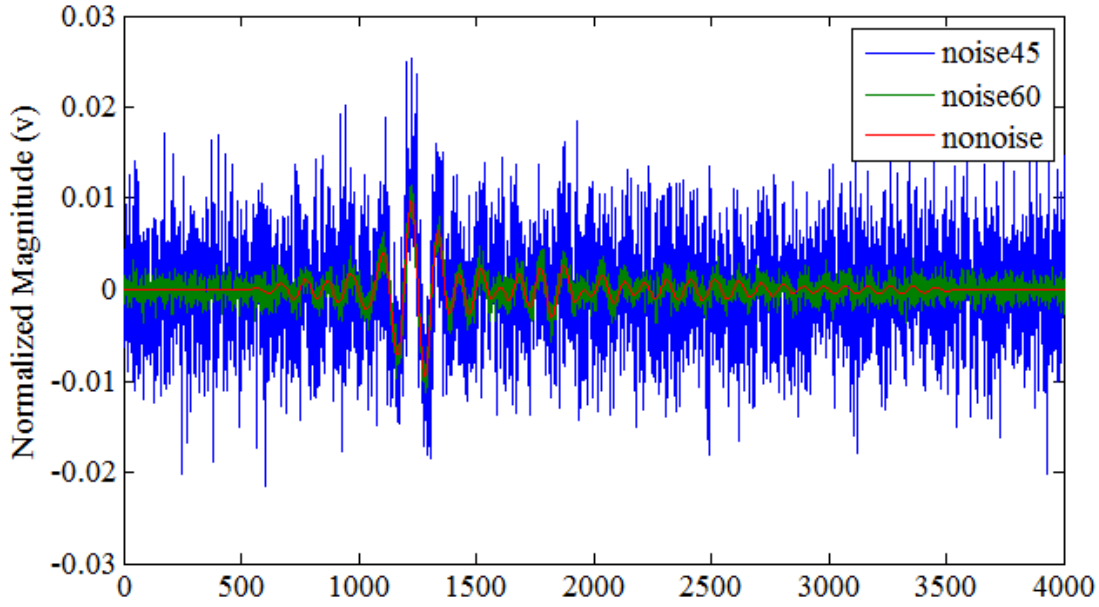

(a)

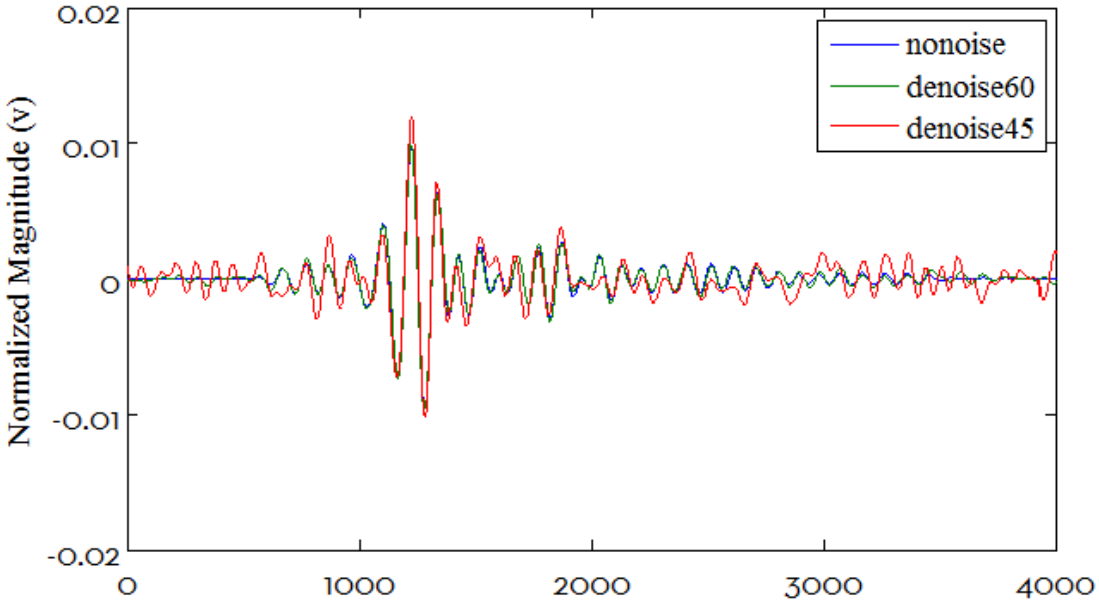

(b)

Fig 6.25 (a) The transient scattering signal (red curve), with noise added such that the SNRs are 60 dB (green curve) and 45 dB (blue curve).

It can be observed that the noise in the signal when the SNR is 60 dB (green cure) has been greatly suppressed while the red curve (signal with and SNR of 45 dB) still contains significant noise. This section describes the creation of the microwave images using these three de-noised curves shown in **Fig 6.25** (b).

Fig 6.26 (a-i) shows the resulting images created for brain cancer detection. **Fig 6.26** (a-c) show the 3-D cross-section of the tumour's position with no added noise. The brain tumour is clearly and correctly indicated. **Fig 6.26** (d-f) show the tumour's location when the transient scattering signal has a 60dB SNR. The tumour's position is still clearly visible although the noise becomes stronger. **Fig 6.26** (g-i) are created using the transient scattering signal with a SNR of 45dB. The tumour's location is still visible, but it begins to be masked by the noise.

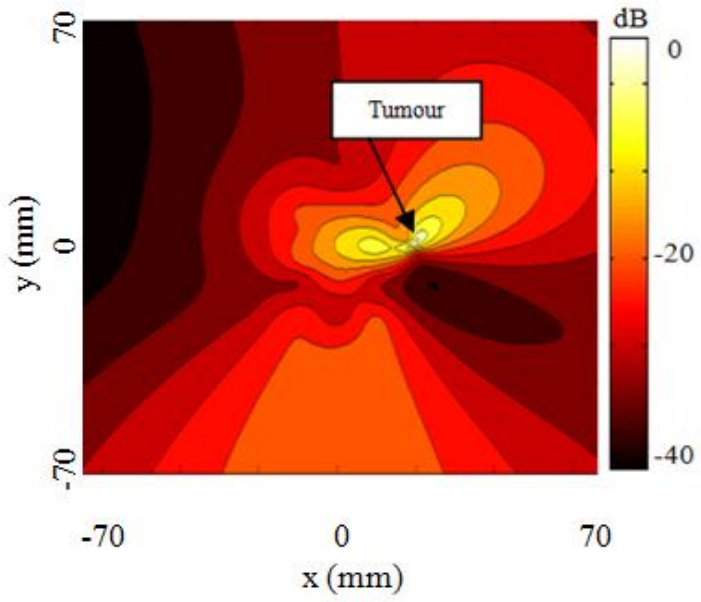

(a)

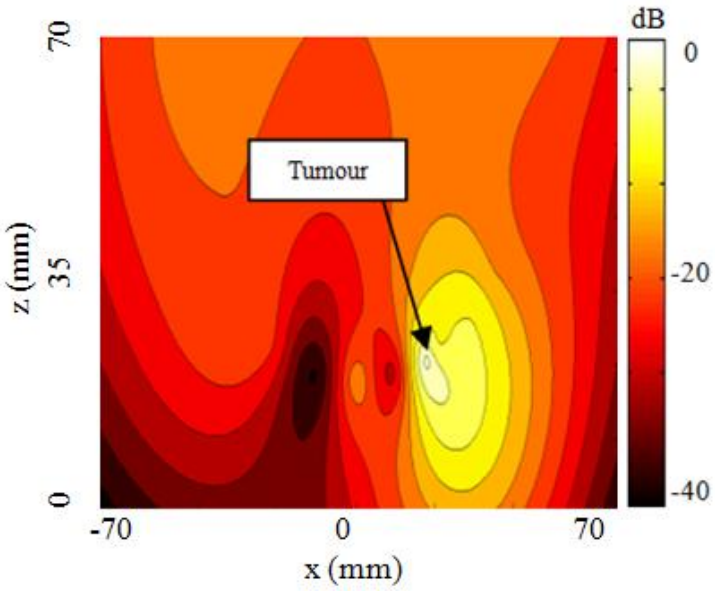
dB
0
-20
-40
Tumour
70
35
0
z (mm)
-70
0
70
x (mm)

(b)

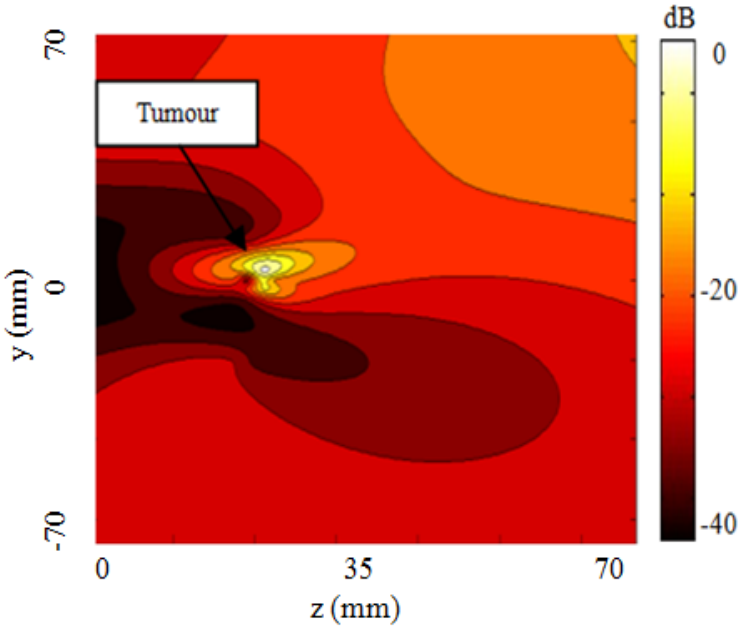
dB
0
-20
-40
Tumour
70
0
-70
y (mm)
0
35
70
z (mm)

(c)

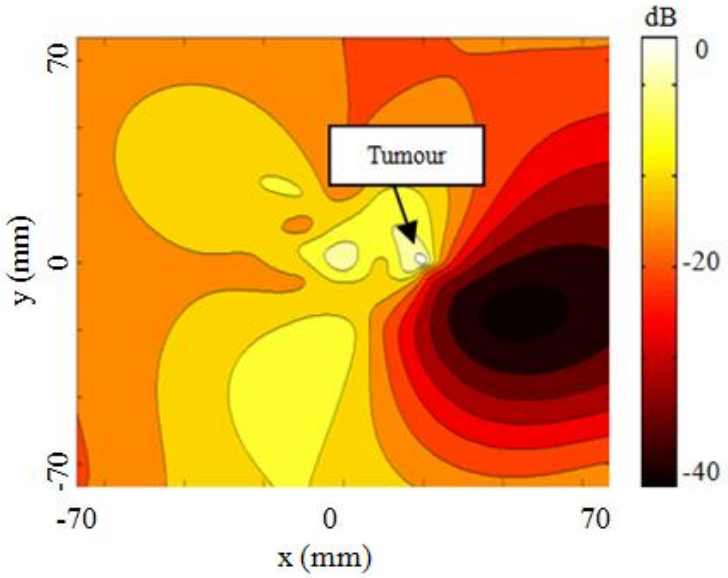
dB
0
-20
-40
Tumour
70
0
-70
y (mm)
-70
0
70
x (mm)

(d)

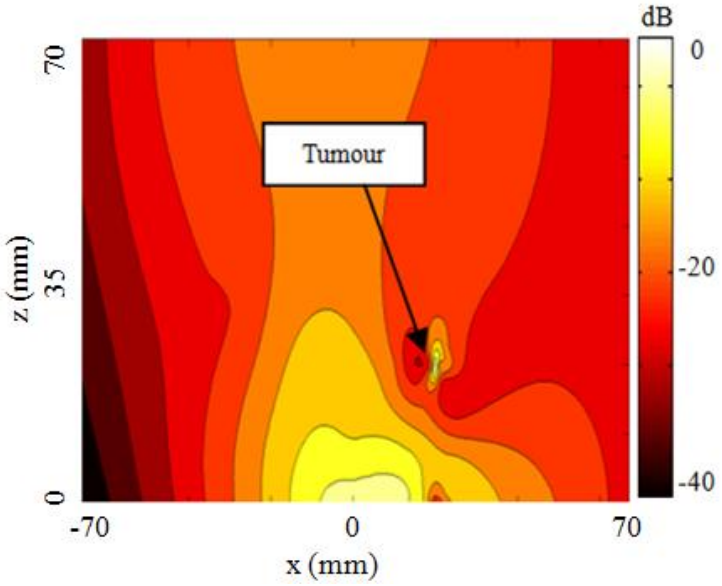
dB
0
-20
-40
Tumour
70
35
0
z (mm)
-70
0
70
x (mm)

(e)

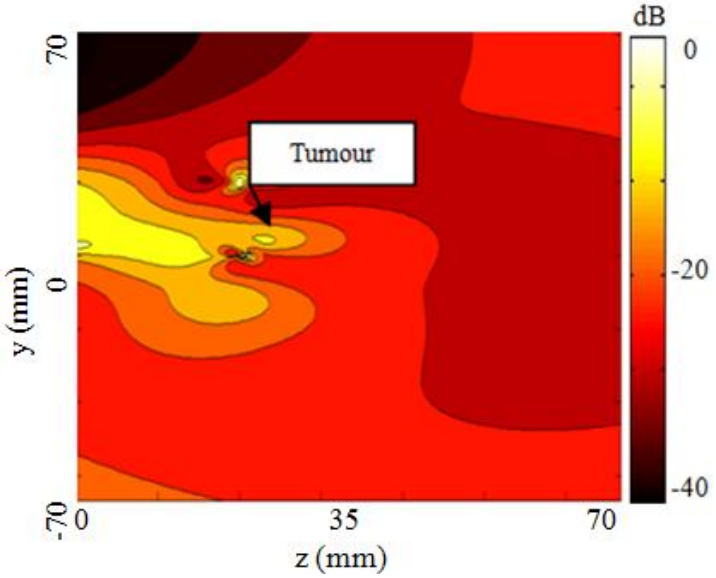
dB
0
-20
-40
Tumour
70
0
-70
y (mm)
0
35
70
z (mm)

(f)

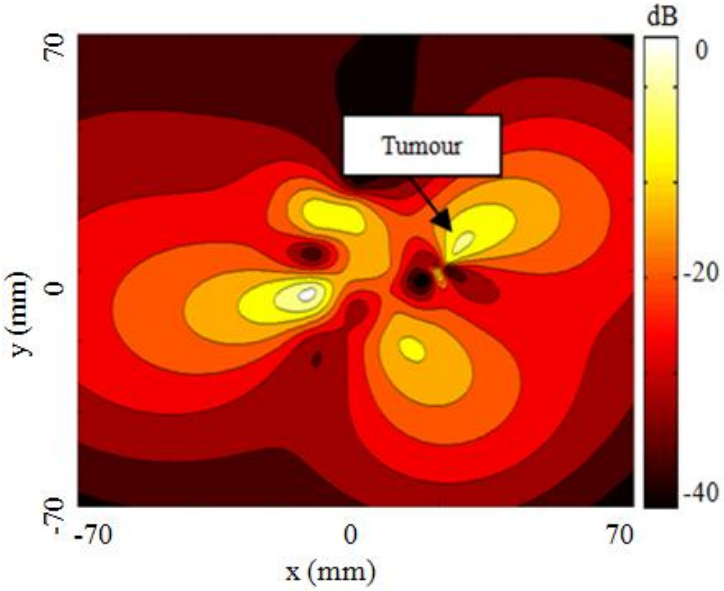
dB
0
-20
-40
Tumour
70
0
-70
y (mm)
-70
0
70
x (mm)

(g)

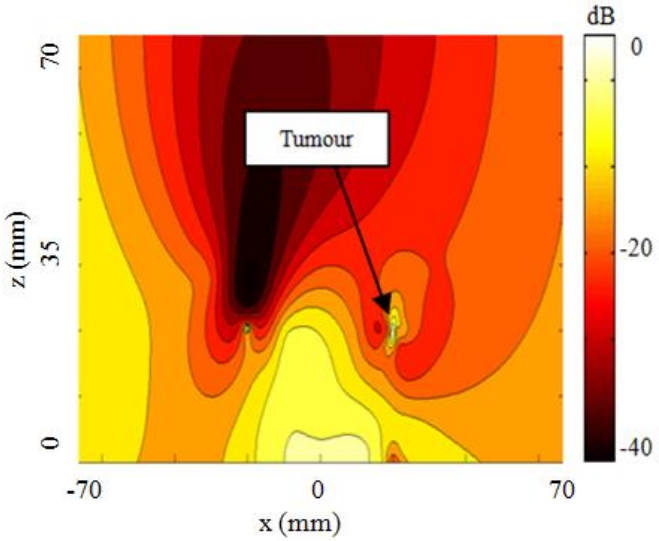

(h)

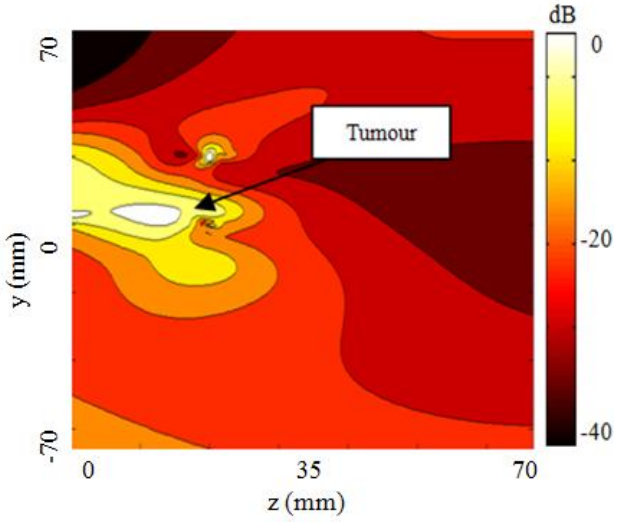

(i)

Fig 6.26 The microwave images of the brain cancer detections in (a) x-y with no noise added (b) x-z with no noise added, (c) y-z with no noise added, (d) x-y with noise added (SNR=60 dB) (e) x-z with noise added (SNR=60 dB), (f) y-z with noise added (SNR=60 dB), (g) x-y with noise added (SNR=45 dB) (h) x-z with noise added (SNR=45 dB), (i) y-z with noise added (SNR=45 dB).

6.4.4 Conclusion for Brain Cancer Detection

A preliminary study of brain cancer detection has been described in this section. Brain tumour and its electrical properties have been discussed first. A cancerous brain model is then designed and simulated in the CST. The antenna pair configuration is used to scan the cancerous brain with the transmission coefficients recorded. The analysis of the received transmission coefficients indicates that the reflected energy increases when the antenna moves close to the tumour, which is identical to the breast cancer detection. Based on this principle, the microwave images for the brain cancer detection have been created. The tumour is correctly indicated in the resulting images. To gain insight into brain cancer detection, white Gaussian noise is added to the received transient scattering signals. The wavelet de-noising method is then used to de-noise the signals. The de-noised signals are then used to create microwave images. The results show that wavelet de-noising is an effective tool for signal de-noising.

The simulation presents that brain cancer can be detected using the radar based microwave imaging. However, the designed brain model still needs to be improved, since the structure of human head is much more complex than in the designed phantom. The use of a more realistic brain phantom will help to gain insight into radar based brain cancer detection.

6.5 Summary

Microwave images are created based on the simulation and experimental results using the non-slot Vivaldi antenna and the slot Vivaldi antenna. The imaging results indicate that a 5 mm tumour is detectable. The use of the non-slot Vivaldi antenna

provides clearer imaging results compared with the slot Vivaldi antenna in both simulation and experimental results. The experimental imaging results contain more noise than the simulated images, but the tumour position is still clearly indicated.

The tumour buried depth is also studied. A multi bio-layer phantom which contains deeply and shallow buried tumours is simulated and measured using the Vivaldi antenna. However, it is still difficult to distinguish between these two tumours from the imaging results due to the very weak amplitude difference in tumour response. A spectrum analysis method is proposed to distinguish between tumour depth differences. The results indicate that a difference of 15 mm in depth between two tumours leads to a mean change of 0.3 dB in the magnitude of spectrum, ranging from 4 to 10 GHz. This information can be used as an effective tool for determining the tumour depth information. Besides, imaging results for the non-slot and slot Vivaldi antenna are also presented. The deeply buried tumour is still difficult to distinguish. However, the use of the slot Vivaldi antenna provides images with low noise due to the wider bandwidth as well as the lower frequency components.

The electromagnetic scattering mechanism for the breast cancer detection has been also studied in Chapter 5. The natural response of object depends only on its properties in terms of surface, material, relative permittivity and conductivity. Malignant and benign tumours have different morphologies, and this, causes different natural responses. The use of the SEM extracts the natural response of the benign and malignant tumour, which is an important factor in discriminating between them. Two cancerous breast phantoms are developed in the CST. The benign tumour has a radius of 5mm and the malignant tumour has an irregular surface with an average radius of 5mm. The single antenna configuration is applied to these two phantoms and the microwave images are created. The benign and malignant tumours cannot be discriminated from the imaging results. Hence, the natural response and the spectrum of the tumour response are extracted from the transient signals. The results show that

the damping factors of the benign tumour are lower than those of the malignant tumour. Besides, the spectrum of the malignant tumour response is lower than that of the malignant tumour. The use of the SEM provides a solution to discriminate benign and malignant tumours with a similar size when the result images themselves cannot provide sufficient resolution.

Furthermore, a preliminary study of brain cancer detection is also carried out. A cancerous brain phantom is measured and imaged using the Vivaldi antenna, and the wavelet de-noising method is applied. The tumour is correctly indicated in these resulting images. However, the designed brain model still needs to be improved since the human head structure is much more complex than the designed phantom. The preliminary study confirms that the brain tumour is also detectable using the radar based imaging method.

Chapter 7 Conclusions and Future Work

7.1 Introduction

This thesis presents several novel aspects of microwave imaging based breast cancer detection, which are the ultra-wideband antenna design, cancerous breast phantom design, experimental setup, signal processing and imaging processing. Besides, a preliminary study of the brain cancer detection is also carried out. This chapter gives a summary of the study and achievements in this thesis. The objectives, main contributions and achievements are reviewed, assessed and evaluated. In the end, the future work and final comments are suggested.

7.2 Summary of the Research

In chapter 3, an ultra-wideband Vivaldi antenna and a slot Vivaldi antenna have been proposed for the breast cancer detection. The desired antenna performance in terms of bandwidth, gain, beam width and radiation pattern is achieved by optimizing structural parameters of the Vivaldi antenna. The designed Vivaldi antenna exhibits an ultra-wideband working frequency ranging from 5 to 10 GHz. The transmission coefficient S_{21} shows a very flat profile, which will provide minimal distortion when creating microwave images. The gains ranging from 5 to 10 GHz achieve the values of 3.613, 6.151, 4.476, 7.207, 9.625 and 3.067 respectively. Furthermore, desired

directional radiation patterns from 5 to 10 GHz are also achieved. The Vivaldi antenna is then fabricated, with the scatter parameters measured in the frequency and time domains using the VNA. The simulated and experimental results show good agreement. Another slot Vivaldi antenna is also proposed in which the Vivaldi antenna parameters are modified in order to achieve a wider bandwidth while maintaining the original dimensions. The equivalent circuit schematic based optimization method is proposed for the modification of the Vivaldi antenna. A slot is optimized and added to the ground of the Vivaldi antenna in order to increase the capacitance, and this, increases the impedance matching in the lower working frequency component. The final design achieves a 3-10 GHz bandwidth while maintaining the original dimensions (73.4mm * 41.9mm). The gains ranging from 3 to 10 GHz achieve the values of 2.5, 5.1, 6, 7.2, 7.1, 8.1, 10, and 4.8, respectively. The increase in bandwidth provides stronger penetration ability to detect more deeply buried tumours.

In chapter 4, the planar breast phantom and hemi-sphere breast phantom are proposed. The use of the planar breast phantom simplifies the experiment and the use of the hemi-sphere breast phantom is more realistic. These two breast phantoms are simulated and fabricated using the CST and tissue-mimicking materials, respectively. Mono-static radar systems based on single antenna and antenna pair configurations are then proposed. These two systems are used to measure the planar breast phantom and hemi-sphere breast phantom respectively, with the reflection coefficients and the transmission coefficients recorded in the time and frequency domains. Based on the measurement results, it is concluded that the reflected energy increases when the antenna moves close to the tumour; otherwise, the reflected energy reduces when the antenna moves away from the tumour. This is the basic principle which is used to create the microwave images to indicate the tumour position. Furthermore, a multi bio-layer phantom which contains skin and fat layers with two tumours buried at different depths is proposed. The slot-Vivaldi antenna is used to measure these two

tumours. The results indicate that the shallow buried tumour response is stronger than that of the deeply buried tumour, but, the difference in response between these two tumours is quite weak.

In chapter 5, the electromagnetic scattering mechanism for breast cancer detection is studied. The singularity expansion method (SEM) for the breast cancer is then proposed. The natural response of the object depends only on its properties in terms of surface, material, relative permittivity and conductivity. The Hilbert Transform and skin and clutter removal methods are proposed to extract the tumour response from the received signals. Nonetheless, white Gaussian noise is added to the received transient scattering signals. The wavelet de-noising method is proposed and used to de-noise the signals. The de-nosing results present that the wavelet de-noising is an effective tools for the signal de-noising.

In chapter 6, the microwave images are created based on the simulation and experimental results using the non-slot Vivaldi antenna and the slot Vivaldi antenna, respectively. The imaging results indicate that a 5 mm tumour can be detected. The use of the Vivaldi antenna provides clearer imaging results compared with the slot Vivaldi antenna in both simulation and experimental results. The experimental imaging results contain more noise than the simulated images but the tumour position is still clearly indicated.

Tumour buried depth is also studied. A multi bio-layer phantom which contains a deep and a shallow buried tumour is simulated and measured using the Vivaldi antenna. However, it is difficult to distinguish between these two tumours from the imaging results due to the very weak amplitude difference in tumour response. a spectrum analysis method is proposed to distinguish the tumour depth difference. The results indicate that 15 mm depth difference between two tumours leads to a mean change of 0.3 dB in the magnitude of spectrum. This information can be used as an effective tool for determining the tumour depth information. Nonetheless, this 0.3 dB

difference is still very weak, which could easily be drowned out in noise. Hence, the signal should be de-noised first. Besides, imaging results based on the non-slot and slot Vivaldi antenna configurations are also compared. The imaging results indicate that the use of the slot Vivaldi antenna provides an image with lower noise due to the wider bandwidth as well as the lower frequency components.

The natural response of object depends only on its properties in terms of surface, material, relative permittivity and conductivity. Malignant and benign tumours have different morphologies, and this, causes different natural response. The use of the SEM extracts the natural response of the benign and malignant tumours, which is an important factor in discriminating benign and malignant tumours. Two cancerous breast phantoms are developed in the CST. The benign tumour has a radius of 5mm and the malignant tumour has an irregular surface with an average radius of 5mm. These two phantoms are measured using the single antenna configuration, and microwave images are created. The benign and malignant tumours cannot be discriminated from the imaging results. Hence, the natural response and the spectrum of the tumour response are extracted from the transient signals. The results show that the damping factors of the benign tumour are lower than those of the malignant tumour. Also, the spectrum of the malignant tumour response is lower than that of the benign tumour. The use of the SEM provides a solution to discriminate between benign and malignant tumours with similar sizes when the resulting images cannot provide sufficient resolution.

A preliminary study of brain cancer detection is described in this chapter. The brain tumour and its electrical properties are discussed first. A cancerous brain model is then designed and simulated in the CST. The antenna pair configuration is used to scan the cancerous brain with the transmission coefficients recorded. The analysis of the received transmission coefficients indicates that the reflected energy increases when the antenna moves close to the tumour, as with breast cancer detection. Based

on this principle, microwave images for the brain cancer detection are created, which correctly indicates the tumour. The simulation shows that brain cancer can be detected using the microwave imaging method. However, the brain model requires improvement, since the structure of human head is much more complex than that of the designed brain phantom. The use of a more realistic brain phantom will help to gain insight into the radar based brain cancer detection.

7.3 Contributions

1. A novel ultra-wideband directional Vivaldi antenna is proposed, simulated and fabricated. This Vivaldi antenna operates as a breast cancer detector with the following advantages: a) ultra-wideband performance (5-10 GHz) to obtain high resolution images; b) directional radiation pattern; c) high near-field power flow density to radiate enough power into the breast phantom; d) compact dimension to obtain enough of signals during the experiment.
2. A modified slot-Vivaldi antenna is proposed, simulated and fabricated based on the original designed Vivaldi antenna. As well as maintaining the advantages of the original Vivaldi antenna, the slot Vivaldi antenna expands the working frequency to (3-10 GHz), and this, increases the penetration ability of the antenna and the image resolution.
3. A planar cancerous breast phantom and a hemi-sphere cancerous breast phantom are proposed, simulated and fabricated for experimental studies.
4. The single and antenna pair configurations are proposed. These two antenna configurations are then used to measure the planar breast phantom and the hemi-sphere breast phantom, with the simulated and measured signals recorded and analyzed.
5. A novel signal processing method is proposed and applied to the scattering signals

received. This method is able to remove unwanted parts of the signals such as skin reflections and clutter. Compared with the traditional skin effect and clutter removal method, the proposed method does not require a reference breast phantom, and therefore can be applied in clinical work.

6. The single antenna and antenna pair configurations based microwave image are created to indicate the tumour position. A tumour with 5 mm radius is clearly detected. The Vivaldi antenna and the slot Vivaldi antenna based imaging results are also compared. The use of the Vivaldi antenna provides clearer imaging results compared with the slot Vivaldi antenna in both simulation and experimental results. The experimental imaging results contain more noise than the simulated images but the tumour position is still clearly indicated.
7. Near-field electromagnetic theory for breast cancer detection is analyzed. The Singularity Expansion Method (SEM) for breast cancer detection is then proposed and applied to discriminate the benign and malignant tumours. A benign tumour with 5 mm radius and a malignant tumour with an average radius of 5 mm can be distinguished using the SEM. The use of the SEM provides a solution to discriminate between benign and malignant tumours with similar sizes when the resulting images themselves cannot provide sufficient resolution.
8. A spectrum analysis based tumour depth detection method is proposed. The Vivaldi antenna and the slot Vivaldi antenna are used to detect tumours at different depth. The results indicate that the use of the slot Vivaldi antenna provides a better detection capability.
9. A wavelet de-noising method is proposed and applied to the scattering signals. The de-noised signals are used to create the microwave images. The results indicate that the wavelet de-noising method can significantly suppress noise.
10. A preliminary study of the microwave imaging based brain cancer detection is carried out. A cancerous brain model is proposed and simulated using the CST. This brain phantom is then measured using the antenna pair based mono-static

imaging system, with the microwave images created to indicate the tumour location. To the best knowledge, similar research has never been implemented. The results show that a brain tumour can be detected using the microwave imaging approach.

7.4 Future work

The possible topics are discussed for further investigation.

7.4.1 The experimental setup

The proposed Vivaldi antenna and the slot Vivaldi antenna achieve the required bandwidth, gain, radiation pattern and beam width for cancer detection. In this thesis, the mono-static radar system is employed for the experiments. This system uses a single antenna or an antenna pair to scan the breast phantom, with the received scattering signals recorded to create microwave images for locating the tumour position. The future work can be carried out from the following steps:

7.4.1.1 The cancerous breast phantom

The breast phantom is simulated and fabricated based on the CST and tissue-mimicking approaches. The main structural components of the cancerous breast phantom are skin, fat and tumours. However, real cancerous breasts are much more complex than the designed phantom. The detailed structure of breast has been discussed in Chapter 2. Also, the designed breast phantom has a hemi-sphere shape. Actually, the shape of the breast can vary between different

people and ages, and may be a hemi-sphere, a bowl shape or a spindle shape. Hence, the next step is to design a more realistic breast phantom. This target should not be difficult to achieve by simulation but fabrication may be more complicated. Hence, the experimental work should be carried out on real patients.

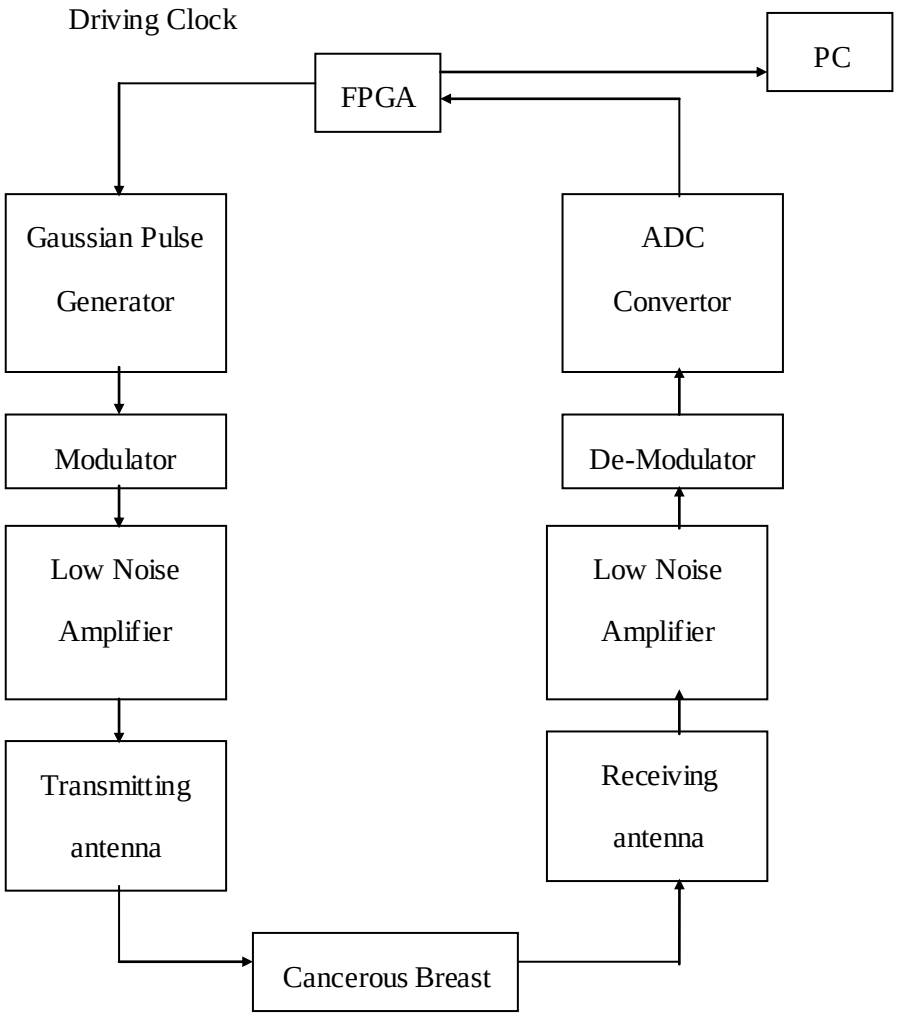

Fig 7.3.1 The proposed imaging system

7.4.1.2 Imaging system design

In this thesis, the antenna is connected to the VNA, with the scattering signals measured. The use of the VNA simplifies the design of mono-static imaging system. However, the disadvantages of the VNA include its high cost and heavy weight. Hence, the future work is to design an imaging system without using the VNA. Here, an imaging system can be proposed based on FPGA for real time signal processing, as shown in Fig 7.3.1. A driving clock is generated by an FPGA and then used to drive a Gaussian Pulse Generator. The Generated pulse is modulated by a modulator. This modulated signal is then amplified by a low noise amplifier and transmitted by the transmitting antenna. This is the transmitting part of the whole imaging system. The receiving part is quite similar to the transmitting part. The scattering signal is received by the receiving antenna and then amplified by the low noise amplifier. Next, the amplified signals are de-modulated and digitalized using the ADC Convertor. The digitalized signals are then sent to the FPGA for storage. Finally, the collected signals are transferred to a PC for signal and imaging processing. This imaging system is quite cheap and easily to be implemented.

Another issue which should be considered in the future work is the distance between the antenna and the skin layer. As discussed, the mono-static imaging system uses the antenna to move to scan the breast while maintaining a constant distance between the antenna and the skin, since the scattering parameter is sensitive to their distance between the antenna and the skin layer. In this thesis, the breast phantom is designed as a hemi-sphere shape. Hence, it is easy to maintain the distance while moving the antenna to scan the breast. However, real breast is not uniform, which increases the difficult of maintaining a steady distance. Here we suggest using an infrared ranging system which could be mounted on the antenna. The use of the infrared ranging system provides a

precise distance detecting approach which would be able to maintain the constant distance to the skin.

Furthermore, some of the studies such as the tumour depth investigation, and discrimination between malignant and benign tumours have only been carried out by simulation so far. Practical experimental work is still required.

7.4.2 The brain cancer detection

The results of the preliminary study of the brain cancer detection indicate that the microwave imaging method can be applied to brain cancer detection. The brain phantom has been simulated as a sphere composed of skin, skull and white matter. However, the head structure is much more complex in structure than the simulated brain phantom. A more realistic brain model is required for future work.

7.4.3 Image processing

The resulting images from the methods proposed clearly indicate tumour location. However, noise also gathers to mask the tumour. A wavelet de-noising method has been proposed and applied to the received signals, but image quality still needs to be improved. It is worth noting that strategies for the improvement of image quality should not only focus on image processing algorithms such as for image de-noising. The antenna design, experimental setup and signal processing all contribute to final image quality.

7.5 Final Comment

Today's high incidence of cancer requires effective, low cost, diagnostic methods which are safe and comfortable for patients to detect cancer in its early stages. The microwave imaging based cancer detection method can be an attractive solution to satisfy all of these requirements. Currently, this type of emerging technology has not been fully studied and the mainstream clinical cancer diagnostic methods are still X-Ray, MRI and Ultra-sonic. In this thesis, several techniques to contribute to the study of microwave imaging based cancer detection have been proposed and developed. It is hoped that future will see the wide use of this potential cancer detection method in our daily lives.

References

[1] J. Guo, S.Wu, W.Wei, J. Zhang, J. Fang, J.Wang, "Nanosecond pulsed electric fields combined with Gemcitabine as a potential breast cancer therapy,"*Plasma Science (ICOPS), 2011 Abstracts IEEE International Conference on* , vol., no., pp.1,1, 26-30 June 2011

[2] A. Langtry, *Understanding Cancer of the Breast*, J. Kelly (Editor). Irish Cancer Society. Dublin, Ireland, 2008.

[3] J. G. Elmore, M. B. Barton, V. M. Moceri, S. Polk, P. J. Arena and S. W. Fletcher, "Ten-Year Risk of False Positive Screening Mammograms and Clinical Breast Examinations", *The New England Journal of Medicine*, Vol.338, No. 16, pp. 1089-1096, 1998.

[4] C. K. Kuhl, S. Schrading, C. C. Leutner, N. Morakkabati-Spitz, E. Wardelmann, R. Fimmers, W. Kuhn and H. H. Schild, "Mammography, Breast Ultrasound, and Magnetic Resonance Imaging for Surveillance of Women at High Familial Risk for Breast Cancer", *Journal of Clinical Oncology*, Vol. 23, No. 33, pp. 8469-8476, 2005.

[5] W. T. Joines, Y. Zhang, C. Li and R. L. Jirtle, "The Measured Electrical Properties of Normal and Malignant Human Tissues from 50 to 900 MHz", *Medical Physics*, Vol. 21, No. 4, 1994.

[6] C. Gabriel, S. Gabriel and E. Corthout, "The Dielectric Properties of Biological Tissues: I. Literature Survey", *Physics in Medicine and Biology*, Vol. 41, pp. 2231-2249, 1996.

[7] A. M. Campbell and D. V. Land, "Dielectric Properties of Female Human Breast Tissue Measured *In Vitro* at 3.2 GHz", *Physics in Medicine and Biology*, Vol. 37, No. 1, pp. 193-210, 1992.

[8] S. Gabriel, R. W. Lau and C. Gabriel, "The Dielectric Properties of Biological Tissues: II. Measurements in the Frequency Range 10 Hz to 20 GHz", *Physics in Medicine and Biology*, Vol. 41, pp. 2251-2269, 1996.

[9] J. Jossinet and M. Schmitt, “A Review of Parameters for the Bioelectrical Characterization of Breast Tissue”, *Annals of the New York Academy of Sciences*, Vol. 873, pp. 30-41, 1999.

[10] S. C. Hagness, A. Taflove, and J. E. Bridges, "FDTD modeling of a coherent-addition antenna array for early-stage detection of breast cancer," in IEEE Antennas and Propagation Society International Symposium, Atlanta, GA, 1998, pp. 1220-1223.

[11] E. C. Fear, X. Li, and S. C. Hagness, "Confocal microwave imaging for breast tumor detection: localization of tumors in three dimensions," IEEE Transactions on Biomedical Engineering, vol. 49, no. 8, pp. 812-822, Aug. 2002.

[12] E. J. Bond, X. Li, S. C. Hagness, and B. D. Van Veen, "Microwave imaging via space-time beamforming for early detection of breast cancer," *IEEE Transaction on Antennas and Propagation*, vol. 51, no. 8, pp. 1690-1705, Aug 2003.

[13] P. M. Meaney, M. W. Fanning, T. Raynolds, C. J. Fox, Q. Fang, C. A. Kogel, S. P. Poplack and K. D. Paulsen, “Initial Clinical Experience with Microwave Breast Imaging in Women with Normal Mammography”, *Academic Radiology*, Vol. 14, No. 2, pp. 207-218, 2007.

[14] A. E. Souvorov, A. E. Bulyshev, S. Y. Semenov, R. H. Svenson and G. P. Tatsis, “Two-Dimensional Computer Analysis of a Microwave Flat Antenna Array for Breast Cancer Tomography”, *IEEE Transactions on Microwave Theory and Techniques*, Vol. 48, No. 8, pp. 1413-1415, 2000.

[15] Y. Xie , B. Guo , L. Xu , J. Li and P. Stoica "Multi-static adaptive microwave imaging for early breast cancer detection", *Proc. 39th Asilomar Conf. on Signals, Syst. and Comput.*, pp.285 -289 2005.

[16] J. M. Sill and E. C. Fear 'Tissue sensing adaptive radar for breast cancer detection—experimental investigation of simple tumor models", *IEEE Trans. Microw. Theory Tech.*, vol. 53, pp.3312 -3319 2005.

[17] M. Klemm, I. J. Craddock, J. A. Leendertz, A. Preece, and R. Benjamin, "Radar-based breast cancer detection using a hemispherical antenna array—experimental results," *IEEE Transactions on Antennas and Propagation,* vol. 57, no. 6, pp. 1692–1704, 2009.

[18] D.Gibbins, M.Klemm, I.J.Craddock, J.A.Leendertz, A.Preece, R. Benjamin, "A Comparison of a Wide-Slot and a Stacked Patch Antenna for the Purpose of Breast Cancer Detection," *Antennas and Propagation, IEEE Transactions on* , vol.58, no.3, pp.665,674, March 2010.

[19] E. Pancera, "Medical applications of the Ultra Wideband technology," *2010 Loughborough Antennas and Propagation Conference (LAPC),* pp.52-56, 8-9 Nov. 2010.

[20] P. Kosmas and C. M. Rappaport, "Time Reversal with the FDTD Method for Microwave Breast Cancer Detection", *IEEE Transactions on Microwave Theory and Techniques*, Vol. 53, No. 7, pp. 2317-2323, 2005.

[21] P. Kosmas and C. M. Rappaport, "A Matched-Filter FDTD-Based Time Reversal Approach for Microwave Breast Cancer Detection", *IEEE Transactions on Antennas and Propagation*, Vol. 54, No. 4, pp. 1257-1264, 2006.

[22] M. Lazebnik.E. L. Madsen.G. R. Frank and S. C. Hagness, 2005, "Tissue-mimicking phantom materials for narrowband and ultrawideband microwave applications" *Phys Med Biol,* 50, pp. 4245-58.

[23] E, Porter, J. Fakhoury, R. Oprisor, M.Coates, M. Popović, "Improved tissue phantoms for experimental validation of microwave breast cancer detection," *Antennas and Propagation (EuCAP), 2010 Proceedings of the Fourth European Conference* on , pp.1,5, 12-16 April 2010.

[24] Y. Chen, E. Gunawan, K. S. Low, S.-C. Wang, C. B. Soh, and L. L. Thi, 'Time of

Arrival Data Fusion Method for Two-Dimensional Ultrawideband Breast Cancer Detection," *IEEE Transaction on Antennas and Propagation*, vol. 55, no. 10, pp. 2852-2865, Oct. 2007.

[25] M. Sajjadieh, F. Foroozan, and A. Asif, "Breast cancer detection using time reversal signal processing," in *Multitopic Conference, 2009. INMIC 2009. IEEE 13th International*, 2009.

[26] World Cancer Report 2014. World Health Organization. 2014.

[27] Song HJ, Xue YL, Qiu ZL, Luo QY. "Uncommon metastases from differentiated thyroid carcinoma". Hell J Nucl Med 15 (3): 233–40.

[28] Gill SS, Heuman DM, Mihas AA. "Small intestinal neoplasms". J. Clin. Gastroenterol. 33 (4): 267–82.

[29] R. M. Rangayyan , N. M. El-Faramawy , J. E. L. Desautels and O. A. Alim "Measures of acutance and shape for classification of breast tumors", *IEEE Trans. Med. Imag.*, vol. 16, no. 6, pp.799 -810 1997.

[30] Y. Chen, E. Gunawan, K. S. Low, S. Wang, C. B. Soh, and T. C. Putti, "Effect of lesion morphology on microwave signature in 2-D ultra-wideband breast imaging," *IEEE Trans. Biomed. Eng.*, vol. 55, no. 8, pp. 2011-2021, Aug. 2008.

[31] Y. Huo, R. Bansal, and Q. Zhu, “Modeling of noninvasive microwave characterization of breast tumors,” IEEE Trans. Biomed. Eng., vol. 51, no. 7, pp. 1089–1094, Jul. 2004.

[32] E. C. Fear, P. M. Meaney, and M. A. Stuchly, “Microwaves for breast cancer detection,” *IEEE Potentials*, vol. 22, no. 1, pp. 12–18, Feb.- Mar. 2003.

[33] S. C. Hagness , A. Taflove and J. E. Bridges "Two-dimensional FDTD analysis of a pulsed microwave confocal system for breast cancer detection: Fixed-focus and antenna-array sensors", *IEEE Trans. Biomed. Eng.*, vol. 45, pp.1470 -1479 1998.

[34] R. Benjamin, “Synthetic, post-reception focusing in near-field radar,” i*nProc. EUREL Int. Conf. on the Detection of Abandoned Land Mines: A Humanitarian Imperative Seeking a Tech. Solution,* Oct. 7–9, 1996, pp. 133–137.

[35] R. Nilavalan , J. Leendertz , I. J. Craddock , R. Benjamin and A. Preece "Breast tumor detection using a flat 16 element array", Proc. 16th Int. Symp. on Electromagn. Compat. Topical Meeting on Biomed. EMC, pp.81 -84 2005.

[36] Y. Xie , B. Guo , L. Xu , J. Li and P. Stoica "Multi-static adaptive microwave imaging for early breast cancer detection", Proc. 39th Asilomar Conf. on Signals, Syst. and Comput., pp.285 -289 2005.

[37] R. Benjamin , I. J. Craddock , G. S. Hilton , S. Litobarski , E. McCutcheon , R. Nilavalan and G. N. Crisp "Microwave detection of buried mines using non-contact, synthetic near-field focusing", Proc. Inst. Elect. Eng. Radar, Sonar and Navigation, vol. 148, no. 4, pp.233 -240 2001.

[38] J. M. Sill and E. C. Fear "Tissue sensing adaptive radar for breast cancer detection—experimental investigation of simple tumor models", *IEEE Trans. Microw. Theory Tech.*, vol. 53, pp.3312 -3319 2005.

[39] Greenlee RT, Murray T, Bolden S, Wingo PA (2000). "Cancer statistics, 2000". CA Cancer J Clin 50 (1): 7–33.

[40] "SEER Training: Breast Anatomy". National Cancer Institute. Retrieved 9 May 2012.

[41] M. Lazebnik, L. McCartney, D. Popovic, C. B. Watkins, M. J. Lindstrom, J. Harter, S. Sewall, A. Magliocco, J. H. Booske, M. Okoniewski and S. C. Hagness, “A Large-Scale Study of the Ultrawideband Microwave Dielectric Properties of Normal Breast Tissue Obtained from Reduction Surgeries”, *Physics in Medicine and Biology*, Vol. 52, pp. 2637–2656, 2007.

[42] K. I. Bland, E. M. Copeland III, N. E. Davidson, D. L. Page, A. Recht and M. M. Urist, *The Breast: Comprehensive Management of Benign and Malignant Disorders*, Elsevier. Vol. 1, 2004.

[43] Saunders, Christobel; Jassal, Sunil (2009). Breast cancer (1. ed. ed.). Oxford: Oxford University Press.

[44] Cooper GM (1992). Elements of human cancer. Boston: Jones and Bartlett Publishers. p. 16.

[45] R. M. Rangayyan , N. M. El-Faramawy , J. E. L. Desautels and O. A. Alim "Measures of acutance and shape for classification of breast tumors", *IEEE Trans. Med. Imag.*, vol. 16, no. 6, pp.799 -810 1997.

[46] Y. Chen, E. Gunawan, K. S. Low, S. Wang, C. B. Soh, and T. C. Putti, "Effect of lesion morphology on microwave signature in 2-D ultra-wideband breast imaging," *IEEE Trans. Biomed. Eng.*, vol. 55, no. 8, pp. 2011-2021, Aug. 2008.

[47] Y. Huo, R. Bansal, and Q. Zhu, "Modeling of noninvasive microwave characterization of breast tumors," IEEE Trans. Biomed. Eng., vol. 51, no. 7, pp. 1089–1094, Jul. 2004.

[48] W. T. Joines, Y. Zhang, C. Li and R. L. Jirtle, "The Measured Electrical Properties of Normal and Malignant Human Tissues from 50 to 900 MHz", *Medical Physics*, Vol. 21, No. 4, 1994.

[49] C. Gabriel, S. Gabriel and E. Corthout, "The Dielectric Properties of Biological Tissues: I. Literature Survey", *Physics in Medicine and Biology*, Vol. 41, pp. 2231-2249, 1996.

[50] A. M. Campbell and D. V. Land, "Dielectric Properties of Female Human Breast Tissue Measured *In Vitro* at 3.2 GHz", *Physics in Medicine and Biology*, Vol. 37, No. 1, pp. 193-210, 1992.

[51] S. Gabriel, R. W. Lau and C. Gabriel, "The Dielectric Properties of Biological Tissues: II. Measurements in the Frequency Range 10 Hz to 20 GHz", *Physics in Medicine and Biology*, Vol. 41, pp. 2251-2269, 1996.

[52] J. Jossinet and M. Schmitt, "A Review of Parameters for the Bioelectrical Characterization of Breast Tissue", *Annals of the New York Academy of Sciences*, Vol. 873, pp. 30-41, 1999.

[53] S.S. Chaudhary, R. K. Mishra, A. Swarup and J. M. Thomas, "Dielectric Properties of Normal and Malignant Human Breast Tissues at Radiowave and Microwave Frequencies", *Indian Journal of Biochemistry & Biophysics*, Vol.21, pp. 76-79, 1984.

[54] M. Lazebnik, L. McCartney, D. Popovic, C. B. Watkins, M. J. Lindstrom, J. Harter, S. Sewall, A. Magliocco, J. H. Booske, M. Okoniewski and S. C. Hagness, "A Large-Scale Study of the Ultrawideband Microwave Dielectric Properties of Normal Breast Tissue Obtained from Reduction Surgeries", *Physics in Medicine and Biology*, Vol. 52, pp.

2637–2656, 2007.

[55] E. Pancera, "Medical applications of the Ultra Wideband technology," *2010 Loughborough Antennas and Propagation Conference (LAPC),* pp.52-56, 8-9 Nov. 2010.

[56] C. K. Kuhl, S. Schrading, C. C. Leutner, N. Morakkabati-Spitz, E. Wardelmann, R. Fimmers, W. Kuhn and H. H. Schild, "Mammography, Breast Ultrasound, and Magnetic Resonance Imaging for Surveillance of Women at High Familial Risk for Breast Cancer", *Journal of Clinical Oncology*, Vol. 23, No. 33, pp. 8469-8476, 2005.

[57] J. G. Elmore, M. B. Barton, V. M. Moceri, S. Polk, P. J. Arena and S. W. Fletcher, "Ten-Year Risk of False Positive Screening Mammograms and Clinical Breast Examinations", *The New England Journal of Medicine*, Vol.338, No. 16, pp. 1089-1096, 1998.

[58] D.J. Watmough and K.M. Quan, "X-ray mammography and breast compression", *Lancet*, 340, p.122, 1992.

[59] S. Davis, B. Van Veen, S. Hagness, and F. Kelcz, "Breast tumor characterization based on ultrawideband microwave backscatter," IEEE Trans. Biomed. Eng., vol. 55, pp. 237–246, Jan. 2008.

[60] Vitaliy Zhurbenko, "Challenges in the Design of Microwave Imaging Systems for Breast Cancer Detection", Advances in Electrical and Computer Engineering, Volume 11, Number 1, 2011.

[61] P. Meaney, M. Fanning, D. Li, S. Poplack, and K. Paulsen, "A clinical prototype for active microwave imaging of the breast," IEEE Transactions on Microwave Theory and Techniques, vol. 48, no. 111, pp.1841–1853, 2000.

[62] Y. Xie , B. Guo , L. Xu , J. Li and P. Stoica "Multi-static adaptive microwave imaging for early breast cancer detection", *Proc. 39th Asilomar Conf. on Signals, Syst. and Comput.,* pp.285 -289 2005.

[63] J. M. Sill and E. C. Fear "Tissue sensing adaptive radar for breast cancer detection—experimental investigation of simple tumor models", *IEEE Trans. Microw. Theory Tech.*, vol. 53, pp.3312 -3319 2005.

[64] M. Klemm, I. J. Craddock, J. A. Leendertz, A. Preece, and R. Benjamin, "Radar-based breast cancer detection using a hemispherical antenna array—experimental results," *IEEE Transactions on Antennas and Propagation,* vol. 57, no. 6, pp. 1692–1704, 2009.

[65] D.Gibbins, M.Klemm, I.J.Craddock, J.A.Leendertz, A.Preece, R. Benjamin, "A Comparison of a Wide-Slot and a Stacked Patch Antenna for the Purpose of Breast Cancer Detection," *Antennas and Propagation, IEEE Transactions on* , vol.58, no.3, pp.665,674, March 2010.

[66] "http://www.cancer.ca/en/cancer-information/cancer-type/breast/anatomy-and-physiology/?region=on"

[67] "http://www.medindia.net/patients/patientinfo/breast-cancer-anatomy.htm"

[68] Liu, Jie; Page, David; Nassif, Houssam; Shavlik, Jude; Peissig, Peggy; McCarty, Catherine; Onitilo, Adedayo A; Burnside, Elizabeth."Genetic Variants Improve Breast Cancer Risk Prediction on Mammograms".American Medical Informatics Association Symposium (AMIA),: 876–885.

[69] Kearon, Clive; Julian, JA; Newman, TE; Ginsberg, JS. "Noninvasive Diagnosis of Deep Venous Thrombosis". Annals of Internal Medicine 128 (8): 663–77.

[70] "http://www.saintanneshospital.org/Saint-Annes/Services-and-Clinical-Centers/Diagnostic-Imaging-Services"

[71] http://www.chalmers.se/en/projects/Pages/Microwave-tomography-for-breast-cancer.aspx

[72] M. Klemm, I. J. Craddock, J. A. Leendertz, A. Preece, and R. Benjamin, "Experimental and clinical results of breast cancer detection using UWB microwave radar," Antennas and Propagation Society International Symposium, 2008. AP-S 2008. IEEE , vol., no., pp.1,4, 5-11 July 2008.

[73] Amineh, R.K.; Ravan, M.; Trehan, A.; Nikolova, N.K.; , "Near-Field Microwave Imaging Based on ScanRaster Scanning With TEM Horn Antennas," Antennas and Propagation, IEEE Transactions on , vol.59, no.3, pp.928-940, March 2011

[74] S. C. Hagness , A. Taflove and J. E. Bridges "Two-dimensional FDTD analysis of a pulsed microwave confocal system for breast cancer detection: Fixed-focus and antenna-array sensors", *IEEE Trans. Biomed. Eng.*, vol. 45, pp.1470 -1479 1998.

[75] R. Benjamin, “Synthetic, post-reception focusing in near-field radar,” i*nProc. EUREL Int. Conf. on the Detection of Abandoned Land Mines: A Humanitarian Imperative Seeking a Tech. Solution,* Oct. 7–9, 1996, pp. 133–137.

[76] R. Nilavalan , J. Leendertz , I. J. Craddock , R. Benjamin and A. Preece "Breast tumor detection using a flat 16 element array", *Proc. 16th Int. Symp. on Electromagn. Compat. Topical Meeting on Biomed. EMC,* pp.81 -84 2005.

[77] Y. Xie , B. Guo , L. Xu , J. Li and P. Stoica "Multi-static adaptive microwave imaging for early breast cancer detection", *Proc. 39th Asilomar Conf. on Signals, Syst. and Comput.,* pp.285 -289 2005.

[78] R. Benjamin , I. J. Craddock , G. S. Hilton , S. Litobarski , E. McCutcheon , R. Nilavalan and G. N. Crisp "Microwave detection of buried mines using non-contact, synthetic near-field focusing", *Proc. Inst. Elect. Eng. Radar, Sonar and Navigation,* vol. 148, no. 4, pp.233 -240 2001.

[79] J. M. Sill and E. C. Fear "Tissue sensing adaptive radar for breast cancer detection—experimental investigation of simple tumor models", *IEEE Trans. Microw. Theory Tech.,* vol. 53, pp.3312 -3319 2005.

[80] E. C. Fear, X. Li, S. C. Hagness and M. A. Stuchly, “Confocal Microwave Imaging for Breast Cancer Detection: Localization of Tumors in Three Dimensions”, *IEEE Transactions on Biomedical Engineering*, Vol. 49, No. 8, pp. 812-822, 2002.

[81] E. J. Bond, X. Li, S. C. Hagness and B. D. Van Veen, “Microwave Imaging via Space-Time Beamforming for Early Detection of Breast Cancer”, *IEEE Transactions on Antennas and Propogation*, Vol. 51, No. 8, pp. 1690-1705, 2003.

[82] R. Nilavalan, A. Gbedemah, I. J. Craddock, X. Li and S. C. Hagness, “Numerical Investigation of Breast Tumour Detection Using Multi-Static Radar”, *IET Electronics Letters*, Vol. 39, No. 25, pp. 1787–1789, 2003.

[83] E. C. Fear and M. A. Stuchly, “Microwave Detection of Breast Cancer”, *IEEE Transactions on Microwave Theory and Techniques*, Vol. 48, No. 11, pp. 1854-1863, 2000.

[84] E. C. Fear, J. Sill and M. A. Stuchly, “Experimental Feasibility Study of Confocal Microwave Imaging for Breast Tumor Detection”, *IEEE Transactions on Microwave Theory and Techniques*, Vol. 51, No. 3, pp. 887- 892, 2003.

[85] Y. Xie, B. Guo, L. Xu, J. Li and P. Stoica, “Multistatic Adaptive Microwave Imaging for Early Breast Cancer Detection”, *IEEE Transactions on Biomedical Engineering*, Vol. 53, No. 8, pp. 1647-1657, 2006.

[86] I. J. Craddock, M. Klemm, J. Leendertz, A. W. Preece and R. Benjamin, “Development and Application of a UWB Radar System for Breast Imaging”, *2008 Loughborough Antennas & Propagation Conference*, 2008.

[87] M. Klemm, I. J. Craddock, J. Leendertz, A.W. Preece and R. Benjamin, “Breast Cancer Detection Using Symmetrical Antenna Array”, *Antennas and Propagation, 2007. EuCAP 2007. The Second European Conference*, Edinburgh, UK, pp. 1-5, 2007.

[88] M. Klemm, I. J. Craddock, J. A. Leendertz, A. Preece, and R. Benjamin, “Radar-based breast cancer detection using a hemispherical antenna array—experimental results,” *IEEE Transactions on Antennas and Propagation,* vol. 57, no. 6, pp. 1692–1704, 2009.

[89] D.Gibbins, M.Klemm, I.J.Craddock, J.A.Leendertz, A.Preece, R. Benjamin, "A Comparison of a Wide-Slot and a Stacked Patch Antenna for the Purpose of Breast Cancer Detection," *Antennas and Propagation, IEEE Transactions on* , vol.58, no.3, pp.665,674, March 2010.

[90] Federal Communications Commission, First report and order 02–48, 2002.

[91] M.Z. Win and R.A. Scholtz, "Ultra-wide bandwidth time-hopping spread-spectrum impulse radio for wireless multiple-access communications", *IEEE Trans. Comm.,* 48, 679–91, 2000.

[92] C. A. Balanis, *Antenna Theory: Analysis And Design*, 3rd ed.: John Wiley & Sons Inc, 2005.

[93] J. Bourqui, M. Okoniewski, E.C.Fear, "Balanced Antipodal Vivaldi Antenna With Dielectric Director for Near-Field Microwave Imaging," *Antennas and Propagation,*

IEEE Transactions on , vol.58, no.7, pp.2318,2326, July 2010

[94] P. J. Gibson, "The Vivaldi Aerial," *Proc. 9th European Microwave Conference, Brighton, U.K.,* Oct. 1979, pp. 101-105.

[95] Hojjat, N., S. Yarasi, S. Safavi-Naeini, and T. Manku, "Design and Analysis of new Fermi-like Tapered Slot Antennas," *IEEE Antennas and Propagation Society International Symposium*, Vol. 3, 2000, pp. 1616-1619.

[96] J. B. Knorr, "Slotline transitions," *IEEE Trans.*, Vol. MTT-22, May 1974, pp. 548-554.

[97] B. Shuppert, "Microstrip/slotline transitions: modeling and experimental investigation," *Microwave Theory and Techniques, IEEE Transactions on*, vol.36, no.8, pp.1272,1282, Aug 1988.

[98] Chao Deng; Yong-jun Xie, "Design of Resistive Loading Vivaldi Antenna," *Antennas and Wireless Propagation Letters, IEEE* , vol.8, no., pp.240,243, 2009

[99] J. B. Knorr, "Slotline transitions," *IEEE Trans.*, Vol. MTT-22, May 1974, pp. 548-554.

[100] Chio, T.H., and D.H. Schaubert, "Parameter Study and Design of Wide-band Widescan Dual-polarized Tapered Slot Antenna Arrays," *IEEE Transactions on Antennas and Propagation*, Vol. 48, No. 6, Jun 2000, pp. 879-886.

[101] D. A. Burrell, J.T. Aberle, "Characterization of Vivaldi antennas utilizing a microstrip-to-slotline transition," *Antennas and Propagation Society International Symposium, 1993. AP-S. Digest* , vol., no., pp.1212,1215 vol.3, June 28 1993-July 2 1993.

[102] D. M. Pozar, Microwave Engineering, John Wiley & Sons Inc, Third edition, 2005.

[103] Schuneman, N., J. Irion, and R. Hodges, "Decade Bandwidth Tapered Notch Antenna Array Element," *Proc. 2001 Antenna Applications Symposium*, Allerton Park, Monticello, Illinois, 2001, pp. 280-294.

[104] http://www.antenna-theory.com/antennas/aperture/vivaldi.php

[105] Antenna Theory: Analysis and Design, Constantine A. Balanis 3rd edition (2005) Ch. 2 p. 34

[106] E. Pancera, "Medical applications of the Ultra Wideband technology," *2010 Loughborough Antennas and Propagation Conference (LAPC),* pp.52-56, 8-9 Nov. 2010.

[107] M. Lazebnik, L. McCartney, D. Popovic, C. B. Watkins, M. J. Lindstrom, J. Harter, S. Sewall, A. Magliocco, J. H. Booske, M. Okoniewski and S. C. Hagness, "A Large-Scale Study of the Ultrawideband Microwave Dielectric Properties of Normal Breast Tissue Obtained from Reduction Surgeries", *Physics in Medicine and Biology*, Vol. 52, pp. 2637–2656, 2007.

[108] F. Thiel, O. Kosch, F. Seifert, "Contrast agent based tumour detection by ultra-wideband radar: A model approach," *2010 Proceedings of the Fourth European Conference on Antennas and Propagation (EuCAP)*, pp.1-3, 12-16 April 2010.

[109] R. Ortega-Palacios, L. Leija, A. Vera, M. F J Cepeda, "Measurement of breast - tumor phantom dielectric properties for microwave breast cancer treatment evaluation," *Electrical Engineering Computing Science and Automatic Control (CCE), 2010 7th International Conference on*, pp.216,219, 8-10 Sept. 2010.

[110] E, Porter, J. Fakhoury, R. Oprisor, M.Coates, M. Popović, "Improved tissue phantoms for experimental validation of microwave breast cancer detection," *Antennas and Propagation (EuCAP), 2010 Proceedings of the Fourth European Conference on* , pp.1,5, 12-16 April 2010.

[111] M. Lazebnik, E. Madsen, G. Frank and S. Hagness, "Tissue-mimicking phantom materials for narrowband and ultrawideband microwave applications," *Phys. Med. Biol., Vol. 50*, pp. 4245-4258, 2005.

[112] S. Gabriel, R.W. Lau and C. Gabriel, "The dielectric properties of biological tissues: II. Measurements in the frequency range 10 Hz to 20 GHz," *Phys. Med. Biol.*, Vol. 41, pp. 2251-2269, 1996.

[113] R. M. Rangayyan , N. M. El-Faramawy , J. E. L. Desautels and O. A. Alim "Measures of acutance and shape for classification of breast tumors", *IEEE Trans. Med. Imag.,* vol. 16, no. 6, pp.799 -810 1997.

[114] Y. Chen, E. Gunawan, K. S. Low, S. Wang, C. B. Soh, and T. C. Putti, "Effect of lesion morphology on microwave signature in 2-D ultra-wideband breast imaging," *IEEE Trans. Biomed. Eng.*, vol. 55, no. 8, pp. 2011-2021, Aug. 2008.

[115] Y. Huo, R. Bansal, and Q. Zhu, "Modeling of noninvasive microwave characterization of breast tumors," *IEEE Trans. Biomed. Eng.*, vol. 51, no. 7, pp. 1089–1094, Jul. 2004.

[116] E. C. Fear, P. M. Meaney, and M. A. Stuchly, "Microwaves for breast cancer detection," *IEEE Potentials*, vol. 22, no. 1, pp. 12–18, Feb.- Mar. 2003.

[117] S. C. Hagness , A. Taflove and J. E. Bridges "Two-dimensional FDTD analysis of a pulsed microwave confocal system for breast cancer detection: Fixed-focus and antenna-array sensors", *IEEE Trans. Biomed. Eng.,* vol. 45, pp.1470 -1479 1998.

[118] R. Benjamin, "Synthetic, post-reception focusing in near-field radar," in*Proc. EUREL Int. Conf. on the Detection of Abandoned Land Mines: A Humanitarian Imperative Seeking a Tech. Solution*, Oct. 7–9, 1996, pp. 133–137.

[119] R. Nilavalan , J. Leendertz , I. J. Craddock , R. Benjamin and A. Preece "Breast tumor detection using a flat 16 element array", *Proc. 16th Int. Symp. on Electromagn. Compat. Topical Meeting on Biomed. EMC,* pp.81 -84 2005.

[120] Y. Xie , B. Guo , L. Xu , J. Li and P. Stoica "Multi-static adaptive microwave imaging for early breast cancer detection", *Proc. 39th Asilomar Conf. on Signals, Syst. and Comput.,* pp.285 -289 2005.

[121] R. Benjamin , I. J. Craddock , G. S. Hilton , S. Litobarski , E. McCutcheon , R. Nilavalan and G. N. Crisp "Microwave detection of buried mines using non-contact, synthetic near-field focusing", *Proc. Inst. Elect. Eng. Radar, Sonar and Navigation,* vol. 148, no. 4, pp.233 -240 2001.

[122] J. M. Sill and E. C. Fear "Tissue sensing adaptive radar for breast cancer detection—experimental investigation of simple tumor models", *IEEE Trans. Microw. Theory Tech.,* vol. 53, pp.3312 -3319 2005.

[123] K. H. Sun, "Resonance-Based Techniques for Microwave Breast Cancer Applications", Virginia Tech, Blacksburg, VA, 2012.

[124] C. E. Baum *On the singularity expansion method for the solution electromagnetic interaction problems,* 1971.

[125] C. E. Baum *Singularity expansion of electromagnetic fields and potentials radiated from antennas or scattered from objects in free space,* 1973.

[126] M. A. Morgan, "Singularity expansion representations of fields and currents in transient scattering", *IEEE Trans. Antennas Propagation.*, vol. AP-32, pp.466 -473 1984.

[127] C. A. Balanis, Advanced Engineering Electromagnetics: John Wiley & Sons, 1989.

[128] E. Heyman and L. B. Felsen "Creeping waves and resonances in transient scattering by smooth convex objects", *IEEE Trans. Antennas. Propagation.*, vol. AP-31, pp.426 -437 1983.

[129] M. L. Van Blaricum and R. Mittra "A technique for extracting the poles and residues of a system directly from its transient response", *IEEE Trans. Antennas Propagation.*, vol. AP-23, pp.777 -781 1975.

[130] A. Poggio , M. L. Van Blaricum , E. K. Miller and R. Mittra "Evaluation of a processing technique for transient data", *IEEE Trans. Antennas Propagation.*, vol. AP-26, pp.165 -173 1978.

[131] H Ouibrahim , D. D. Weiner and T K. Sarkar "Matrix pencil approach to direction finding", *IEEE Transactions on Acoustics, Speech and Signal Processing,* vol. ASSP-36, pp.610 -612 1988.

[132] S. K. Hong, W. S. Wall, T. D. Andreadis, and W. A. Davis, "Practical Implications of Pole Series Convergence and the Early-time in Transient Backscatter," *NRL Memorandum Report*, NRL/MR/5740--12-9411, Apr. 2012.

[133] E. Pancera, "Medical applications of the Ultra Wideband technology," *2010 Loughborough Antennas and Propagation Conference (LAPC),* pp.52-56, 8-9 Nov. 2010.

[134] D. M. Pozar, Microwave Engineering, John Wiley & Sons Inc, Third edition, 2005.

[135] E. Heyman and L. B. Felsen"Creeping waves and resonances in transient scattering by smooth convex objects", IEEE *Trans. Antennas. Propagation.*, vol. AP-31, pp.426 -437 1983.

[136] M. L. Van Blaricum and R. Mittra "A technique for extracting the poles and residues of a system directly from its transient response", *IEEE Trans. Antennas Propagation.*, vol. AP-23, pp.777 -781 1975.

[137] A. Poggio , M. L. Van Blaricum , E. K. Miller and R. Mittra "Evaluation of a processing technique for transient data", *IEEE Trans. Antennas Propagation.*, vol. AP-26, pp.165 -173 1978.

[138] H Ouibrahim , D. D. Weiner and T K. Sarkar "Matrix pencil approach to direction finding", *IEEE Transactions on Acoustics, Speech and Signal Processing,* vol. ASSP-36, pp.610 -612 1988.

[139] S. K. Hong, W. S. Wall, T. D. Andreadis, and W. A. Davis, "Practical Implications of Pole Series Convergence and the Early-time in Transient Backscatter," *NRL Memorandum Report,* NRL/MR/5740--12-9411, Apr. 2012.

[140] M. Klemm, I. J. Craddock, J. A. Leendertz, A. Preece, and R. Benjamin, "Radar-based breast cancer detection using a hemispherical antenna array—experimental results," *IEEE Transactions on Antennas and Propagation,* vol. 57, no. 6, pp. 1692–1704, 2009.

[141] M. Klemm, I. J. Craddock, J. A. Leendertz, A. Preece, and R. Benjamin, "Radar-based breast cancer detection using a hemispherical antenna array—experimental results," *IEEE Transactions on Antennas and Propagation,* vol. 57, no. 6, pp. 1692–1704, 2009.

[142] A. Lazaro, D. Girbau, and R. Villarino, "Wavelet-based breast tumour localization technique using a UWB radar," *Progress In Electromagnetics Research,* Vol. 98, 75-95, 2009.

[143] Li, H. J. and K. M. Li, "Application of wavelet transform in target identification," *Progress In Electromagnetics Research,* Vol. 12, 57-73, 1996.

[144] Lazaro, A., D. Girbau, and R. Villarino, "Simulated and experimental investigation of microwave imaging using UWB," *Progress In Electromagnetics Research,* Vol. 94, 263-280, 2009.

[145] Chui C.K., An introduction to wavelet, Academic Press, 1992.

[146] H. J. Li and K. M. Li, "Application of wavelet transform in target identification," *Progress In Electromagnetics Research,* Vol. 12, 57-73, 1996.

[147] F.Thiel, O. Kosch, F. Seifert, "Contrast agent based tumour detection by ultra-wideband radar: A model approach," *2010 Proceedings of the Fourth European Conference on Antennas and Propagation (EuCAP),* pp.1-3, 12-16 April 2010.

[148] "Brain Tumour Facts 2011". Brain Tumour Alliance Australia. Retrieved 9 June 2014.

[149] E. Pancera, "Medical applications of the Ultra Wideband technology," *2010 Loughborough Antennas and Propagation Conference (LAPC),* pp.52-56, 8-9 Nov. 2010.

Appendix I

Design requirements of the microwave imaging based cancer detection and the research investigations of this thesis are summarized in Figure 1-5. Each figure details the specific design tasks carried out in the appendix chapter and the design tools used to carry out the task.

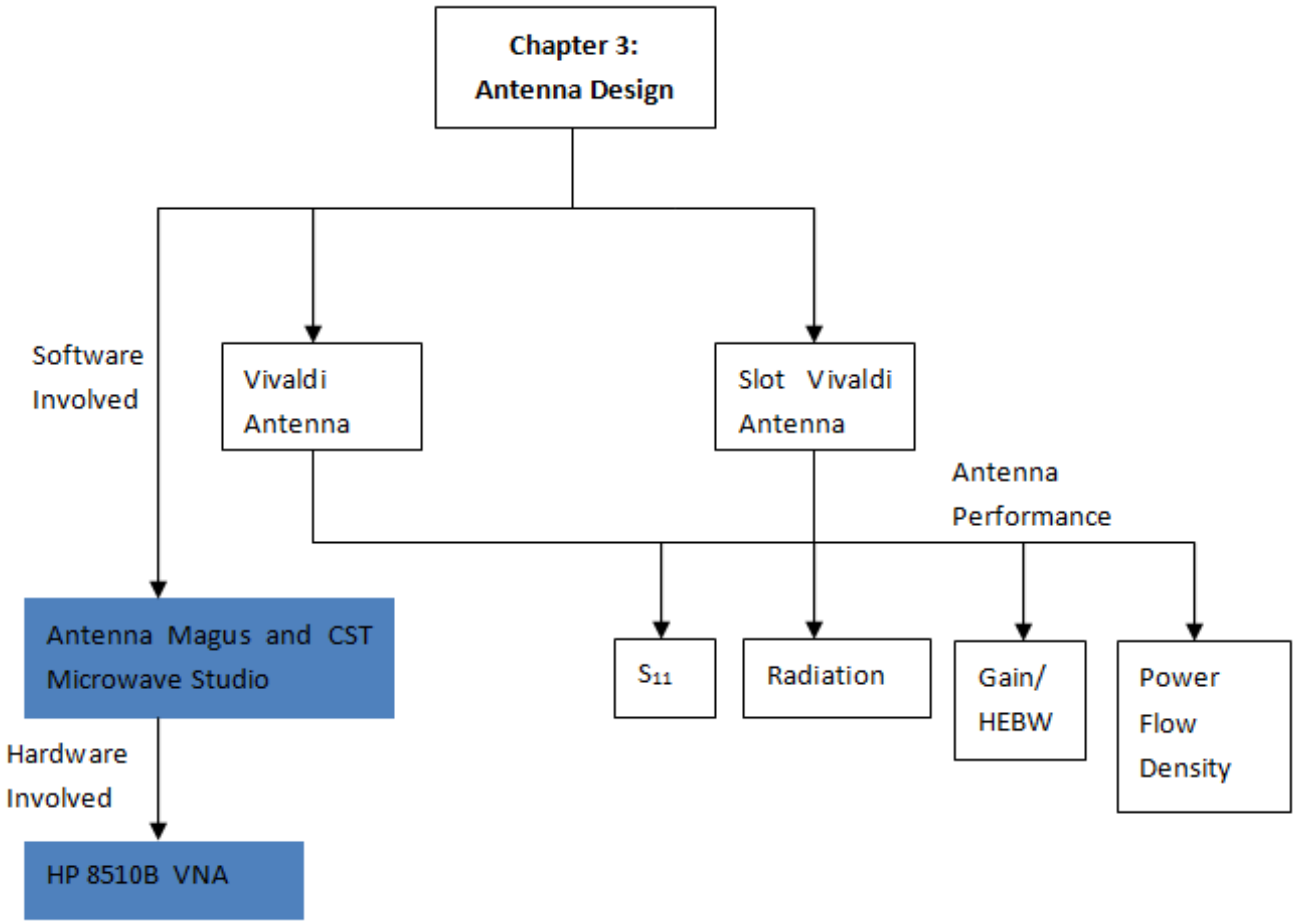

Fig 1. The structure of Chapter 3- antenna design.

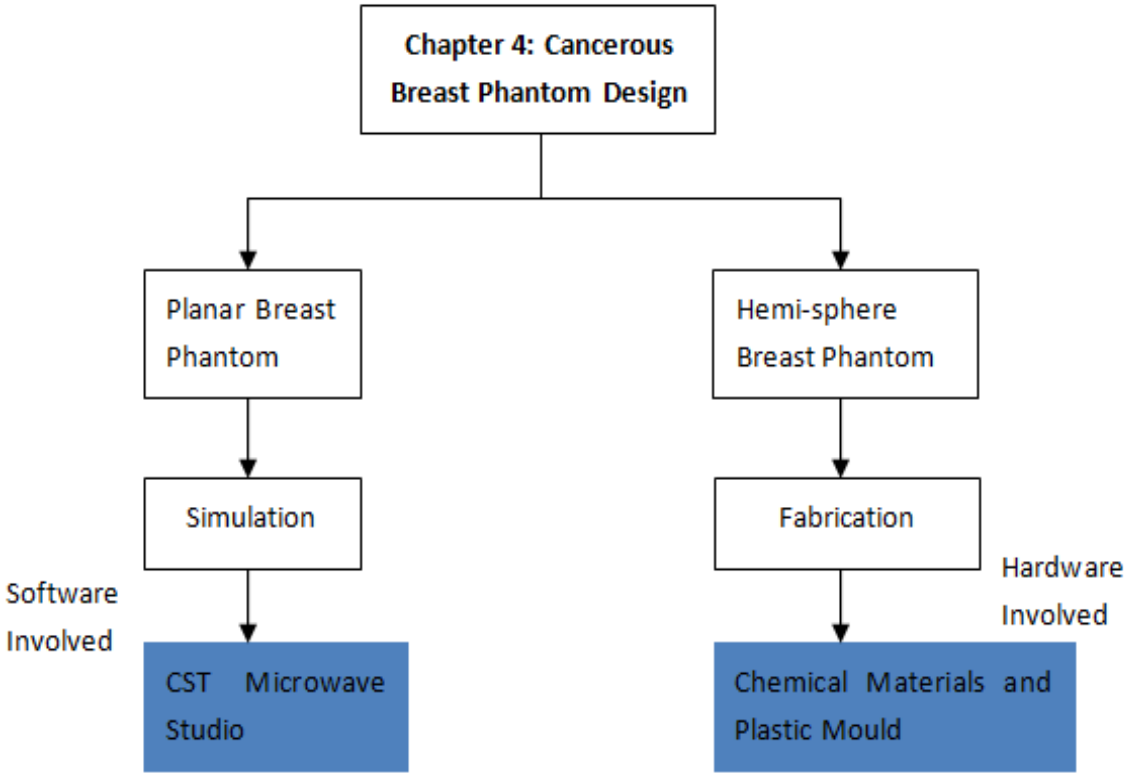

Fig 2. The structure of Chapter 4- cancerous breast phantom design.

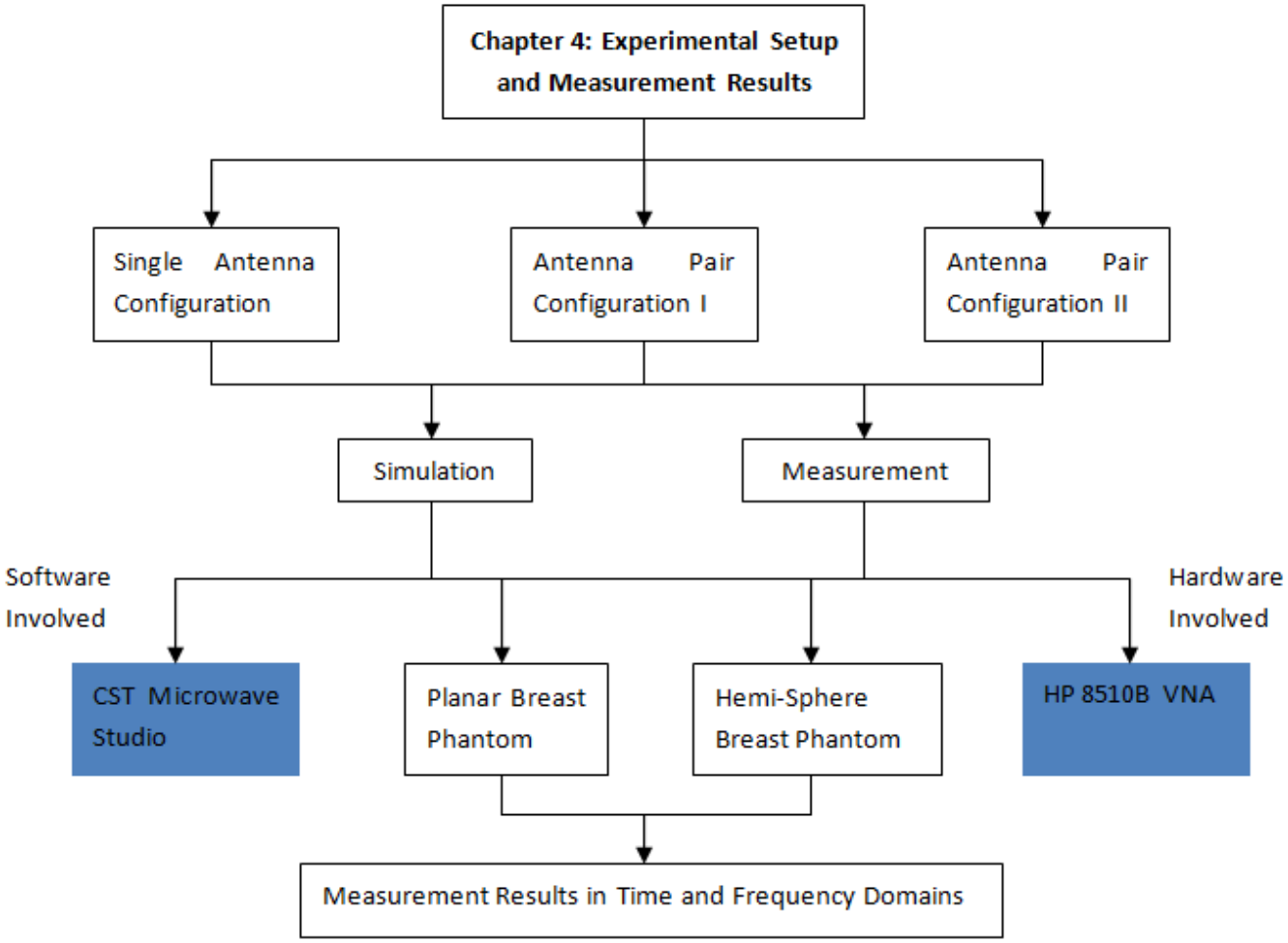

Fig 3. The structure of Chapter 4- experimental setup and measurement results.

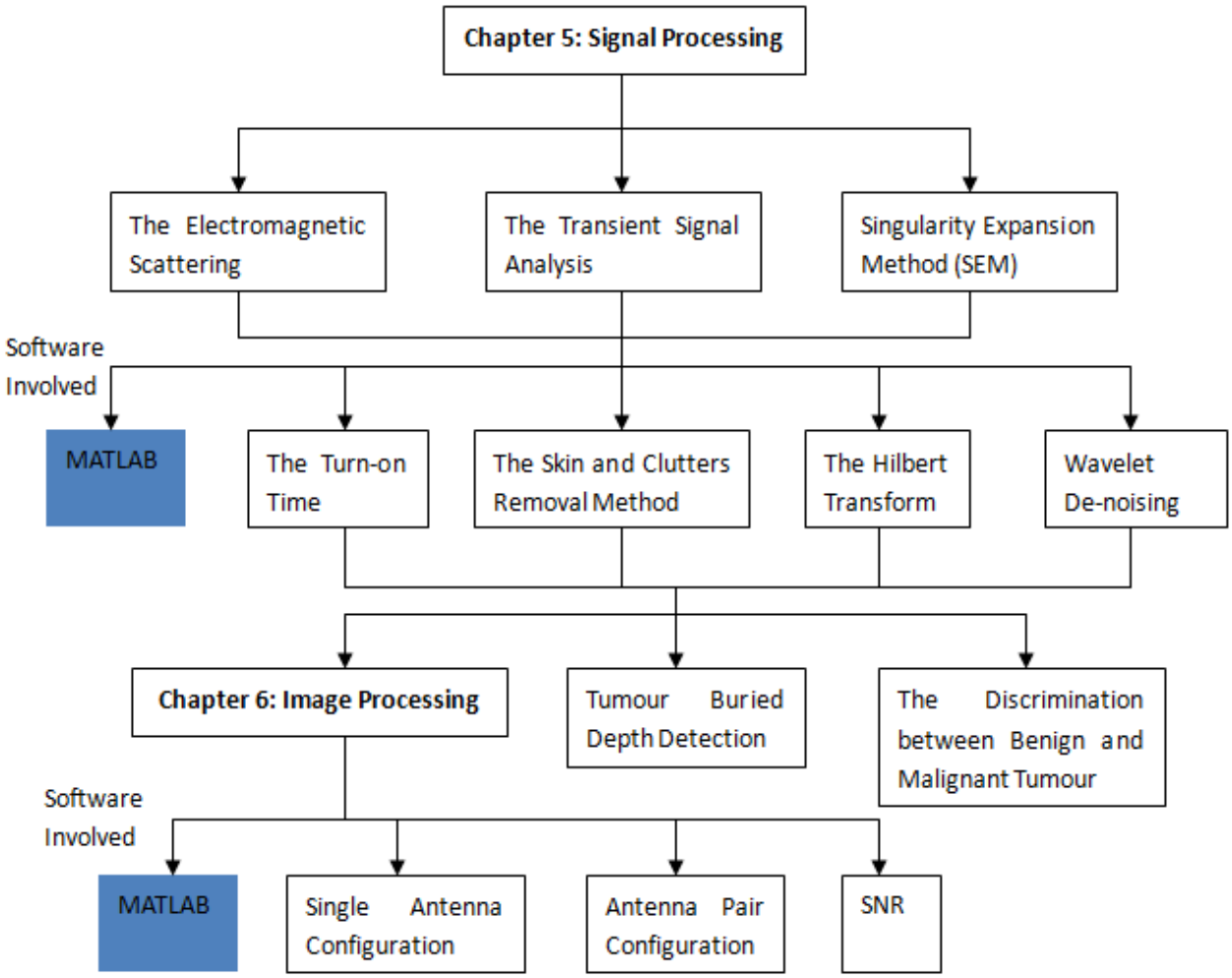

Fig 4. The structure of Chapter 5&6 - signal and image processing results.

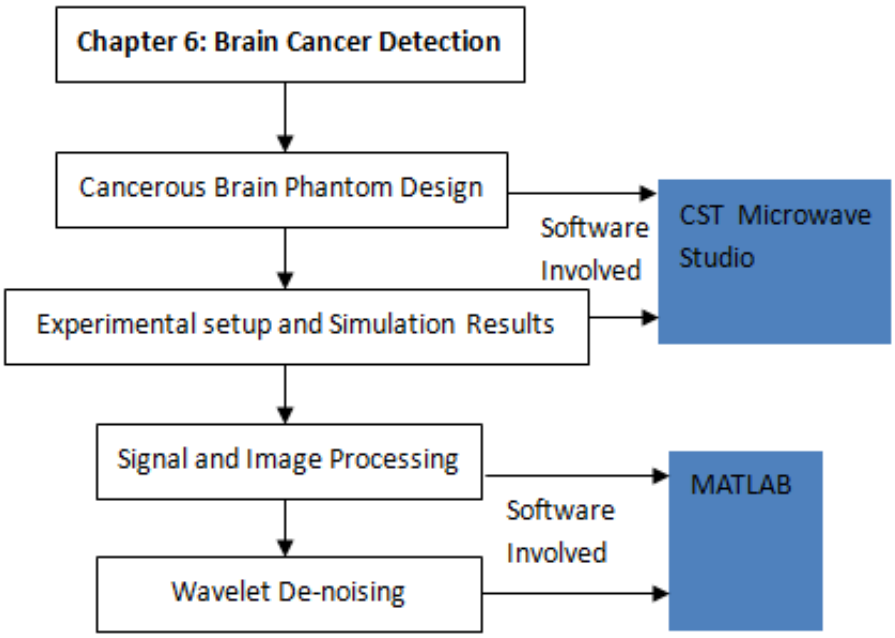

Fig 5. The structure of Chapter 6 – brain cancer detection.